Thermodynamics and transport properties of the ferromagnetic metal $SrRuO_3$ and the frustrated magnet $Cs_3Fe_2Br_9$

Inaugural-Dissertation

zur

Erlangung des Doktorgrades
der Mathematisch-Naturwissenschaftlichen Fakultät
der Universität zu Köln

vorgelegt von
Daniel Brüning
aus Menden (Sauerland)

Köln, 2020

Berichterstatter:	Prof. Dr. Thomas Lorenz
	Prof. Dr. Markus Braden
Vorsitzender der Prüfungskommission:	Prof. Dr. Simon Trebst
Tag der mündlichen Prüfung:	26.06.2020

Contents

1 Introduction

Magnetism fascinated humans ever since its discovery. From the first technical application as a compass [1] through the use for data storage in information technology [2] to possible future applications like spintronics [3], magnetism plays an important role in our everyday life and is a dominant engine of the technological progress. The spirit of understanding the underlying mechanisms fascinated and is still fascinating uncountable scientists.

Magnetic materials mostly consist of elements with partially filled shells. Very different magnetically ordered states exist, ranging from ferromagnetic metals like iron, cobalt, and nickel to antiferromagnetic oxides like MnO, FeO, CoO, and NiO [4], to complex magnetic systems like skyrmions in MnSi [5], to name a few examples. Fundamental interactions that play the most important role in such magnetic materials are coulomb interaction, exchange interaction, and spin-orbit coupling. In materials with 3d transition-metal ions, the magnetism is typically dominated by electron-electron correlations. The increased orbital size of 4d and 5d ions reduces the energy scale for the electron correlations, while the spin-orbit interaction grows to a comparable level. The interplay of these interactions yields many interesting phenomena. An example for systems where the spin-orbit interaction is very important are Kitaev materials [6] with a spin-liquid ground state which may be realized in α-$RuCl_3$ [7] and Na_2IrO_3 [8, 9]. Another candidate was $Ba_3CeIr_2O_9$ [10], which turned out to be a so-called cluster material with Ir_2O_9 bi-octahedra and strong spin-orbit coupling [11]. This thesis studies two related materials in this context, the first is the ferromagnetic metal $SrRuO_3$ with sizable spin-orbit interaction. The second is the new material $Cs_3Fe_2Br_9$, which is an analogon to the cluster material $Ba_3CeIr_2O_9$ but with weak spin-orbit interaction in the Fe_2Br_9 bi-octahedra.

Ruthenates became scientifically popular by the observation of superconductivity in Sr_2RuO_4 [12]. The material itself is not interesting from a technological perspective because of its low transition temperature, but due to its structural similarity to the high-T_C cuprates like $YBa_2Cu_3O_{7-\delta}$ [13]. Both materials consist of layers of corner-sharing MO_6 octahedra with M = Ru, Cu, respectively. The pairing symmetry in Sr_2RuO_4 has been discussed controversially since the discovery of superconductivity in this material. There is evidence for spin-triplet Cooper pairs [14] but only recently new insights raised questions

about this result [15]. Ferromagnetic fluctuations have been proposed as the pairing mechanism. This motivated studies of the closely related ferromagnetic metal $SrRuO_3$, which is the infinite-layered member ($n = \infty$) of the Ruddlesden-Popper series $Sr_{n-1}Ru_nO_{3n+1}$, where the octahedra are also corner-sharing in the third dimension. $SrRuO_3$ is widely studied in thin films and also used as a ferromagnetic layer in perovskite heterostructures [16]. Another hot topic in solid-state physics is topology. Recently, the extraordinary behavior of the anomalous Hall conductivity and of the temperature dependence of magnetic excitations have been explained with the topology of the band structure [17, 18]. The presence of sizable spin-orbit coupling and Weyl points close to the Fermi energy yield an additional contribution to the electron velocity based on the concept of the Berry curvature. In Cologne, a recipe was found to synthesize large high-quality single crystals with the floating-zone technique [19]. This work provides a detailed study of these single crystals. The thermodynamic characterization yields new insights in the criticality of the ferromagnetic phase transition. The magnetic anisotropy is clarified and a previously unknown shape-memory effect of $SrRuO_3$ is found. The combined analysis of electric transport and magnetization measurements gives new insights in the anomalous Hall effect induced by the Berry-curvature effect. Its signature is found in neutron-scattering experiments. The reported analysis is improved by showing the anomalous temperature dependence not only for the magnon gap but also for the stiffness.

The second material studied in this work is the new potential cluster material $Cs_3Fe_2Br_9$. Magnetic cluster materials contain separated structural building blocks of highly-connected metal coordination polyhedra. Inside these units, the metal-metal interaction is dominant and the metal-metal distance can be shorter than in the corresponding elemental metal [20]. The relative size of the intra-cluster and inter-cluster exchange determines the magnetism of such materials. In $Cs_3Fe_2Br_9$, the main building blocks are face-sharing Fe_2Br_9 bi-octahedra arranged in triangular layers that are stacked to build a hexagonal structure. $Ba_3CeIr_2O_9$ is structurally very similar and consists of face-sharing Ir_2O_9 bi-octahedra. In this material, the iridium ions form molecular orbitals inside each bi-octahedron with strong spin-orbit coupling [11]. $Cs_3Cr_2Br_9$ and $Cs_3Cr_2Cl_9$ also consist of face-sharing Cr_2X_9 bi-octahedra [21] and are isostructural to $Cs_3Fe_2Br_9$. However, in these 3d spin systems the spin-orbit interaction is only a small perturbation. The chromium ions are strongly bound so that their antiferromagnetic exchange dominates, leading to a singlet ground state. An applied magnetic field reduces the energy of the magnetic states and induces a phase transition to a magnetically ordered state [22]. Interestingly, $Cs_3Fe_2Br_9$ shows antiferromagnetic magnetic order. The phase diagram is studied with thermal expansion, magnetostriction, and magnetization. These studies also make use of high-field

facilities with the capability of magnetic fields up to 57 T. The magnetic ground-state structure is determined by neutron scattering. The results are compared to related materials and numerical predictions for appropriate model Hamiltonians. This allows first approximations of the underlying coupling strengths.

The thesis is structured as follows. Chapter 2 introduces required theoretical concepts, with special focus on transverse transport mechanisms and numerical predictions for magnetic model Hamiltonians. The following introductory Chapter 3 presents the experimental techniques and setups used in this work. Chapter 4 presents a study of the magnetoelastic coupling, criticality, and electric transport of floating-zone-grown single crystals of the ferromagnetic metal $SrRuO_3$. The new potential cluster material $Cs_3Fe_2Br_9$ is studied in Chapter 5 via multiple thermodynamic quantities. The obtained magnetic structure and the magnetic phase diagram are compared to related materials and model systems.

2 Theory

Contents

This chapter introduces some basic models and concepts that are employed in the discussion and interpretation of experimental results on $SrRuO_3$ and $Cs_3Fe_2Br_9$ in Chapters 4 and 5. Starting from a basic motivation of electric transport and the underlying scattering effects, special attention is paid to transverse transport mechanisms. Besides the extrinsic effects skew scattering and side jump, especially the intrinsic effect caused by spin-orbit coupling and the topology of the band structure is discussed. Furthermore, magnetic exchange mechanisms and magnetic order are introduced. Finally, analytical and numerical predictions for the magnetic order on the 2D triangular lattice and the hexagonal closed packed structure are presented.

2.1 Electric transport

The theory of electric transport can often be captured efficiently by a straight-forward, semiclassical picture. While the topic is extensively covered in many text books [23], here, the central results to establish the sign convention used throughout the thesis are recapitulated briefly.

An electric current density $\boldsymbol{j}$ through a material induces a voltage drop per length $\boldsymbol{U}$. The quantities are connected via the resistivity tensor $\underline{\underline{\rho}}$ through

$$\begin{pmatrix} U_x \\ U_y \end{pmatrix} = \begin{pmatrix} \rho_{xx} & \rho_{xy} \\ \rho_{yx} & \rho_{yy} \end{pmatrix} \cdot \begin{pmatrix} j_x \\ j_y \end{pmatrix} \tag{2.1}$$

or equally formulated in terms of the electric field $\boldsymbol{E}$ and the conductivity $\underline{\underline{\sigma}}$ with

$$\begin{pmatrix} j_x \\ j_y \end{pmatrix} = \begin{pmatrix} \sigma_{xx} & \sigma_{xy} \\ \sigma_{yx} & \sigma_{yy} \end{pmatrix} \cdot \begin{pmatrix} E_x \\ E_y \end{pmatrix} \quad . \tag{2.2}$$

Combining Eqns. (2.1) and (2.2) obtains

$$\begin{pmatrix} \sigma_{xx} & \sigma_{xy} \\ \sigma_{yx} & \sigma_{yy} \end{pmatrix} \cdot \begin{pmatrix} \rho_{xx} & \rho_{xy} \\ \rho_{yx} & \rho_{yy} \end{pmatrix} = \begin{pmatrix} 1 & 0 \\ 0 & 1 \end{pmatrix} \quad ,$$

and especially $\sigma_{xy} = \frac{-\rho_{xy}}{\rho_{xx}^2+\rho_{xy}^2}$.

In the following, a current along the x-axis is considered which is the typical case in a transport measurement and thus $j_y = 0$. Equation (2.1) then simplifies to Ohm's law for the longitudinal transport and the transverse Hall transport yields

$$U_y = \rho_{yx} \cdot j_x \quad .$$

2.1.1 Longitudinal transport

The longitudinal transport is described by the conductivity σ_{xx}. According to the Drude-Sommerfeld transport theory, quasi-free electrons are scattered inside the material which limits the transport. This yields a conductivity of

$$\sigma_{xx} = \frac{n_e e^2 \tau}{m_e} \quad ,$$

with the density of electrons n_e, their charge e, mass m_e, and the time constant between two scattering events τ. For a metal, all entities, except τ, can be considered temperature independent. Thus, the conductivity only depends on the temperature dependence of the scattering effects. With the Fermi velocity v_F, a mean free path l between two scattering events can be defined as

$$l = v_\mathrm{F} \cdot \tau \quad .$$

Let us assume a free-electron gas with a spherical Fermi surface and the Fermi velocity $v_\mathrm{F} = \frac{\hbar}{m_e} \cdot \left(3\pi^2 n_e\right)^{1/3}$. For the resistivity follows

$$\rho(T) = \frac{\hbar \left(3\pi^2\right)^{1/3}}{e^2} \cdot \frac{1}{l n_e^{2/3}} \quad .$$

According to Ioffe, Regel [24], and Mott [25] there is a high-temperature saturation limit for the resistivity ρ_sat in usual metals, if the scattering length is comparable to the lattice constant $l \sim a$:

$$\rho_\mathrm{sat} = \frac{1.29 \cdot 10^{18}}{n^{2/3} a} \, \mu\Omega\mathrm{cm} \quad .$$

At lower temperatures, different scattering mechanisms are relevant, which show different temperature dependencies:

- **Scattering on defects**: A constant defect density implies a constant scattering time. This yields the so-called residual resistivity $\rho_0 = \rho(T = 0\,\mathrm{K})$, which is often used to quantify the quality of a sample.

- **Electron-phonon-scattering**: Phonons that describe excitations of the lattice, destroy the periodicity of the lattice, and, thus, they lead to scattering with conduction electrons. Their contribution can be described by the Bloch-Grüneisen formula [26]

  $$\rho_\text{el-ph}(T) \propto \frac{T^5}{\theta_\mathrm{D}^6} \int_0^{\frac{\theta_\mathrm{D}}{T}} \frac{x^5}{(e^x - 1)\,(1 - e^{-x})} \mathrm{d}x \quad ,$$

  with the Debye temperature θ_D. Because the phonon density increases with temperature, so does the scattering. For high and low temperatures relative to the Debye temperature this yields the limits

  $$\rho_\text{el-ph}(T) \propto \begin{cases} T^5 & \text{for} \quad T \ll \theta_\mathrm{D} \\ T & \text{for} \quad T \gg \theta_\mathrm{D} \end{cases} \quad .$$

- **Electron-electron scattering**: The electron-electron scattering is typically negligibly in normal metals due to Pauli principle.

2.1.2 Transverse transport

The transverse transport consists of the normal or ordinary Hall effect (NHE) caused by a deflection of charge carriers due to a magnetic field [27] and also of an anomalous Hall effect (AHE), which was found in ferromagnetic metals and that scales with the magnetization M [28]. The total Hall resistance

$$\begin{aligned}\rho_{xy}(T,B) &= \rho_{xy}^{\mathrm{NHE}} + \rho_{xy}^{\mathrm{AHE}} \\ &= R_{\mathrm{H}}(T)B_{\mathrm{ext}} + R_{\mathrm{AHE}}(T)\mu_0 M(T,B_{\mathrm{ext}})\end{aligned} \tag{2.3}$$

contains the normal and anomalous Hall coefficient R_{H} and R_{AHE}. The normal Hall coefficient of a single conduction band only depends on the charge carrier density n via

$$R_{\mathrm{H}} = \frac{1}{nq} \quad . \tag{2.4}$$

Thus, the sign directly tells, whether the transport is dominated by electrons (negative charge $q < 0 \Rightarrow R_{\mathrm{H}} < 0$) or holes ($q, R_{\mathrm{H}} > 0$). Multiple bands with electron and hole carriers can compensate each other.

The anomalous Hall contribution contains intrinsic and extrinsic effects. Intrinsic contributions are independent of impurities and consequently dissipationless [29], while extrinsic contributions base on spin-dependent scattering processes and thus depend on the impurity concentration. In the following, the possible effects are discussed adapting the explanation from Ref. [23]:

Extrinsic processes

- Skew scattering:
  In the following, electron scattering at an electric impurity potential ϕ_{imp} in the background of an external electric field $\boldsymbol{E}_{\mathrm{ext}} = -\nabla\phi_{\mathrm{ext}}$ is considered. The spin of an electron $\boldsymbol{s} = \frac{\hbar}{2}\boldsymbol{\sigma}$, where $\sigma_x = \begin{pmatrix} 0 & 1 \\ 1 & 0 \end{pmatrix}$, $\sigma_y = \begin{pmatrix} 0 & -i \\ i & 0 \end{pmatrix}$, $\sigma_z = \begin{pmatrix} 1 & 0 \\ 0 & -1 \end{pmatrix}$ are the Pauli matrices, interacts with both electric fields according to the spin-orbit exchange energy

  $$E_{\mathrm{so}} = \sum_i \alpha\,(\boldsymbol{k} \times \boldsymbol{\sigma}) \cdot \nabla\phi_{\mathrm{i}} \quad ,$$

  where $\alpha = q\hbar/2m_e^2c^2$. Furthermore, the total Hamiltonian of an electron contains the

potential energies $E_{\text{pot}} = \sum_i q\phi_i$ and the kinetic energy:

$$\mathcal{H} = \frac{\hbar^2 \boldsymbol{k}^2}{2m} + q\phi_{\text{ext}} + \alpha\,(\boldsymbol{k} \times \boldsymbol{\sigma}) \cdot \nabla\phi_{\text{ext}} + q\phi_{\text{imp}} + \alpha\,(\boldsymbol{k} \times \boldsymbol{\sigma}) \cdot \nabla\phi_{\text{imp}} \quad . \tag{2.5}$$

Only the last two terms contain the potential of the impurity and can lead to skew scattering. Both contributions can scatter an electron from a state with momentum $\boldsymbol{k}$ and spin quantum number s to another state $\boldsymbol{k}'$, s' with the matrix element

$$\left\langle \boldsymbol{k}', s' \left| q\phi_{\text{imp}} + \alpha\,(\boldsymbol{k} \times \boldsymbol{\sigma}) \cdot \nabla\phi_{\text{imp}} \right| \boldsymbol{k}, s \right\rangle = V_{kk'}\{\delta_{s,s'} - i\alpha\,(\boldsymbol{k} \times \boldsymbol{k}') \cdot \langle s' \,|\boldsymbol{\sigma}|\, s\rangle\} \quad .$$

The first term results from spin-conserving scattering at the impurity, while the second term occurs due to spin-orbit coupling. The sign of this term depends on the relative orientation of $\boldsymbol{k} \times \boldsymbol{k}'$ and the spin s. Figure 2.1 indicates the scenarios for elastic scattering of spins with two different spin orientations and incident moment $\boldsymbol{k}$ by an angle $\pm\theta$ into $\boldsymbol{k}'$ or $\boldsymbol{k}''$, respectively. In panel (a), $\boldsymbol{k} \times \boldsymbol{k}'$ is antiparallel to s, and, thus, it results in a larger matrix element than the scattering to $\boldsymbol{k}''$. In panel (b), the spin is inverted and consequently $\boldsymbol{k}''$ becomes favorable. Because of this asymmetric scattering, a Hall voltage can occur. The scattering at these defects does not only influence the Hall signal but similarly contributes to the longitudinal resistance ρ_{xx}. Obviously, in a spin-degenerate material both skew scattering contributions would compensate each other, and, thus, a preferred spin orientation is required. Consequently, the Hall resistance has to be proportional to the spin-polarization of the charge carriers, as it is the case for a band ferromagnet ($\propto M$). Thus, the Hall resistivity induced by skew scattering follows

$$\rho_{\text{AHE}} \propto \rho_{xx} M(B_{\text{ext}}) \quad .$$

- Side Jump:
  Another asymmetric scattering mechanism is called side-jump mechanism [30, 31]. Because elastic scattering is assumed ($|\boldsymbol{k}| = |\boldsymbol{k'}|$), the kinetic energy term of Eqn. (2.5) is constant. Nonetheless, the spin-orbit exchange energy of the electron in the static electric field changes according to $E_{\text{SO}} = \alpha\,(\boldsymbol{k} \times \boldsymbol{\sigma}) \cdot \nabla\phi_{\text{ext}}$. In order to maintain energy conservation, the potential energy $E_{\text{pot}} = q\phi_{\text{ext}}$ has to change accordingly. For a linear external potential, i.e., $\phi_{\text{ext}} = \boldsymbol{E} \cdot \boldsymbol{r}$, this results in a change of the scattering parameter $\boldsymbol{r}$. Thus, the side-jump effect causes a vertical deflection δ, see Fig. 2.1(c), which is typically of the order of 10^{-14} to 10^{-10} m [31]. The number of scattering

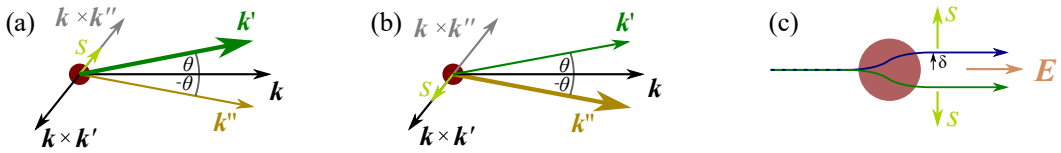

Figure 2.1 Spin-dependent transverse scattering mechanisms. (a) and (b) illustrate the skew-scattering mechanism. For panel (a), electrons with moment $\boldsymbol{k}$ and spin s ($s \perp \boldsymbol{k}$) favor elastic scattering to $\boldsymbol{k}'$ (up by angle θ) instead of $\boldsymbol{k}''$ ($-\theta$), because $\boldsymbol{k} \times \boldsymbol{k}'$ is anti-parallel to the spin s. In panel (b), the spin is inverted and, thus, $\boldsymbol{k}''$ becomes favorable. The effect requires a net spin polarization in order to be finite. The side-jump mechanism shown in (c) yields a deflection δ that depends on the spin direction resulting from energy conservation during a scattering process at an impurity in an external electric field $\boldsymbol{E}$. Figure adapted from Ref. [23].

events and also the size of the deflection are proportional to the longitudinal resistivity ρ_{xx}. Furthermore, the effect depends on the spin-polarization and, therefore, on the magnetization M. Thus, the side-jump mechanism yields

$$\rho_{\mathrm{AHE}} \propto \rho_{xx}^2 M(B_{\mathrm{ext}}) \quad .$$

Intrinsic effects

An explanation for the anomalous Hall effect was already proposed by Karplus and Luttinger in 1954 who suggested a contribution due to spin-split bands caused by spin-orbit coupling [32, 33]. This effect should not depend on the impurity concentration (intrinsic).

The elementary explanation of their proposition is based on the concept of the *Berry phase*, which is explained in Appendix A.1. The explanation below follows Ref. [23]. For further reading see e.g. Refs. [34, 35]. We consider a system with parameter $\boldsymbol{R}$ that moves adiabatically in the phase space along a path Γ and starts in an eigenstate $|\Psi(t_0)\rangle = |m[\boldsymbol{R}(t_0)]\rangle$ with the eigenenergy $\epsilon_m(t_0)$ where m denotes the band index. The system remains in the time-dependent eigenstate $|m(t)\rangle$. The phase difference along the path consists of a dynamical and a geometrical part, see Appendix A.1. This phase

$$\gamma_m(\Gamma) = \int_{\Gamma} \boldsymbol{A}_m(\boldsymbol{R}) \cdot \mathrm{d}\boldsymbol{R} \tag{2.6}$$

contains the Berry potential

$$\boldsymbol{A}_m(\boldsymbol{R}) = i \left\langle m[\boldsymbol{R}(t)] \left| \frac{\mathrm{d}}{\mathrm{d}t} \right| m[\boldsymbol{R}(t)] \right\rangle \quad .$$

This connects to the Berry flux or Berry curvature $\boldsymbol{\Omega}_m$ via

$$\boldsymbol{\Omega}_m(\boldsymbol{R}) = \nabla_{\boldsymbol{R}} \times \boldsymbol{A}_m(\boldsymbol{R}) \quad . \tag{2.7}$$

The path integral from Eqn. (2.6) can be rewritten to a surface integral using Stokes theorem and the Berry curvature

$$\int_S \boldsymbol{\Omega}_m(\boldsymbol{R}) \cdot \hat{\boldsymbol{n}} \mathrm{d}^2 R \quad .$$

Thus, the Berry phase can be understood as an Aharonov-Bohm phase induced by an effective magnetic-flux density $\boldsymbol{\Omega}_m(\boldsymbol{R})$ in the parameter space. Still, the question about the origin of this flux density remains. Here, we focus on the spin-orbit coupling.

We assume Bloch waves $\Psi_{m,\boldsymbol{k}} = \mathrm{e}^{i\boldsymbol{k}\cdot\boldsymbol{r}} u_{m,\boldsymbol{k}}(\boldsymbol{r})$ with a lattice-periodic function $u_{m,\boldsymbol{k}}(\boldsymbol{r})$. In $\boldsymbol{k}$ space, the position operator is $\boldsymbol{R} = i\nabla_{\boldsymbol{k}}$ and the Hamiltonian

$$\mathcal{H}(\boldsymbol{k}) = \mathcal{H}_0(\boldsymbol{k}) + V(\boldsymbol{R})$$

has eigenstates $|u_m(\boldsymbol{k})\rangle$ with the eigenenergy $\epsilon_m(\boldsymbol{k})$. The gradient of the potential $V(\boldsymbol{R})$ results in a force

$$\hbar \frac{\mathrm{d}\boldsymbol{k}}{\mathrm{d}t} = -i[\boldsymbol{k}, \mathcal{H}] = -\frac{\partial V}{\partial \boldsymbol{R}} \quad .$$

This force is assumed to be small in order to result in an adiabatic motion, and, thus, in a drift of $\boldsymbol{k}$ along some path Γ. Appendix A.1 shows that this results in the Berry phase

$$\gamma_m(\Gamma) = \int_\Gamma \boldsymbol{A}_m(\boldsymbol{k}) \cdot \mathrm{d}\boldsymbol{k} \quad .$$

The corresponding Berry curvature, see Eqn. (2.7), can now change the behavior of the charge carriers due to the potential. This can be shown by using the gauge transformation that compensates the Berry phase

$$\boldsymbol{X}_m = i\nabla_{\boldsymbol{k}} + \mathbf{A}_m(\boldsymbol{k}) \quad , \quad \tilde{\mathcal{H}} = \mathcal{H}_0 + V\left(i\nabla_{\boldsymbol{k}} + \boldsymbol{A}_m\right)$$

This transformation does not influence the force $\hbar\dot{\boldsymbol{k}}$, but adds an additional term to the

group velocity, which results from the Berry phase[1]:

$$\hbar \boldsymbol{v}_m = -i[\boldsymbol{X}_m, \tilde{\mathcal{H}}] = \nabla_{\boldsymbol{k}} \epsilon_m(\boldsymbol{k}) + \left(\frac{\partial V}{\partial \boldsymbol{X}_m}\right) \times \boldsymbol{\Omega}_m(\boldsymbol{k})$$
$$\hbar \frac{\mathrm{d}\boldsymbol{k}}{\mathrm{d}t} = -i[\boldsymbol{k}, \tilde{\mathcal{H}}] = -\frac{\partial V}{\partial \boldsymbol{X}_m} \quad .$$

The additional term is called anomalous Luttinger velocity [32].

In an electric transport measurement, we apply an electric field $\boldsymbol{E}$ and additionally a magnetic field $\boldsymbol{B}$. This results in the potential $V = q\boldsymbol{E} \cdot \boldsymbol{X}_m$ and the modified equation of motion:

$$\hbar \boldsymbol{v}_m = \nabla_{\boldsymbol{k}} \epsilon_m(\boldsymbol{k}) - \underbrace{q\boldsymbol{E} \times \boldsymbol{\Omega}_m(\boldsymbol{k})}_{\hbar \boldsymbol{v}_{\mathrm{AHE}}} \tag{2.8}$$

$$\hbar \frac{\mathrm{d}\boldsymbol{k}}{\mathrm{d}t} = q\left[\boldsymbol{E} + \boldsymbol{v}_m(\boldsymbol{k}) \times \boldsymbol{B}\right] \quad . \tag{2.9}$$

With the Boltzmann transport equation we can find the current density for $\boldsymbol{B} = 0$

$$\boldsymbol{J}_q = \frac{1}{4\pi^3} \int q\boldsymbol{v}(\boldsymbol{k}) \left[f_0(\boldsymbol{k}) + g(\boldsymbol{k})\right] \mathrm{d}^3k \quad . \tag{2.10}$$

Here, $f_0(\boldsymbol{k})$ denotes the equilibrium Fermi distribution and $g(\boldsymbol{k}) = -q\tau \boldsymbol{v}(\boldsymbol{k}) \cdot \boldsymbol{E}(\partial f_0/\partial \epsilon)$ the correction due to the electric field with the relaxation time τ. Without the anomalous Luttinger velocity, the first term of Eqn. 2.10 vanishes, while the second term yields the longitudinal conductivity. In the case of a finite $\boldsymbol{v}_{\mathrm{AHE}}$, $f_0(\boldsymbol{k})$ yields a finite contribution to $\boldsymbol{J}_q$, for which follows

$$\begin{aligned}
\boldsymbol{J}_{q,\mathrm{AHE}} &= \frac{1}{4\pi^3} \int -\frac{q^2}{\hbar} \boldsymbol{E} \times \boldsymbol{\Omega}_m(\boldsymbol{k}) f_0(\boldsymbol{k}) \mathrm{d}^3k \\
&= -\frac{q^2}{\hbar} \boldsymbol{E} \times n\langle \boldsymbol{\Omega}_m \rangle && \text{used } \langle \boldsymbol{\Omega}_m \rangle = \frac{1}{n} \frac{1}{4\pi^3} \int_{\mathrm{BZ}} \boldsymbol{\Omega}_m(\boldsymbol{k}) f_0(\boldsymbol{k}) \mathrm{d}^3k \\
&= nq\langle \boldsymbol{v}_{\mathrm{AHE}} \rangle && \text{used } \langle \boldsymbol{v}_{\mathrm{AHE}} \rangle = -\frac{q}{\hbar} \boldsymbol{E} \times \langle \boldsymbol{\Omega}_m \rangle \\
&= \sigma_{\mathrm{AHE}} \boldsymbol{E} && \text{used } \sigma_{\mathrm{AHE}} = n\frac{q^2}{\hbar} \langle \boldsymbol{\Omega}_m \rangle \quad .
\end{aligned}$$

$\langle \boldsymbol{\Omega}_m \rangle$ scales the mean value of the Berry flux over the Brillouin zone with the particle

[1] Here, the commutation relation $\left[X_{m,i}, X_{m,j}\right] = i\mathcal{E}_{ijk} F_{m,k}$ with the Levi-Civita symbol $\mathcal{E}_{ijk}$ is used.

density n. Interestingly, $\boldsymbol{J}_{q,\mathrm{AHE}}$ and σ_{AHE} are independent of the scattering time τ, i.e., the anomalous contribution only depends on the topology of the electronic band structure via the Berry flux. This makes it dissipationless. Note, that in an experiment the Hall resistance ρ_{xy}^{AHE} is measured and follows

$$\sigma_{yx} = \frac{\rho_{xy}}{\rho_{xx}^2 + \rho_{xy}^2} \quad \overset{\rho_{xx} \gg \rho_{xy}}{\Longrightarrow} \quad \rho_{xy}^{\mathrm{AHE}} \approx \sigma_{\mathrm{AHE}} \rho_{xx}^2 \quad .$$

For a system with space and time inversion symmetry $\boldsymbol{\Omega}_m(-\boldsymbol{k}) = \boldsymbol{\Omega}_m(\boldsymbol{k})$ and $\boldsymbol{\Omega}_m(-\boldsymbol{k}) = -\boldsymbol{\Omega}_m(\boldsymbol{k})$, the Berry flux vanishes $\boldsymbol{\Omega}_m(\boldsymbol{k}) = 0$. If the time-reversal symmetry is broken, as it is in a ferromagnet, $\boldsymbol{\Omega}_m(\boldsymbol{k})$ can be finite. Via the spin-orbit coupling, the symmetry is transferred to the conduction bands. This yields an emergent magnetic-flux density inside the Brillouin zone. In the spin-orbit coupling with the spin $\boldsymbol{s}$ and the momentum $\boldsymbol{k}$

$$\mathcal{H}_{\mathrm{SO}} = \frac{e}{2m_e^2 c^2} (\boldsymbol{s} \times \nabla \phi_{\mathrm{el}}) \cdot \boldsymbol{k} = \boldsymbol{A}_{\mathrm{SO}} \cdot \boldsymbol{k}$$

$\boldsymbol{A}_{\mathrm{SO}}$ acts as the emergent Berry potential. The induced emergent magnetic-flux density is typically much larger than any external flux density applied by a magnet. It only depends on the size of the spin-orbit coupling and the topology of the $\boldsymbol{k}$ space.

The anomalous Hall contribution of the Berry flux can be calculated via ab-initio methods, see e.g., Ref. [36]. The remaining question is how to illustrate the Berry contribution to the anomalous Hall effect. In a single-band picture, the Berry phase is always zero. It can be finite in the presence of other bands and especially degeneracies are important. Special attention has been paid to point-like degeneracies, where the band is shaped like a diabolo, and thus called diabolic point [37]. Figure 2.2(a) illustrates such a diabolic energy band crossing. Calculating the Berry flux of this system one finds

$$\boldsymbol{\Omega}(k) = \frac{1}{2} \frac{\boldsymbol{k}}{k^3} \quad . \tag{2.11}$$

This vector field is exactly of the form of a magnetic (Dirac) monopole with the magnetic charge $1/2$, see Fig. 2.2(b). This monopole in $\boldsymbol{k}$ space induces the Berry flux, and, therefore, it contributes to the anomalous Hall effect. For any band structure, it is important to identify such points and to interpret their relevance for the anomalous Hall conductivity. Figure 2.2(c) shows the calculated band structure of iron close to the Fermi energy. The lower panel presents the corresponding Berry curvature along the symmetry lines. This is almost zero all over the Brillouin zone but shows a few sharp peaks. These peaks correspond to avoided band crossings and are driven by spin-orbit coupling. These calculations

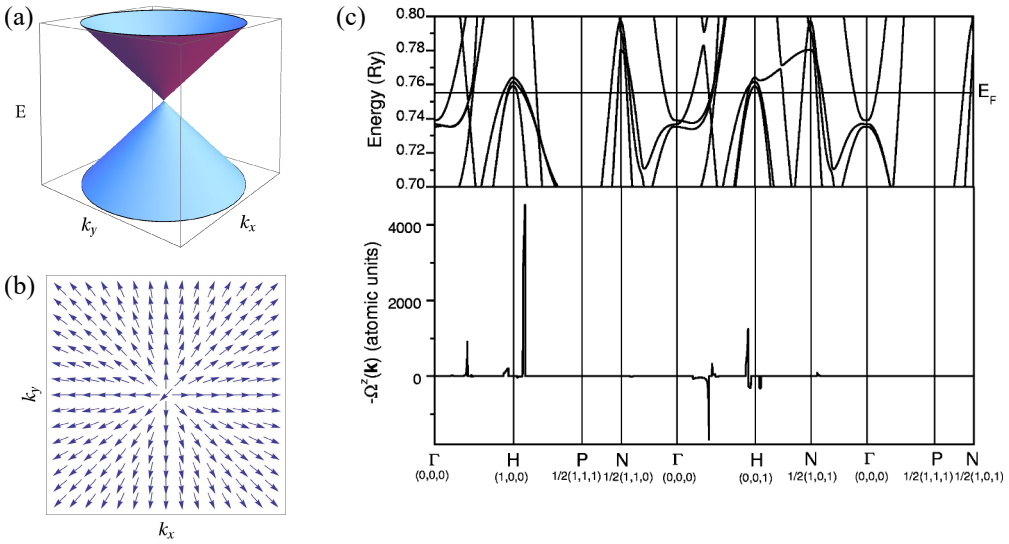

Figure 2.2 Berry phase of band structures. (a) shows a conical band crossing with the corresponding Berry curvature $\mathbf{\Omega}$ in (b), taken from Ref. [36]. This equals the field profile of a monopole. (c) The Berry curvature $-\mathbf{\Omega}(\boldsymbol{k})$ (lower panel) of iron is calculated from the band structure close to the Fermi energy, from Ref. [38]. It is essentially zero except for small regions where it becomes finite. These positions in $\boldsymbol{k}$ space correspond to avoided band crossings driven by spin-orbit coupling.

yield an intrinsic anomalous Hall contribution due to Berry phase effects, which is only slightly smaller than what was found experimentally [38].

However, such ab-initio calculations of the band structure – and hence the Berry curvature – in general are very challenging. Already small errors in the predicted Fermi energy can have a strong impact on the result [39].

2.2 Magnetism

This part does not present a general introduction into magnetism, but only focuses on the relevant topics and fundamentals that are essential for the following studies. A more general introduction to magnetism is topic of undergraduate lectures and described in numerous textbooks.

Paramagnetism

Paramagnetic materials host permanent magnetic moments that occur due to non-vanishing angular momentum. Partially-filled shells can yield a nonzero total angular momentum $\boldsymbol{J}$. Without an external magnetic field, these moments are oriented statistically, and, thus,

there is no net magnetization. Inside a magnetic field, the moments favor to align to the field to reduce their energy. This causes a macroscopic magnetization along the field, and, thus, the magnetic susceptibility $\chi = \partial M/\partial B$ is positive. A system with angular momentum $\boldsymbol{J}$ hosts $2J + 1$ equidistant Zeeman states that are populated according to the Boltzmann statistics depending on the temperature T of the system. Lower-lying energy states are preferred compared to higher ones. A typical textbook derivation yields the magnetization of a system of N magnetic moments

$$M(T, B) = N g_J J \mu_\mathrm{B} \cdot B_J\left(\frac{g_J \mu_\mathrm{B} J B}{k_\mathrm{B} T}\right) \quad ,$$

where B_J denotes the Brillouin function

$$B_J(x) = \frac{2J+1}{2J}\coth\left(\frac{(2J+1)x}{2J}\right) - \frac{1}{2J}\coth\left(\frac{x}{2J}\right) \quad .$$

With the approximations $x \ll 1$ and small magnetic field, the susceptibility yields

$$\chi = \mu_0 \frac{M}{B} \approx \frac{N\mu_0 g_J^2 \mu_\mathrm{B}^2 J(J+1)}{3k_\mathrm{B}T} = \frac{N\mu_0 \mu_\mathrm{eff}}{3k_\mathrm{B}T} = \frac{C}{T} \quad .$$

This equation is known as Curie's law. C denotes the Curie constant that contains the effective moment μ_eff, which is used regularly to compare magnetic materials. It is related to the saturation moment μ_sat via

$$\mu_\mathrm{sat} = \mu_\mathrm{eff} \frac{J}{\sqrt{J(J+1)}} \quad .$$

2.2.1 Magnetic exchange

So far, the influence of a magnetic field on individual atoms and magnetic moments that yields a macroscopic magnetization has been discussed. The reason for a collective alignment of magnetic moments without an external magnetic field could in principle be the dipole field of each moment, but the corresponding energy scale is far too small to explain collective phenomena at elevated temperatures and does not account for the multiple types of ordering that have been found. The basic principle of magnetic exchange is a result of the Coulomb repulsion that gains energy if two electrons are as far apart as possible. Considering the wave function of two electrons, it can be shown that the spin-dependent

part of the Hamiltonian can be written as

$$\mathcal{H}_{\text{spin}} = 2J\boldsymbol{S}_1 \cdot \boldsymbol{S}_2 \quad \text{, with} \quad J = \frac{E_\text{T} - E_\text{S}}{2} \quad .$$

Here, E_S and E_T are the energy levels of the antiparallel (singlet) and parallel (triplet) alignment of the spins, respectively. J is called the magnetic exchange coupling constant. It defines the energy scale of the exchange and the sign denotes whether the singlet ($J > 0 \rightarrow E_\text{S} < E_\text{T} \rightarrow S = 0$) or triplet ($J < 0 \rightarrow E_\text{S} > E_\text{T} \rightarrow S = 1$) is the ground state.[2] Heisenberg projected this idea onto the many-body problem as it is valid inside a solid state with many magnetic moments

$$\mathcal{H}_{\text{Heisenberg}} = \sum_{ij} J_{ij} \boldsymbol{S}_i \boldsymbol{S}_j \quad . \tag{2.12}$$

J_{ij} is the exchange constant between two sites i and j. Depending on the lattice and the size and sign of multiple couplings J_{ij}, different long-range ordering structures can be realized.

The definition of J_{ij} via the singlet or triplet state of the wave function between two sites requires the overlap of the wave functions of the two electrons. This phenomenon is called direct exchange. In this case, the electron is no longer localized but is delocalized between the two sites. The low-lying singlet, so-called binding state, is thus not only a state of one site but two. Consequently, such a state is called a molecular orbital.

Besides direct exchange, there is magnetic exchange via other ligand ions with noble gas configuration, often O^{2-} or halides like Cl^-/Br^-, called super-exchange. These ions have filled p orbitals whose wave functions overlap with the magnetic ion's wave function. The size and even the sign of this exchange crucially depends on the angle of the metal-ligand-metal path. An angle of 90° for example yields a ferromagnetic exchange, while an 180° configuration favors antiferromagnetically ordered moments. This exchange is explained by the Goodenough-Kanamori-Anderson rules [40, 41, 42].

The Heisenberg model can be generalized by using a directional (anisotropic) exchange. For the Hamiltonian follows

$$\mathcal{H} = \sum_{i,j} \left(J_{ij}^x S_i^x S_j^x + J_{ij}^y S_i^y S_j^y + J_{ij}^z S_i^z S_j^z \right) \quad .$$

[2] Another sign convention uses $\mathcal{H}_{\text{spin}} = -2J\boldsymbol{S}_1 \cdot \boldsymbol{S}_2$ and consequently $J < 0$ corresponds to a singlet ground state. Different conventions count J per site or per bond which results in a factor of 2 between both conventions.

The XXZ model and the Ising model, with

$$\mathcal{H}_{\mathrm{XXZ}} = \sum_{i,j} J_{ij} \left(S_i^x S_j^x + S_i^y S_j^y + \Delta S_i^z S_j^z \right)$$
$$\text{and} \quad \mathcal{H}_{\mathrm{Ising}} = \sum_{i,j} J_{ij} S_i^z S_j^z \quad ,$$

are two extreme cases of the generalized Heisenberg exchange. For a small Δ in the XXZ model, spins are lying in the XY-plane. For the Ising model ($\Delta \gg 1$), spins are forced to the z axis.

2.2.2 Magnetic order

All the discussed magnetic exchange mechanisms prefer an ordered state, while the temperature-induced fluctuations work against the order. Typically, at a critical temperature, a phase transition occurs and magnetic order is established. In the following, the main types of magnetic order are discussed.

Ferromagnetism

In a ferromagnetic system, the net exchange coupling J is negative. Below the critical temperature T_{C}, the material shows a spontaneous macroscopic magnetization without an applied magnetic field. At zero temperature, all moments are aligned and yield the saturation magnetization M_{sat}. In reality, not all moments are aligned parallel to reduce the stray fields. Regions of aligned moments are called domains and the boundaries between two such domains are called domain walls. The reduced stray fields overcompensate the energy cost of violated exchange energy at the domain walls. Above T_{C}, a ferromagnet behaves like a paramagnet with the susceptibility that follows the Curie-Weiss law

$$\chi = \frac{C}{T - \theta} \quad . \tag{2.13}$$

θ is the paramagnetic Curie temperature and is not necessarily equal to T_{C}.

According to Landau [43], phase transitions, here from the paramagnetic to the ferromagnetic state, can be divided into first-order and second-order phase transitions. At a first-order phase transition, the order parameter, e.g., the magnetization M of a ferromagnet, instantaneously jumps to a finite value. This discontinuity stems from the also discontinuous behavior of the entropy S, which results in an infinite specific heat. The phase transition is connected to so-called latent heat. First-order phase transitions can be

hysteretic, i.e., the critical temperature depends on the history, e.g., whether a measurement is performed on increasing or decreasing temperature.

At a second-order transition, the order parameter grows continuously from zero. The entropy has an inflection point and the specific heat a so-called λ-shaped maximum. The Landau theory of a ferromagnet yields the temperature-dependent magnetization

$$M = M_{\text{sat}} \sqrt{1 - \frac{T}{T_{\text{C}}}} = M_{\text{sat}} \left(1 - \frac{T}{T_{\text{C}}}\right)^{\beta} \quad \text{, with} \quad \beta = \frac{1}{2} \quad . \tag{2.14}$$

Basically, the Landau theory yields power laws not only for the order parameter, but also for other (thermodynamic) quantities

$$c_p \propto (\pm t)^{-\alpha} \quad \text{, with} \quad \alpha = 0 \tag{2.15}$$

$$\chi \propto (\pm t)^{-\gamma} \quad \text{, with} \quad \gamma = 1 \tag{2.16}$$

$$M(H, T = T_{\text{C}}) \propto H^{1/\delta} \quad \text{, with} \quad \delta = 3 \quad . \tag{2.17}$$

Here, $t = (1 - {}^{T}/_{T_{\text{C}}})$ denotes the reduced temperature.

The simple mean-field approximation of Landau does not account for critical fluctuations caused by correlation effects that dominate close to the transition temperature. To capture also these critical effects, numerical methods are required that yield redefined critical exponents. These exponents group up into so-called universality classes. The exponents are universal as they do not depend on microscopic details but only on the lattice dimensionality, the spin dimensionality, and the range of the exchange mechanism as defined by Griffiths [44].

Table 2.1 compares the critical exponents of the mean-field Landau theory to the renormalization-group findings for the 3D Ising and Heisenberg system.

	α	β	γ	δ
MF Landau theory	0 (step)	0.5	1	3
3D Heisenberg	0.11	0.325	1.24	4.815
3D Ising	-0.12	0.365	1.39	4.808

Table 2.1 Critical exponents of different universality classes.

The Arrott plot is a special way of presenting magnetization measurements of a ferromagnet, see Fig. 2.3. If a material shows a second-order phase transition of Landau-type, M^2 is linear in M/H in the vicinity of the transition temperature. The intercept of this curve is temperature-dependent, i.e., positive for $T < T_{\text{C}}$ and negative for $T > T_{\text{C}}$. Thus,

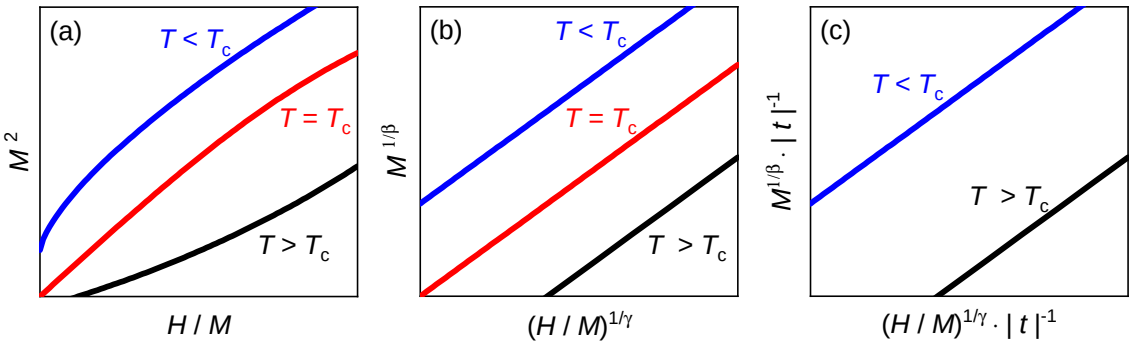

Figure 2.3 Arrot plots for magnetization measurements. The original Arrott plot (a) displays magnetization measurements for temperatures close to the ferromagnetic ordering temperature as M^2 vs. H/M. For a system that can be described with mean-field exponents, this yields a linear behavior around T_C. (b) shows the modified Arrott plot, which takes critical fluctuations into account and allows to describe the critical behavior around T_C for other universality classes. In the scaled Arrott plot (c), all temperatures collapse onto two different curves.

the critical temperature can be determined precisely by measuring the magnetization of a ferromagnet for different temperatures close to T_C and using the Arrott plot scheme. Often, a material does not follow the mean-field theory, but critical fluctuations are dominating. In this case, the Arrott plot does not yield straight lines due to changes of the critical exponents of the system. The modified Arrott plot, which relates $M^{1/\beta}$ and $(H/M)^{1/\gamma}$, accounts for these changes. This allows an analysis of the criticality and the corresponding universality class of the material. Magnetization curves for multiple temperatures follow a scaling relation and collapse onto two linear curves, see panel (c).[3]

Antiferromagnetism

If the exchange constant J_{ij} is positive, the involved magnetic moments favor an antiparallel alignment, see Eqn. (2.12). The corresponding long-range order is called antiferromagnetic order. An antiferromagnet often consists of two sublattices of ferromagnetic moments whose magnetization is equally large but differs in sign, which yields a vanishing net magnetization without an external magnetic field. Above the critical ordering temperature T_N, called Néel temperature, the susceptibility follows the Curie-Weiss law of Eqn. (2.13) but with a negative Curie-Weiss temperature θ. Below T_N, the susceptibility is anisotropic. For a magnetic field parallel to the ordered moments, the susceptibility approaches zero, while it remains constant for the perpendicular alignment.

[3] Another way of checking the scaling behavior is by plotting $M^2(T/T_C - 1)^{1/\beta}$ vs. $H/M(T/T_C - 1)^{1/\gamma}$.

Frustration

Frustration in solid-state physics is known as the problem of competing interactions due to local (geometric) constraints. An elementary unit for frustration is a triangle, see Fig 2.4(a). The Ising spins on the edges of a triangle shall have a nearest-neighbor antiferromagnetic coupling. If one pair is aligned antiparallel, the third spin is frustrated since both orientations have the same energy and in any case one neighbor is oriented antiparallel, while the other is parallel. It cannot gain coupling energy with both nearest neighbors. In 1950, Wannier showed that this system does not order down to zero temperature and possesses a degenerate ground state [45]. The ground state degeneracy grows exponentially with the number of spins that obey this frustration. Thus, e.g., the triangular lattice has a residual entropy violating the third law of thermodynamics, which demands a vanishing entropy as the temperature approaches 0 K. Further predictions and realizations of the triangular lattice will be discussed below.

Another example of frustration is the interplay of nearest neighbor (NN) and next-nearest neighbor (NNN) interaction on a chain, see Fig. 2.4(b). In such a chain with ferromagnetic or antiferromagnetic coupling J for the NN and antiferromagnetic NNN J', not all couplings can be satisfied at once. The ground state of this system is the ↑↑↓↓ configuration if $J' > |J|/2$. For a system without Ising anisotropy, see Fig. 2.4(c), a cycloidal spin arrangement minimizes the energy for $J' > |J|/4$. The cycloid can break the inversion symmetry, and, thus, it can lead to a polar structure. Via the inverse Dzyaloshinskii-Moriya interaction, which is mediated by spin-orbit coupling, a ferroelectric polarization can occur. In such a system, the direction of the ferroelectric polarization is directly related to the handedness of the spin-cycloid, and, thus, a large magnetoelectric coupling is found. This type of coupled order is called multiferroicity.

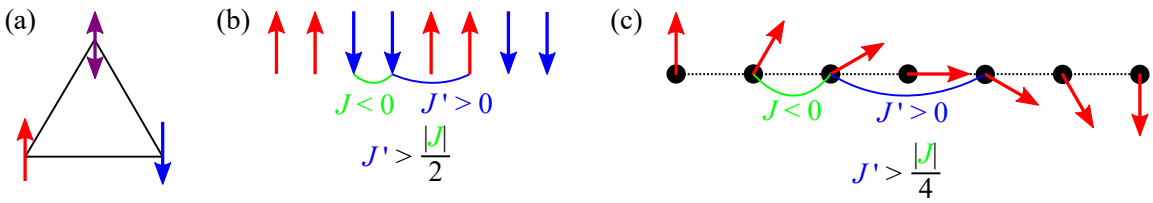

Figure 2.4 Examples for geometrical frustration. (a) shows magnetic frustration on a triangle with antiferromagnetic coupling. (b) and (c) show spin chains with ferromagnetic NN coupling J and antiferromagnetic NNN coupling J'. The chain in (b) has Ising anisotropy and the ground state shows ↑↑↓↓ order for $J' > |J|/2$, while the chain in (c) with isotropic Heisenberg spins and $J' > |J|/4$ has a cycloidal ground state.

2.2.3 2D triangular lattice

The 2D triangular lattice with antiferromagnetic interaction is a highly-frustrated model system that has been studied extensively by different theoretical approaches. According to Mermin-Wagner theorem [46], it is impossible for any continuous symmetry to be broken spontaneously in a two-dimensional lattice at finite temperatures, and, thus, magnetic long-range order cannot emerge. There is the possibility of a quasi-long-range order through a topological phase transition, which is called (Berezinskii-) Kosterlitz-Thouless (BKT) transition. In such a transition, the correlation length diverges exponentially. Below the transition temperature, vortex-antivortex pairs are bound, while they are free above the transition [47].

For the spin-$1/2$ Heisenberg antiferromagnet, it was shown that in the ground state neighboring moments form a relative angle of 120° [48]. This ground state has two possible chiralities, see Fig. 2.5(a). Without any anisotropy, the system still has a large degeneracy since the direction of the moments is not defined, but only their relative angle. This degeneracy can also be broken by further neighbor interactions which then stabilize multiple fractional magnetization states with sublattice (SL) structures [49]. Besides the quantum-mechanical nature of the $S = 1/2$ moments, also the classical version hosts interesting phases at finite temperatures. In a magnetic field, see Fig. 2.5(b), Monte-Carlo simulations reveal three ordered phases [50]. Two temperature-driven phase transitions are found in small magnetic fields. The transition from the paramagnetic phase to the 2up-1dw phase with a $1/3 M_{\mathrm{sat}}$ magnetization is continuous, while the following transition to the ground state, the so-called Y phase, a canted version of the 120° state, is a BKT transition. In larger magnetic fields, a continuous phase transition into a canted 2up-1dw state is found. The magnetic-field driven transition from the pure 2up-1dw to the canted version is another BKT transition and occurs at a field strength of $\sim 3J$. Further studies take different perturbations into account. If there is an easy-axis anisotropy present, the 2up-1dw phase is stabilized further [51]. For a large anisotropy ($D \gg J$), a zero-magnetization plateau was proposed up to magnetic fields of $B_c \sim J^3/D^2$ [52]. An infinite anisotropy Ising system was studied by Metcalf [53] and Tanaka and Uryû [54] who propose four possible ground states for the triangular lattice depending on the ratio of the NN and NNN interaction.

Any 3D crystal also has a finite interlayer coupling, that motivates studies of more complex models in order to explain experimental results of materials, e.g., $AgNiO_2$ [55]. Such models that also include further neighbor interactions with competing influence or anisotropic exchange interactions, exhibit even more complicated magnetic field vs. temperature phase diagrams [56, 57]. An exemplary phase diagram is shown in Fig. 2.5(c), which is calculated for a system of triangular layers with NN coupling $J_1 = 1$, the NNN interaction

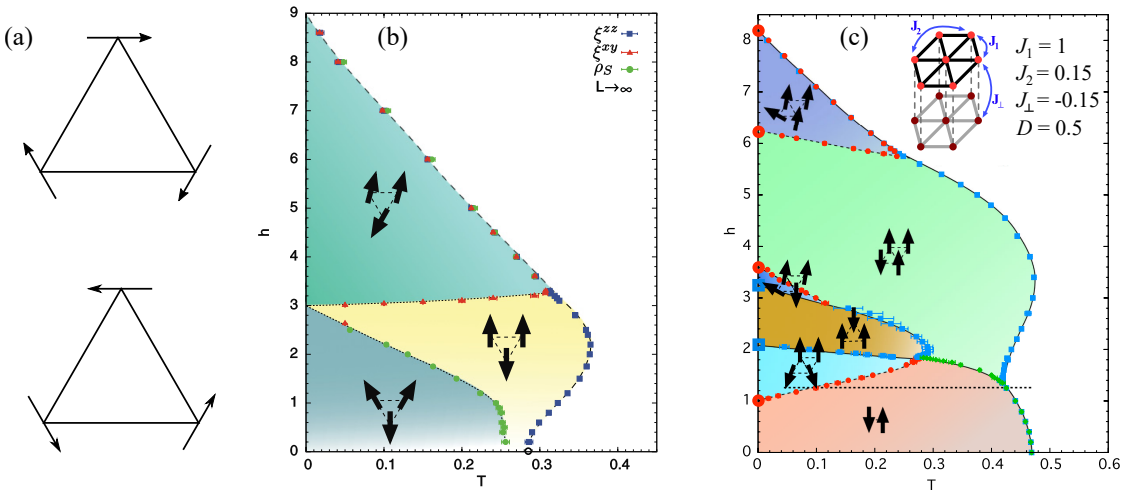

Figure 2.5 Magnetic structure and phase diagrams for triangular lattice models. (a) shows the two 120° ordered magnetic ground states of the $S = 1/2$ with different chirality. The phase diagram of the classical spin model on a triangular lattice in a magnetic field (b) was adapted from Ref. [50]. (c) shows the phase diagram for a stacked triangular lattice with $J_1 = 1$, $J_2 = 0.15$, $J_\perp = -0.15$, and $D = 0.5$ from Ref. [57]. The axes are measured in units of J_1.

$J_2 = 0.15$, a ferromagnetic interlayer coupling $J_\perp = -0.15$, and an easy-axis anisotropy $D = 0.5$ using the following Hamiltonian:

$$\mathcal{H} = J_1 \sum_{\langle ij \rangle_1} \boldsymbol{S}_i \cdot \boldsymbol{S}_j + J_2 \sum_{\langle ij \rangle_2} \boldsymbol{S}_i \cdot \boldsymbol{S}_j + J_\perp \sum_{\langle ij \rangle_\perp} \boldsymbol{S}_i \cdot \boldsymbol{S}_j - D \sum_i (S_i^z)^2 - h \sum_i S_i^z \quad .$$

The resulting phase diagram consists of six ordered phases below the ordering temperature of about $0.43 J_1$. At zero temperature, three magnetization plateaus are found with values of 0, $1/3 M_{\mathrm{sat}}$, and $1/2 M_{\mathrm{sat}}$.

2.2.4 Hexagonal closed packed structure

The ABAB stacking of triangular layers yields the hexagonal closed packed (hcp) lattice. The magnetism of Ising moments on this lattice was studied with multiple techniques. In the following, two different approaches are presented, one numerical and one analytical.

The model of Matsubara and Inawashiro [58] takes three couplings into account, the out-of-plane coupling J_0 and the in-plane NN and NNN couplings J_1 and J_2, see Fig. 2.6(a). It is further assumed that $J_0 \ll J_1$, which results in a quasi 2D system. Depending on the ratio of J_0 and J_2 different ground state orderings are found by Monte-Carlo simulations. For

an antiferromagnetic J_2, the ground state shows ferromagnetic stripes along one crystallographic axes that are alternating in the other direction, see Fig. 2.6(a). This state of course occurs in three twin domains. In an intermediate range $0 < J_2 < J_0/3$, the ground state shows an antiferromagnetic arrangement in one direction, while the other two are ordered in an 2up-2dw manner. This state can equally be described by ferromagnetic zig-zag chains. In the case of $J_0/3 < J_2$, the ground state has a net-magnetization of $1/3 M_{\mathrm{sat}}$, resulting from a hexagonal arrangement of ferromagnetic spins with a centered antiferromagnetic spin.

A more general perspective was studied by Kudo and Katsura [59]. They evaluated the phase diagram for the hcp lattice with Ising moments including NN and NNN interaction (J_1 and J_2) with an analytical approach. Additionally, their model captures the influence of a magnetic field. The obtained J_1-J_2-H phase diagram is shown in Fig. 2.6(b). In total, they find nine ordered phases and show the corresponding magnetic structures. In zero-field, the phases VII, V, and IX correspond to a more or less complex antiferromagnetic ground state with a vanishing magnetization, while phase I reflects the (fully polarized) ferromagnetic ground state. By applying a magnetic field, numerous phase transitions occur, depending on the ratio of J_1 and J_2. Up to four phase transitions into the finally fully polarized phase are possible. Some of these intermediate phases exhibit a fractional magnetization. Phases IV and VI obey $1/3 M_{\mathrm{sat}}$, III and VIII $1/2 M_{\mathrm{sat}}$, and II $2/3 M_{\mathrm{sat}}$. Further studies of the magnetic order on the hcp lattice with further neighbor interactions do not take magnetic-field influences into account [60, 61].

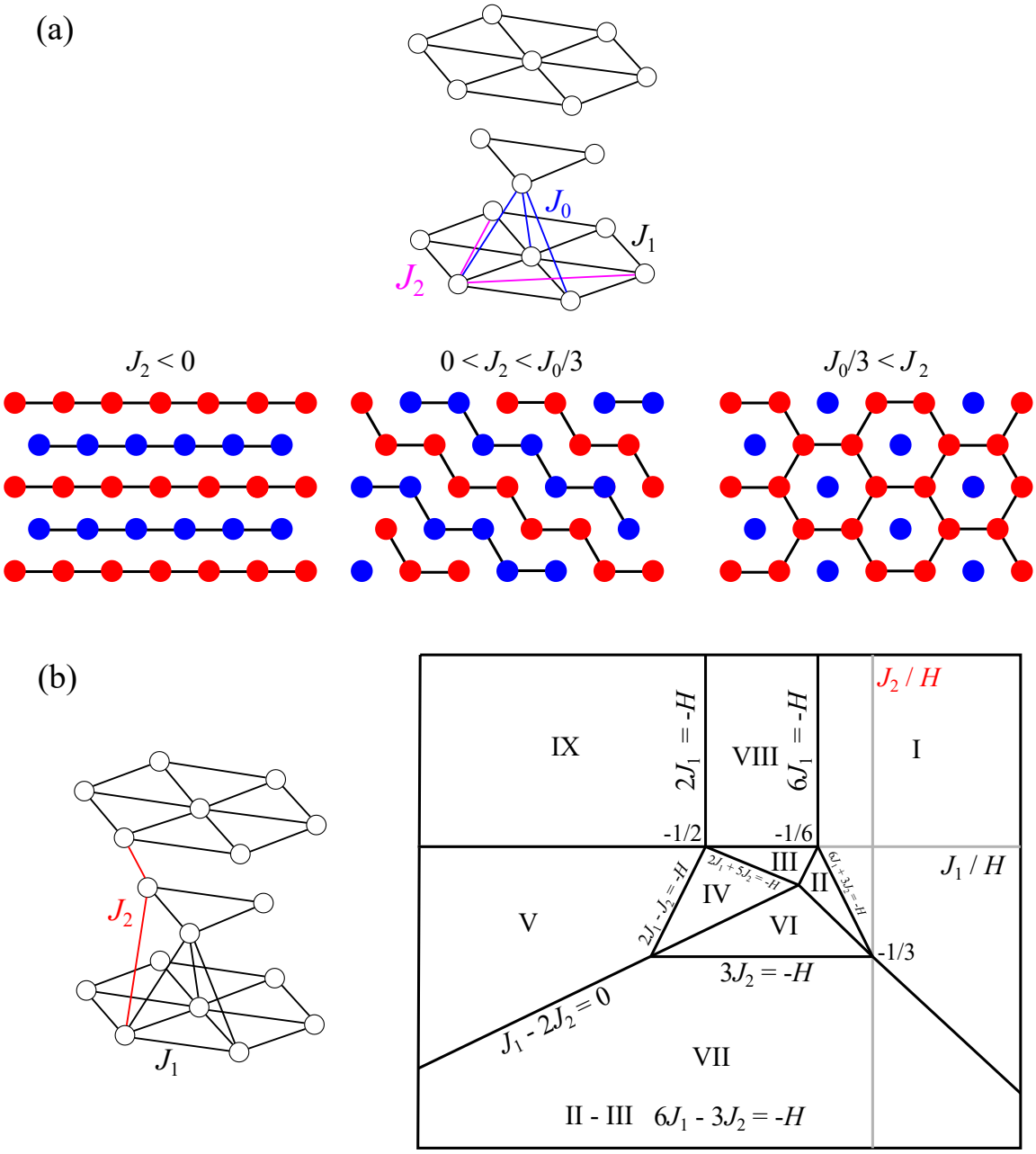

Figure 2.6 Magnetic structures and phase diagrams of Ising moments on the hcp lattice with different exchange couplings. The model of (a) includes the in-plane NN and NNN interactions J_1 and J_2 and the NN interlayer coupling J_0 [58]. Furthermore, $J_0 \ll J_1$ is assumed. There are three different ground states depending on the ratio of J_0 and J_2. The model in (b) uses Ising moments connected via the NN interaction J_1 and the NNN interaction J_2. The corresponding rich J_1-J_2 phase diagram in a magnetic field is adapted from Ref. [59].

3 Experimental

Contents

The experimental investigations of this work study thermodynamic and transport properties under extreme conditions, namely at low temperature and in strong magnetic fields. This requires different cryogenic setups and magnets. The following quantities are studied: magnetization, thermal expansion, magnetostriction, specific heat, dielectric polarization, and electric dc transport. The relevant experimental fundamentals and important details about the used setups are presented in the following. Hereby, a focus is put on magnetization measurements as it is essential to explore the magnetism of any magnetic material for a general understanding and also a basic characterization. In the scope of this thesis, multiple standard techniques were used to characterize materials in different temperature and magnetic-field ranges. Additionally, a new magnet was set up to improve the resolution of the Faraday magnetometer. The developed principle is explained in detail.

3.1 Cryogenic setups

In general, liquid helium is used to provide the cooling power for low-temperature measurements. With a variable temperature insert (VTI) for a ^{4}He bath cryostat and a Physical Property Measurement system (PPMS, Quantum Design) it is possible to cover the temperature range from 1.8 K to 400 K. For the PPMS, there are multiple options available that allow to measure, e.g., specific heat, magnetization, and resistivity easily and with a good reproducibility. Nonetheless, each option of this commercial equipment itself lacks in terms of versatility. All options function automated with only little possibilities for manual user optimization. In addition to the PPMS, the VTI allows for custom probes, e.g., a dilatometer to measure the thermal expansion of a sample. Information about the VTI can be found in Ref. [62]. Furthermore, evacuated dipsticks were used for measurements in the range from 7 K to 300 K. The temperature is controlled via a manganin wire heater wound around a beaker that covers the sample space and which is controlled by a Lakeshore 340 temperature controller. Such dipsticks have very good temperature stability. Further information about the systems can be found in Refs. [63, 64].

To reach temperatures below 1.8 K, a ^{3}He cooling unit is required. The HelioxVL probe (Oxford Instruments), see Fig. 3.1 is operated in a bath cryostat and reaches temperatures down to 250 mK. Custom sample holders allow an extensive pool of measurement techniques. The HelioxVL is inserted into a ^{4}He bath dewar through a sliding seal. The first cooling stage is the so-called 1-K pot or λ plate. The vapor pressure of Helium is reduced via a needle valve to about 20 mbar and, thus, the 1-K pot is cooled down to 1.8 K. At this temperature, gaseous ^{3}He in a closed system condenses and gathers at the bottom of the HelioxVL in the ^{3}He pot. Via pumping on this ^{3}He bath, it is possible to reach the base temperature of about 250 mK. The pumping is performed by an active-coal sorb that acts as a cryo pump. The cooling power ends once all the liquid ^{3}He is evaporated, which happens after about 20 h at base temperature. Afterwards, the ^{3}He sorb has to be heated to about 30 K, so that the adsorbed gas degases. Then, it can reliquify at the λ plate. This process is called regeneration or recondensation. Within this process, the sample temperature increases to about 2 K. The base temperature is restored by cooling the sorb. For measurements at temperatures that differ from the base temperature, two different heaters are used. Below 2 K, the cooling power is controlled by the vapor pressure of the ^{3}He via the temperature of the cryo-pump sorb. Above 2 K, the ^{3}He pot is heated directly so that temperature control is possible up to 50 K. The temperature stability strongly depends on the absolute temperature. The temperature control is poor close to 2 K when switching between the two heaters. Therefore, stabilized temperatures and especially heating ramps

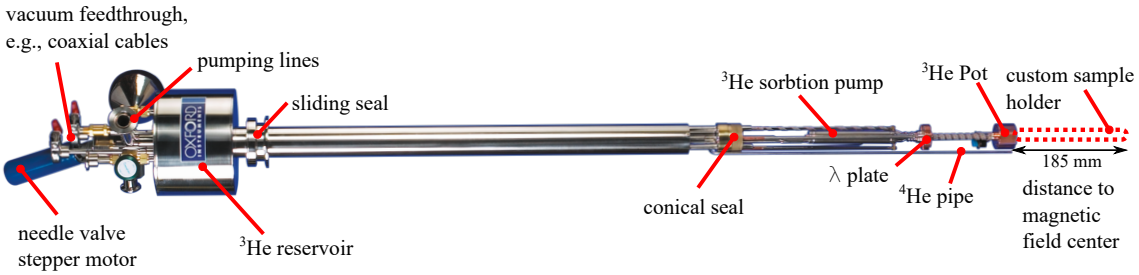

Figure 3.1 Components of the HelioxVL (Oxford Instruments) that reaches temperatures down to 250 mK using a closed system of ^{3}He to generate the cooling power. It can be equipped with custom sample holders in order to perform measurements of various physical properties. The picture is taken from Ref. [66].

in this range are problematic. Attempts to solve these issues are explained in Ref. [65].

3.2 Magnetic field

In 1820, Oersted discovered that a current I through a wire induces a magnetic field H circular around it, which decreases with distance r [67] according to $H = \frac{I}{2\pi r}$. A coil of multiple windings n can generate large and homogeneous magnetic fields. The magnetic field of a long coil (length l much larger than the diameter d) depends on the applied current I via $H = {}^{n}/_{l}\, I$. In usual ^{4}He bath cryostats, superconducting coils are used with currents up to 120 A. These can generate magnetic fields up to ~20 T depending on the critical field of the used superconductor. The superconducting magnet with vanishing electrical resistivity does not consume any energy with a static magnetic field, as long as the coil stays below the superconducting transition temperature.

Different techniques have been used throughout this work to generate even larger magnetic fields. A Bitter solenoid magnet is a special type of a normal-conducting coil, see Fig. 3.2(a). This construction principle was named after the inventor Bitter [68, 69]. The coil consists of so called *Bitter* plates made from copper, which are stacked such that they build up a solenoid. The windings are separated by insulating plates. All plates have a symmetric arrangement of holes, which are passed by cooling water. Such a coil, or even a combination of two, can be run with currents of multiple kilo Ampere. One of the magnets used in the high-field laboratory HFML in Nijmegen (NL) has a bore hole of 50 mm and uses a current of 37 kA to induce a magnetic flux density of 30 T. This requires the power of 17 MW. The magnet is cooled by 250 L water per second, which heat up by 15 °C. Due to the high power consumption, it is possible to use the maximum field for a few hours per day only.

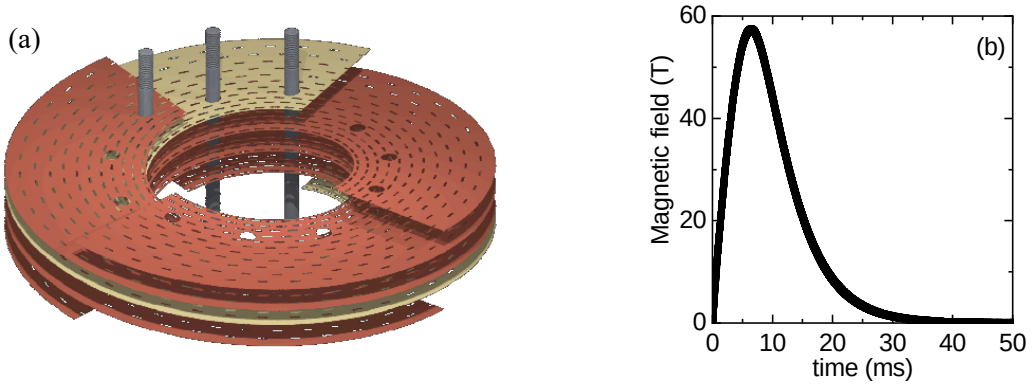

Figure 3.2 Bitter magnet and time dependence of a magnetic-field pulse. (a) shows a schematic drawing of a Bitter magnet. The solenoid consists of copper discs separated by insulating rings. Cooling water flows through the small holes (Figure adapted from HFML [70]). (b) shows the time dependence of a magnetic-field pulse as measured in a magnetization measurement at the *Helmholtz Zentrum Dresden Rossendorf*.

Another technique to generate even higher magnetic fields is a pulsed setup. A huge current pulse of only a few milliseconds is applied to a coil and generates a magnetic field as shown in Fig. 3.2(b). The coil is designed to stand the mechanical forces that arise during large field ramps [71]. The energy is stored in an array of capacitors, which allows to release the pulse within a short time. The magnet used in this work for magnetization measurements at the Helmholtz Zentrum Dresden Rossendorf (HZDR) creates up to 58 T in 30 ms. After each pulse, the magnet has to cool down for about 3 h before the next pulse can be started. Such measurements require fast data acquisition with oscilloscopes, which measure voltages at GHz frequencies.

3.3 Magnetization

3.3.1 SQUID magnetometer

The most common and widespread technique to measure magnetization is a superconducting quantum interference device (SQUID) magnetometer. Such a setup works as a flux-voltage transformer, i.e., a voltage proportional to the magnetic flux is measured. A dc SQUID is realized by a superconducting ring with two small normal conducting parts, so-called Josephson junctions. Cooper pairs can tunnel through these barriers and gain a phase change. The magnetic flux through this loop is quantized to multiples of a flux quantum $\Phi_0 = 2.0678 \cdot 10^{-15}$ Vs. The loop is additionally driven by a current that induces a flux of exactly ½ Φ_0. A magnetized sample that is moved through a pick-up coil as de-

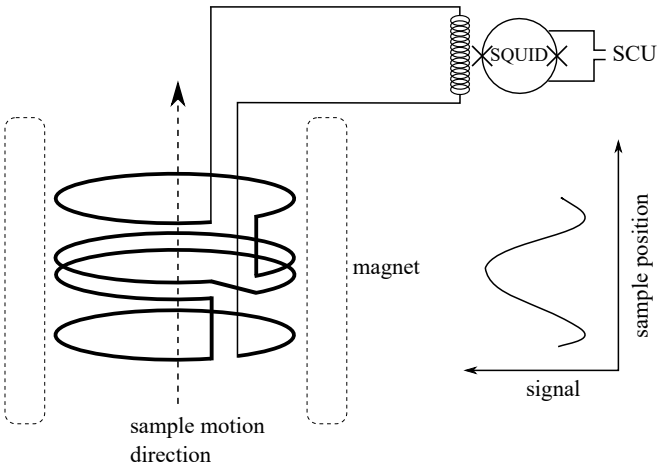

Figure 3.3 Schematic drawing of a SQUID magnetometer with the pick-up coils, the magnet, the SQUID, and the SQUID controlling unit (SCU). The measured signal induced by the motion of the sample is also indicated.

picted in Fig. 3.3 changes the flux through that coil and, therefore, induces an additional current that is coupled inductively into the SQUID unit. Consequently, the applied current to the SQUID has to be varied in order to keep the flux constant. The corresponding signal is also shown in Fig. 3.3. Fitting these data yields the magnetic moment of the sample. By this technique, it is even possible to measure fractions of Φ_0, and, thus, it is a very precise technique for measuring magnetization. Further information about the principle and the setup can be found in Refs. [72, 73, 74]. The commercial Magnetic Property Measurement System (Quantum Design) realizes this principle and is equipped with a 7 T magnet. It covers the temperature range from 1.8 K to 400 K. Because measurements to lower temperatures and higher magnetic fields cannot be performed with this technique, additional equipment is needed for those conditions.

3.3.2 Pick-up techniques

The usual pick-up technique also uses induction due to the change of magnetic flux inside a coil by a moving magnetized sample. Two normal conducting coils, which are wound in opposite directions, are placed around the desired sample. In a vibrating sample magnetometer (VSM), the sample with magnetic moment μ is vibrating inside the pick-up coils with a typical amplitude A of 2 mm and a frequency ν of 40 Hz. The oscillation induces a periodic voltage U_{ind} inside the coil, which is detected with a lock-in amplifier

$$U_{\mathrm{ind}} \propto 2\nu A\mu \sin(2\pi\nu t) \quad .$$

From this signal, the magnetic moment can be deduced. A correction factor has to be taken into account if the sample geometry differs from a point-like shape, see Ref. [75]. This

technique is realized as an option for the PPMS. It allows to measure the magnetization in fields up to 14 T and in the temperature range from 1.8 K to 400 K. Temperatures up to 1000 K are possible with an additional oven option [76].

An even simpler setup is used for pulsed magnetization measurements in the high-field laboratory in Dresden. During the millisecond magnetic-field pulse, the induced voltage inside a pick-up coil that is placed around the sample is measured with an oscilloscope. The position of the sample and coil are fixed. A signal that is proportional to the magnetization of the sample is obtained by integration. The background signal induced by the pick-up coil itself can be measured without a sample. This method does not yield absolute values of magnetization, but the data for low magnetic fields can be scaled onto the data that were collected with a different method.

3.3.3 Faraday magnetometer

The basic principle of a Faraday magnetometer uses the force $\boldsymbol{F}$ along the gradient of the magnetic energy

$$\boldsymbol{F} = \nabla (\boldsymbol{\mu} \cdot \boldsymbol{B}) \quad .$$

For a magnetic field in z direction with a constant gradient $\mathrm{d}B/\mathrm{d}z$ and a homogeneous magnetization, this simplifies to a force that is proportional to the magnetic moment

$$F_z = \mu_z \frac{\mathrm{d}B}{\mathrm{d}z} \quad . \tag{3.1}$$

A Faraday magnetometer, see Fig. 3.4, indirectly measures this force in order to determine the magnetization. A capacitor is setup by two capacitor plates, one mounted to a fixed body and the other one movable. Both parts are connected by copper beryllium (CuBe) springs. The sample is fixed to the movable part. Furthermore, a coil is placed around the sample space. In zero magnetic field and at constant temperature, the distance d_0 between the two capacitor plates follows from $d_0 = \epsilon_0 \pi r^2 / C_0$ with the initial capacitance C_0, the vacuum permittivity ϵ_0, and the radius r of the smaller capacitor plate. The capacitance is measured with a commercial ac capacitance bridge (Andeen Hagerling AH2500/2550) that operates at a fixed frequency of 1 kHz. In a magnetic-field gradient, the force on the magnetized sample results in a change of the distance between the capacitor plates Δd obtained from the changed capacitance C via

$$\Delta d = \epsilon_0 \pi r^2 \left(\frac{1}{C} - \frac{1}{C_0} \right) \quad . \tag{3.2}$$

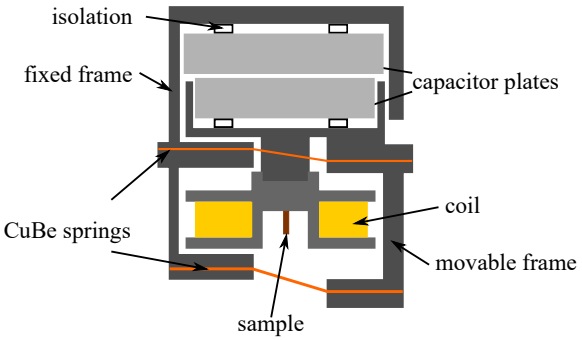

Figure 3.4 Schematic drawing of a Faraday magnetometer. It uses the force onto a sample inside a magnetic-field gradient that changes the distance between two capacitor plates to measure its magnetization. The coil can produce a known additional magnetic moment in order to have an absolute scale.

An additional magnetic moment can be created by a current I_c through the coil. The additionally generated magnetic field can be neglected due to the tiny currents that are used. The magnetic moment of that coil equals $\mu_c = n\,I_c\,A$ with the known winding number n and the area of the coil A. The created moment leads to an additional deflection Δd_c. The linearity of the spring $F_z = k\Delta d$ is used to extrapolate the magnetic moment of the sample. A magnetometer using this principle has been constructed to work with the HelioxVL [77].

Previously, the magnetic field gradient was achieved by adjusting the sample position 2 cm to 7 cm above the field center. At this position, the sample and the whole dilatometer are no longer in the homogeneous field center but in a reduced field with a field gradient. On the one hand, this yields a large signal at large fields since the field gradient scales with the absolute field, but on the other hand it implies the disadvantage of a vanishing gradient towards zero magnetic field.

A magnet with a controllable magnetic-field gradient can overcome this issue and allows to measure the magnetization with the same technique but with a higher resolution in small magnetic fields. Such a magnet was bought from Oxford Instruments via the CRC-1238 and delivered and set up in May 2018, see Fig. 3.5(a). The special advantage of this magnet is the tunability of the magnetic-field gradient with a special coil, that generates a field gradient independent from the absolute magnetic field. The maximum field gradient is $\pm 3\,\mathrm{T\,m^{-1}}$, see Fig. 3.5(b). Figure 3.5(d) shows the magnetic-field profile of the magnet, which is quadratic in vertical dimension. The field center is located 144.7 mm below the top flange. To stay within 0.1 % of the applied maximum field, the setup has to be as accurate as ±0.5 cm. Another feature of the new magnet is a compensation coil. This coil is mounted 30 cm above the field center and wound such that any stray field from the main coil is compensated to zero, see Fig. 3.5(c). The distance is chosen such that the mixing chamber of the dilution refrigerator Kelvinox (Oxford Instruments) can be operated exactly in the compensated field zone. This allows a field calibration of the thermometers, which becomes more and more important for temperatures below 2 K.

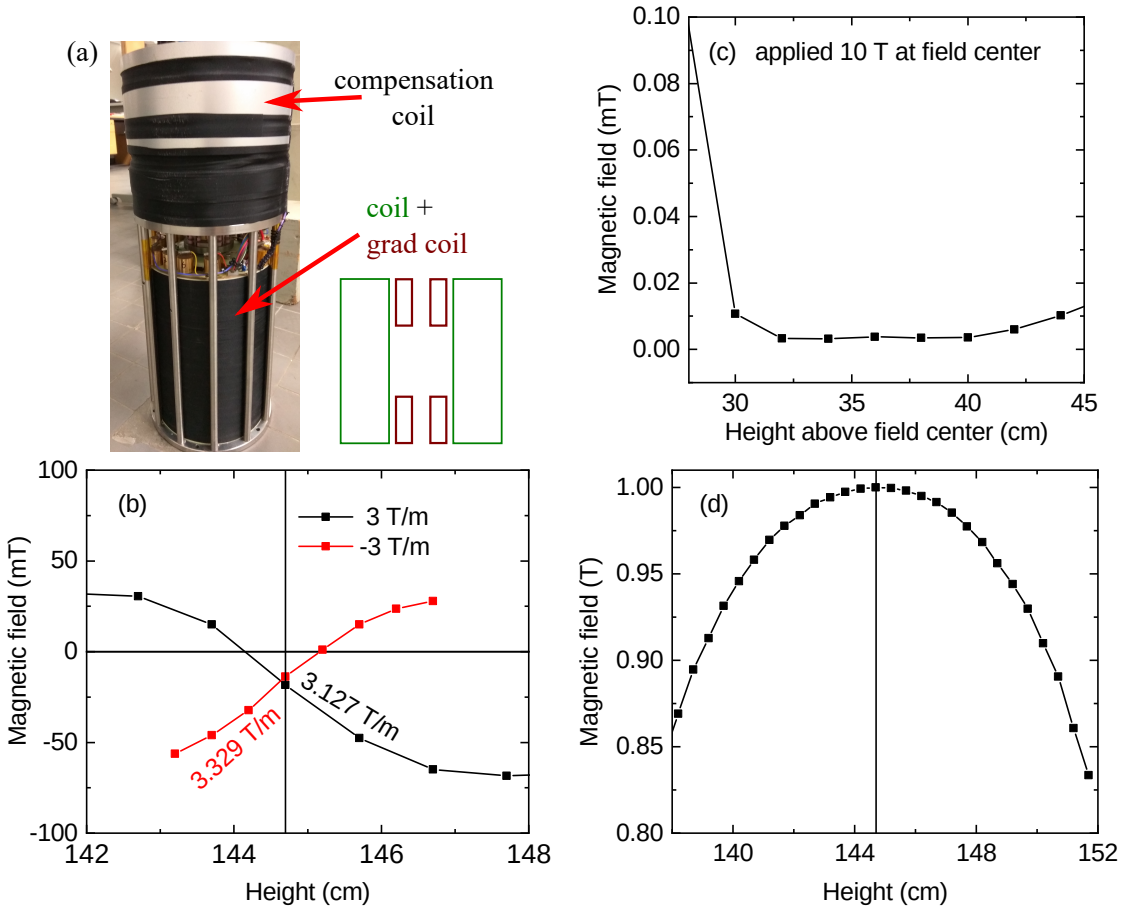

Figure 3.5 Specifications of the gradient magnet. (a) shows a picture of the magnet insert with the 15 T magnet, the gradient coil and the compensation area. (b) depicts the magnetic field around the field center at 0 T absolute field with maximum gradient field of $\pm 3\,\mathrm{T\,m^{-1}}$. (c) shows the magnetic-field height profile in the compensated area at an applied field of 10 T. (d) shows the vertical magnetic-field profile of the main coil at 1 T.

Within the scope of this thesis, different approaches to perform the magnetization measurements in the new magnet were compared. The following technique turned out to be the best compromise between time efficiency and reproducibility.

At a desired temperature T_1 and magnetic field H_1, the capacitance C_i is measured for four different settings:

$$\begin{aligned} &C_1\left(\frac{\mathrm{d}B}{\mathrm{d}z} = 3\,\mathrm{T\,m^{-1}},\ I_\mathrm{c} = +10\,\mu\mathrm{A}\right) \\ &C_2\left(\frac{\mathrm{d}B}{\mathrm{d}z} = 3\,\mathrm{T\,m^{-1}},\ I_\mathrm{c} = -10\,\mu\mathrm{A}\right) \\ &C_3\left(\frac{\mathrm{d}B}{\mathrm{d}z} = 0,\ I_\mathrm{c} = +10\,\mu\mathrm{A}\right) \\ &C_4\left(\frac{\mathrm{d}B}{\mathrm{d}z} = 0,\ I_\mathrm{c} = -10\,\mu\mathrm{A}\right) \quad . \end{aligned}$$

In the beginning, the gradient field is at its maximum value of $3\,\mathrm{T\,m^{-1}}$. A positive and negative current of $10\,\mu\mathrm{A}$ in the coil induce an additional moment. Afterwards, the gradient field is switched off and again the coil moment is poled in both directions. Figure 3.6 schematically supports the following calculation of the magnetization. We see, switching the magnetic moment of the coil creates a small deflection Δd even with $\mathrm{d}B/\mathrm{d}z = 0$. In order to find the equilibrium field gradient $(\mathrm{d}B/\mathrm{d}z)_0$ and the corresponding distance d_0, where switching the coil current does not yield a deflection[1], we assume a linear deflection $d \propto \mathrm{d}B/\mathrm{d}z$ following Eqn. (3.1). Thus, we look for the crossing point of the linear curves for $d(I > 0)$ and $d(I < 0)$ which is obtained via

$$\left(\frac{\mathrm{d}B}{\mathrm{d}z}\right)_0 = \frac{d_4 - d_3}{m - n} \tag{3.3}$$

$$\text{and} \quad d_0 = \frac{d_4 - d_3}{m - n} \cdot n + d_4 \quad , \tag{3.4}$$

where m and n denote the slopes of the d vs. $\mathrm{d}B/\mathrm{d}z$ curves, see Fig. 3.6.

At the maximum gradient field of $3\,\mathrm{T\,m^{-1}}$, $\Delta d_\mathrm{c} = d_2 - d_1$ corresponds to the magnetization induced by the coil current, while the sample magnetic moment yields a general deflection $\Delta d_\mathrm{s} = d_0 - (d_1 + d_2)/2$. The sample moment is calculated using the known coil

[1] $(\mathrm{d}B/\mathrm{d}z)_0$ should not depend on the external magnetic field. If it varies substantially during a field-dependent magnetization measurement, this is an indication that the setup is not placed accurately inside the field center.

moment μ_c via

$$\mu_{\text{sample}} = \frac{\Delta d_s}{\Delta d_c} \cdot \mu_c \quad . \tag{3.5}$$

The LabView VI *Magnetization_Gradient.vi*, see Fig. 3.7, can be used for the data analysis. The software is capable of subtracting a cell effect, which is the measured magnetization of the empty cell that mainly stems from the diamagnetism of the copper body. The measured cell effect is presented in Appendix A.7.

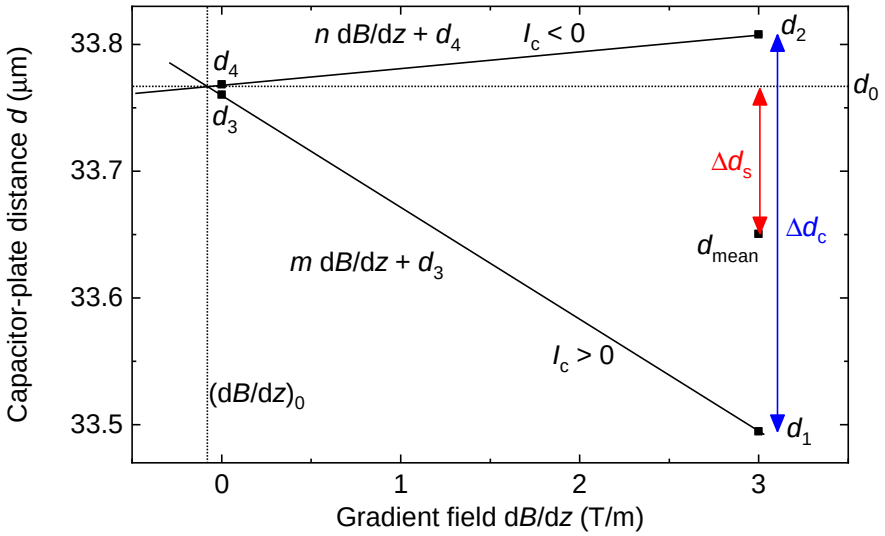

Figure 3.6 Magnetization determination with the Faraday magnetometer. At a constant temperature T_1 and external magnetic field H_1, four different capacitances C_i are measured (see text) that correspond to the presented capacitor-plate distances d_i. From these, the equilibrium distance d_0 is calculated. The deflection Δd_s of the mean value $d_{\text{mean}} = (d_1 + d_2)/2$ from the equilibrium distance is a measure of the magnetization. The deflection of an additional magnetic moment induced by the coil Δd_c yields an absolute scale.

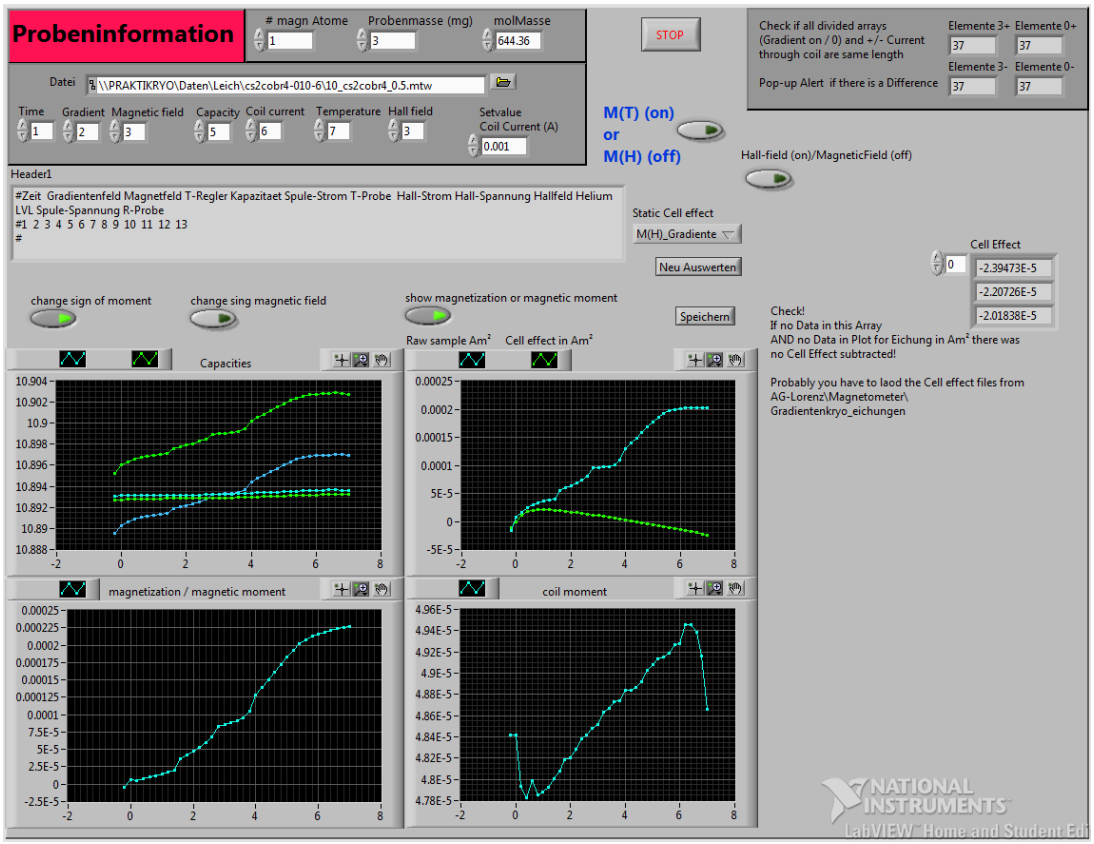

Figure 3.7 Magnetization data-analysis software. The sample information, data file, and its structure have to be defined in the top part. The top left plot shows the measured capacitances, the top right plot the calculated magnetic moment and the corresponding cell effect. In the bottom left plot one can show the magnetization or the magnetic moment, while the bottom right plot shows the coil moment allowing to check the data quality.

3.4 Thermal expansion and magnetostriction

The uniaxial thermal-expansion coefficient α_i of a material can be obtained by measuring the temperature-dependent length change $\Delta L_i(T)$ of a sample along the axis i. A well-known method to detect length changes with a resolution of up to 10^{-10} m is the capacitance dilatometry. Several setups have been designed and built to measure thermal expansion in different cryogenic conditions in our institute, see Refs. [62, 78]. All of them base on the original design of a capacitive dilatometer from Brändli and Griessen from 1973 [79]. The dilatometers are made from copper and consist of a fixed frame and a movable part as shown schematically in Fig. 3.8. Two capacitor plates are electrically isolated from the frame. The movable part is mounted to the fixed part via CuBe springs. The sample is clamped between the movable and fixed part such that the length change of the sample is converted into a distance change between the capacitor plates, which results in a capacitance change

$$\Delta L = \epsilon_0 \pi r^2 \left(\frac{1}{C_1} - \frac{1}{C_2} \right) \quad ,$$

where ϵ_0 is the vacuum permittivity and r the radius of the smaller capacitor plate. Measurements can be performed as a function of temperature and magnetic field. To obtain the thermal-expansion coefficient α_i, the temperature derivative of the relative length change is calculated numerically via

$$\alpha_i = \frac{1}{L_0} \frac{\partial \Delta L_i(T)}{\partial T} \quad . \tag{3.6}$$

For measurements as a function of magnetic field, the magnetostrictive coefficient λ_i is obtained analogous to Eqn. (3.6) with $\Delta L_i(H)$ and the field-dependent derivative.

A copper-based body and capacitor plates are impractical for measurements in large magnetic fields. Magnetic-field rates of the order of 1 T/min induce large eddy-currents which change the signal drastically. A dilatometer made from one piece of CuBe was designed by Küchler *et al.* [80] and is sold commercially. CuBe has an increased resistivity compared to pure copper, which damps the eddy-currents. Nonetheless, the static cell effect is still comparable to the pure copper dilatometers. The thermal conductivity, which is important for the thermalization of the sample and the thermometer, is also comparable. Such a dilatometer was used in the High Field Magnet Laboratory (HFML) Nijmegen (Netherlands) to measure thermal expansion and magnetostriction in the temperature range from 1.4 K to 20 K in magnetic fields up to 30 T. A dilatometer of the same type was bought for the use in a VTI to increase the resolution above 200 K where the other dilatometers produce large and non-reproducible cell effects. The measured cell effect can be found in Appendix A.6. Furthermore, a miniaturized version of the Küchler dilatometer

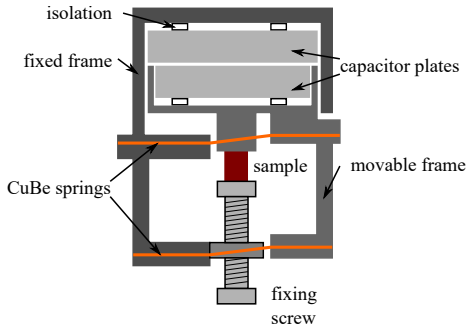

Figure 3.8 Schematic drawing of a capacitance dilatometer. The sample (brown) is clamped between a fixed and a movable frame. A length change of the sample yields a change of the distance of the capacitor plates. CuBe springs are used for the restoring force.

[81] was used in a second high-field experiment in Nijmegen that fits into a smaller bore Bitter magnet with a maximum field of 38 T.

Several issues that occurred during the high-field thermal-expansion and magnetostriction experiments are presented in the following. Figure 3.9(a) shows the length change of $Cs_3Fe_2Br_9$ measured with the larger Küchler dilatometer at the HFML Nijmegen. The dilatometer is usually used with ∼1 mbar ^{4}He exchange gas inside the sample space, to ensure good thermal coupling between the sample, the dilatometer, and the surrounding flow cryostat. The measured length change with the usual amount of contact gas yields two anomalies at ∼12.4 K and 12.7 K (black data). The critical temperatures deviate from the results measured in the HelioxVL dilatometer (purple) that shows transitions at 13.2 K and 13.4 K. These transition temperatures were reproduced with several instruments on different samples in Cologne. By adding more and more contact gas, the transition shifts to higher temperatures indicating a bad thermal coupling between the sample and the thermometer. Even though it was not possible to shift the temperature to the expected value, the differences can be neglected, as the qualitative behavior is reproduced. The difference of the measured relative length changes shows the imperfections of the dilatometry for large spontaneous length changes.

During magnetostriction measurements, the temperature of the large dilatometer setup is controlled by a PID loop. However, for the measurements with $\boldsymbol{H} \perp \boldsymbol{c}$, the heater output was not controlled but set to a constant value, that was adjusted in zero field. In the case of a field-independent heater power, this routine should correct for magnetoresistance effects of the thermometer.[2] However, in these measurements only the heater current was constant and thus the magnetoresistivity of the heater also changes the heater power. Figure 3.9(b) shows the measured temperature change of the sensor normalized to the zero-field temperature during these magnetostriction measurements. Obviously, at temperatures above 4.2 K, there is a huge temperature change around 20 T. Furthermore, this effect differs

[2]The magnetoresistance of the used Cernox sensor was measured by the local contacts at the HFML Nijmegen and the corresponding errors above 4 K are below 10 %.

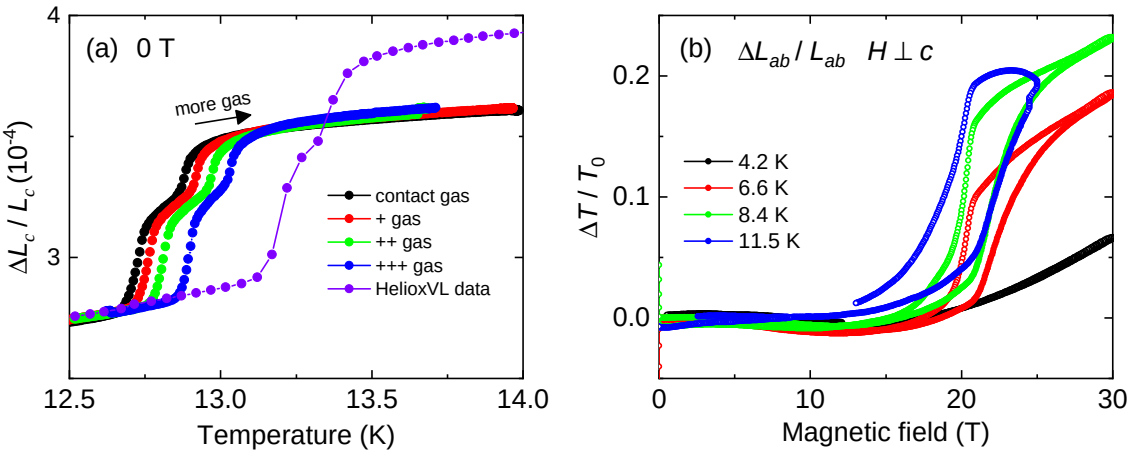

Figure 3.9 Issues with the temperature control in high-field thermal expansion and magnetostriction measurements. (a) shows the thermal expansion of $Cs_3Fe_2Br_9$ in zero field measured in the large Küchler dilatometer [80] at the HFML Nijmegen. All measurements were performed on increasing temperature. Between different data sets, additional ^{4}He exchange gas was put into the sample space. For comparison, the data from the HelioxVL are presented. (b) shows the temperature changes during magnetostriction measurements with $\boldsymbol{H} \perp \boldsymbol{c}$ that will will be shown in Fig. 5.16. The measured temperatures are normalized to the zero-field value. The measurements were performed with a fixed heater output. At 4.2 K, the heater is switched off.

between increasing and decreasing magnetic field, which makes it hysteretic. These temperature deviations were used when defining the critical temperatures and magnetic fields for the phase diagram.

The small dilatometer [81] that is used for magnetostriction measurements in fields up to 38 T has not yet been optimized for the use at temperatures above 4.2 K. For lower temperatures, this is controlled by the gas pressure of the He bath. Above these temperatures, it is controlled by the PID loop without correcting for the magnetoresistance Cernox sensor. Nonetheless, the expected small errors are irrelevant for the interpretation of the results.

3.5 Specific heat and magnetocaloric effect

In statistical physics, the heat capacity C_i at a constant volume V and at constant pressure P are defined via the temperature derivative of the thermodynamic potentials

$$\begin{aligned}
&\text{internal energy} && E = E(S,V),\\
&\text{enthalpy} && W = W(S,P) = E + PV,\\
&\text{free energy} && F = F(T,V) = E - TS,\\
&\text{Gibbs free energy} && G = G(T,P) = E - TS + PV
\end{aligned}$$

with the entropy S

$$S_V = -\left.\frac{\partial F}{\partial T}\right|_V \quad \text{and} \quad S_P = -\left.\frac{\partial G}{\partial T}\right|_P$$

$$\text{to be} \qquad C_V = \left.\frac{\partial E}{\partial T}\right|_V = T\left.\frac{\partial S}{\partial T}\right|_V = -T\left.\frac{\partial^2 F}{\partial T \partial T}\right|_V$$

$$\text{and} \qquad C_P = \left.\frac{\partial W}{\partial T}\right|_P = T\left.\frac{\partial S}{\partial T}\right|_P = -T\left.\frac{\partial^2 G}{\partial T \partial T}\right|_P \quad .$$

Typically, C_P is measured because it is easy to keep the pressure constant in experiment and impractical to keep the volume unchanged. Nonetheless, typical theoretical considerations take C_V into account. The two quantities are related via the compressibility $\kappa = -\frac{1}{V}\frac{\partial V}{\partial P}$ and the volume thermal expansion $\beta = \frac{1}{V}\frac{\partial V}{\partial T}$ via

$$C_P - C_V = VT\frac{\beta^2}{\kappa} \quad . \tag{3.7}$$

In practice, the difference between C_P and C_V is negligible for solids since the volume thermal expansion is small.

Because the heat capacity relates the energy change of a system to a change of temperature, it probes all excitations of the system, e.g., lattice, electronic, and magnetic excitations. In general, the distinction of different origins can be complicated, as all contributions overlap. Additionally, it is a sensitive probe for phase transitions of any kind.

The heat capacity of a sample can be measured with different methods. All methods apply heat to the sample and measure the temperature response over time. Typically, the heat capacity is normalized to the sample mass and given in J/molK. The most common method is the so-called relaxation method, presented in Fig. 3.10. Via the conductance K_2, the sample is thermally coupled to a platform with a thermometer and a heater. This whole setup is coupled to a heat bath via K_1. Ideally, the coupling of the sample to the platform is infinite and the coupling to the bath is finite but not too small. The heat capacity is deduced from the time constant of the relaxation process after switching the heater on and off. Figure 3.10(b) shows the typical time dependence of the platform temperature for one relaxation measurement. For an equilibrated state with the temperature T_0, a heater power ΔP is applied at the time t_1. This causes a rise of the sample temperature with an exponential time dependence. The heater is switched off at t_2 and the sample temperature relaxes back to T_0. According to the first law of thermodynamics

$$\Delta Q = C\Delta T \quad ,$$

the temperature change of the system caused by the heat ΔQ depends on the heat capacity C. The heat change contains the applied heater power reduced by the heat flow from the platform to the bath via K_1

$$C\mathrm{d}T = \Delta P\mathrm{d}t - K_1(T - T_0)\mathrm{d}t \quad . \tag{3.8}$$

Thus, the time dependence of the temperature for the time range $t_1 < t < t_2$ follows via integration of Eqn. (3.8)

$$T_{\mathrm{heat}}(t) = T_0 + \frac{\Delta P}{K_1}\left(1 - \mathrm{e}^{-(t-t_1)/\tau}\right), \quad \text{with} \quad \tau = \frac{C}{K_1}$$

and analogous for the cooling regime with $t > t_2$

$$T_{\mathrm{relax}}(t) = T_0 + \frac{\Delta P}{K_1}\mathrm{e}^{-(t-t_2)/\tau} \quad .$$

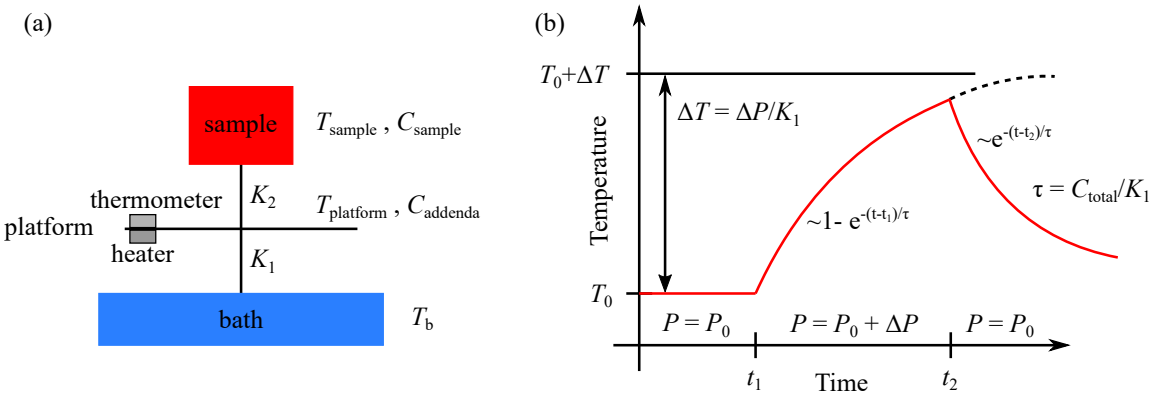

Figure 3.10 Schematic setup and measurement principle for specific-heat measurements. (a) shows the experimental setup for specific-heat measurements consisting of a sample coupled to the platform on which also a thermometer and a heater are mounted. This setup is coupled to the bath. (b) shows the typical time dependence of the sample temperature in a relaxation measurement. At t_1, the power ΔP is applied and yields an exponentially saturating temperature dependence. At t_2, the heater is switched off and the temperature relaxes back. The heat capacity C is obtained from the time constant τ, the temperature rise ΔT, and the thermal conductance K_1.

The thermal conductance and heat capacity are obtained by fitting both regimes. A setup and software have been designed in order to perform automatized measurements at low temperatures with the HelioxVL [82]. The same principle is used by the commercial heat-capacity option for the PPMS, covering a temperature range from 1.8 K to 400 K.

In a usual heat pulse, ΔT equals 3 % of the absolute temperature, e.g., 0.3 K at 10 K. In this spanned temperature interval, the relaxation time τ and thus the specific heat c_p is assumed to be constant. At a first-order transitions, the heat capacity changes drastically and becomes infinite due to latent heat. If the first-order phase transition occurs in the spanned temperature interval, this assumption is wrong and the method underestimates the specific heat. In such a case, a continuous evaluation method for the specific heat by numerical derivation of the temperature during a heat pulse should be chosen. Such a technique was already used in Ref. [83] to analyze heat pulses over the first-order phase transitions in $(NH_4)_2FeCl_5(H_2O)$ and was also applied to analyze the specific-heat measurements on $Cs_3Fe_2Br_9$. A. Scheie proposed a similar routine to analyze relaxation-method data from the PPMS [84].

In addition to the already available pucks for specific-heat measurements, a vertical puck (No. 444) was bought, see Fig. 3.11. For the common specific-heat pucks, the magnetic field is applied perpendicular to the sample platform. The vertical puck allows an in-plane magnetic field. Furthermore, the sample platform is located at the field center. The sample

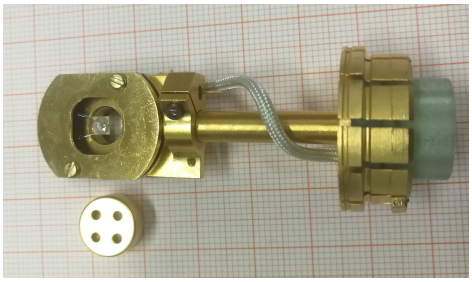

Figure 3.11 Vertical puck for specific heat measurements with the magnetic field in the plane of the sample platform. The sample platform is located a few centimeters above the usual sample position to be located in the field center.

temperature of this puck does not always reach the base temperature of 1.8 K presumably because of a reduced thermal coupling.

The entropy of a system does not only depend on the temperature, but also on the magnetic field. This behavior is related to the temperature dependence of the magnetization via the Maxwell relation

$$\left.\frac{\partial S}{\partial H}\right|_T = \left.\frac{\partial M}{\partial T}\right|_H \quad .$$

Combining this with the differential of the entropy dS

$$\mathrm{d}S = \frac{C_H}{T}\mathrm{d}T + \left.\frac{\partial M}{\partial T}\right|_H \mathrm{d}H \quad ,$$

the temperature change ΔT_{ad} in an adiabatic experiment with a change of the magnetic field is defined by

$$\Delta T_{\mathrm{ad}} = -\int_{H_0}^{H_1} \frac{T}{C_H}\left.\frac{\partial M}{\partial T}\right|_H \mathrm{d}H \quad .$$

In an experiment, only quasi-adiabatic conditions can be fulfilled. The measured temperature change is called (quasi-)adiabatic magnetocaloric effect (MCE). From such measurements, it is difficult to determine the field-dependent entropy of the system, because C_H is also temperature dependent. Nonetheless, a qualitative statement of the entropy landscape can be made and phase transitions can be identified. For example, this technique was applied to see the quantum-critical behavior of $BaCo_2V_2O_8$ [85]. In an isothermal process (dT = 0), it is possible to determine the actual field-dependence of the entropy. The principle and the experimental realization are described in Ref. [82].

For this thesis, measurements of the quasi-adiabatic MCE were performed on $Cs_3Fe_2Br_9$ in pulsed magnetic fields at HZDR by T. Nomura. The setup consists of a thermometer that is directly attached to the sample. Grease is used to ensure good thermal contact between the sample and the thermometer to get most direct access to the sample temperature. Figure 3.12 shows the field dependence of the sample temperature during magnetic-field pulses

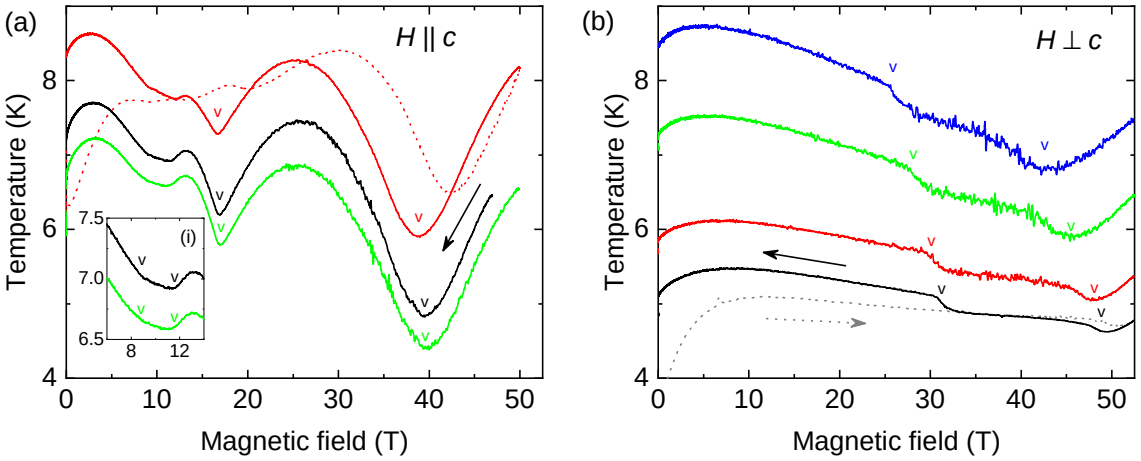

Figure 3.12 Magnetocaloric effect of $Cs_3Fe_2Br_9$ for $\boldsymbol{H} \parallel \boldsymbol{c}$ (a) and $\perp \boldsymbol{c}$ (b) in pulsed magnetic fields up to 52 T. The measurements were performed by T. Nomura at the HZDR under quasi-adiabatic conditions as described in the text. Identified anomalies are marked by ∨.

for two different magnetic-field orientations. These were performed to quantify possible temperature changes during pulsed experiments that might explain deviations between thermal expansion and pulsed magnetization measurements. Both panels show strongly field-dependent temperatures with several anomalies. Upon increasing magnetic field in both field orientations, a large temperature increase is found up to about 10 T (dashed lines in Fig. 3.12), that is absent on decreasing the field. This signal is an experimental artifact and does not originate from the sample [86]. Furthermore, measurements on increasing and decreasing field show large hysteresis effects, indicating that the thermometer is not perfectly coupled to the sample. Qualitatively, the temperature changes are different for both field orientations. For $\boldsymbol{H} \parallel \boldsymbol{c}$, there are two prominent minima, one at 18 T and one at 40 T. These minima correspond to maxima of the entropy. Further kinks in $T(H)$ can be found in this field orientation, see inset. Knowing the phase diagram from measurements of other quantities like magnetostriction or magnetization, all features in $T(H)$ can be attributed to phase transitions. However not all occuring phase transitions are visible in the magnetocaloric-effect data. For the perpendicular field orientation, two features are visible which also correspond to phase transitions of $Cs_3Fe_2Br_9$. For magnetic fields above $H^{\parallel c} \approx 40$ T and $H^{\perp c} \approx 50$ T, the temperature increases again. The measured temperature changes of ~2 K performed with the quasi-adiabatic setup are an upper limit for temperature changes due to the magnetocaloric effect in a pulsed field experiment. For pulsed magnetization measurements, the sample is coupled to the environment via contact gas and thus the changes should be smaller.

3.6 Pyrocurrent

The pyroelectric effect describes the temperature dependence of the pyroelectric polarization via

$$\Delta P_i = p_i(T)\Delta T \quad . \tag{3.9}$$

A polarization change of ΔP_i is induced along a certain direction i, called polar axis, by changing the temperature by ΔT .

To measure the electric polarization of a material, a modification of the principle of Byer and Roudy is used [87]. Two opposing sample surfaces are metallized to form a capacitor with plates of area A, see Fig. 3.13. Usually, this is done by metallizing the surfaces with sputtered gold or silver paint. In the case of $Cs_3Fe_2Br_9$, this procedure does not work because the material is reactive and degrades in contact to alcoholic solvents and even pure gold. To keep the sample intact and set up a capacitor, the sample surfaces were covered with Apiezon N grease and, then, a copper foil of area A was attached to the greased surface.

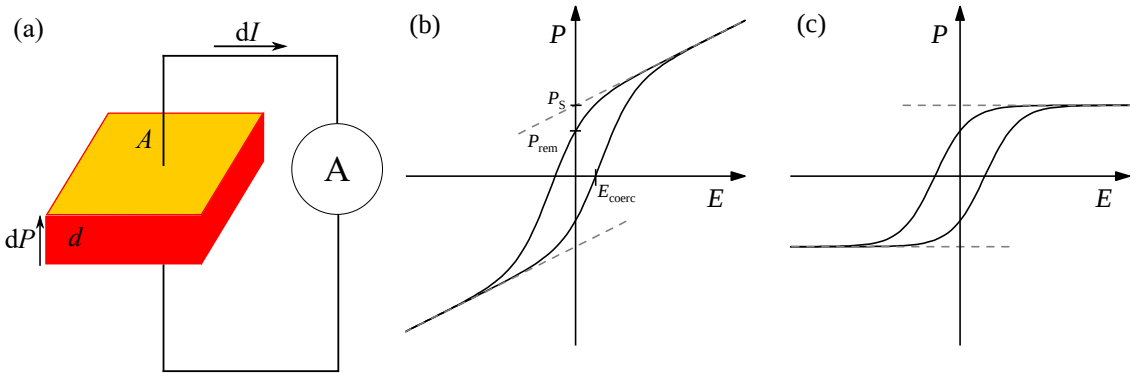

Figure 3.13 Pyrocurrent setup and generic hysteresis loop. (a) schematically shows the experimental setup for pyroelectric-current measurements. A polarization change dP induces a current dI which is measured at a picoamperemeter. (b) shows a generic hysteresis loop for a ferroelectric material with the coercive field E_{coerc}, the spontaneous polarization P_{S}, and the remanent polarization P_{rem}. The same hysteresis loop with subtracted induced polarization $\chi\epsilon_0 E = (\epsilon - 1)\epsilon_0 E$ is shown in (c).

Both plates are then connected to a picoamperemeter (Keithley 6517), which has a small input resistance. If the polarization changes, a current is induced as $I(T) = Ap(T)\mathrm{d}T/\mathrm{d}t$. The change of electric polarization ΔP is obtained by integration

$$\Delta P = \frac{1}{A}\int_{t_0}^{t} I(T(t))\mathrm{d}t \quad . \tag{3.10}$$

It has to be noted, that this technique is only sensitive to changes of the polarization ΔP and cannot quantify the absolute polarization P. However, if a material shows a phase transition from paraelectric with $P = 0$ to ferroelectric or pyroelectric also the absolute polarization can be measured. A ferroelectric sample usually consists of multiple domains oriented such that the net polarization is zero. An external electric field can be applied by the amperemeter to overcome this multi-domain state and align all domains to form a single-domain state. In a pyrocurrent measurement, such a poling voltage is applied upon cooling through the transition. Before the subsequent heating curve, this voltage is switched off to avoid an additional signal induced by changes of the dielectric constant ϵ via $\Delta P = \Delta\epsilon\epsilon_0 E$. Further information on the technique and the measurement setup can be found in Refs. [88, 89, 90].

With the very same setup it is possible to measure hysteresis loops of the polarization, see Fig. 3.13(b). This requires the ability to apply electric fields larger than the coercive field E_{coerc}. For materials with a small spontaneous polarization it is useful to subtract the field-induced polarization

$$P_{\mathrm{ind}} = \chi\epsilon_0 E \quad .$$

The resulting hysteresis is shown in Fig. 3.13(c). The saturation polarization P_{sat} is the maximum value of P in large electric fields and the remanent polarization P_{rem} is the value in a vanishing electric field that is smaller due to the formation of domains. The coercive field E_{coerc} is required to suppress the remanent polarization and is a measure of the energy barrier between the different domain orientations.

3.7 Electric transport properties

Transport measurement to determine the longitudinal and transverse transport as defined in Chapter 2.1 are performed with a 6-terminal measurement that excludes contact effects from the measured voltages. Different cryostats to measure the electric transport are available. Depending on the desired temperature regime, there are, e.g., a dipstick for the use

inside a magnet bath cryostat, a HelioxVL probe, and the PPMS. The PPMS software is not able to measure longitudinal and transversal voltages with only one current device or two samples at the same time. Thus, it would require eight contacts for a single sample. A breakout box was designed to use the PPMS only as a controllable temperature setup with a superconducting magnet. All current and voltage measurements were performed using Keithley devices of types 6220, 2400, and 2182. With the new breakout box it is possible to measure two samples at the same time.

In this context, it is important to keep full track of the direction of current, field, and poling of voltmeters in order not to get a sign error. This is still a source of confusion, e.g., for the transport properties of $SrRuO_3$ thin films. One should stick to the following procedure, which directly yields the correct sign of ρ_{yx}. Figure 3.14 shows the schematic drawing of a 6-terminal contacted sample. A current I_x is induced in x direction, the Hall voltage U_y over the sample is measured along y and the longitudinal voltage U_x along the current. For a sample with thickness d, the Hall voltage U_y follows

$$U_y = \frac{1}{d}\rho_{yx} I_x \quad .$$

It is experimentally impossible to have perfectly opposing contacts U_y, and, thus, the signal is contaminated by a longitudinal resistive signal. Because this part is an even function of the magnetic field and the Hall signal is odd, both contributions can easily be separated by measuring the voltage for positive and negative magnetic fields and calculate the

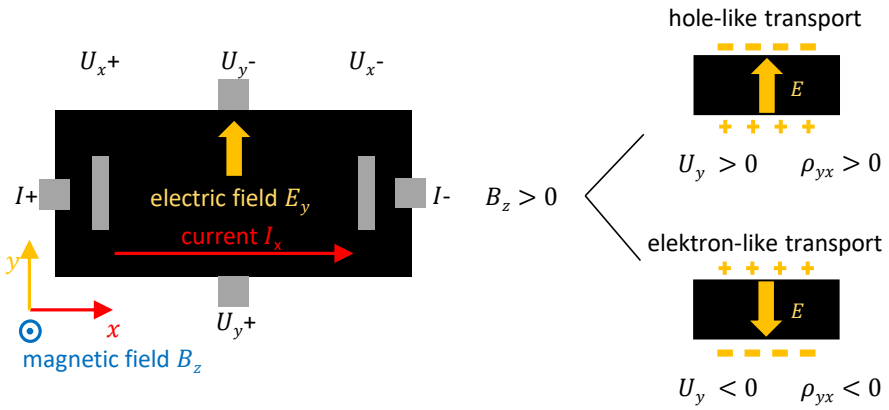

Figure 3.14 Schematic drawing of a transport measurement. The current runs in x direction, a magnetic field points along z, and the Hall voltage is measured in y direction. For a positive magnetic field, a hole-like transport yields a positive voltage and an electron-like transport yields a negative voltage.

symmetric (even) and antisymmetric (odd) parts via

$$U_y^{\text{odd}} = \frac{U_y(B) - U_y(-B)}{2} \quad \text{and} \quad U_y^{\text{even}} = \frac{U_y(B) + U_y(-B)}{2} \quad .$$

The symmetric part represents the longitudinal resistivity and the fraction U_y^{even}/U_x is a measure of the quality of the contact alignment. Generally, the misalignment should be below 10 %. U_y^{odd} yields the usual Hall signal.

This analysis does not account for deviations from a perfectly even or odd behavior. Hysteresis effects when crossing $B = 0$ may induce such deviations. To keep full track of these effects, a full hysteresis is measured and the antisymmetrization is done from two independent measurements, one with increasing and the other with decreasing magnetic field via

$$U_y^{\text{odd}} = \frac{U_y^{\uparrow}(B) - U_y^{\downarrow}(-B)}{2} \quad . \tag{3.11}$$

The resulting effective field-sweep direction is an up-sweep.

Figure 3.15 illustrates the difference between a usual antisymmetrized ρ_{yx} measurement in panel (a) and the use of a full hysteresis loop in panel (b). For the full hysteresis analysis, ρ_{yx} decreases linearly with increasing magnetic field, then a step occurs at $B = 0$. The step does not yield a perfectly antisymmetric value, but ρ_{yx} shows a plateau up to ~1.5 T. From there on, the signal recovers the antisymmetric value. In contrast to this, the antisymmetrized signal of a single file is perfectly antisymmetric by construction. The directional information is lost.

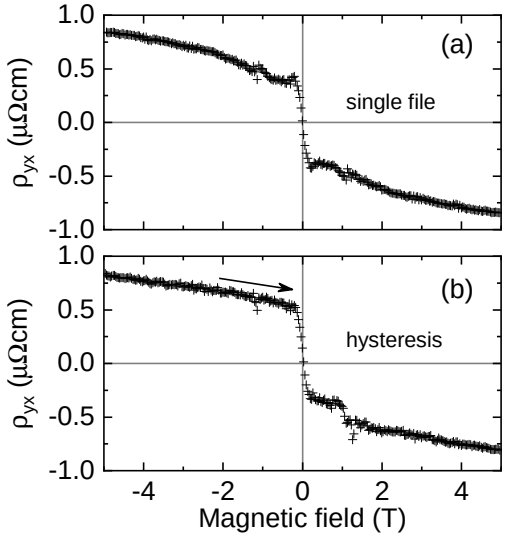

Figure 3.15 Antisymmetrization of the Hall resistivity ρ_{yx}. (a) shows a usual antisymmetrized file. The direction information is lost. (b) uses two measurements, one with increasing field and one with decreasing field. The antisymmetrization is performed according to Eqn. (3.11). The resulting file has an effectively increasing magnetic field.

Using a full hysteresis for the antisymmetrization, the resulting signal contains a directional information and is no longer perfectly antisymmetric by construction. Besides usual hysteresis effects also time-dependent drifts become visible. For example this may result in an offset. This offset is a measure of the quality of the data. To describe the Hall resistivity including this correction, the following equation is applied:

$$\rho_{yx}(T, B) = R_{\mathrm{H}}(T)B_{\mathrm{ext}} + R_{\mathrm{AHE}}(T)\mu_0 M(T, B_{\mathrm{ext}}) + C \quad . \tag{3.12}$$

4 $SrRuO_3$

Contents

This chapter covers the thermodynamics and transport investigations of the ferromagnetic metal $SrRuO_3$. After an introduction and a presentation of relevant literature, the criticality of the ferromagnetic phase transition at 163 K is analyzed. High-quality single crystals grown with the floating-zone technique were used. The results prefer the Ising over the Heisenberg or mean-field universality class. Furthermore, the magnetic anisotropy is investigated and the magnetoelastic coupling is studied. $SrRuO_3$ turns out to host a shape-memory effect. Electric transport measurements were performed to analyze the origin of the anomalous Hall effect. The effect is observed even above T_C, where no spontaneous magnetization is present but induced by finite magnetic fields. Spin orbit coupling allows a topological contribution to the electron velocity that is based on the theoretical concept of the Berry phase. Furthermore, its signature in the anomalous softening of the magnon gap and the stiffness has been found. Parts of the results have already been published in S. Kunkemöller *et al.*, Phys. Rev. B **96**, 220406(R) (2017) and K. Jenni *et al.*, Phys. Rev. Lett. **132**, 017202 (2019).

4.1 Introduction

Ruddlesden-Popper Series

The mineral $CaTiO_3$ was found in 1839 and named Perovskite after the Russian mineralogist. The structure with the generalized chemical formula ABX_3 is cubic. Many other materials also crystallize in this structure that consist of a divalent A^{2+} ion and a 4-valent B^{4+} ion that differ drastically in size. The anion X^{2-} binds to both. In the ideal cubic structure, B is 6-fold octahedrally coordinated and A is 12-fold coordinated, see Fig. 4.2(a). There are many symmetry-reduced distorted versions in which the coordination number is reduced. Such distortions can arise from a tilting of the oxygen octahedron or from a displacement of the B ion, as observed, e.g., in $BaTiO_3$ [91].

The Ruddlesden-Popper series with the sum formula $A_{n-1}B_nX_{3n+1}$ describes a special stacking of layers with corner-sharing BX_6 octahedra. Along $\boldsymbol{c}$, n of these layers are separated by an AX rock-salt layer, so that singly, doubly, triply, etc. layered compounds form. The members of the series are basically tetragonal, only for $n \rightarrow \infty$ this yields the cubic perovskite structure, where the octahedra are also corner-sharing along $\boldsymbol{c}$. Materials forming a Ruddlesden-Popper series are, e.g., $SrTiO_3$ and $CaMnO_3$. In most of the early-studied members of such series, the B ions were 3d transition-metal ions, like Ti and Mn. Fundamental interactions that play the most important role in such magnetic materials are coulomb interaction, exchange interaction, and spin-orbit coupling. In 3d transition elements, the tendency for strong correlations is dominating, whereas the other interactions are comparably weak. Especially the spin-orbit exchange is treated as a small perturbation. On the other hand for 5d ions like Re, Ir, and Hf the spin-orbit coupling is strongly enhanced, since it scales with the atomic number via Z^4 [92]. In 4d transition-metal compounds, all three energy scales are comparably large, which makes subtle changes cause drastic effects. Two such materials that are relevant for this thesis are Sr_2RuO_4 and $SrRuO_3$. Both materials contain the 4d ion Ru^{4+} and are discussed in the following.

$Sr_{n\text{-}1}Ru_nO_{3n+1}$

The first publication on a ruthenate stems from 1959, where Sr_2RuO_4 was synthesized and structurally characterized [93]. From this finding, it took until 1994 to discover superconductivity in this material, which afterwards forced tremendous research activities on the ruthenates $Sr_{n-1}Ru_nO_{3n+1}$. In these compounds, Ru^{4+} ions are octahedrally coordinated. A regular octahedron causes a cubic crystal field, which splits the single-ion levels into a high-energy doublet e_g and a low-energy triplet t_{2g} niveau, see Fig. 4.1. Due to the splitting

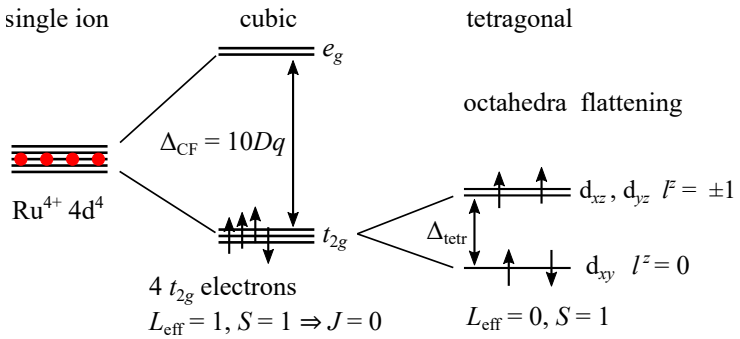

Figure 4.1 Crystal-field splitting for Ru^{4+} in a cubic and tetragonal environment. Ru^{4+} ions have the electronic configuration $5d^4$. In a perfect octahedral (cubic) environment, the d orbital energies split up into a high-energy doublet e_g and a low-energy triplet t_{2g}. For a large splitting Δ_{CF}, the ground state is nonmagnetic $J = 0$. For a tetragonal distortion Δ_{tetr} of flattened octahedra, the t_{2g} states split and yield a magnetic ground state with $L_{eff} = 0$ and $S = 1$.

of $\Delta_{CF} = 10Dq \approx 3\,\text{eV}$ [94], only the t_{2g} states are occupied. The resulting configuration t_{2g}^4 has total spin $S = 1$ and an effective angular momentum $L_{eff} = 1$. In the J multiplet, $J = L_{eff} - S = 0$ is the lowest in energy resulting in a nonmagnetic ground state. Nonetheless, many ruthenates order magnetically or show at least an enhanced paramagnetism [95]. This can be explained by two different scenarios. If the oxygen surrounding is not perfectly octahedral but contracted along z, the d_{xz} and d_{yz} orbitals with $l^z = \pm 1$ have an increased energy, while the d_{xy} with $l^z = 0$ is lowered. This distortion is typically tetrahedral, because it implies a doubling of the unit cell with reduced symmetry. If the distortion, and, thus, the splitting of the energy levels is large enough, the low-lying state is doubly occupied and d_{xz} and d_{yz} are singly occupied. This yields a quenched angular momentum $L_{eff} = 0$. The total spin $S = 1$ yields a magnetic ground state. This state can gain further energy via magnetic exchange between Ru^{4+} ions. An elongation of the octahedron causes the opposite shifting of the d-orbital energies. This results in a non-quenched angular momentum and a nonmagnetic ground state. This state is stabilized by spin-orbit coupling. Overall, the interplay of distortion, exchange interaction, and spin-orbit coupling is the driving force of many effects found in the ruthenates and determines the magnetic properties.

The Ruddlesden-Popper series of $Sr_{n-1}Ru_nO_{3n+1}$ hosts an enormous variety of physical phenomena. For sure, the big boost of research activity arose from the discovery of superconductivity in Sr_2RuO_4 by Maeno *et al.* in 1994 [12]. The superconductivity is particularly interesting in the context of high-temperature superconductivity in the cuprates, which had been found by Bednorz and Müller in 1986 [96], because Sr_2RuO_4 was the

first superconducting layered perovskite material besides the cuprates without containing copper. It is not relevant for any applications because of the transition temperature of at best 1.5 K in very pure samples. Nonetheless, it is relevant to investigate and understand the differences to the cuprate superconductors. Ferromagnetic fluctuations were proposed as the pairing mechanism already in early publications. Over the time, more and more evidence for spin-triplet Cooper pairs was collected, see various review articles [97, 98, 99]. But only recently an essential experiment disproved the first nuclear magnetic resonance results [15]. Thus, the pairing mechanism in Sr_2RuO_4 is still under debate.

The structural vicinity to Sr_2RuO_4 stimulated the research on other members of the Ruddlesden-Popper series $Sr_{n-1}Ru_nO_{3n+1}$. In the following, the focus is put on the infinite layered $SrRuO_3$.

4.2 $SrRuO_3$ literature

$SrRuO_3$ is the only simple member of $Sr_{n-1}Ru_nO_{3n+1}$ that shows ferromagnetic order at ambient conditions, which is by its own a rare phenomenon in transition-metal oxides. Additionally, it inspired the proposal of p-wave superconductivity in Sr_2RuO_4 mediated by ferromagnetic fluctuations, to briefly name two main research-driving forces.

Similar to other perovskites, $SrRuO_3$ undergoes two distortive structural phase transitions. The material is cubic above 950 K with space group $Pm\bar{3}m$ and tetragonal below this temperature because of an alternating rotation of neighboring oxygen octahedra around the $\boldsymbol{b}$ axis by Φ_{rot}, see Fig. 4.2(c), which results in a symmetry reduction to $I4/mcm$. This transition results in three tetragonal twins because each cubic axis can become the long tetragonal axis. Upon cooling further, $SrRuO_3$ becomes orthorhombic at 820 K with space group *Pnma* in which the oxygen octahedra are tilted away from $\boldsymbol{b}$ by θ_{tilt}, see Fig. 4.2(b). Through this transition, each tetragonal twin splits into two orthorhombic twins resulting in a total number of six twin domains. In the orthorhombic structure at room temperature, the distortions amount to $\theta_{\mathrm{tilt}} = 8.7°$ and $\Phi_{\mathrm{rot}} = 6.1°$ [19, 100, 101, 102, 103]. The orthorhombic axes $\boldsymbol{a}$, $\boldsymbol{b}$, and $\boldsymbol{c}$ are related to the cubic axes (cubic lattice constant $a_{\mathrm{c}} \approx 3.93$Å) via

$$\begin{aligned} \boldsymbol{a} \parallel [1\,0\,1]_c \quad & |\boldsymbol{a}| = 5.5322(1)\,\text{Å} \approx \sqrt{2}a_{\mathrm{c}} \\ \boldsymbol{b} \parallel [0\,1\,0]_c \quad & |\boldsymbol{b}| = 7.8495(2)\,\text{Å} \approx \quad 2a_{\mathrm{c}} \\ \boldsymbol{c} \parallel [\bar{1}\,0\,1]_c \quad & |\boldsymbol{c}| = 5.5730(1)\,\text{Å} \approx \sqrt{2}a_{\mathrm{c}} \quad . \end{aligned}$$

Note, that this setting describes only one possible twin and the others obey equivalent *h k l*

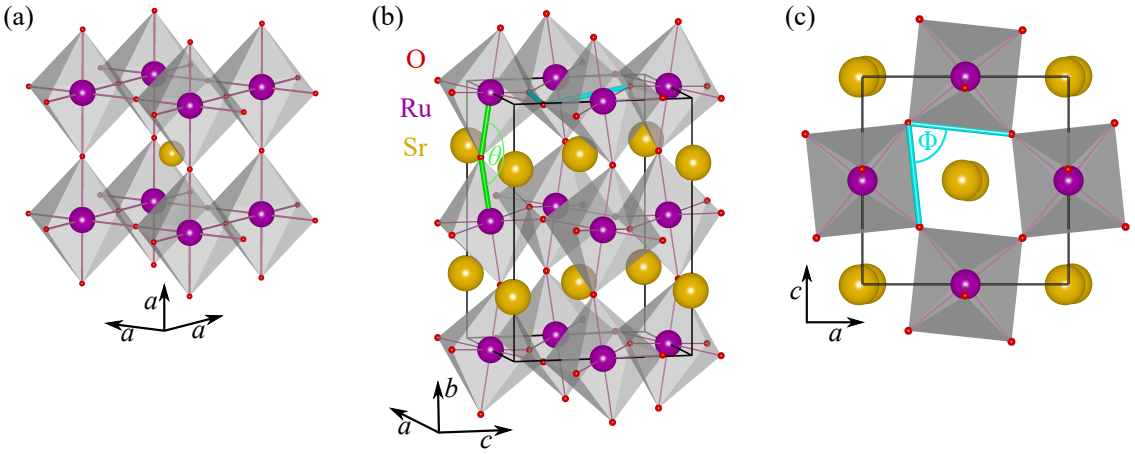

Figure 4.2 Crystal structure of $SrRuO_3$. (a) shows the high-temperature cubic unit cell ($Pm\bar{3}m$) that contains one formula unit. (b) and (c) show the distorted orthorhombic room-temperature structure (*Pnma*) that contains four formula units per unit cell. The RuO_6 octahedra are tilted away from $\boldsymbol{b}$ by $\theta_{\text{tilt}} = (180° - \theta)/2$ and rotated around $\boldsymbol{b}$ by $\Phi_{\text{rot}} = (90° - \Phi)/2$.

permutations. In literature, there is also another setting reported for the room-temperature structure. The *Pbnm* setting is equivalent to *Pnma* with a different coordinate system. The axis from *Pbnm* correspond to those of *Pnma* via $a_{Pbnm} = a_{Pnma}$, $b_{Pbnm} = c_{Pnma}$, and $c_{Pbnm} = b_{Pnma}$.

The first synthesis of $SrRuO_3$ was reported by Randall and Ward in 1959 [93]. Single crystals were grown with the flux method but only mg of weight and host by far more impurities compared to crystals of other layered ruthenates grown with the floating zone technique [104]. Only recently, in Cologne a recipe was found to grow high-quality single crystals of centimeter size by the floating-zone technique [19]. The main problem in the growth process is the evaporation of RuO_2. An excess of 90% is used to compensate for that. Additionally, the optimized growth speed of 15 mm/h is comparably high in order to further reduce the evaporation. $SrRuO_3$ has the largest Ru concentration in the $Sr_{n-1}Ru_nO_{3n+1}$ series and the evaporation of Ru causes the growth of other layered members of the Ruddlesden-Popper series Sr_2RuO_4 and $Sr_3Ru_2O_7$.

A substantial part of the research activity of the last decade on $SrRuO_3$ is performed on thin-film samples. Typically, these films are grown by pulsed laser deposition (PLD) where $SrRuO_3$ is illuminated with a pulsed laser that produces a plasma plume onto a hot substrate, where the film crystallizes. $SrTiO_3$ is used as a substrate, because it has a similar lattice constant, which minimizes strain effects. Bulk crystals of $SrRuO_3$ become ferromagnetic at $T_C = 164$ K. In thin films, this transition is reduced to approximately

150 K and also depends on the film thickness.

$SrRuO_3$ is a band ferromagnet with conduction electrons mainly from the Ruthenium 4d band. Nonetheless, the magnetism is rather local. This follows from a comparison of the high-temperature Curie-Weiss behavior to the magnetic saturation moment at low temperature. In $SrRuO_3$, the Curie-Weiss analysis yields an effective moment of $2\,\mu_B$, while $M_{sat} = 1.6\,\mu_B$ [105]. Thus, the ratio is $q = 1.25$, which is comparable to Co, Ni with $q \sim 1 - 2$ but much smaller than the itinerant material $ZrZn_2$ with $q \leq 5$ [106] .

The anisotropy of $SrRuO_3$ has been discussed controversially [107, 108, 109]. Finally, there is consensus that the easy-axis is the $\boldsymbol{c}$ axis. In thin films of $SrRuO_3$, the easy axis grows at an angle of ~45° relative to the film normal [109]. Below T_C, the magnetization continuously rotates to have an angle of 60° to the surface normal at low temperatures because of the shape anisotropy of the film [110]. Furthermore, strain effects and twinning can further influence the anisotropy [111, 112].

The following studies of $SrRuO_3$ are performed on single-crystals from the recipe by Kunkemöller [19]. Figure 4.3 shows the magnetization along a cubic axis $[0\,1\,0]_c$ and a pseudocubic $[1\,0\,1]_c$ axis. The magnetization along $[1\,0\,1]_c$ increases rapidly to the saturation value of ~$1.6\,\mu_B$/Ru, while the $[0\,1\,0]_c$ direction grows fast to ~$0.8\,\mu_B$/Ru and increases continuously from there on. This data confirms the easy-axis character of the $[1\,0\,1]_c$ axis. Panel (b) shows the low-field regime for both directions. The hard axis has a coercive field of ~10 mT and the easy axis shows a negligibly small coercive field.

The critical behavior of the ferromagnetic phase transition of $SrRuO_3$ was investigated in multiple studies. For single-crystals, different results are reported. Kim *et al.* found critical exponents $\beta = 0.50 \pm 0.03$, $\gamma = 0.99 \pm 0.03$, and $\delta = 3.1 \pm 0.3$, which are in agreement with the mean-field theory values [113]. Snyder reported critical exponents that show a change from low-temperature Ising-like behavior $\beta = 0.32$ to a Heisenberg exponent $\beta = 0.39$ close to T_C [114]. For thin films, also data is reported that hints to a behavior according to the Ising universality class [115].

The ferromagnetism of $SrRuO_3$ is associated with the anomalous behavior of different properties. Thermal expansion shows an Invar effect in the ferromagnetic phase, i.e., the lattice parameters hardly change below the ferromagnetic transition. This effect is attributed to the compensation of a positive thermal expansion due to phonons and a negative thermal expansion based on the reduction of the magnetic moment with increasing temperature [16, 116, 117]. Transport measurements have been performed and analyzed in detail on films and single crystals by various groups. The longitudinal resistivity in the low-temperature limit follows a quadratic behavior, $\rho = \rho_0 + aT^2$ [118]. The quadratic contribution is attributed to Fermi-liquid behavior, but this is only observable in high-

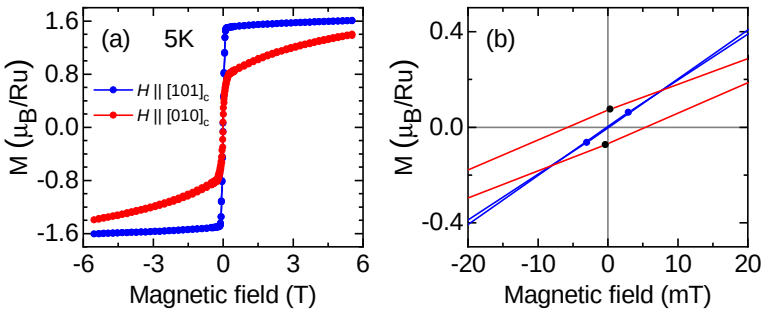

Figure 4.3 Magnetization of $SrRuO_3$. (a) shows the magnetization along the pseudocubic axes $[1\,0\,1]_c$ and $[0\,1\,0]_c$. (b) enlarges the low-field regime. The data stem from Ref. [19].

purity samples with a small residual resistance ρ_0. For other ferromagnetic metals like Fe, $a{\sim}10^{-11}\,\Omega\text{cm/K}^2$, which is attributed to electron-electron scattering [119]. For $SrRuO_3$, a is about 3 orders of magnitude larger [19, 120]. This enhanced value has not been explained finally. ρ_{xx} shows a kink at the ferromagnetic ordering temperature. In the paramagnetic phase, the resistivity shows essentially linear metallic behavior up to 1000 K. The Ioffe-Regel criterion [24], which describes the saturation of the resistivity if the mean-free path reaches the atomic distance a and results in a resistivity of approximately 200 μΩ cm, is exceeded already at 500 K [121]. This property makes $SrRuO_3$ a so-called 'bad metal'.

The anomalous or extraordinary Hall effect (AHE) was discussed controversially for $SrRuO_3$. Most data stem from thin-film measurements due to the lack of large single-crystals and the fact that the Hall signal scales with the inverse of the sample thickness $1/d$. Figure 4.4 shows exemplary literature results for the AHE of $SrRuO_3$.[1] The temperature dependence of the anomalous Hall resistivity ρ_{yx}^{AHE} is nonmonotonic. It shows a minimum around 90 K, a sign change around 130 K and vanishes at the ferromagnetic ordering transition. Typical extrinsic mechanisms for the AHE like skew scattering and side jump effects, see Chapter 2.1.2, require $R^{\text{AHE}} = a\rho + b\rho^2$ for the anomalous Hall coefficient and fail to explain the observed temperature dependence. Thus, it was suggested that Berry-phase effects in momentum space can also induce an AHE [17]. This explanation is supported by density functional theory (DFT) band-structure calculations predicting a similar temperature dependence and size. Nonetheless, the results of DFT band structure calculations for $SrRuO_3$ are very sensitive to the input parameters, see Refs. [17, 125]. Thus, this interpretation requires further tests. Another way to prove the Berry phase effect in $SrRuO_3$ is to find its trace in other measures. Itoh *et al.* reported on unusual spin dynamics in $SrRuO_3$. They studied spin-wave excitations by neutron Brillouin scattering on polycrystalline samples and deduced a nonmonotonic temperature-dependent magnon gap of ~1.8 eV. Their data is highly contaminated by the elastic scattering. This work in combi-

[1] The presented data from Ref. [122] have a different sign of ρ_{xy} compared to other publications [123, 124]. The presented data of this work agree to the sign of the latter two.

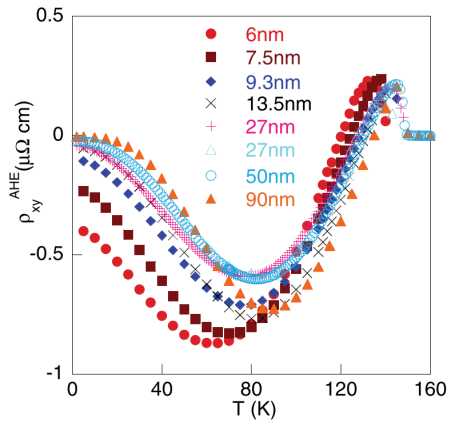

Figure 4.4 Anomalous Hall contribution $\rho_{xy}(T)$ for different $SrRuO_3$ film thicknesses from Ref. [122]. Note, that the presented data uses a different sign convention than this work.

nation with neutron scattering performs a detailed study on single crystals which improves the data, see Section 4.6. Additionally, a topological Hall effect (THE) has been proposed for $SrRuO_3$-heterostructures of $SrRuO_3/La_{0.7}Sr_{0.3}MnO_3$ [126] and $SrRuO_3/SrIrO_3$ [127], where the additional Hall contribution is assigned to a non-collinear or skyrmionic magnetic structure. This effect is discussed controversially [128].

4.3 Criticality of the ferromagnetic phase transition

The criticality of $SrRuO_3$ was studied on large single-crystalline samples grown by Stefan Kunkemöller and Kevin Jenni following the recipe of Ref. [19]. The literature reports about the criticality are not fully conclusive and the floating-zone-grown crystals shall be compared to those results. This chapter clarifies the type of universality class that can be applied in order to describe the occurring critical phenomena at the ferromagnetic ordering transition.

Different critical exponents are expected for the critical behavior close to the ordering temperature depending on the underlying symmetry and dimensionality of the model and categorized into universality classes, see Chapter 2.2.2. Here, magnetization and specific-heat measurements are analyzed with the critical exponents α, β, γ, and δ to evaluate whether $SrRuO_3$ shows criticality according to the Heisenberg or Ising universality class. Most of the data were analyzed together with the Bachelor student L. Thomas [129].

Specific heat

The specific heat of $SrRuO_3$ presented in Fig. 4.5, shows a λ-peak at 162 K indicating a second-order phase transition. In the low-temperature regime, see Fig. 4.5(i), $c_p(T)/T$ is

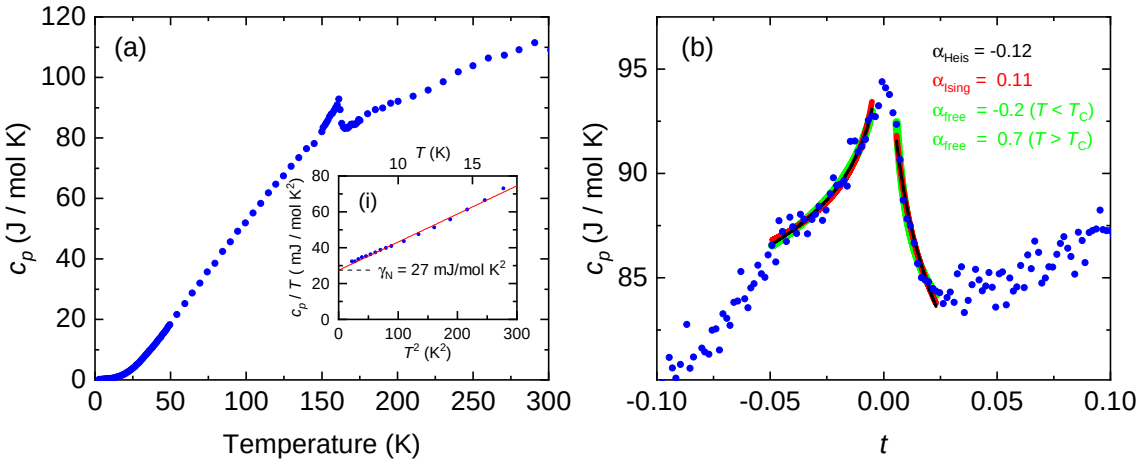

Figure 4.5 Specific heat of $SrRuO_3$. (a) presents the temperature dependence of the specific heat of $SrRuO_3$. Inset (i) shows c_p/T vs. T^2 for temperatures below 20 K, which highlights the electronic contribution. (b) shows the specific heat versus the reduced temperature $t = (T/T_C - 1)$ with fits using the critical exponent α_i of different universality classes according to Eqn. (4.1).

linear in T^2 and shows a finite y-intercept $\gamma_N = 27\,\mathrm{mJ\,mol^{-1}\,K^2}$. γ_N expresses the electronic part of the specific heat and is consistent with literature results [130, 131, 132]. The large value of γ_N reflects the mass enhancement, which is also seen in the other ruthenates like Sr_2RuO_4 and $Sr_3Ru_2O_7$ [133, 134]. Panel (b) resolves the regime around T_C to analyze the critical behavior. The specific heat is fitted according to

$$c_p(t) = \frac{A^{\pm}}{\alpha}\left(\pm t^{\alpha} - 1\right) + B^{\pm} \quad . \tag{4.1}$$

Additionally, fits with fixed values $\alpha_{\mathrm{Heis}} = -0.12$ and $\alpha_{\mathrm{Ising}} = 0.11$ according to, respectively, the Heisenberg and Ising universality class are shown. It is obvious that the specific heat does not diverge at the transition temperature. Moreover, it only changes by 10 % between the maximum and the phononic background. Furthermore, the slope for temperatures below the ferromagnetic transition only increases slightly, which does not agree to the symmetric behavior according to Eqn. (4.1). All three different fits are astonishingly similar in the presented temperature regime. Of course, the functions $t^{-0.11}$ and $t^{0.1}$ differ especially for small t, but in the range $-0.05 < t < -0.005$ the difference can easily be hidden in the prefactor $A^{\pm}$ and the offset value $B^{\pm}$. The real difference would be dominating in the close vicinity of T_C, but the specific heat is not measurable with a sufficiently high temperature resolution in that range. For $t > 0$, the temperature range where the specific heat is dominated by magnetic fluctuations is even smaller $0.005 < t < 0.025$. More

details about the fitting can be found in the bachelor thesis of L. Thomas [129].

A distinction of the Heisenberg and the Ising universality classes based on the critical exponent α from the specific-heat measurements is not possible.

Magnetic susceptibility and magnetization

Besides the critical exponent of the specific heat α, the exponents β, γ, and δ can be analyzed by magnetization measurements. The magnetization curves using the SQUID magnetometer were collected such that a temperature was stabilized at 3 T. Afterwards, the magnetization was measured with decreasing magnetic field down to −3 T. Figure 4.6 shows selected magnetization measurements close to the transition temperature. The coercive field is negligibly small. The following criticality analysis requires a single-domain ferromagnetic state. To ensure this, the data were cut below 45 mT. The spontaneous magnetization M_s is obtained by extrapolating the data points at 30 mT and 45 mT to zero field.

Figure 4.7 presents an analysis of the critical exponents via these magnetization measurements. The mean-field exponents used in the ordinary Arrott plot of Fig. 4.7(a) do not yield linear curves, and, thus, they fail to describe the critical magnetism in $SrRuO_3$. For 160 K, 162.5 K, and 166 K also the data-points at 15 mT and 30 mT (open symbols) are included, which show an obvious deviation from the general behavior and thus justify the restriction to $\mu_0 H > 45$ mT. The modified Arrott plot uses the critical exponents β and γ, see Fig. 4.7(b).

The magnetization curves at 163.25 K and 163.75 K are presented with three different sets of critical exponents, the Ising and Heisenberg values and a freely adjusted set. For the Heisenberg universality class, the slope is increasing continuously. Also for the Ising

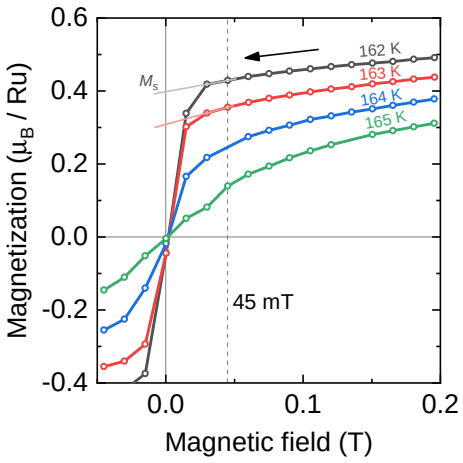

Figure 4.6 Magnetization along the easy axis close to T_C. The spontaneous magnetization M_s is obtained by extrapolating the data points at 30 mT and 45 mT to zero field. In the following analysis of the critical exponents, the files were cut below 45 mT to ensure a single-domain ferromagnetic state. At 164 K and 165 K, $SrRuO_3$ is in the paramagnetic phase.

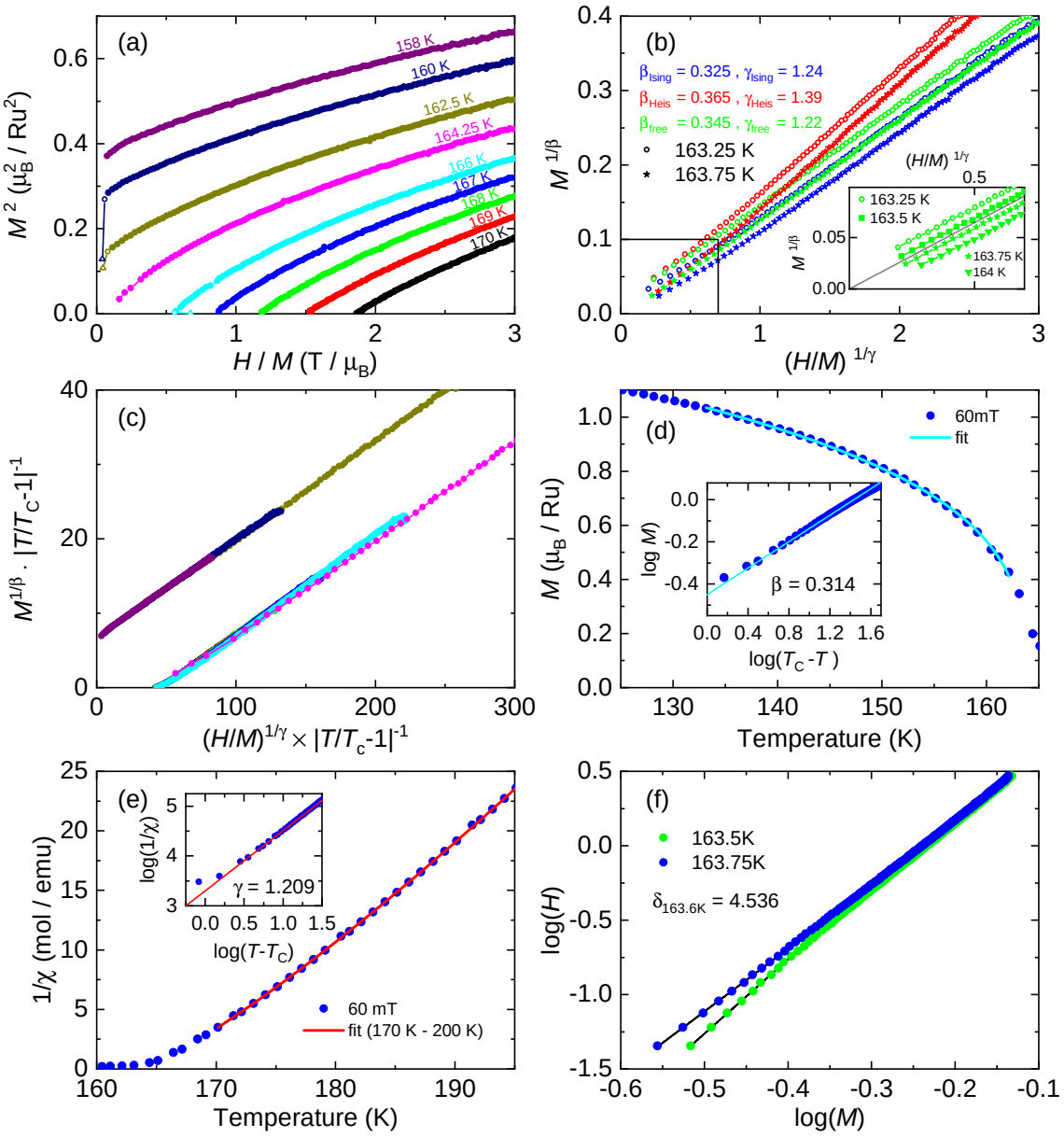

Figure 4.7 Arrott plots and critical exponents for $SrRuO_3$. (a) shows magnetization measurements for temperatures close to T_C presented according to the Arrott plot M^2 vs. H/M. Only fields above 45 mT are shown (except open symbols, see text). (b) presents the modified Arrott plot for two temperatures very close to T_C using β and γ according to the Ising and Heisenberg universality class and parameters adjusted to show a linear behavior. Inset: Linearity close to zero. T_C is between 163.5 K and 163.75 K. Linear interpolation yields T_C=163.6 K which is fixed in the following. (c) shows the scaled modified Arrott plot for β_{free} and γ_{free} using the data from (a). (d) shows $M(T)$ for 60 mT fitted with Eqn. (2.14) and (e) $1/\chi(T)$ fitted with Eqn. (2.16). Insets of (d) and (e) show the corresponding log-log plots. (f) shows the log-log plot of $M(H)$ close to T_C. The slope of linear fits is the critical exponent δ see Eqn. (2.17).

exponents the curves are not perfectly linear, which is corrected by the adjusted values $\beta_{\text{free}} = 0.345$ and $\gamma_{\text{free}} = 1.22$. These values yield perfectly linear curves in the modified Arrott plot. With these exponents, it is then possible to determine the critical temperature extremely accurate, see inset. The presented $M(H)$ curves are separated by 0.25 K. Right at T_C, the data should show no y-intercept in the modified Arrott plot. The transition temperature is extrapolated from the obtained intercepts to $T_C = 163.6$ K. Figure 4.7(c) shows the scaled modified Arrott plot to prove the validity of this procedure. All magnetization data from Fig. 4.7(a) collapse onto two linear curves, confirming the quality of the chosen critical temperature and exponents.

The critical exponents β and γ can also be found directly via the temperature-dependent magnetization and susceptibility. These data have to be described in the vicinity of the transition temperature because the whole theory only applies for small values of the order parameter. The temperature-dependent magnetization shown in Fig. 4.7(d) represents a continuous phase transition. It should follow the power law $M(t) \propto |t|^{\beta}$. The benefit of the Arrott plots is the precise determination of T_C, which is used for the following fits. Many publications try to describe the data over the full temperature range down to smallest temperatures, but this temperature regime is not relevant for the critical exponent. Here, the fit uses the data from 130 K to 162 K and yields $\beta = 0.304$. It does not yield reasonable values for the saturation magnetization for lowest temperatures ($M_{\text{sat}}^{\text{fit}} = 1.724$ μ_B/Ru) compared to the measured value of 1.6 μ_B. The magnetization measurement above T_C yields the critical exponent γ, see Fig. 4.7(e). The inverse of the susceptibility $1/\chi = H/M$ does not show the mean-field Curie-Weiss exponent $\gamma_{\text{MF}} = 1$ but $\gamma = 1.209$. Finally, the isothermal critical magnetization $M(H, T = T_C)$ presented in Fig. 4.7(f) should show a power-law behavior according to Eqn. (2.17). This behavior is proven and the exponent is found to be $\delta = 4.536$.

Figure 4.8 compares the main results from this study to the results of Snyder, who performed an analogous study on flux-grown single crystals [114]. The best critical exponent to distinguish the Ising and Heisenberg universality classes is β. Panels (a) and (b) show temperature-dependent magnetization measurements. Because of the small coercive field, the measurement in panel (a) was performed in a field of 60 mT in order to have a single ferromagnetic domain. For comparison also the extrapolated spontaneous magnetization M_s from $M(H)$ measurements, as defined in Fig. 4.6, is shown. Panel (b) also uses extrapolated spontaneous magnetization values from isothermal $M(H)$ measurements. In the vicinity of the transition, 60 mT induce an additional magnetization as a surplus to the spontaneous magnetization. Due to this, the magnetization can only be fitted up to 162 K. This yields $\beta = 0.314$. Snyder obtains $\beta = 0.32$. Only close to the phase transition he finds

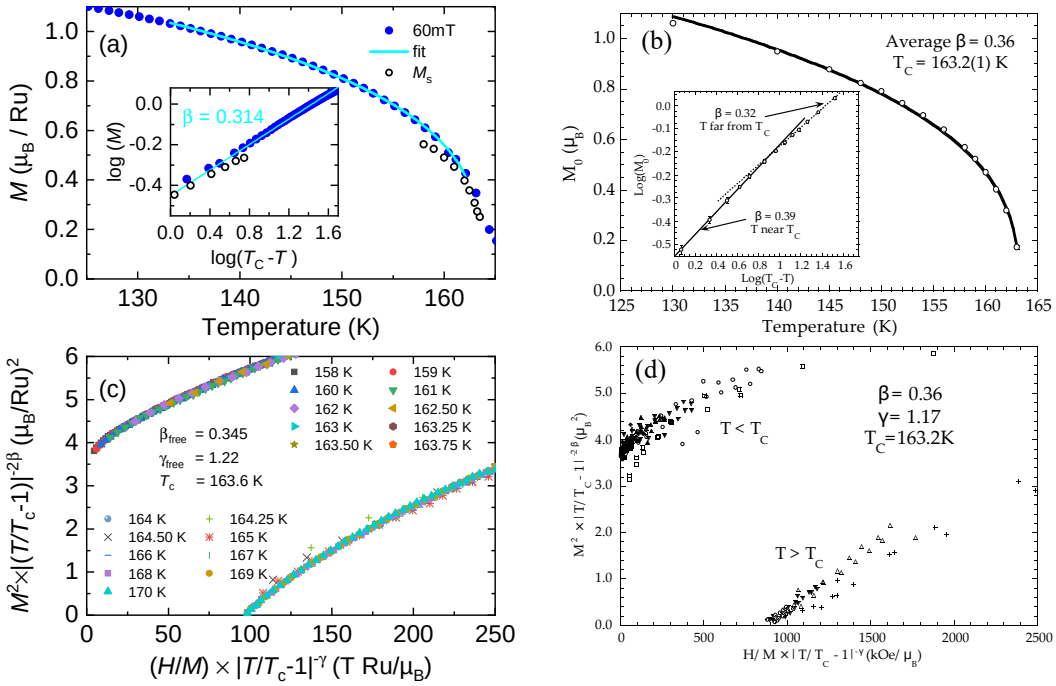

Figure 4.8 Comparison of the criticality study to the work of Snyder from Ref. [114]. (a) shows the temperature-dependent magnetization measured as a function of temperature at 60 mK and extrapolated from magnetization measurements to zero field M_s (open symbols). (b) shows the data from Ref. [114] which also uses extrapolated M_0 from $M(H)$ measurements to zero field. The insets show the data in a log-log scale to show the power-law behavior. Panels (c) and (d) compare the scaled Arrot plots for magnetization measurements at various temperatures. Panel (c) uses the $\beta_{\text{free}} = 0.345$ and $\gamma_{\text{free}} = 1.22$, panel (d) uses $\beta = 0.36$ and $\gamma = 1.17$.

an enhanced $\beta = 0.39$ which is close to the Heisenberg universality class. The scaling behavior of the isothermal magnetization measurements shown in panels (c) and (d) proves that the adjusted exponents yield a better scaling behavior. The scatter is much smaller in (c) compared to (d). Overall, the presented data of our single crystals do not show a changing exponent when approaching T_C.

Table 4.1 compares the critical exponents from the universality classes to the results for $SrRuO_3$ obtained above and those of Ref. [114].

	Landau (MF)	Heisenberg	Ising	adjusted to modified Arrott plot	power laws	Snyder Ref. [114]
β	0.5	0.365	0.325	0.345	0.314	0.39
γ	1	1.39	1.24	1.22	1.217	1.17
δ	3	4.808	4.815	4.536 [2]	4.84	4.2

Table 4.1 Critical exponents of several universality classes and experimental results for $SrRuO_3$.

Obviously, the mean-field description does not agree to the measured results. The adjusted β falls between the values for the Ising and Heisenberg universality class and does not allow any characterization. Nonetheless, $\gamma = 1.22$ is close to the Ising value, which is a first indication of this universality class. All critical exponents obtained directly from fits of $M(T)$, $\chi(T)$, and $M(H, T = T_C)$ with the corresponding power laws, are closer to the Ising than the Heisenberg values. In general, this study favors a critical behavior according to the universality class of the Ising model compared to the Heisenberg and mean-field criticality. This result differs from the description of Snyder [114], who proposed the Heisenberg class.

4.4 Magnetic anisotropy

In the following, a study of the magnetic anisotropy of $SrRuO_3$ is presented, which was performed to clarify the different and even contradicting reports from literature. The advantage of this study are large high-quality and well orientable single crystals.

Magnetization measurements at 2 K parallel to the high-symmetry directions $[1\,0\,1]_c$ and $[0\,1\,0]_c$ that reflect the tetragonal axes, are shown in Fig. 4.9. The samples were

[2] This value is calculated from the scaling relation $\delta = \frac{\gamma}{\beta} + 1$.

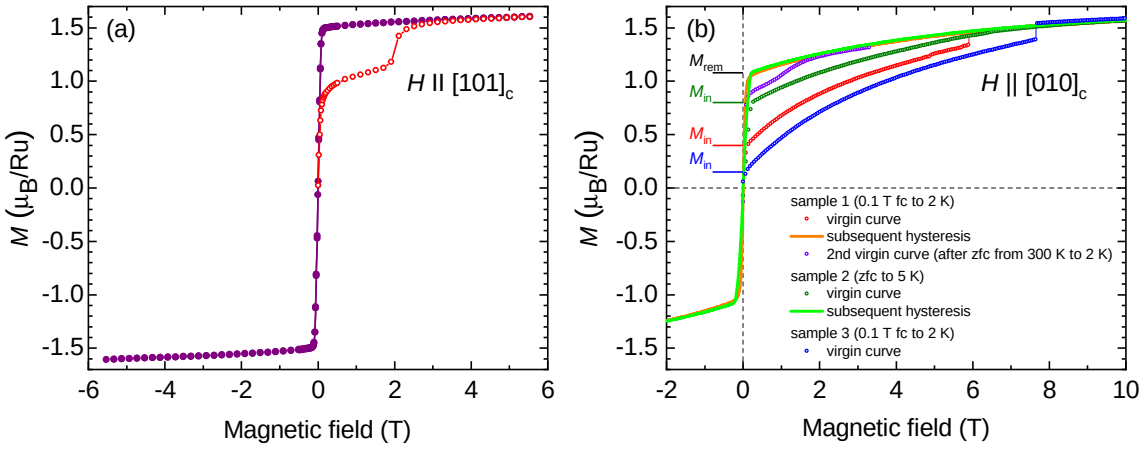

Figure 4.9 Magnetization measurements $M(H)$ at 2 K for the high-symmetry directions $[1\,0\,1]_c$ (a) and $[0\,1\,0]_c$ (b). Open symbols denote virgin curves, solid lines subsequent hysteresis loops. Three different samples were measured for $\boldsymbol{H} \parallel [0\,1\,0]_c$ that were prepared with a uniaxial pressure detwinning routine.

cooled from room temperature in small fields of 0.1 T or zero field, followed by the virgin curves and subsequent hysteresis loops. The most striking observation is, that the virgin curve for both axes lies outside of the corresponding hysteresis loop. The magnetization along the pseudocubic $[1\,0\,1]_c$ direction shows a jump in small fields to $0.9\,\mu_B$/Ru, see Fig. 4.9(a). Then, a plateau follows up to ~2 T, where another step occurs. From there on, the magnetization is almost constant. The saturation magnetization is determined by linear extrapolation of the high-field regime to zero and yields $M_{sat} = 1.6\,\mu_B$/Ru. This value equals literature reports [105]. In the subsequent hysteresis loop, the intermediate plateau is absent. The magnetization essentially switches between the saturation plateaus with a coercive field of ~10 Oe.

For the cubic axis presented in Fig. 4.9(b), the virgin curve is even further outside of the subsequent hysteresis loop. Here, three different samples are compared. Each of them shows a rapidly increasing magnetization, but the height of the initial jump differs. Sample 1 jumps to $M_{in} = 0.4\,\mu_B$/Ru, sample 2 to $0.8\,\mu_B$/Ru, and sample 3 to $0.15\,\mu_B$/Ru. With further increasing field, the magnetization increases continuously. For sample 2 with the highest initial jump, the magnetization increases continuously. At about 10 T, the slope vanishes and the magnetization is ~$1.6\,\mu_B$/Ru, which equals the saturation magnetization for the $[1\,0\,1]_c$ direction. The other samples show an intermediate jump, where the magnetization reaches the same value as the continuously growing magnetization. The critical field of this jump is 5.9 T for sample 1 and 7.5 T for sample 3. On decreasing magnetic field, the magnetization for all samples does not follow the virgin curve but is enhanced.

In zero field, a remanent magnetization $M_{\mathrm{rem}} \approx 1.08\ \mu_{\mathrm{B}}$/Ru is obtained. This branch is reverted for negative fields.

Obviously, $[1\,0\,1]_{\mathrm{c}}$ is the easy-axis direction as it has the largest remanent magnetization. The jump of the virgin curve at 2 T and the beforehand reduced magnetization can be explained by a geometrical consideration. Figure 4.10 shows the three possible tetragonal domains, which are equivalently populated when cooling the sample from high temperatures during the growth process. A sample whose magnetization is measured along a $[1\,0\,1]_{\mathrm{c}}$ direction has one of these domains aligned to the desired direction. The other two domains have their $\{1\,0\,1\}_{\mathrm{c}}$ directions within an angle of 60° towards the field direction. Very small fields orient the magnetization of the well aligned domain to its saturation value. The other two domains have their magnetization aligned but only contribute by the projected magnetization of cos 60°. This yields a magnetization plateau depending on the population of the three tetragonal domains d_1, d_2, d_3

$$M_{[1\,0\,1]} = (d_1 + (d_2 + d_3) \cdot \cos 60°) \cdot M_{\mathrm{sat}} \quad . \tag{4.2}$$

At 2 T, the Zeeman energy overcomes the energy barrier between different structural domains and changes the domain structure resulting in a single-domain state with the full saturation magnetization. This transition is coupled to a change of the oxygen positions, which changes the rotation and tilting scheme. In this transition, no atoms have to pass each other, which makes the energy barrier relatively small, although the corresponding structural ordering transition temperature is 950 K. From these measurements, it is not possible to distinguish between the two orthorhombic axes ***a*** and ***c***. The following Chapter 4.5 on the magnetoelastic coupling will further clarify this aspect.

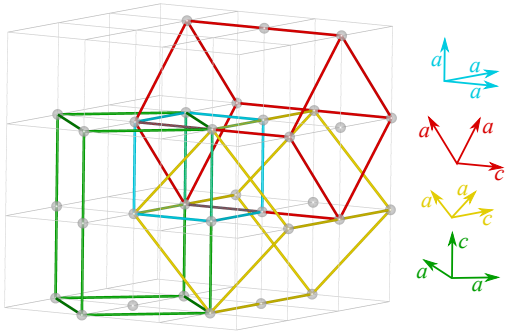

Figure 4.10 The structural transition from cubic to tetragonal allows for three possible tetragonal domains. The long tetragonal axis c is a cubic $\{1\,0\,0\}_{\mathrm{c}}$ axis and the short a axes are $\{1\,0\,1\}_{\mathrm{c}}$ axes. The a axes of different domains draw a relative angle of 60°.

Along the $[0\,1\,0]_c$ axis, one domain does not contribute to the magnetization because the easy axis is perpendicular to the magnetic field, whereas the other two domains contribute with a projection of an angle of 45°. The initial jump of the magnetization should yield

$$M_{[0\,1\,0]} = (d_2 + d_3)\cos 45° \cdot M_{\mathrm{sat}} \quad . \tag{4.3}$$

The magnetization jump in higher fields can then be attributed to a change of the domain population. Here, the d_1-domain is depopulated and the other two domains with an easy-axis component along the magnetic field are favored. Consequently, it is not possible to generate a single-domain state in this field orientation. The magnetic field then tilts the magnetization from the easy axis towards the magnetic field. At about $\mu_0 H_{\mathrm{an}} = 10\,\mathrm{T}$, the magnetization is fully aligned to the field because the magnetization reaches the same value as along $[1\,0\,1]_c$. This anisotropy field agrees with the energy of the ferromagnetic resonance observed in time-resolved magneto-optical Kerr effect measurements [135].

The domain population cannot only be influenced by applying a magnetic field in the ferromagnetic phase but also by applying a mechanical force onto a $\{1\,0\,1\}_c$ direction on cooling from the cubic to the tetragonal and orthorhombic phase. At the first structural transition, the tetragonal axis elongates. Thus, this axis orients perpendicular to the force. When $SrRuO_3$ becomes orthorhombic, the ***a*** axis contracts and the ***c*** axis elongates. So finally the sample should consist of a single domain with ***a*** parallel to the uniaxial pressure and the ***b*** and ***c*** axis perpendicular.

The magnetization measurements along the hard axis $[0\,1\,0]_c$ are a perfect indication for the degree of detwinning. According to Eqn. (4.3) an equally-twinned sample with $d_1 = d_2 = d_3 = 0.33$ should show a initial magnetization of $M_{\mathrm{in}} \approx 0.47 M_{\mathrm{sat}} \approx 0.75\ \mu_B$/Ru. This is the case for sample 2. Samples 1 and 3 have been treated with the above-mentioned uniaxial pressure-temperature procedure to influence the domain population. Both samples show a reduced initial magnetization because domain d_1 is predominantly populated. It has the easy-axis perpendicular to the magnetic field. For sample 1, the measured initial magnetization corresponds to a population of the pressure-induced domain $d_1 = 0.75$ and for sample 3 $d_1 = 0.82$. The jump of the magnetization in magnetic fields of the order of 7 T indicates the depopulation of domain d_1 in favor of the domains d_2 and d_3, which possess a finite projected magnetization along the magnetic field. The remanent magnetization of about 1.1 μ_B/Ru obtained for the new domain population when reducing the field to 0 T corresponds to $d_2 + d_3 = 1$ in Eqn. (4.3). Furthermore, sample 1 was heated back to room temperature, and, thus well above the ordering temperature (300 K), to check whether the initial domain population is recovered. The second virgin curve initially jumps

to 0.9 μ_B/Ru, which is close to the remanent magnetization after field-poling the domains. Already 1.6 T bring the magnetization to the single-domain value. It can be concluded that the initial domain population is not recovered by heating to the paramagnetic phase.

In the following, the magnetic field is again applied along a $\{1\,0\,1\}_c$ axis. Figure 4.11 shows magnetization curves for elevated temperatures up to 200 K. This data have been carried out after the first magnetization process, and, thus, no intermediate plateau is visible. Nonetheless, the magnetization upon increasing and decreasing the magnetic field deviate in the range from 0.1 T to 3 T with a reduced magnetization on the increasing run. The reduced magnetization always occurs after passing through zero and thus after switching the magnetization by 180°. This is not a typical ferromagnetic hysteresis effect. The difference between increasing and decreasing magnetic field can also be attributed to the structural domains. In some part of the sample, the magnetization is not inverted but switches to another structural domain, which results in a reduced magnetization. With increasing temperature this effect broadens and is still visible above the ferromagnetic ordering temperature. For the interpretation of all further measurements, this has to be taken into account.

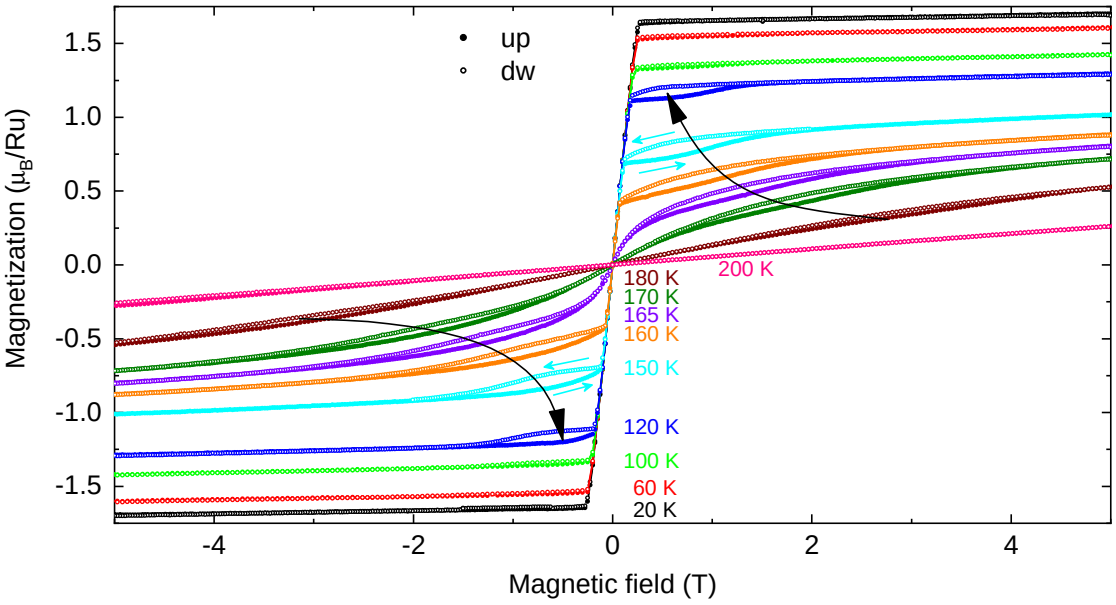

Figure 4.11 Magnetization curves of $SrRuO_3$ for $\boldsymbol{H} \parallel [1\,0\,1]_c \mathrel{\hat{=}}$ easy axis from 20 K to 200 K. Closed symbols denote curves with increasing magnetic field, open symbols decreasing field.

4.5 Magnetoelastic coupling and shape-memory effect

In the following, the magnetoelastic coupling of $SrRuO_3$ is analyzed in detail. Hereby, the main focus is put on the twinning effects and their low-temperature stability. The thermal expansion and magnetostriction of $SrRuO_3$ was measured on a single crystal of approximately cubic shape of ~1x1x1 mm^3 in the VTI dilatometer. The low-temperature magnetostriction in Fig. 4.12(a) compares three directions of the very same sample. All data were obtained after zero-field cooling from room temperature. The virgin curve for the $[1\,0\,1]_c$ direction shows a sharp jump of $\Delta L/L = 6 \cdot 10^{-3}$ at $H_{crit} = 1.8$ T. During the subsequent hysteresis loop, the length is basically constant. The perpendicular direction $[\bar{1}\,0\,1]_c$ also shows a jump at 1.8 T of $\Delta L/L = 10^{-3}$. For larger magnetic fields, the length increases further to a saturation of $3 \cdot 10^{-3}$. On decreasing magnetic field, this value remains constant down to ~1 T. In the vicinity of 0 T, the sample shrinks by about $3 \cdot 10^{-4}$. Compared to these two axes, the length changes for the cubic axis $[0\,1\,0]_c$ are much smaller. Here, the length shows a minimum at 3.5 T and increases for higher magnetic fields. In order to understand these effects, this data has to be compared to the virgin curves of the magnetization along the same field direction. $M_{[1\,0\,1]}(H)$ showed a plateau up to ~2 T at 2 K, before reaching the high-field saturation value, see Fig. 4.9(a). So both information together yield a good insight into the field-induced reorientation of magnetic and structural domains. It can be concluded that the magnetic field favors the long orthorhombic $\boldsymbol{c}$ axis because both, $[1\,0\,1]_c$ and $[\bar{1}\,0\,1]_c$ elongate at 1.8 T. In a twinned sample, small magnetic fields along a $\{101\}_c$ direction orient the magnetization of all structural domains, because they all have a component parallel to the applied magnetic field. This results in the initial jump of magnetization. At the critical field H_{crit}, further magnetic Zeeman energy can be gained by switching the structural domains, so that the orthorhombic $\boldsymbol{c}$ axis aligns to the magnetic field, as indicated schematically in Fig. 4.13(a). The relative difference between the orthorhombic lattice constants ($c/a = 1.0064$ and $\sqrt{2}c/b = 1.0033$) causes the obtained drastic length changes of the virgin curves.

The stability of the single-domain structure was analyzed by thermal-expansion measurements, see Fig. 4.12(b). A multi-domain sample was zero-field cooled (zfc) to 4 K. In a subsequent thermal expansion measurement in zero-field, $SrRuO_3$ shows a moderate thermal expansion with an anomaly at $T_C = 163$ K, see inset. If the sample was field-poled at 5 K as presented in panel (a), a drastically different length change is observed upon heating in zero field. The sample starts at the elongated value of $6 \cdot 10^{-3}$ and shrinks monotonically. The slope increases continuously and the length shows a pronounced discontinuity at 172 K. The length of the multi-domain sample is recovered above 240 K.

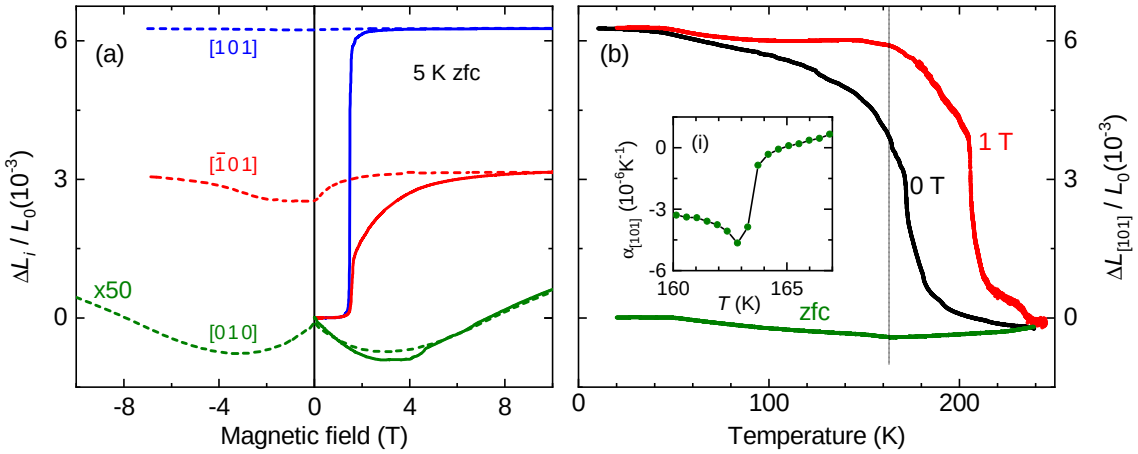

Figure 4.12 Magnetostriction and shape-memory effect of $SrRuO_3$. (a) shows the field-dependent length change of the [1 0 1], [$\bar{1}$ 0 1], and [0 1 0] axis at 5 K. Virgin curves are depicted with solid lines and subsequent hysteresis measurements with dashed lines. (b) shows thermal expansion measurements for the [1 0 1] direction. The black and red data ran the following protocol before the presented data were collected: zfc from room temperature to 5 K, magnetic field to +9 T→-7 T. Then, the given magnetic field was applied and the thermal expansion was measured. For the green data, no magnetic field was applied and after zfc from room temperature a subsequent heating curve was measured. Inset (i) shows the corresponding thermal-expansion coefficient.

The single-domain state that was established by the magnetic-field poling below T_C, is stable up to rather high temperatures, but the multi-domain state is recovered above T_C, see Fig. 4.13(a). This cycle (zfc, magnetostriction at 5 K, thermal expansion upon heating) was also performed for a magnetic field of 1 T on heating. The applied field results in a shift of the discontinuous drop in $\Delta L/L$ to 205 K. Thus, already small magnetic fields further stabilize the domain structure even in the paramagnetic phase.

Figure 4.13(b) shows the measured length change for the $[1\,0\,1]_c$ direction for different temperatures. All data sets follow the same protocol. The multi-domain sample was cooled from room temperature in zero field to the desired temperature followed by a magnetic-field sweep to 7 T. These virgin curves are shown. Afterwards, the sample was heated above the ferromagnetic ordering temperature to erase the single-domain state and recover the multi-domain structure. The measured length change is well reproducible, the 5 K and 70 K data perfectly match and the length change is slightly larger for the 20 K curve. Fig. 4.13(i) shows the temperature dependence of the critical field H_{crit} of the domain switching, which is temperature activated.

These measurements are in full agreement with neutron diffraction data presented in Fig. 4.14, which shows the collected intensities of three different reflections. Here, a

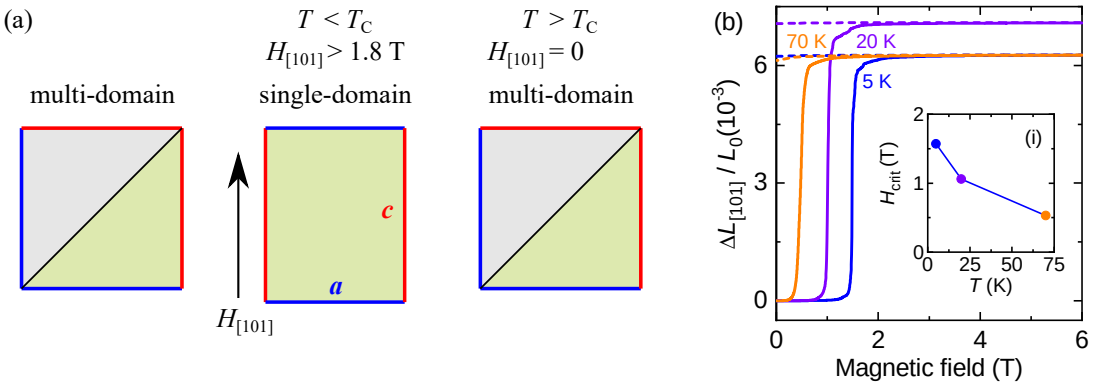

Figure 4.13 Field-poling of $SrRuO_3$. (a) schematically shows the domain switching by a magnetic field along $[1\,0\,1]_c$. Red lines indicate orthorhombic ***c*** axes and blue lines orthorhombic ***a*** axes. A multi-domain sample becomes field poled by applying a magnetic field $H > 1.8\,\mathrm{T}$ along a $\{1\,0\,1\}_c$ axis. The ***c*** axis is aligned to the magnetic field. If the magnetic field is switched off and the temperature raised above T_C, the sample becomes multi-domain again. This is called shape-memory effect. (b) shows the field-poling in the magnetostriction at different temperatures. It was measured after zero-field cooling from room temperature to 5 K, 20 K, and 70 K. Inset (i) shows the temperature dependence of the critical magnetic field H_{crit} at which the sample becomes single-domain.

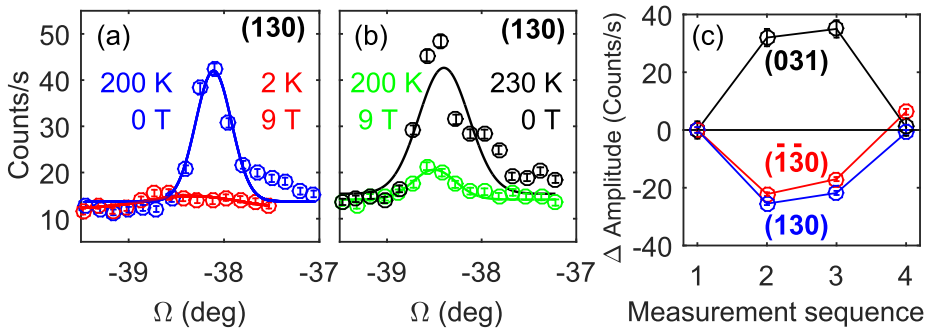

Figure 4.14 Shape-memory effect of $SrRuO_3$ in neutron scattering. The figure shows the intensities of the (1 3 0), (0 3 1), and $(\bar{1}\,\bar{3}\,0)$ reflections at various conditions. (a) and (b) show rocking scans of the (1 3 0) reflection at the starting point 200 K and 0 T (1), after cooling the sample to 2 K in 9 T (2), after heating to 200 K in 9 T (3), and finally at 230 K in 0 T (4). (c) shows the difference between the amplitudes at the starting point (1) and the successive steps (2)–(4). Amplitudes are obtained by fitting Gaussians with a constant background. The figure is adapted from Ref. [136].

partially detwinned multi-domain crystal has been studied and *h k l* are assigned to the majority domain. The (1 3 0) reflection is forbidden in space group *Pnma*. Its intensity has to stem from the reflections of the other five twin orientations, namely (0 3 1), (2 $\overline{1}$ $\overline{1}$), ($\overline{1}$ $\overline{1}$ 2), (1 1 2), and (2 1 1) where they possess a sizable structure factor. The neutron intensity shows a peak indicating a multi-domain sample at 200 K, see panel (a). After field cooling in 9 T to 2 K, this intensity is gone indicating the presence of a single domain. After heating again to 200 K with the magnetic field applied, the sample is still nearly single-domain because the peak is still suppressed, see panel (b). After switching off the magnetic field, the intensity is recovered to its initial value proving the recovery of the multi-domain state. Figure 4.14(c) compares the intensities of the (1 3 0) reflection to those of the Friedel equivalent ($\overline{1}$ $\overline{3}$ 0). Both show the same behavior in the aforementioned routine. The (0 3 1) reflection, that is allowed in the preferred twin domain and forbidden or obeys a reduced structure factor in the other twins, shows the inverse behavior. The intensity increases when establishing the single-domain state and recovers its initial value at the end of the routine. Whether the very same domain configuration is recovered on a microscopic scale cannot be verified by these macroscopic techniques but seems probable.

A split-coil magnet allows to change the relative orientation of the sample and the magnetic field without changing any other conditions by rotating the stick inside the dewar. This equipment was used to switch between domain states at 4.2 K for $\boldsymbol{H} \parallel \{1\,0\,1\}_c$, see Fig. 4.15. After the virgin curve stabilized a single-domain state, see also schematically in Fig. 4.15(b), the magnetic field was switched off. Then, the relative orientation between the sample and the magnetic field was changed by 90° so that the orthorhombic $\boldsymbol{a}$ axis, is parallel to the magnetic field and parallel to the measured length variation. The magnetic field is ramped up, which results in a measured elongation of the sample. The magnetic field changes the single-domain sample from being $\boldsymbol{H} \parallel \boldsymbol{a}$ to $\boldsymbol{H} \parallel \boldsymbol{c}$ so that the easy axis is aligned to the magnetic field again. On a subsequent hysteresis loop, the length hardly changes. After switching the magnetic field off again, the stick was rotated again, so that the length change is measured perpendicular to the magnetic field. During the following magnetic-field ramp, the sample length shrinks, indicating that the axis becomes the $\boldsymbol{a}$ axis, while the magnetic-field direction becomes the $\boldsymbol{c}$ axis. Thus, the magnetic field again aligns the $\boldsymbol{c}$ axis, which is the longer orthogonal axis. The samples shorter $\boldsymbol{a}$ axis orients perpendicular to this. Note, that the measured length changes are no real magnetostriction, but stem from a change in shape from switching between $\boldsymbol{a}$ and $\boldsymbol{c}$. $SrRuO_3$ is ferroelastic meaning it is possible to switch between two ferroelastic domain states. With this process, the sample can be switched back and forth between the $\boldsymbol{a}$ and $\boldsymbol{c}$ axis. Consequently, $SrRuO_3$ is multiferroic because it hosts two ferroic effects, namely ferromagnetism and

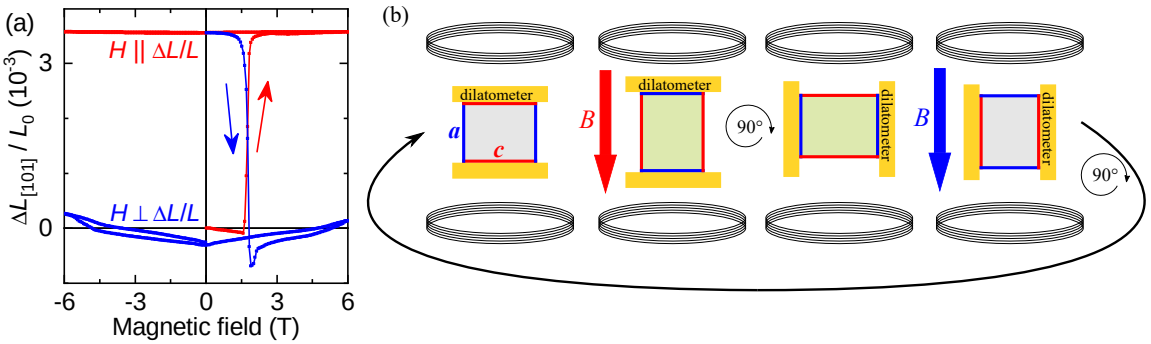

Figure 4.15 Measured and schematic switching of structural domains in $SrRuO_3$ with magnetic field. (a) shows the relative length change of a $\{1\,0\,1\}_c$ direction that was measured parallel and perpendicular to the magnetic field. Between the two shown data sets the dilatometer with the sample was rotated by 90° around $\boldsymbol{b}$. Panel (b) schematically shows the structural domains influenced by the magnetic field. The dilatometer can be rotated around $\boldsymbol{b}$ inside a split-coil magnet. Red lines indicate the orthorhombic $\boldsymbol{c}$ axis and blue lines the orthorhombic $\boldsymbol{a}$ axis.

ferroelasticity.

The magnetic-field control of the structural domains in $SrRuO_3$ is remarkable. The structural transition temperature is much larger than the ferromagnetic transition temperature. The combination of a large magnetic anisotropy of $\mu_0 H_{an} = 10\,\mathrm{T}$ and a weak pinning of structural domains gives rise to the observed effects. The energy density of the domain alignment can be estimated from the saturation moment $M_{sat} \simeq 1.6\mu_B/\mathrm{Ru}$, the low-temperature critical magnetic field $\mu_0 H_{crit} \simeq 1.8\,\mathrm{T}$, and the volume per formula unit $V_{fu} \simeq 60\text{Å}^3$

$$E_{mag} = \mu_0 H_{crit} M_{sat} / V_{fu} \approx 0.4\,\mathrm{MPa} \quad .$$

This small energy density is sufficient to induce a macroscopic length change of the order of 10^{-3} in this direction. Usual elastic distortions in single-domain solids would require energy densities of the order of GPa. This domain flop seems to be visible in data of Kanbayasi [107] who reported anomalous switching effects and tetragonal symmetry in flux-grown single crystals in high magnetic fields. Additionally, these findings can be relevant for thin film samples, e.g., to explain the angular hysteresis in the magnetoresistance [137].

The shape-memory effect arises from the alignment of the magnetic easy axis $\boldsymbol{c}$ and the corresponding structural domains by a magnetic field. This is a meta-stable state that decays above the ferromagnetic transition temperature. The domain formation and its dynamics are well studied for ferromagnetic and ferroelectric materials such as FeO and $BaTiO_3$ and also multiferroics with coupled magnetic and dielectric order parameters. The

corresponding ferroelastic domains emerge to reduce local strains, which has been shown for thin films [138, 139]. For ferroelastic transitions, though, much less in known. For $La_{2-x}Sr_xCuO_4$, that undergoes a structural phase transition with a similar rotation of octahedra, it was shown that cycling through this transition always yields the same domain pattern [140]. The observed shape-memory effect in $SrRuO_3$ seems to be caused by such a strain memory. Nonetheless, it has to be noted that this effect does not occur at the structural phase transition $T_S = 950\,K$, but at the much lower ferromagnetic transition $T_C = 163\,K$. One reason is of course that only the ferromagnetic state allows to apply a force onto the ferroelastic domains. Furthermore, it requires a large magnetic anisotropy in order to have this effect. Nonetheless, it is interesting that the restoring force is large enough to destroy the single-domain state once the ferromagnetic order breaks down. This is also a clear difference between $SrRuO_3$ and typical shape-memory materials like Heusler alloys that have to be heated above the structural phase transition to recover the initial state.

4.6 Electric transport properties

Sample preparation

For the measurements of the electric resistivity and the Hall effect, $SrRuO_3$ samples were cut in oriented cuboids with $[1\,0\,1]_c$ x $[0\,1\,0]_c$ x $[\bar{1}\,0\,1]_c$ and dimensions ~3x1x1 mm^3. These samples were then detwinned by uniaxial pressure. Afterwards, they were ground down to enhance the Hall signal that scales with the inverse thickness $1/d$. Two samples were measured with geometry 3x1x0.197 mm^3 (dipstick) and 3x1x0.19 mm^3 (PPMS). The samples are contacted as described in Chapter 3.7 with a 6-probe geometry. The magnetic field is applied along the short $[\bar{1}\,0\,1]_c$, the current is applied along the $[1\,0\,1]_c$ direction and the Hall signal is detected along $[0\,1\,0]_c$. Measurements were performed for stabilized temperatures from 200 K down to 2 K. At each temperature, the magnetic field was driven through a full hysteresis loop to catch all hysteresis and domain effects. The current was switched every 10 seconds in order to eliminate offset voltages. The sample from the dipstick was used to measure the magnetization with the very same geometry afterwards. These data have already been shown in Fig. 4.11.

Longitudinal resistivity

The longitudinal resistivity of $SrRuO_3$ is a good measure of the sample quality. Figure 4.16 shows the longitudinal resistivity for both samples. These data perfectly reproduce

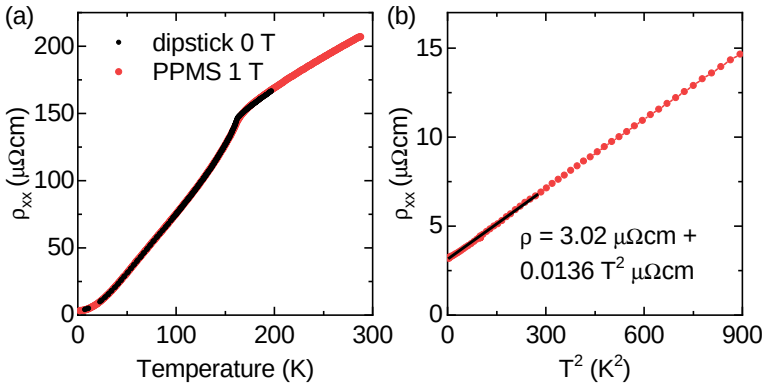

Figure 4.16 Longitudinal resistivity of $SrRuO_3$. (a) compares the temperature-dependent resistivity measurements performed in the dipstick (sample 1) and PPMS (sample 2). (b) shows the low-temperature behavior of ρ vs. T^2 with a linear fit according to $\rho_{xx} = \rho_0 + aT^2$.

the data of the high-quality sample presented in Ref. [19]. The resistivity of a good crystal of $SrRuO_3$ reduces by a factor of ~60 from room temperature to 4 K, whereas a bad crystal only changes by a factor of ~20. At the ferromagnetic transition, ρ_{xx} shows a kink, with a reduced slope for $T > T_C$. The low-temperature resistivity is quadratic in temperature up to 30 K. Furthermore, both samples used in this work show the same residual resistivity $\rho_0 \approx 3\,\mu\Omega$cm.

Figures 4.17(a) and (b) show the magnetoresistance of $SrRuO_3$ for various temperatures, where ρ_{xx} was symmetrized with respect to the magnetic field. Panel a) focuses on temperatures in the ferromagnetic phase. All curves show a negative magnetoresistance, meaning the resistivity in a magnetic field is smaller than in zero field. There is no indication of a domain effect when switching the magnetic field in the longitudinal transport. The magnetoresistance $\Delta\rho(H)/\rho(0\,\mathrm{T})$ increases from low temperatures towards the ferromagnetic transition, where it is maximal with $-7\,\%$ at 3 T. Above T_C the effect decreases. The temperature dependence is shown in panel (c). This behavior is expected for a ferromagnetic metal. In some ferromagnetic metals a colossal magnetoresistance is observed, e.g., in $Tl_2Mn_2O_7$ [141]. These material have a much smaller carrier concentration which is important for a large magnetoresistance [142]. However, in $SrRuO_3$ with approximately one electron per formula unit, the carrier concentration is large and thus the magnetoresistance comparably small.

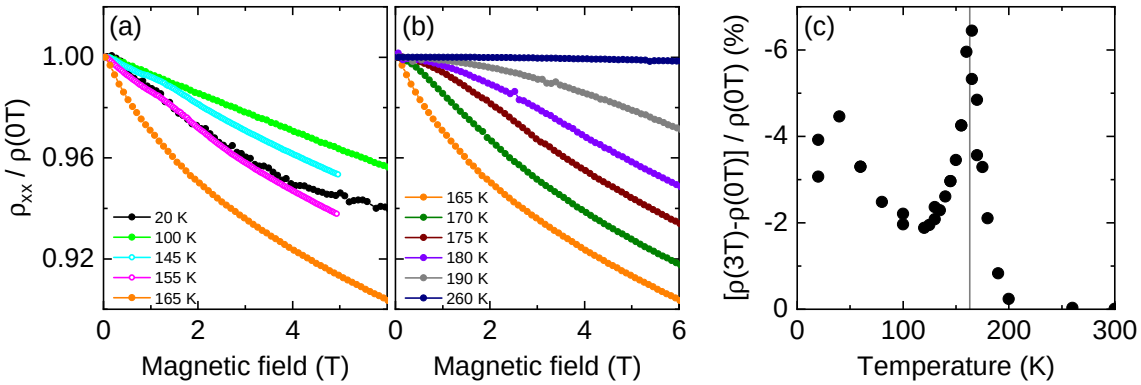

Figure 4.17 Magnetoresistance of $SrRuO_3$. (a) shows the field dependence of ρ_{xx} for temperatures below T_C and (b) for $T > T_C$. All measurements have been normalized to their zero-field resistivity $\rho(0\,T)$. Open symbols were measured on sample 1 in the dipstick, filled symbols on sample 2 in the PPMS. (c) presents the corresponding temperature-dependent magnetoresistance calculated via $[\rho(3\,\mathrm{T}) - \rho(0\,\mathrm{T}]/\rho(0\,\mathrm{T})$.

Anomalous Hall effect

Ferromagnetism is known to cause an additional Hall signal that scales with the magnetization via Eqn. (2.3). This caused a lot of interest for $SrRuO_3$ recently due to publications that attribute this to a topological effect of the band structure [17, 18]. In this work, detailed measurements on detwinned single crystals and a combined analysis with magnetization measurements were performed in comparison to those publications.

Figure 4.18 shows the antisymmetrized Hall signals ρ_{yx} for three temperatures exemplarily. A full hysteresis was used as described in the experimental Chapter 3.7 to perform the antizymmetrization according to Eqn. (3.11). The resulting data are effective up-sweeps. Panel (a) with $T = 40\,\mathrm{K}$ shows the Hall resistivity ρ_{yx} that contains both effects, the normal Hall effect (NHE) and the anomalous Hall effect (AHE). The normal Hall effect causes a linear Hall resistivity in a magnetic field indicated in blue. Additionally, there is a jump at zero field that indicates the anomalous Hall contribution. With increasing magnetic field, the Hall resistivity drops down. Thus, the anomalous Hall constant R_{AHE} is negative. At low temperatures R_{AHE} is small. For 80 K, see panel (b), the AHE is much larger. For 160 K, see panel (c) the jump is no longer sharp but broadened as the magnetization. Furthermore, ρ_{yx} increases at zero field and thus the anomalous Hall constant is positive as well.

Figure 4.19 shows ρ_{yx} for multiple temperatures up to T_C. The Hall-resistivity data of all temperatures have been fitted according to Eqn. (2.3) using the magnetization measurements from Fig. 4.11. For low temperatures, the step at $H = 0$ vanishes and consequently

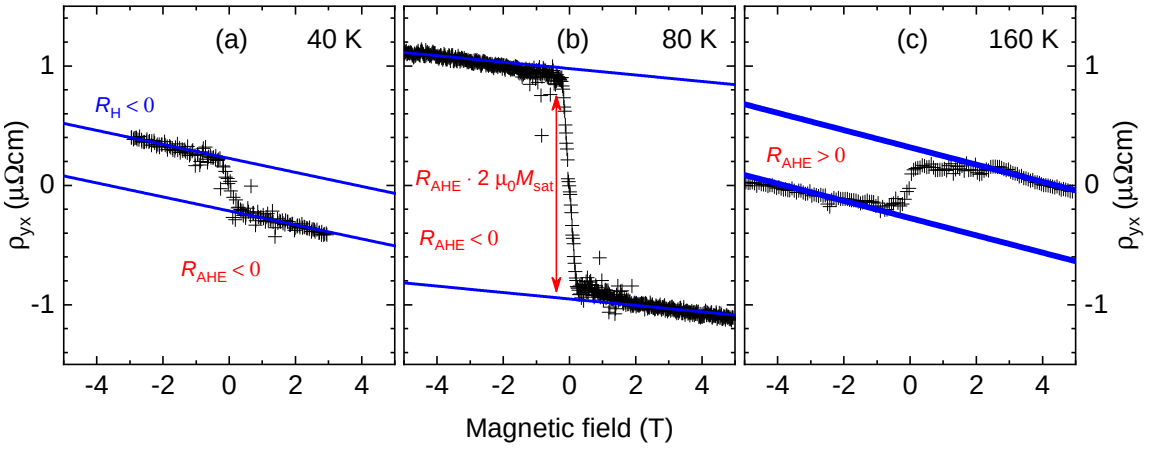

Figure 4.18 Exemplary antisymmetrized Hall effect data. The data were antisymmetrized with respect to a complete hysteresis loop according to Eqn. (3.11), so that hysteresis effects are taken into account.

the AHE vanishes and only the NHE remains. The AHE increases strongly with increasing temperature and is maximal at ~100 K. With further increasing temperature, the step height reduces and is zero at 150 K. Furthermore, there is a sign change of the anomalous Hall constant, meaning ρ_{yx} increases at $H = 0$ with increasing magnetic field. With increasing temperature, the signal increases further up to the ferromagnetic transition temperature. The jump broadens analogous to the magnetization curves (see Fig. 4.11). The slope in the high-field regime that depicts the NHE, is always negative and approximately constant over the whole temperature range. All data sets can be described by Eqn. (2.3) as is depicted in red. The two individual components ρ_{yx}^{AHE} and ρ_{yx}^{NHE} are shown in green and blue, respectively.

Another interesting behavior of the Hall effect data is shown in Fig. 4.20 for two temperatures exemplarily. As described above, the raw-data were antisymmetrized for a full hysteresis loop in order to keep control over the switching effects. The antisymmetrized data contain an effective field-sweep direction with this method. All data sets are effective up-sweeps, as described in Chapter 3.7. The Hall resistivity ρ_{yx} changes its sign at zero magnetic field, where the magnetization inverts. However, $-\rho_{yx}(-H) \neq \rho_{yx}(H)$, and there is an intermediate plateau up to ~1.5 T, where $\rho_{yx}(B)$ increases via another step to the fully antisymmetric value. This analogous behavior is observed in the magnetization data, see panel (c). It is attributed to the occurrence of structural domains with inverted $\boldsymbol{a}$ and $\boldsymbol{c}$ axes showing a spontaneous magnetization $M \perp B$ and consequently, these domains do not contribute to the measured anomalous Hall effect voltage. The Hall effect illustrates

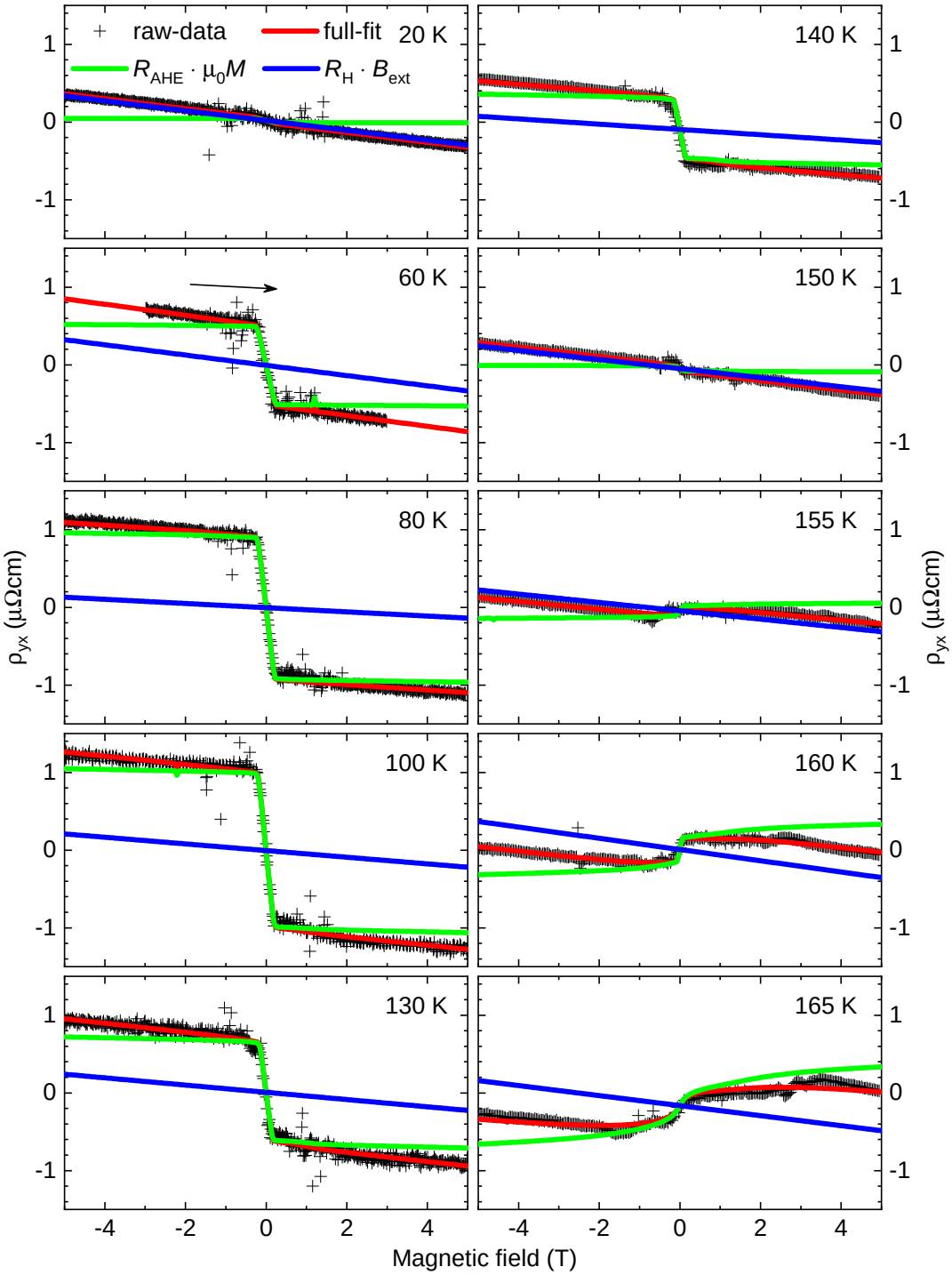

Figure 4.19 Antisymmetrized Hall effect data on sample 1 in the ferromagnetic phase. The data were symmetrized with respect to a full hysteresis loop such that hysteresis effects are taken into account. The data were fitted via $\rho_{yx} = R_{\mathrm{AHE}} \cdot \mu_0 M + R_{\mathrm{H}} \cdot B_{\mathrm{ext}} + C$ (red). The contributions ρ_{yx}^{AHE} and ρ_{yx}^{NHE} are depicted in green and blue, respectively.

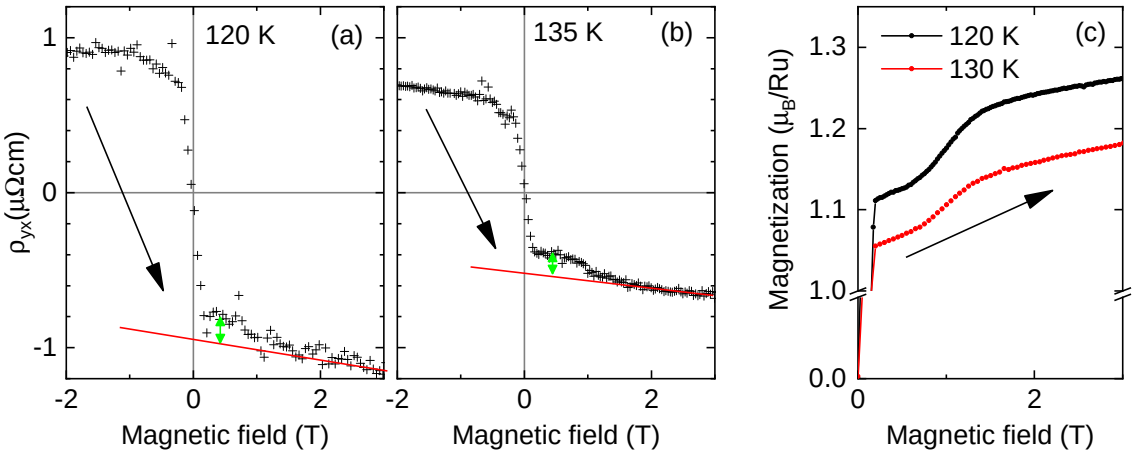

Figure 4.20 Domain effects in the Hall effect of $SrRuO_3$. The antisymmetrized Hall-effect data on Sample 1 are measured for $T = 120\,\mathrm{K}$ (a) and 135 K (b). Red lines mark the linear approximation of the high-field range. From 0 T to 1 T the data are significantly reduced (green arrow). (c) shows the corresponding magnetization measurements that show are also reduced after inverting the magnetic field.

the importance of the knowledge of the domain effects.[3]

The existing literature results do not give information about the temperatures above T_C. The problem is the separation of the normal Hall effect from the anomalous Hall effect. The magnetization in the paramagnetic phase becomes more and more linear with increasing temperature. Figure 4.11 proves that especially the magnetization at 170 K and 180 K is not linear but shows a curvature. Thus, it is still possible to distinguish both Hall contributions. The Hall effect data for this temperature range with the corresponding fits are presented in Fig. 4.21. The fits up to 180 K describe the data perfectly. For higher temperatures, a separation is no longer possible without further assumptions. Because the obtained normal Hall coefficient R_H does not show an anomaly at T_C, it is assumed to remain constant for higher temperatures. Using this assumption, also the data for 190 K and 200 K can be described. The obtained anomalous Hall constant increases further.

The resulting fit parameters R_{AHE} and R_H are shown in Fig. 4.22. The normal Hall constant R_H is negative in the whole temperature range. This corresponds to an electron-dominated transport. R_H does not change systematically over the whole temperature range. The average value for both samples is $R_H^{avg} \approx -0.05\,\mu\Omega\,\mathrm{cm\,T^{-1}}$. According to Eqn. (2.4) this corresponds to ~0.8 electrons per formula unit. The anomalous Hall constant is shown in Fig. 4.22(b). R_{AHE} vanishes at lowest temperatures and decreases to a minimum of

[3] The THE discussed in Refs. [126, 127] also occurs only after inverting the magnetic field. In contrast to these domain effects, it results in an enhanced Hall resistance.

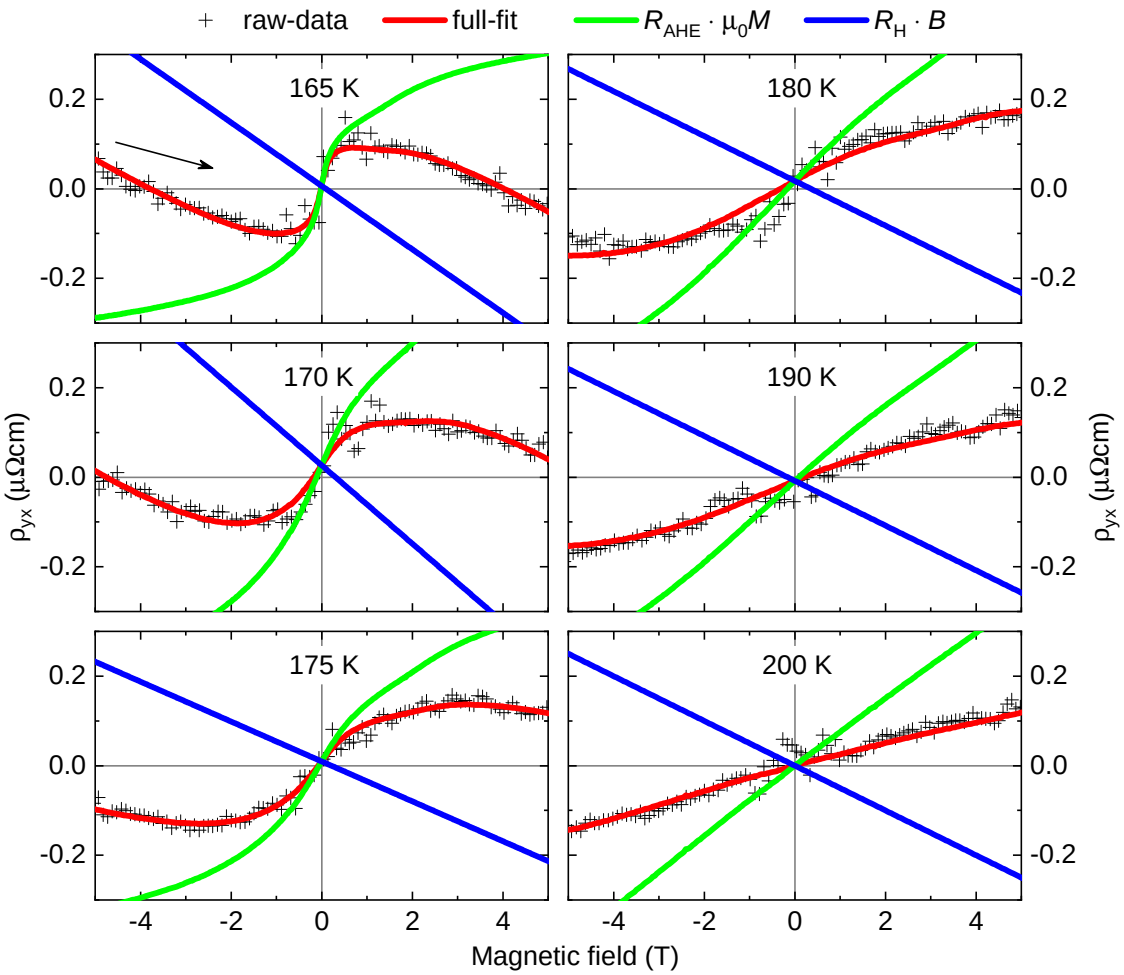

Figure 4.21 Hall effect raw-data for $SrRuO_3$ for $T < T_C$. The data were measured on sample 2. The data are antisymmetrized with respect to a full hysteresis loop such that hysteresis effects are taken into account. The data are fitted via $\rho_{yx} = R_{AHE} \cdot \mu_0 M + R_H \cdot B + C$ (red). For $T > 180\,K$, the normal Hall constant was set to the average value of all other temperatures $R_H^{avg} = -0.05\,\mu\Omega\,cm\,T^{-1}$. The contributions ρ_{yx}^{AHE} and ρ_{yx}^{NHE} are depicted in green and blue, respectively.

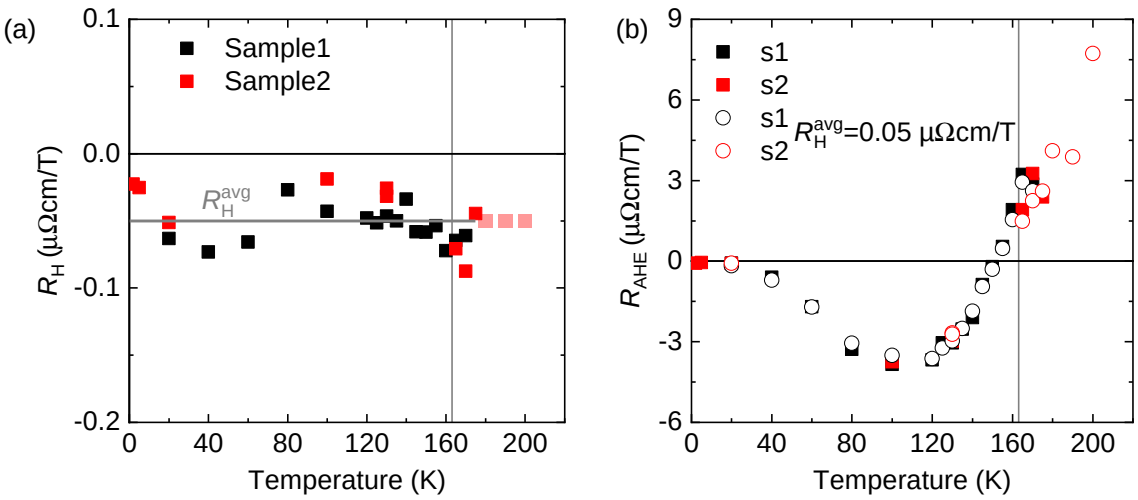

Figure 4.22 Temperature dependence of the Hall constant R_H and anomalous Hall constant R_{AHE}. The ρ_{yx} measurements have been fitted with $\rho_{yx} = R_{AHE} \cdot \mu_0 M + R_H \cdot B_{ext} + C$. The obtained fit parameters R_H and R_{AHE} are shown in (a) and (b), respectively. The open symbols in (b) were obtained from fits with a fixed normal Hall constant $R_H^{avg} = -0.05\,\mu\Omega\,\mathrm{cm\,T^{-1}}$, which equals the mean value of all fits, as indicated with a line in (a).

$-4\,\mu\Omega\,\mathrm{cm\,T^{-1}}$ at 100 K. From there on, the anomalous Hall constant increases, becomes positive at ~150 K and increases further up to T_C. All fits were performed again with fixed $R_H^{avg} = -0.05\,\mu\Omega\,\mathrm{cm\,T^{-1}}$ in order to check the fit quality. The corresponding R_{AHE} does not deviate qualitatively. Thus, the fit is stable and R_{AHE} hardly depends on R_H. These results agree to the literature [122, 143, 144]. There is general consensus that the anomalous Hall effect cannot be described with the extrinsic effects skew scattering and side jump. An explanation via an intrinsic effect due to spin-split bands because of spin-orbit coupling was proposed in Ref. [17]. If the band structure hosts Weyl points close to the Fermi energy, these can cause large contributions to the Berry curvature, which adds a term to the electron velocity. Such a Weyl point acts as a magnetic monopole in momentum space.

Generally, the anomalous Hall effect does not have to vanish in the paramagnetic phase. However, there is no spontaneous magnetization, and, thus the anomalous Hall effect is not present in zero magnetic field. An external field varies the population of spin up and spin down bands and induces a magnetization, which then induces an anomalous Hall effect in analogy to the anomalous Hall effect arising form the (spontaneous) magnetization in the ferromagnetic phase. Temperature-dependent band structure calculations are necessary to determine the Berry curvature at elevated temperatures and then compare these to the presented results shown in Fig. 4.22(b).

4.7 Magnetic excitations

Itoh *et al.* [18] found further fingerprints of the Berry curvature in the spin gap via neutron scattering on polycrystalline samples. Together with K. Jenni, a similar study was performed on single crystals [145] using the previously shown transport results to describe the anomalous temperature dependence. Theory predicts the following entities for the magnon gap Δ and the stiffness constant D

$$\Delta = \frac{\kappa(T)}{\alpha(T)} \quad \text{and} \quad D = \frac{A(T)}{\alpha(T)} \quad . \tag{4.4}$$

Reference [18] only described the temperature dependence of Δ. In the absence of spin-orbit coupling, α is determined by the magnetization density $m(T)$ via $\alpha_0 = 1/[2m(T)\mu_B]$. The anomalous Hall effect becomes important once the spin-orbit coupling and the Weyl points are taken into account. This induces time-dependent currents close to the Weyl points which yield a local magnetization[4]. This yields $\alpha(T) \approx \frac{1}{g\mu_B m(T)} + c(T)\sigma_{xy}(T)$. Neglecting the temperature dependence of all entities except α(T), Eqn. (4.4) can be written as

$$\Delta(T) \approx \frac{a_\Delta \frac{m(T)}{m_0}}{1 + b\frac{m(T)}{m_0}\frac{\sigma_{xy}(T)}{\sigma_0}} \quad \text{and} \quad D(T) \approx \frac{a_D \frac{m(T)}{m_0}}{1 + b\frac{m(T)}{m_0}\frac{\sigma_{xy}(T)}{\sigma_0}} \quad , \tag{4.5}$$

where $m_0 = m(T = 0)$ and $\sigma_0 = e^2/2\pi\hbar a_c$.

The Hall conductivity σ_{xy} shown in Fig. 4.23(a) is obtained from the Hall resistance via

$$\sigma_{xy} = \frac{-\rho_{xy}}{\rho_{xx}^2 + \rho_{xy}^2} \approx \frac{\rho_{yx}}{\rho_{xx}^2} \quad . \tag{4.6}$$

Note, that a different sign convention for σ_{xy} is used in Ref. [145] because we followed the convention of Ref. [122]. Here, the opposite convention as in [17, 18, 146] is used, because this is the formally correct one. Using this and the previously presented magnetization data, the neutron scattering results for Δ and D are fitted via a_Δ, b, and a_D, see Fig. 4.23(b) and (c). Agreement with the spin gap is found with $a_\Delta = 1.66\,\text{meV}$ and $b = 4.98$. The softening of the stiffness constant yields $a_D = 160.90\,\text{meV\AA}^2$. Note, that both, spin gap Δ and stiffness D have been fitted with the same b. The agreement is satisfactory since any further temperature dependence of $\kappa(T)$, $A(T)$, and $c(T)$ was neglected. According to Eqn (4.5), the stiffness should vanish at T_C. However, this cannot be extracted from the neutron data, because the magnons smoothly transform into paramagnon scattering [145].

[4] For further information, see Ref. [18] and the supplementary information of Ref. [145].

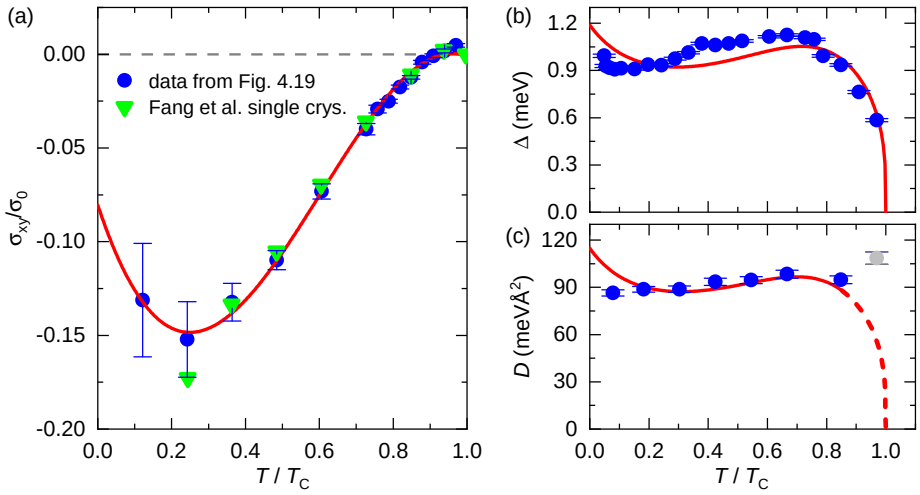

Figure 4.23 Temperature dependence of the Hall conductivity, magnon gap, and spin stiffness. (a) compares the Hall conductivity corresponding to the previously shown Hall-effect data with literature results. The anomalous softening of the magnon gap Δ (b) and spin stiffness D (c) was fitted according to Eqn. (4.5). Panels (b) and (c) are taken from Ref. [145].

From an oversimplified local Heisenberg picture with the Hamiltonian $\mathcal{H} = \sum_{ij} JS_iS_j - KS_{i,z}^2$, the gap follows $\Delta = K\langle S_z\rangle$ and the stiffness follows $D = 2J\langle S_z\rangle a_c^2$. From the obtained results we can deduce the anisotropy $K = 1.25\,\text{meV}$ and the coupling $J = 3.5\,\text{meV}$.[5] For a comparison of K and J we have to take the nearest neighbors into account. This yields a factor of 3 for J. Thus, $3J/K \approx 10\,\%$. Thus, the system contains sizable anisotropy but compared to the ordering temperature $T_C = 163\,\text{K}$ this is not very large. The system is definitely not in the Ising limit. Nonetheless, the gap of 1 meV is in good agreement to the anisotropy field of 10 T.[6] This result agrees to the large anisotropy field of $\mu_0 H_{an} = 10\,\text{T}$. Note, however, that the local Heisenberg picture is of limited validity for the metallic magnetism in $SrRuO_3$ and thus only a rough estimation.

Overall, the magnon gap and the magnon stiffness do not scale with the temperature dependence of the spontaneous magnetization. Both quantities soften below the ferromagnetic ordering temperature. This behavior can be well explained by the influence of Weyl points close to the Fermi surface. These Weyl points not only dominate the anomalous Hall effect via their contribution to the Berry curvature, but also yield a correction term to the magnon gap and the stiffness, as is confirmed by this experimental study.

[5] $\langle S_z\rangle = 0.8$ is estimated from the saturation magnetization assuming a g factor of 2.
[6] $E_{an} = M_{sat}B \approx 1.5 \cdot 10^{-22}\,\text{J} \approx 1\,\text{meV}$.

4.8 Conclusion

In this work, the large high-quality $SrRuO_3$ single crystals grown with the floating-zone technique were used to analyze the criticality of the ferromagnetic phase transition, the magnetic anisotropy, structural domain effects, and intrinsic Berry phase effects on the transverse transport properties and on the spin gap and stiffness.

The ferromagnetic phase transition at 163.6 K cannot be described with a mean-field theory but requires to take critical fluctuations into account. Generally, the Heisenberg and Ising universality classes are promising candidates to describe the critical phenomena. The presented analysis of magnetization measurements close the the transition temperature yields critical exponents β, γ, and δ that favor the Ising universality class. The deviations from the critical exponents according to the Heisenberg universality class are most striking for γ. Generally, Ising-like exchange implies a strong magnetic anisotropy. In literature, the $\boldsymbol{c}$ axis has been reported as the easy-axis direction. In this work, the combination of dilatometry and magnetization measurements confirmed that the longer orthorhombic $\boldsymbol{c}$ axis is the easy axis.

Due to high-temperature structural phase transitions from cubic via tetragonal to orthorhombic, $SrRuO_3$ crystals host six twin domains. Magnetization measurements along a possible easy axis showed that structural domains align their $\boldsymbol{c}$ axis at a critical field of $\sim$2 T. It is astonishing that structural domains that form at 950 K, can be switched at 2 K with magnetic fields as small as 2 T. Consequently, a single-domain state can be established by a magnetic field along a possible easy axis in the ferromagnetic phase. It is even possible to switch between different domain orientations at low temperatures, which makes $SrRuO_3$ a multiferroic material. The reason is that the pinning of the structural domains is weak and thus allows a reorientation of the rotation/tilting scheme of the oxygen octahedra. These domain populations are stable in the ferromagnetic state. Upon heating to the paramagnetic phase, the original domain population is recovered. This effect is called shape-memory effect. The recovery of the original state does not require to enter the high-symmetry phase (here cubic at 950 K) in contrast to usual shape-memory alloys.

A uniaxial pressure along a $\{1\,0\,1\}_c$ axis influences the domain population and can yield up to $\sim$90 % single-domain purity. The magnetization along $\{0\,1\,0\}_c$ has been studied for different pressure-induced initial domain populations. At a critical field of $\sim$7 T, the structural domains are reoriented such that all domains have an easy-axis component along the field axis. Furthermore, this new meta-stable domain population persists at least up to room temperature. It requires $\sim$10 T to fully cant the magnetic moments from their easy axis into the field which defines the intrinsic anisotropy field.

The electric transport measurements confirmed the high quality of the $SrRuO_3$ single crystals by a small residual resistivity of $\rho_0 \simeq 3\,\mu\Omega\,\mathrm{cm}$. The magnetoresistance shows a maximum at T_C of about 7 % at 3 T. Furthermore, the detailed analysis of transverse transport measurements on detwinned single-crystalline samples yields new insights into the nonmonotonic temperature dependence of the anomalous Hall effect. With the combination of magnetization and resistivity measurements on the very same sample it is possible to track the anomalous Hall effect even above T_C. Because of the vanished spontaneous magnetization, the anomalous Hall effect is not present in zero magnetic field. An external field varies the population of spin up and spin down bands and induces a magnetization, which then induces an anomalous Hall effect in analogy to the anomalous Hall effect arising form the (spontaneous) magnetization in the ferromagnetic phase. Additionally, the subtle influence of domain effects observed in the magnetization is consistently found in the Hall resistivity. The ordinary Hall effect is constant up to 200 K and corresponds to electron-dominated transport of ~0.8 electrons per unit cell. The anomalous Hall effect cannot be described with the extrinsic effects skew scattering and side jump. An explanation via an intrinsic effect that bases on spin-split bands because of spin-orbit coupling was already found in Ref. [17]. Weyl points in the band structure close to the Fermi energy can cause large contributions to the Berry curvature, which adds a term to the electron velocity and thus causes the anomalous Hall effect. Its impact is not only seen in the anomalous Hall effect but also in other quantities. Without spin-orbit coupling, the magnon gap and the stiffness would scale with the spontaneous magnetization. With spin-orbit coupling, there is an induced local magnetization. The correction of the magnon gap and of the stiffness scales with the Hall conductivity and softens both quantities on decreasing temperature. This is an extension of the results of Ref. [18], which only proposed a softening of the gap. The observed behavior can be described with the theoretical prediction. This is a strong indication for the validity of the interpretation of these effects using the topology of the band structure.

5 $Cs_3Fe_2Br_9$

Contents

$Cs_3Fe_2Br_9$ is a new candidate for a 3d cluster material that consists of face-sharing Fe_2Br_9 bi-octahedra on a hexagonal lattice. The two iron moments do not form nonmagnetic singlets, but the ground state is the triplet state, although for the geometry of the magnetic exchange path inside a bi-ocathedron antiferromagnetic coupling is expected [147]. The material shows antiferromagnetic ordering through two transitions $T_{N1} = 13.3\,\mathrm{K}$ and $T_{N2} = 13.1\,\mathrm{K}$. Both transitions reveal a strong magnetoelastic coupling and the ground-state magnetic structure is characterized by neutron scattering. $Cs_3Fe_2Br_9$ shows a large anisotropy compared to other iron-based compounds. A rich T-H phase diagram that contains ten ordered phases for a magnetic field along the easy axis is obtained via thermal-expansion and magnetostriction measurements. Magnetization measurements show two phases with a fractional magnetization, namely $⅓M_{sat}$ and $½M_{sat}$. The results are compared to different theoretical predictions for magnetic order on the hcp and triangular lattice.

5.1 Introduction

Triangular and hexagonal magnetic structures raise a lot of interest, because they host a large variety of interesting physics, which mainly results from the geometric frustration for antiferromagnetic NN coupling. Furthermore, magnetic order can be suppressed and a spin-liquid ground state can be established. Interesting effects have been found in various Cu-based materials like $Cs_2Cu(Cl/Br)_4$ [148, 149, 150, 151], but also in systems containing 4d and 5d elements Ru, Ir, or Re, in which spin-orbit interaction plays a crucial role (α-$RuCl_3$ and (α-Li,Na)$_2IrO_3$ [152, 153]). For 3d transition metals, especially Fe^{3+} with $S = 5/2$, the spin-orbit interaction is small and the magnetism is dominated by the interplay of multiple magnetic exchange interactions [154]. In this chapter, the 3d material $Cs_3Fe_2Br_9$ is investigated in detail. From a basic characterization by specific heat and magnetic susceptibility to high-field studies of multiple ordered phases, a broad range of techniques is applied to understand the properties of this material and especially its ordered phases. Additionally, theoretical models for triangular and hexagonal lattices are compared to the experimental findings.

5.2 Crystal growth and structure

The material $Cs_3Fe_2Br_9$ was probably originally found by L. Bohatý (*Institut für Geologie und Mineralogie, Abt. Kristallographie Universität zu Köln*) in 2017. The crystals appeared during the attempt to grow single crystals of the erythrosiderite compound $Cs_2[FeBr_5(H_2O)]$, which was of interest because of its possible multiferroic nature. The crystals grew from aqueous solutions of CsCl and $FeBr_3$ in a molar ratio of approximately 2:1 and a surplus of HBr at room temperature during a period of six month. Further studies revealed that $Cs_3Fe_2Br_9$ can be grown from solutions of CsBr and $FeBr_3$ in the range of 3:2 and 4:1 between room temperature and 50 °C [155]. Figure 5.1(a) shows a dark-brown single crystal with natural faces. Because the crystals dissolve in water and any alcoholic solvent, they have to be treated with care and should be covered with silicone oil whenever possible. If this is not the case, the material reacts with moisture from air and degrades. The material does not only react with liquids but also with solids like copper and gold. That is why samples should not be kept in any measurement setup after the measurement is finished. Also the final sample preparation has to be done right before starting the measurement to reduce the exposure time to air and the room-temperature contact to other materials. Nonetheless, the use of inert gas atmospheres is not required for the storage or preparation of the samples.

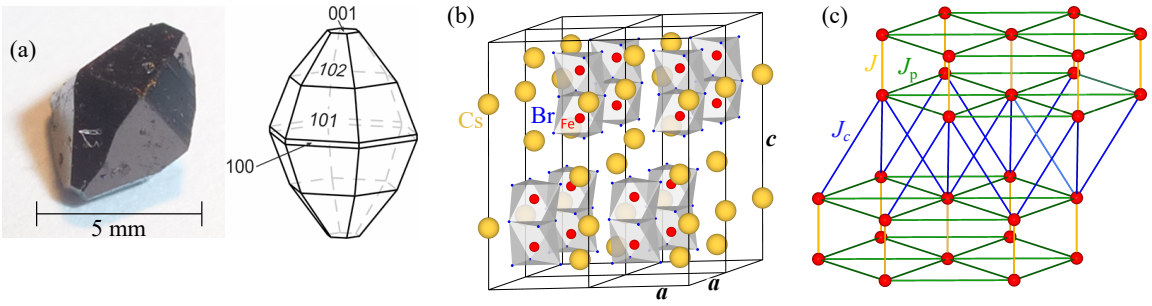

Figure 5.1 Crystals, crystal structure, and magnetic interactions of $Cs_3Fe_2Br_9$. (a) shows an as-grown single crystal of $Cs_3Fe_2Br_9$ with natural faces as indicated in the schematic picture. (b) shows the crystal structure of $Cs_3Fe_2Br_9$ with space group $P6_3/mmc$. Cs atoms are shown in yellow, iron atoms in red, and bromine atoms in blue. (c) shows the magnetic interactions J, J_p, and J_c between Fe sites as defined for other isostructural materials.

All studied samples were prepared from grown crystals by sawing and polishing. Because the samples could not be fixed with glue, it was a long search for a proper fixing material. Cytop™ (AGC Chemicals) is an applicable glue that does not react with $Cs_3Fe_2Br_9$ [156].

The room-temperature crystal structure of the material was characterized by T. Fröhlich [157] using single crystal neutron diffraction and I. Cisarova (Department of Inorganic Chemistry, Charles University, Prague) who did x-ray powder diffraction [158]. Both techniques find the hexagonal space group $P6_3/mmc$ with the lattice parameters given in Table 5.1.

	neutron	x-ray
a	7.5258(5) Å	7.5427(8) Å
c	18.5638(12) Å	18.5849(13) Å

Table 5.1 Lattice parameters of $Cs_3Fe_2Br_9$ obtained by neutron [157] and x-ray diffraction [158].

Figure 5.1(b) shows the structure of $Cs_3Fe_2Br_9$. The main building blocks are face sharing Fe_2Br_9 bi-octahedra. These bi-octahedra are arranged in triangular layers that are stacked, so that the structure is hexagonal. In a regular face-sharing bi-octahedron of $[M_2X_9]$ with centered M ions, the M-X-M angle is 70.5° and the M-M distance is $0.82 \cdot l$, where l denotes the edge length of the octahedron. In $Cs_3Fe_2Br_9$, the iron atoms are not centered in the octahedron. Their distance is increased to 3.5891 Å which corresponds

to a shift of the Fe atoms by ±0.2945 Å.[1] Consequently, the Fe-Br-Fe super-exchange angle is enlarged to ~83.5°. Because the iron atoms are in their oxidation state Fe^{3+}, they have the electronic configuration $3d^5$ and thus a half-filled d orbital. This configuration is usually in the high-spin state $S = 5/2$ with $L = 0$ due to Hund's coupling, and, thus, it forms a spin-only magnetic moment. Typically, Fe^{3+} is an isotropic magnetic ion. In the hexagonal structure, different exchange couplings have been defined for other isostructural materials as indicated in Fig. 5.1(c). Here, J is the intra-dimer coupling. Because the iron atoms are displaced along $\boldsymbol{c}$, there are three equivalent paths governing the Fe-Fe intra-dimer exchange via one Br^- ion, respectively. For the inter-dimer couplings J_p and J_c, every Fe-Fe exchange path passes two Br^- ions. These couplings will be discussed below in more detail.

5.3 Literature about related materials

Polycrystalline $Cs_3Fe_2Br_9$

In 2018, Wei *et al.* [159] reported on the synthesis of polycrystalline samples of $Cs_3Fe_2Br_9$. The basic magnetic characterization shows antiferromagnetic order at 13 K. The paramagnetic susceptibility was described with a dimer model that includes the intra-dimer coupling J and the inter-dimer couplings J_p and J_c. The fit yields the exchange couplings to be antiferromagnetic ($J = 8.2\,\mathrm{K}$, $J_c + J_\mathrm{p} = 3.4\,\mathrm{K}$). Furthermore, the paper reports an insulating direct band gap of ~1.65 eV in accordance to DFT calculations. Further spin-polarized calculations suggest a ground state with antiferromagnetic dimers. In this context, it is worth to look at related materials and their properties.

$Cs_3Cr_2X_9$ with X = Cl, Br

The materials $Cs_3Cr_2Cl_9$ and $Cs_3Cr_2Br_9$ are isostructural to $Cs_3Fe_2Br_9$ with the hexagonal space group $P6_3/mmc$ [21, 160]. In both compounds, the metal ions are shifted away from the regular center position inside each octahedron, which results in an enlarged metal-halide-metal angle, e.g., in the bromine of 75.5° [161]. In both materials, the Cr^{3+} ions with $S = 3/2$ moments inside a bi-octahedron are coupled strongly via J forming a non-magnetic singlet ground state in zero field indicated by a vanishing susceptibility in powder samples [161, 162, 163]. Materials with building blocks of highly connected metal coor-

[1] The edge length of the octahedron is 3.65 Å and the Fe-Fe distance amounts to $0.99 \cdot l$.

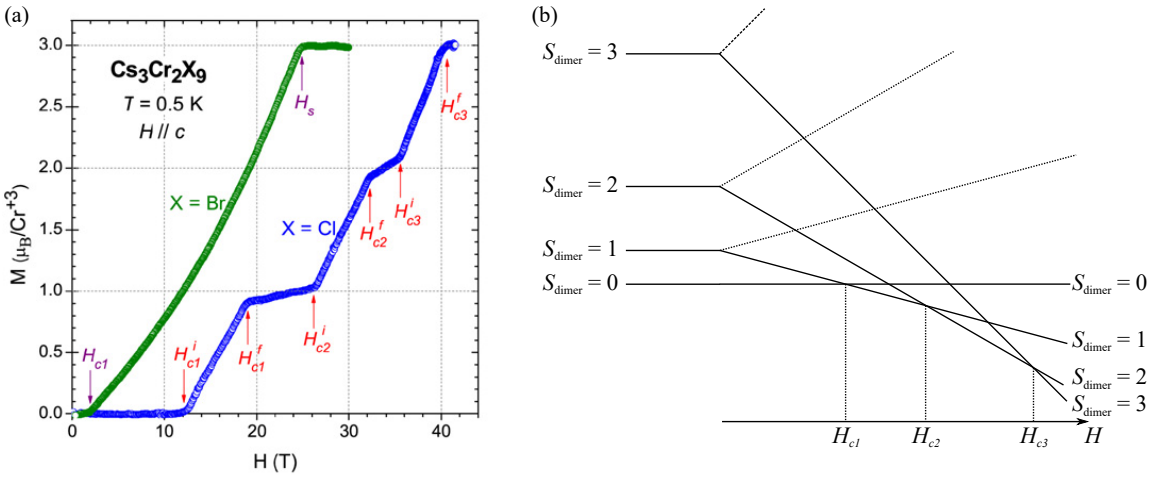

Figure 5.2 Magnetization and dimer level scheme of $Cs_3Cr_2(Cl,Br)_9$. (a) shows the magnetization for $\boldsymbol{H} \parallel \boldsymbol{c}$ of $Cs_3Cr_2Br_9$ (green) and $Cs_3Cr_2Cl_9$ (blue) adapted from Refs. [22, 164]. (b) shows the level scheme of a dimer built up from two $S = 3/2$ moments with a singlet ground state in a magnetic field.

dination polyhedra are called cluster materials.[2] The metal-metal intra-cluster interaction is dominant in these materials. This also applies for $Cs_3Cr_2Br_9$ and $Cs_3Cr_2Cl_9$. Figure 5.2(a) shows the magnetization for magnetic fields applied along the hexagonal $\boldsymbol{c}$ axis for both compounds. The magnetization of $Cs_3Cr_2Cl_9$ (blue) is zero up to H_{c1} and increases linearly from there on. Two intermediate plateau states are found with the fractional magnetization of $1/3 M_{sat}$ and $2/3 M_{sat}$ and saturation is reached at 40 T. The magnetization process of $Cs_3Cr_2Cl_9$ can be explained with a dimer level scheme as depicted in Fig. 5.2(b). The two $S = 3/2$ moments per bi-octahedron can couple to four possible total spin values $S_{\text{dimer}} = 0, 1, 2$, and 3 in each dimer. In a single-dimer picture without interaction between neighboring dimers and at zero temperature, each state has a well defined energy. The singlet formation implies that $S_{\text{dimer}} = 0$ is the ground state and $S_{\text{dimer}} = 1, 2, 3$ are the excited states. An increasing magnetic field splits up the higher-lying states due to Zeeman energy and results in multiple level crossings. An elevated temperature broadens these crossings. The $S_{\text{dimer}} = 1$ state crosses $S_{\text{dimer}} = 0$ at $H = H_{c1}$, and, thus, it becomes favorable. In the single-dimer picture, the magnetization jumps to $1/3 M_{sat}$. An inter-dimer coupling causes a finite bandwidth. The bandwidths of the $S_{\text{dimer}} = 1$ state prevents a jump, but yields a linear magnetization in an intermediate regime between H_{c1}^i and H_{c1}^f. On increasing magnetic field, the magnetization is constant up to H_{c2} and H_{c3}, where the

[2] Another example of a cluster material is $Ba_3CeIr_2O_9$, which also consists of face-sharing bi-octahedra. In this case, the iridium ions form a molecular orbital due to spin-orbit coupling [11].

higher-spin states $S_{\text{dimer}} = 2$ and $S_{\text{dimer}} = 3$ become favorable, respectively. This scenario perfectly describes the magnetization of $Cs_3Cr_2Cl_9$. Inelastic neutron scattering obtained the antiferromagnetic coupling constants given in Table. 5.2.

	$Cs_3Cr_2Cl_9$[165]	$Cs_3Cr_2Br_9$ [163]
J	1.750 meV	1.030 meV
J_p	0.032 meV	0.054 meV
J_c	0.031 meV	0.039 meV

Table 5.2 Coupling constants J, J_p, and J_c for $Cs_3Cr_2Cl_9$ and $Cs_3Cr_2Br_9$ from Refs. [163, 165].

For the Cl-based compound $J/J_p \approx 55$ and, therefore, $J \gg J_p$ is fulfilled and the explanation above works for the magnetization curve. Although the Cs and Br compound are isostructural, the magnetization of $Cs_3Cr_2Br_9$ is different. It is also zero up to H_{c1}, which is much smaller than in the Cl compound. For higher magnetic fields, the magnetization increases continuously and shows no further transitions until the saturation is reached at 25 T. Neutron scattering yields $J/J_p \approx 19$, which results in more band-like excited states that even overlap. This causes a continuous magnetization above H_{c1} up to the saturation.

Above H_{c_1}, where the singlet-triplet gap $\Delta \sim g\mu_B H_{c_1}$ closes, three-dimensional magnetic ordering develops. In this field-induced magnetic ordering, the transverse spin components are ordered. Such a transition can be described as a Bose-Einstein condensation of magnons [166]. Grenier and Ziman performed multiple neutron diffraction studies in order to analyze the transverse magnetic structure and the magnetic excitations. The transverse order is not necessarily trivial but can also show incommensurate propagation vectors [164, 167]. Nonetheless, the two moments of each bi-octahedron are always aligned antiparallel and (the sum of) two out of three intra-plane and inter-plane neighbor spins are aligned antiparallel, while one is parallel. This results from the frustration of the system of antiferromagnetic couplings on the hexagonal lattice. Furthermore, there is sizable anisotropy $D \approx 0.01\,\text{meV} \sim -J/100$ and the critical field consequently shows a directional dependence as indicated by $H_{c1}^{\parallel c} = 2\,\text{T}$ and $H_{c1}^{\perp c} = 1.4\,\text{T}$ for the Cl compound [164].

In general, $Cs_3Cr_2Cl_9$ and $Cs_3Cr_2Br_9$ are examples of spin-dimer systems in a hexagonal structure with anisotropy effects. Changes of the exchange coupling strengths influence the magnetic order and the excitations of such a system.

$CuFeO_2$

The mineral *delafossite* with the chemical formula $CuFeO_2$ is another well-studied magnetic material with a substantial relation to $Cs_3Fe_2Br_9$. In $CuFeO_2$, Fe^{3+} ions form triangular layers with $S = 5/2$ moments separated by nonmagnetic Cu^+ layers [168]. The structure is hexagonal with space group $R\bar{3}m$. It was named after the mineral, which derives from the cubic NaCl structure if two different cations order into alternating (1 1 1) planes and form a layered structure, see Fig. 5.3(a). Antiferromagnetic order in $CuFeO_2$ through two magnetic transitions at $T_{N_1} \approx 14\,\mathrm{K}$ and $T_{N_2} \approx 11\,\mathrm{K}$ is known since decades [169, 170].

Figure 5.3(b) shows the magnetization data from Ref. [171] at 1.5 K deep in the ordered state. For a magnetic field perpendicular to $\boldsymbol{c}$ and thus perpendicular to the collinear moments, $M(H)$ increases linearly up to $B_{c1}^{\perp} = 25\,\mathrm{T}$ where the magnetization jumps slightly above $1.5\,\mu_B/Fe^{3+}$, which is below the fraction of 1/3 of the saturation magnetization of the pure $S = 5/2$ moments.[3] Up to $B_{c2}^{\perp} = 30\,\mathrm{T}$, the magnetization is essentially constant on this plateau and then again increases linearly. At $B_{c3}^{\perp} = 52\,\mathrm{T}$, there is another jump of the magnetization and it increases further from there on. For $B \parallel \boldsymbol{c}$, the magnetization shows multiple anomalies at $B_{c1}^{\parallel} = 7.5\,\mathrm{T}$, $B_{c2}^{\parallel} = 13\,\mathrm{T}$, $B_{c3}^{\parallel} = 20\,\mathrm{T}$, $B_{c4}^{\parallel} = 32.5\,\mathrm{T}$, and $B_{c5}^{\parallel} = 53\,\mathrm{T}$. The magnetization is essentially zero up to $B_{c1}^{\parallel}$, where it discontinuously jumps and grows linearly up to $B_{c2}^{\parallel}$. There, a plateau of $M = 1/5 M_{sat}$ is found. At $B_{c3}^{\parallel}$, the magnetization jumps to a wide plateau. Above $B_{c4}^{\parallel}$, the magnetization increases linearly and again shows a broadened increase at $B_{c5}^{\parallel}$. High-field measurements on powder revealed a saturation field of ~70 T and approximately $5\,\mu_B$/Fe [172].

Figure 5.3(c) shows the corresponding phase diagrams with the proposed or observed magnetic orderings. The zero-field phase between T_{N_1} and T_{N_2} shows a sinusoidal amplitude-modulated collinear magnetic structure with a temperature-dependent incommensurate propagation vector [173]. The ground state below T_{N_2} shows 2up-2down antiferromagnetic order with moments along the $\boldsymbol{c}$ axis [174, 175, 176]. A magnetic field perpendicular to $\boldsymbol{c}$ continuously cants the moments of the 2up-2dw spin state. At $B_{c1}^{\perp}$, the moments order in a 2up-1dw state with moments along the field direction. Above 30 T a canted versions of this state is established.

For $\boldsymbol{B} \parallel \boldsymbol{c}$ at lowest temperatures, the five field-induced phase transitions correspond to changes of the magnetic order: 2up-2dw → incommensurate screw → 3up-2dw → 2up-1dw → canted 2up-1dw → canted high-field [171, 178, 179, 180]. Figure 5.3(d) shows the magnetic structures of $CuFeO_2$.[4]

[3] The authors claim that this plateau is at $1/3 M_{sat}$.

[4] The high-field phases have also been described with a different phase shift between neighboring 3up-2dw chains, see Ref. [171].

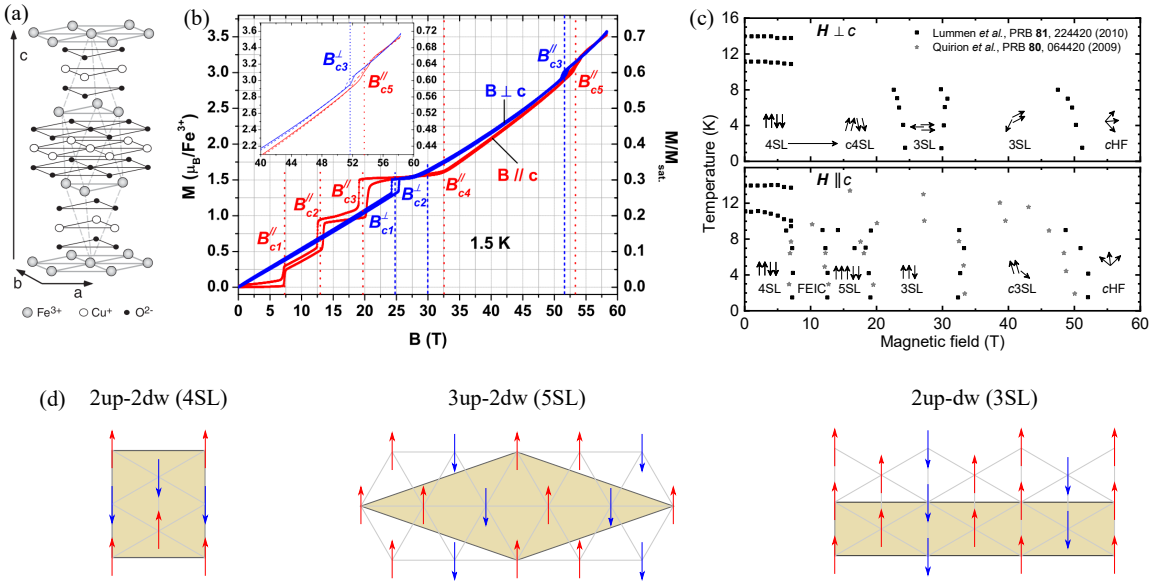

Figure 5.3 Magnetism of $CuFeO_2$. (a) shows the crystal structure of $CuFeO_2$ from Ref. [177]. (b) shows its magnetization for magnetic fields parallel and perpendicular to the hexagonal ***c*** axis from Ref. [171]. (c) presents the phase diagram of $CuFeO_2$ for both field orientations. Data points stem from the given publications. The magnetic orderings for the field-induced phases are shown schematically. (d) shows the measured magnetic structure of the 2up-2dw ground state (Ref. [174]), the 3up-2dw phase (Ref. [178]), and the proposed structure of the 2up-1dw phase (Ref. [171]). The magnetic unit cells are highlighted.

In the first field-induced phase ($B^{\parallel}_{c1} < B^{\parallel} < B^{\parallel}_{c2}$), the incommensurate screw breaks the mirror plane perpendicular to the ***b*** axis and yields the polar point group 21'. A ferroelectric polarization along [1 1 0] was measured [181, 182, 183] and was proposed to be induced by a *d*-*p* hybridization with spin-orbit coupling [184]. Nakajima *et al.* [185] confirmed this mechanism.

Haraldsen *et al.* [186] proposed that the field-induced transitions can arise from spin-wave instabilities. Indeed, neutron spectroscopy measurements in zero field confirmed that the local minima in the magnon dispersion coincide with the incommensurate wave vectors of the ferroelectric phase [187]. It was found that nonmagnetic Al doping stabilizes the ferroelectric ground state to zero magnetic field [188, 189, 190] suggesting that the ferroelectric phase sensitively depends on the magnetic exchange. The importance of the spin-lattice coupling has been shown by the large pressure dependence of the ordering temperature [191, 192] and the bond order in the ⅕-plateau phase [178].

For a basic theoretical description, a model consisting of four Heisenberg exchange interactions J_i and an Ising anisotropy D was proposed [193]. The application of the

model to measured data yields the following coupling strengths [187]:

J_1	J_2	J_3	J_z	D
1.14 meV	0.50 meV	0.65 meV	0.33 meV	0.17 meV

In the phase diagram of the J_1-J_2-J_3-model on the triangular lattice with strong Ising anisotropy [49], these parameters would fall into the region of a four-spin sublattice ground state, which is in agreement to the experimental findings on $CuFeO_2$. Nonetheless, inelastic neutron scattering data on a single-domain antiferromagnetic state achieved by small uniaxial pressure [194, 195] display deviations from this model, which were attributed to a sizable monoclinic distortion [177, 196].

The distortion changes the triangular lattice to a so-called scalene triangle lattice in which the nearest-neighbor coupling J_1 splits into three couplings J_1, J_1', and J_1'' and the further-neighbor couplings J_2, J_3, and J_z split into two couplings J_i and J_i', see Fig. 5.4. Details about the underlying structure and the model can be found in Ref. [195]. Furthermore, an in-plane anisotropy E was added as proposed by electron-spin resonance [197]. This model finally describes the magnon dispersion well. The largest splitting for the exchange constant is found for the nearest-neighbor coupling J_1, which splits into $J_1 \approx 0.445\,\text{meV}$, $J_1' \approx 0.422\,\text{meV}$, and $J_1'' \approx 0.150\,\text{meV}$.

Thus, $CuFeO_2$ is an example of an anisotropic iron-based magnet on a triangular lattice. The influence of lattice distortions on the exchange parameters and the lifting of exchange frustration is important and should be considered in similar materials.

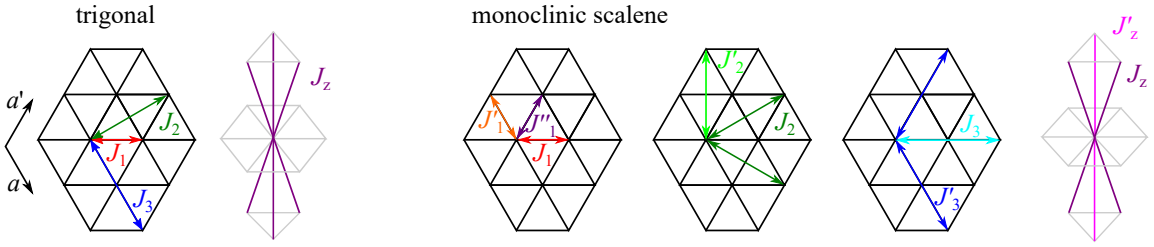

Figure 5.4 Magnetic exchange J_i in the trigonal and monoclinic scalene lattice. In the trigonal case, three different couplings are considered: NN J_1, NNN J_2, and NNNN J_3 plus the out-of-plane coupling J_z. The scalene lattice results in three different nearest neighbor couplings J_1, J_1', and J_1'' due to an additional displacement of the oxygen atoms. The monoclinic distortion splits the other couplings into two couplings J_i and J_i'. For more details see Ref. [195].

5.4 Zero-field characterization of $Cs_3Fe_2Br_9$

5.4.1 Thermodynamic properties

Magnetic susceptibility

The magnetic susceptibility of $Cs_3Fe_2Br_9$ was measured using the SQUID magnetometer with samples oriented in two different orientations, namely the high-symmetry directions $\boldsymbol{H} \parallel \boldsymbol{c}$ and the in-plane orientation $\boldsymbol{H} \perp \boldsymbol{c}$. Figure 5.5 compares both orientations for the whole temperature range. The susceptibility increases with decreasing temperature, following the Curie-Weiss law. Magnetic ordering sets in at $T_\mathrm{N} = 13.3\,\mathrm{K}$. Below T_N, $\chi_\parallel$ reduces towards zero, while $\chi_\perp$ only drops slightly and remains constant at about 0.1 emu/mol. This hints to antiferromagnetic ordering with moments parallel to the $\boldsymbol{c}$ axis. The high-temperature susceptibility basically reproduces the findings from Wei et al. [159], but in detail this allows deeper understanding. Because this is single-crystal data with two different field orientations, it is possible to analyze the magnetic anisotropy of the system. Assuming a $S = 5/2$ spin-only moment on each iron atom, the susceptibility can be fitted from 150 K to 300 K with the Curie-Weiss law

$$\chi = \frac{\mu_0 n g^2 \mu_\mathrm{B}^2}{3k_B} \frac{S(S+1)}{T-\theta} \quad ,$$

where n is the density of iron ions. The fit of the susceptibility yields a g-factor of 2.095(4) and the Curie-Weiss temperature $\theta = -57(3)\,\mathrm{K}$. In the paramagnetic phase, $Cs_3Fe_2Br_9$ is isotropic as can be seen from the plot of $\chi_\parallel/\chi_\perp$, which almost perfectly equals 1, see Fig. 5.5(i). The frustration parameter $f = |\theta|/T_\mathrm{N} \approx 4.4$ indicates a sizable frustration of the magnetic system. A detailed view on the susceptibility around the ordering transition is presented in Fig. 5.5(b). The susceptibility with $\boldsymbol{H} \parallel \boldsymbol{c}$ shows two close drops, which is pronounced by the temperature derivative in inset (ii). This indicates two distinct transitions $T_\mathrm{N1} = 13.3\,\mathrm{K}$ and $T_\mathrm{N2} = 13.1\,\mathrm{K}$. The changes of $\chi_\perp$ are much smaller. It is constant for $T > T_\mathrm{N1}$, shows a kink, reduces to T_N2, and is again constant for smaller temperatures.

These data clearly exclude singlet-dimerization within the bi-octahedra because the susceptibility only vanishes for the $\boldsymbol{c}$ axis, while it remains large in-plane. This is in drastic contrast to the related chromium compounds $Cs_3Cr_2(Cl,Br)_9$. The reason for this behavior and consequences therefrom will be discussed below.

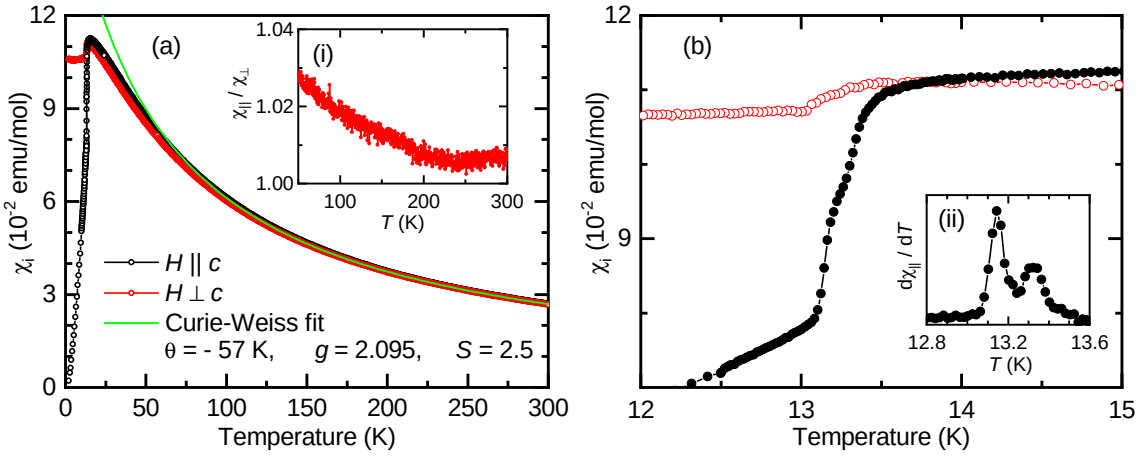

Figure 5.5 Magnetic susceptibility of $Cs_3Fe_2Br_9$. (a) shows the temperature dependence of the magnetic susceptibilities $\chi_\parallel$ and $\chi_\perp$. Inset (i) shows the fraction $\chi_\parallel/\chi_\perp$ for $T > 50\,\mathrm{K}$. (b) enlarges the susceptibilities close to the ordering temperature. Inset (ii) shows the temperature derivative of $\chi_\parallel$.

Specific heat

The specific heat c_p of $Cs_3Fe_2Br_9$ from room temperature to 1.8 K, see Fig. 5.6, was measured in the PPMS. The specific heat shows two huge and sharp anomalies around 13 K that were measured using the continuous analysis described in Chapter 3.5. Figure 5.6(ii) shows a long heat pulse for $Cs_3Fe_2Br_9$ starting from a base temperature of 12.9 K, which was used for the continuous evaluation of c_p. During the heat pulse, the temperature almost levels off twice upon heating and cooling. This indicates an almost first-order phase transition, because there is no hysteresis and no latent heat. The corresponding specific heat is shown in Fig. 5.6(i). Corresponding to the two temperatures, where the $T(t)$ curve levels off, two distinct anomalies are visible. Thus, the specific heat supports the results of the susceptibility data for two transitions. The high-temperature specific heat slightly exceeds the Dulong-Petit limit of ~350 J/molK. To analyze the magnetic entropy, it is required to distinguish the magnetic and the phononic contribution. The total entropy of the magnetic system with two $S = 5/2$ spins per formula unit is $2R\ln(6) = 29.8$ J/molK. Figure 5.7(a) shows the c_p/T data and different background signals. The difference between the data and the background defines the specific heat that is integrated numerically to yield the corresponding entropies S_{mag}, shown in Fig. 5.7(b). The total entropy without subtracting a background exceeds the expected magnetic entropy at the ordering transition and thus a background signal is required. The phononic background consists of Debye and Einstein modes. The Debye and Einstein temperatures were chosen

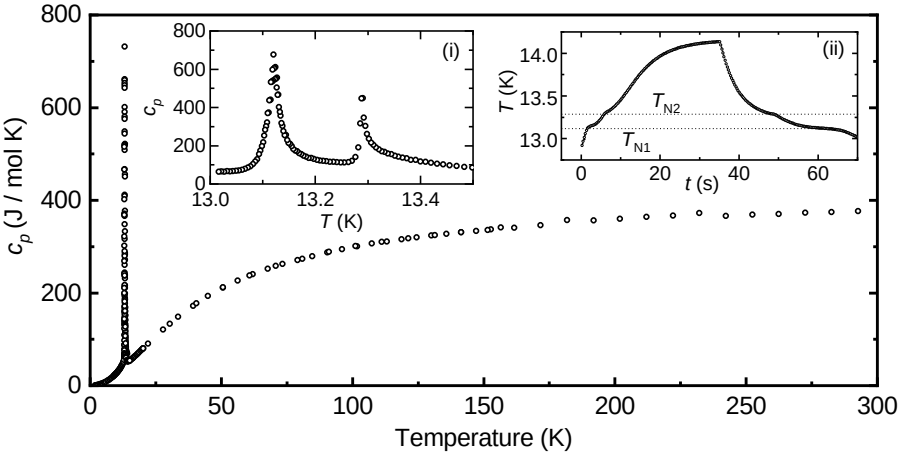

Figure 5.6 Temperature dependence of the specific heat c_p of $Cs_3Fe_2Br_9$. Inset (i) shows the specific heat obtained from a long heat pulse with a continuous analysis. The corresponding heat pulse with the actual temperature versus time behavior is shown in inset (ii).

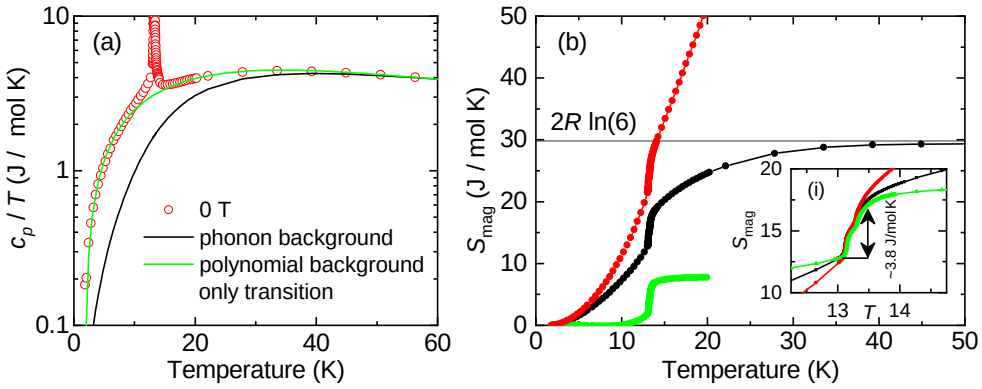

Figure 5.7 Entropy of $Cs_3Fe_2Br_9$. (a) shows the temperature dependence of c_p/T with a phononic background that contains Debye and Einstein modes. Integrating the difference between the data and the background yields the magnetic entropy S_{mag} shown in (b). The expected magnetic entropy of two $S = 5/2$ spins per formula unit is $2R\ln(6) = 29.8$ J/molK. The entropy release at the transition (i) is estimated with $\Delta S_{\mathrm{mag}} = 3.8$ J/molK between 13.1 K and 13.6 K, where all entropy curves are set to the same S_{mag} at 13.1 K.

so that the specific heat of the phonons equals the c_p data above 40 K and the total expected magnetic entropy is released up to this temperature.[5] Using the polynomial background that is defined so that only the peaks of the transitions contribute to the magnetic entropy yields an entropy release right at the transition of $\Delta S_{\mathrm{mag}} = 3.8\,\mathrm{J/molK}$ which is 13 % of the total magnetic entropy of the system. This value does not depend on the chosen background as is indicated by inset (i). Thus, a substantial part of the magnetic entropy is released below T_N similar to other magnets like $EuTiO_3$ [198], but also above the transition as in frustrated magnets like $BiMn_2PO_6$ [199].

A corresponding nonmagnetic material, e.g., $Cs_3V_2Br_9$ is known [20], but no specific-heat data has been reported about this material until now, which would yield a more reliable phononic background to analyze the entropy in more detail.

Thermal expansion

The thermal expansion in zero field was measured for three different directions, namely the out-of-plane $\boldsymbol{c}$ axis, the in-plane direction e_1 and another in-plane direction e_2, which was chosen perpendicular to e_1. Figure 5.8 shows the relative length changes for all three directions in the temperature regime around the magnetic ordering transition. Each data set shows a step-like relative length change at T_N, with $\Delta L_c/L_c \simeq 10^{-4}$ and $\Delta L_{e_1}/L_{e_1} = \Delta L_{e_2}/L_{e_2} \simeq 3 \cdot 10^{-4}$.

Astonishingly, all measured length changes show a contraction at the transition into the ordered phase, resulting in an apparent net volume change of $\Delta V/V \sim 10^{-3}$. As will be discussed below, this transition breaks the three-fold symmetry and, therefore, allows for three twin domains. Figure 5.8(i) shows the thermal-expansion coefficients α_i close to

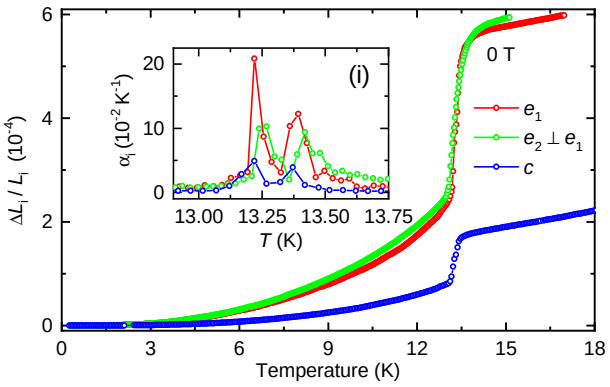

Figure 5.8 Thermal expansion of $Cs_3Fe_2Br_9$ in zero-field along $\boldsymbol{c}$ and two in-plane directions. e_1 is parallel to a bond and e_2 perpendicular to a bond. Inset (i) shows the corresponding thermal-expansion coefficients α_i for each direction.

[5] The chosen Debye temperature is 93 K and c_p of the Debye mode is scaled with 5. Furthermore, three different Einstein modes are used with Einstein temperatures of 100 K, 150 K, and 250 K. The specific heat of each mode is scaled with 3. This reproduces the Dulong-Petit limit for a material with 14 atoms.

the phase transition. Here, again two distinct peaks are visible, which finally makes the interpretation of two separate transitions conclusive.

Because the capacitance dilatometer applies a small force onto the sample along the measured direction, this might cause partial or even full detwinning at the presumably ferroelastic transition. If this is the case, the sum of the measured in-plane length changes e_1 and e_2 does not represent the total in-plane area contraction but result from different twin-domain orientations. The fact that both measured length changes are equal may be surprising at first glance. It can, however, be explained straightforwardly by considering the twinning effects. If a linear magnetoelastic coupling with $\partial J/\partial r = \epsilon$ is included, this yields $J(\epsilon) = J + J\epsilon$, where ϵ denotes a relative distance change between neighbors. The total energy follows

$$\begin{aligned} \Delta E_{\text{tot}} &= E_{\text{mag}} + E_{\text{lattice}} \\ &= cJ(1+\epsilon) + \frac{1}{2}k\epsilon^2 \quad . \end{aligned}$$

In the ordered state, the energy is minimized $\left(\frac{\partial E_{\text{tot}}}{\partial \epsilon} = 0\right)$ for a finite ϵ. On the frustrated triangular lattice with two antiferromagnetic bonds and one ferromagnetic bond per triangle, the linear magnetoelastic coupling causes a transition to an orthorhombic structure. The transition is only distortive and thus area conserving if the orthorhombic lattice vector $\boldsymbol{a}$ elongates by $\Delta L/L = +\epsilon$, while $\boldsymbol{b}$ contracts by $\Delta L/L = -\epsilon$. Figure 5.9(a) shows the resulting structure and the expected length changes along certain directions. The ferromagnetic bonds are a high-symmetry direction of the orthorhombic structure ($+\epsilon$), while the antiferromagnetic bonds are no high-symmetry direction. Geometric considerations yield, that the antiferromagnetic bonds shrink by $\epsilon/2$ and the direction perpendicular to the antiferromagnetic bonds elongates by $\epsilon/2$.

Figure 5.9(b) shows all three possible domains and their length changes along a bond and perpendicular to a bond. The domains occur in the sample with populations α, β, and γ with

$$\alpha + \beta + \gamma = 1 \quad . \tag{5.1}$$

A single-domain sample would show a length change of ϵ if this corresponds to a high-symmetry direction of the orthorhombic state (domain a), or $\epsilon/2$ for the domains b and c. A multi-domain sample with $\alpha = \beta = \gamma = 1/3$ shows a vanishing thermal expansion. Because an antiferromagnetic ground state is observed, it is natural to assume that ferromagnetic bonds elongate and antiferromagnetic bonds contract.[6]

[6] In principle, also the inverted effect is possible, but the chosen case applies for $Cs_3Fe_2Br_9$.

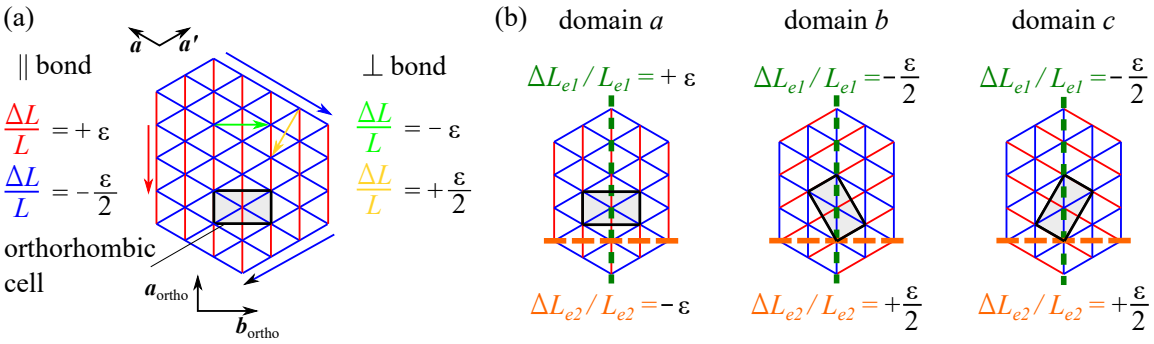

Figure 5.9 (a) Schematic drawing of an orthorhombic domain resulting from breaking the three-fold rotation symmetry. Each triangle is assumed to establish two antiferromagnetic bonds (blue) and one ferromagnetic bond (red). This results in an orthorhombic structure with the marked unit cell. A linear magnetoelastic coupling results in an area-conserving distortion of $\pm\epsilon$ along the orthorhombic high-symmetry directions. The length changes for certain non-high-symmetry directions are given (yellow and green). (b) compares all three possible domains with their length changes along (green) and perpendicular (orange) to a bond.

The presented in-plane thermal-expansion measurements were performed along a hexagonal lattice vector e_1 and perpendicular to it (e_2). Both directions show contraction and thus the sample is not fully twinned.

Uniaxial pressure is known to cause detwinning for transitions with spontaneous distortion. This can yield a single-domain state only along the contracting high-symmetry direction and thus perpendicular to a bond. This favors domain a which causes $\alpha = 1$. The long orthorhombic axis and thus the ferromagnetic bonds orient perpendicular to the uniaxial pressure. If the sample is only partially detwinned, domains b and c both contribute with an elongation of $\epsilon/2$ and are thus equally probable, which results in $\beta = \gamma$. Together with domain a with population α that contract by $-\epsilon$, the length change over all domains amounts to

$$\frac{\Delta L_{e_2}}{L_{e_2}} = -\alpha \cdot \epsilon + 2 \cdot \beta \cdot \frac{\epsilon}{2} \quad .$$

A measurement with uniaxial pressure along a bond favors domains b and c (again both have the same population β') with a contraction of $-\epsilon/2$ and the unfavorable domain a (population α') contributes with the length change $\Delta L/L = +\epsilon$. Consequently, the best detwinning is $\alpha' = 0$ and $\beta' = \gamma' = 0.5$. The length change over all domains amounts to

$$\frac{\Delta L_{e_1}}{L_{e_1}} = -2 \cdot \beta' \cdot \frac{\epsilon}{2} + \alpha' \cdot \epsilon \quad .$$

As was shown in Fig. 5.8, the same contraction was measured along e_1 and e_2, which

results in

$$\begin{aligned} \frac{\Delta L_{e_2}}{L_{e_2}} &= \frac{\Delta L_{e_1}}{L_{e_1}} \\ \Rightarrow \quad \beta - \alpha &= \alpha' - \beta' \quad . \end{aligned}$$

Because the measured length change is negative, the uniaxial pressure of the dilatometer yields at least a partial detwinning. The amount of detwinning cannot be clarified from these measurements, since any detwinning along e_1 has a corresponding twin ratio with the same total length change along e_2.

The maximal length change that can be equal for e_1 and e_2 results from a maximal detwinning along e_1 with $\beta' = 0.5$ and $\alpha' = 0$. The corresponding length change is $\Delta L_{e_1}/L_{e_1} = -\epsilon/2$. The measured length change of $3 \cdot 10^{-4}$ yields a minimum distortion of $\epsilon = 6 \cdot 10^{-4}$. Note, however, that these considerations base on the assumption of a linear magnetoelastic coupling, which causes only a distortive effect. Any higher order terms can also yield an area contraction but temperature-dependent x-ray diffraction did not observe an area reduction [200].

Combining the specific entropy change Δs and the specific volume change Δv at this first-order transition, it is possible to estimate the hydrostatic pressure dependence of the transition temperature via the Clausius-Clapeyron relation

$$\frac{\mathrm{d}T_\mathrm{N}}{\mathrm{d}p} = \frac{\Delta v}{\Delta s} = \frac{\Delta V/V}{\Delta S/V_\mathrm{mol}} = \frac{\Delta L_c/L_c}{\Delta S \cdot Z/(N_A V_\mathrm{cell})} \quad ,$$

where $Z = 2$ denotes the number of formula units per unit cell, N_A Avogadro's constant, and the cell volume amounts to $V_\mathrm{cell} = a^2 c \sin 60° = 915.7\text{Å}^3$. Here, it is assumed that the total volume change results from the $\boldsymbol{c}$ axis, while the ab plane is area conserving as discussed above. The resulting pressure dependence of the transition temperature is $\frac{\mathrm{d}T_\mathrm{N}}{\mathrm{d}p} \approx 10\,\mathrm{K\,GPa^{-1}}$ and the relative change is $\frac{1}{T_N}\frac{\mathrm{d}T_\mathrm{N}}{\mathrm{d}p} \approx 75\,\%\,\mathrm{GPa^{-1}}$, which is a remarkably large magnetoelastic coupling in $Cs_3Fe_2Br_9$.

Concluding these zero-field studies, $Cs_3Fe_2Br_9$ shows no singlet-dimer formation as other isostructural materials but orders antiferromagnetically through two almost first-order phase transitions. The easy axis of the Fe^{3+} $S = 5/2$ moments is the $\boldsymbol{c}$ direction. The transitions show a remarkably large magnetoelastic coupling. The pressure dependence of the transitions is large and the breaking of the three-fold axis yields three domains, which can partially be influenced by pressure.

5.4.2 Neutron scattering

T. Fröhlich and S. Biesenkamp used large single crystals for neutron diffraction to perform a magnetic structure determination. Here, only the main results are presented. For detailed results see Refs. [156, 157].

The temperature-driven two-step transition was further studied with neutron scattering in order to determine microscopic details of the ordered phases. Figure 5.10 shows the temperature-dependent neutron scattering intensity of the (H K 0) space in the vicinity of the (0.5 0.5 0) reflection related to the crystallographic unit cell. At 13.8 K and thus above the Néel temperature, the enhanced intensity at (0.5 0.5 0) signals antiferromagnetic fluctuations. Around 13.4 K, two other intensity maxima occur at the incommensurate positions (0.45 0.39 0) and (0.55 0.61 0), which is (0.5±δ 0.5±ϵ 0) with $\delta = 0.05$ and $\epsilon = 0.11$. These superstructure reflections can be attributed to the magnetic ordering transition T_{N1}. With decreasing temperature, both δ and ϵ decrease, while the intensity increases. At 13.1 K, the intensity at the incommensurate positions instantaneously vanishes, while the intensity of the commensurate peak increases strongly. From this measurement it can be concluded that both transitions are of first order. In the intermediate temperature regime, the magnetic order is incommensurate, while at T_{N2} the propagation vector locks in at a commensurate value.

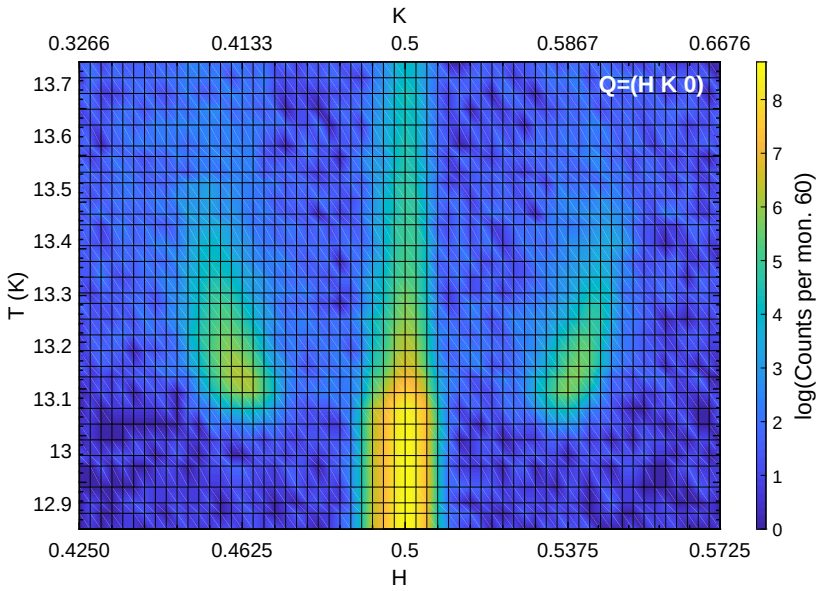

Figure 5.10 Temperature-dependent neutron scattering on $Cs_3Fe_2Br_9$ in the (H K 0) space close to (0.5 0.5 0). The temperature was varied from 13.8 K to 12.8 K covering both phase transitions T_{N1} and T_{N2}. The intensity is color coded. Figure from S. Biesenkamp [156].

5.4.3 Magnetic structure

The magnetic structure of the intermediate incommensurate phase has not yet been refined. The zero-field ground state was refined by T. Fröhlich [157] in the orthorhombic space group *Cmcm* whose basis vectors are obtained from the hexagonal space group $P6_3/mmc$ via the transformation

$$\boldsymbol{a}_{Cmcm} = \boldsymbol{a} + \boldsymbol{a}', \quad \boldsymbol{b}_{Cmcm} = -\boldsymbol{a} + \boldsymbol{a}', \quad \boldsymbol{c}_{Cmcm} = \boldsymbol{c} \quad .$$

The magnetic structure that describes the diffraction best, is shown in Fig. 5.11. All moments point along $\boldsymbol{c}$. Within one face-sharing bi-octahedron, they are aligned parallel. Two thirds of the nearest and next-nearest dimers are antiparallel, while the other part is parallel. The refined twinning ratios of 39.3 %, 30.8 %, and 29.9 % are close to the statistical population of ⅓ [157].

This magnetic structure differs from the proposed structure calculated by DFT methods of Wei *et al.* [159], and the structure of $Cs_3Cr_2(Cl,Br)_9$, which both contain singlet dimers. This could already be excluded from the susceptibility measurements presented above.

The geometry of the intra-dimer exchange path supports antiferromagnetic intra-dimer coupling [147], but in fact, they are aligned parallel. Thus, it is natural to assume that the inter-dimer couplings play an important role. Because ⅔ of these neighbors are antiparallel, the coupling should be antiferromagnetic and the geometry of the lattice induces frustration. Additionally, the in-plane coupling J'_p is introduced that connects Fe moments with different z components of neighboring bi-octahedra, as depicted in pink in Fig. 5.11.

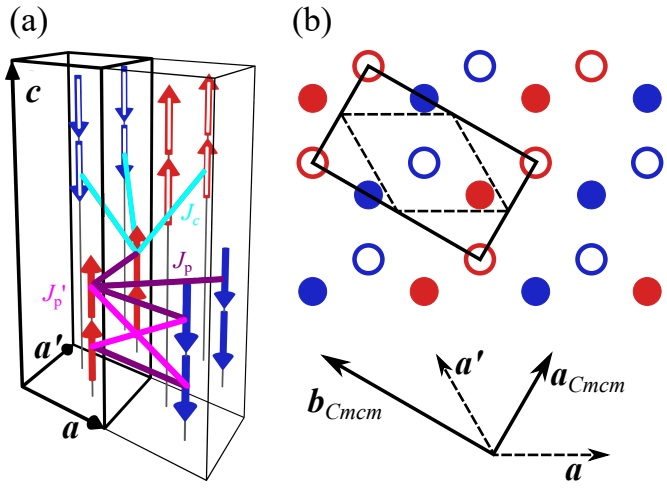

Figure 5.11 Magnetic structure of $Cs_3Fe_2Br_9$ in phase P1 measured and refined at zero-field and 2.5 K. The axes $\boldsymbol{a}$, $\boldsymbol{a}$', $\boldsymbol{c}$ belong to the crystallographic hexagonal unit cell. The magnetic unit cell is doubled along $\boldsymbol{a}$ for P1. The NN inter-dimer couplings J_p, J'_p, and J_c are shown. (b) gives the projection to the *ab* plane. Dashed lines mark the crystallographic unit cell and solid lines the magnetic unit cell. Open and filled arrows (a) and circles (b) assign different layers of bi-octahedra. Red marks up-spins and blue down-spins.

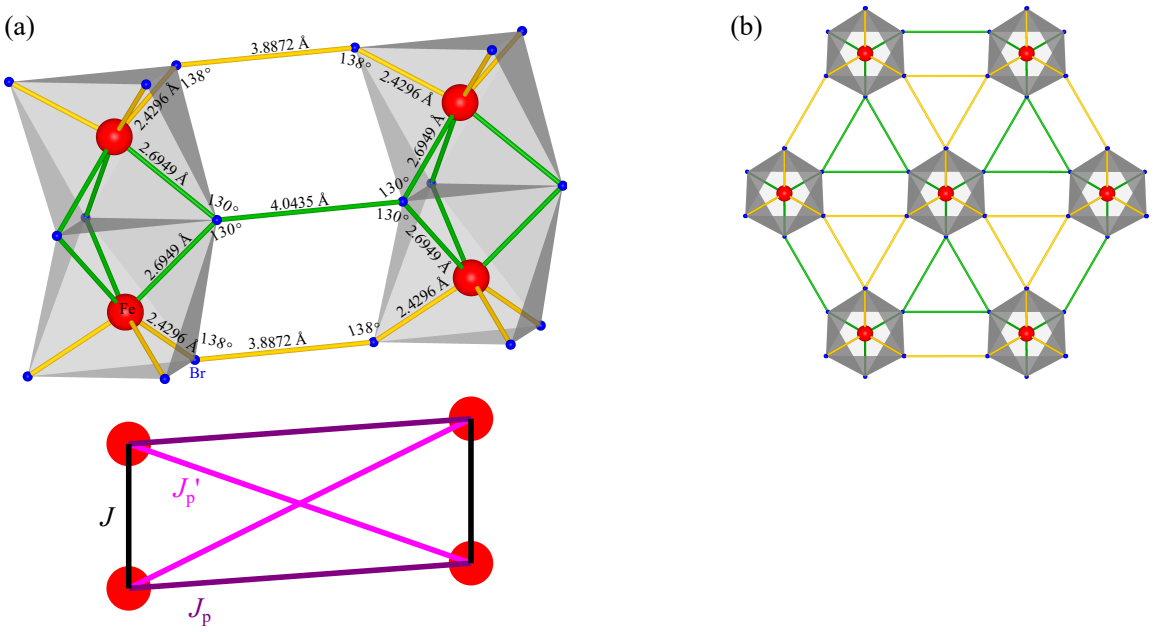

Figure 5.12 Magnetic exchange paths for a Fe-Fe coupling inside a triangular layer. Orange and green depict exchange paths of different lengths and different angles between the individual bonds. The paths are combined to the coupling constants J_p and J'_p. J_p couples iron sites with the same z component of neighboring bi-octahedra, J'_p with different z components. (a) shows a side-view, (b) a view along $\boldsymbol{c}$.

The in-plane environment hosts six neighboring bi-octahedra. Figure 5.12 shows the exchange paths between neighboring bi-octahedra. Each iron of a bi-octahedron couples to both irons of a neighboring bi-octahedron. Due to the fact that the iron atoms are not centered in the octahedra but have an increased Fe-Fe distance, there are different paths to the neighboring bi-octahedra. To the neighboring Fe with the same z component, there are two paths via the outer and the inner Br ions, as is shown in Fig. 5.12 by orange and green lines, respectively. In addition, the upper and the lower iron ions of neighboring bi-octahedra are also coupled by a single exchange path via the inner Br ions. The green path has the bond lengths (Fe-Br-Br-Fe 2.6949 Å – 4.0435 Å – 2.6949 Å) with angles of ~130°. The orange exchange path is shorter (2.4296 Å – 3.8872 Å – 2.4296 Å) with angles of ~138°. For the out-of-plane coupling, there are two equivalent exchange paths of Fe-Br-Br-Fe shown in cyan in Fig. 5.13 with distances 2.4296 Å – 3.9509 Å – 2.4296 Å and angles of ~131.2°. In the following, the Fe-Fe exchange of the same z component (the sum of an orange and a green path) is called J_p and the out-of-plane coupling (the sum of two cyan paths) is called J_c. This nomenclature is equal to the one of Ref. [22] used for $Cs_3Cr_2(Cl,Br)_9$. The exchange of moments with different z components on neighboring

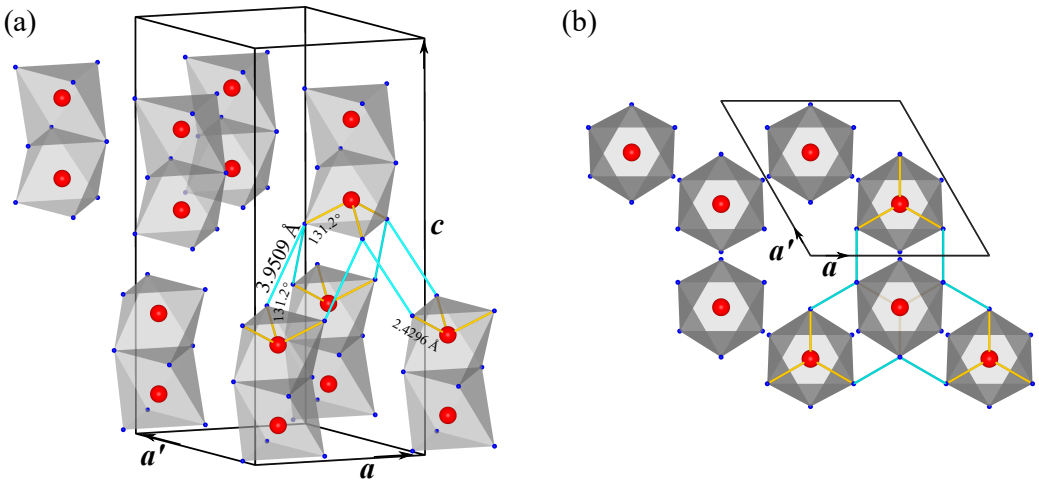

Figure 5.13 Magnetic exchange paths between different triangular layers. Each bi-octahedron has three nearest neighbors in the next layer. The exchange between two iron sites is mediated via a Fe-Br-Br-Fe path of 2.4296 Å-3.9509 Å-2.4296 Å and angles of 131.2°. (a) shows a side-view, (b) a view along $\boldsymbol{c}$.

octahedra (one green path), which was not used in the description of $Cs_3Cr_2(Cl,Br)_9$, is called J'_p. A positive J_i means antiferromagnetic coupling and reduces the energy by a term $-J_i$.

The magnetic unit cell consists of two bi-octahedra per layer. Figure 5.14(a) shows the in-plane couplings J_p and J'_p again. These are merged into a net inter-dimer in-plane coupling $J_{inter} = 2J_p + 2J'_p$ to simplify the couplings in the panels (b) and (c). Panel (b) compares a single layer of the obtained ground state with a state of antiparallel dimers. The energy of both states is calculated via the sum of all couplings.

The comparison of both energies yields the constraint $2J'_p$ is larger than the intra-dimer coupling J. If several layers are included, the additional energy term of the J_c is equal for both states in (b) because ⅔ of these couplings are fulfilled, while ⅓ is violated. Figure 5.14(c) shows another possible state with the same antiparallel dimer on every site. This gains the maximum coupling energy J_c. Comparing the total energy to the measured ground state yields the constraint $J < 4J_p - 2J'_p - J_c$. If we further assume all couplings to be antiferromagnetic $J_i > 0$, it follows $J_c < 4J_p - 2J'_p$.

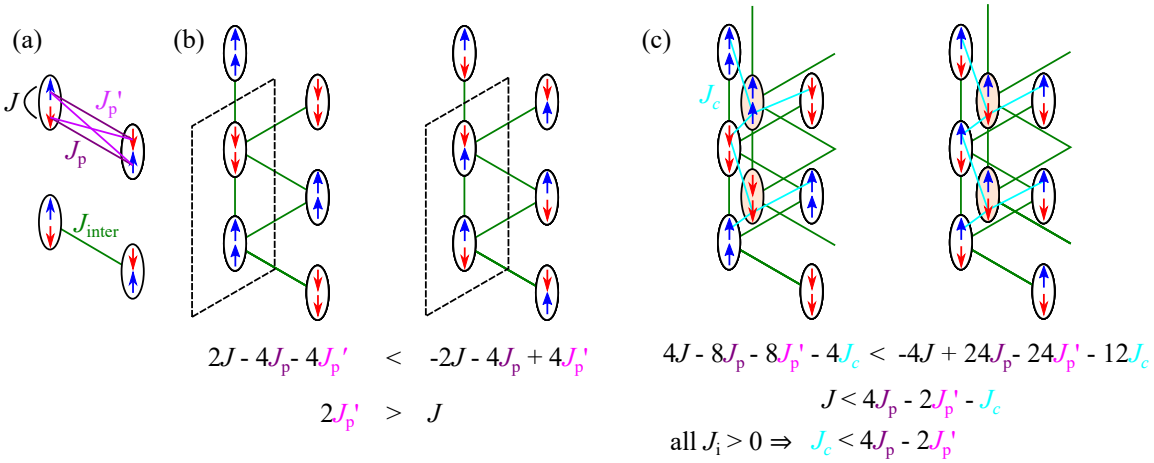

Figure 5.14 Energetical comparison of the obtained magnetic structure with different spin arrangements. (a) defines the coupling constants J_i, see text also. (b) compares the measured ground state to an antiparallel dimer state with alternating chains of up-dw and dw-up dimers. The coupling J_c is neglected because it is equal for both states. The unit cell contains two dimers and six coupling pairs have to be taken into account. (c) compares the measured ground state to the antiparallel dimer state with the same dimer on every site. The unit cell contains four dimers, six coupling pairs per layer and twelve interlayer couplings.

Overall, these considerations show that the dominant interactions are J_p and J'_p, which consequently overcompensates the violated antiferromagnetic intra-dimer coupling J.

In the following, the description of the magnetic system shall be simplified and, therefore, the coupling constants are redefined. The bi-octahedra are treated as a unit with $S = 5$ and, consequently, there is no longer any intra-dimer coupling J. The in-plane nearest-neighbor coupling J_ip results from the sum of all possible paths between two neighboring bi-octahedra, which is four times the green path and twice the orange path or twice J_p and twice J'_p, see Fig. 5.12,

$$J_\mathrm{ip} \cdot 5^2 = (4 \cdot J + 2 \cdot J) \cdot {}^5\!/_2{}^2 = (2 \cdot J_\mathrm{p} + 2 \cdot J'_\mathrm{p}) \cdot {}^5\!/_2{}^2 \quad .$$

The out-of-plane coupling J_op similarly results from the possible exchange paths

$$J_\mathrm{op} \cdot 5^2 = 2 \cdot J \cdot {}^5\!/_2{}^2 = J_c \cdot {}^5\!/_2{}^2 \quad .$$

The resulting system is equivalent to the hexagonal closed packed lattice. Thus, the models described in Chapter 2.2.4 can be used as a comparison. The validity of an Ising anisotropy will be discussed below.

Kudo and Katsura calculated nine different ordered phases for the J_1-J_2-model on the hcp lattice in a magnetic field, see Fig. 2.6(b) on page 24. Note, that they assume the same coupling J_1 for in-plane and out-of-plane nearest neighbors. In our system, this translates to $J_{op} = J_{ip} = J_1$. Phases V, VII, and IX are antiferromagnetic ground states. Furthermore, the authors proposed the possible magnetic orderings for each phase. The configuration IX-1, see Fig. 5.15, agrees with the experimentally observed ground state of $Cs_3Fe_2Br_9$. Coupling J_1 is antiferromagnetic and J_2 is ferromagnetic. In $Cs_3Fe_2Br_9$, the exchange paths for the next-nearest-neighbor coupling Fe-Fe_{NNN} passes three Br^- ions. The model predicts a magnetic-field induced phase transition to phase VIII with a fractional magnetization of $\frac{1}{2}M_{sat}$ at $H = 2|J_1|$. Saturation is reached at $H = 6|J_1|$. Below, after the magnetic-field response of $Cs_3Fe_2Br_9$ is presented, the coupling constants will be discussed again.

In the model of Matsubara and Inawashiro [58] with a quasi-two-dimensional approach with larger in-plane than out-of-plane coupling $J_1 \gg J_0$, the in-plane NNN interaction J_2 determines the actual ground state. The in-plane magnetic structure of $Cs_3Fe_2Br_9$ agrees to the state with antiferromagnetic J_2, see Fig. 2.6(a) on page 24.

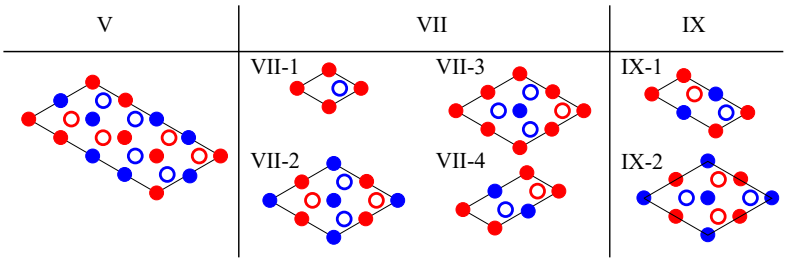

Figure 5.15 Magnetic structures of the J_1-J_2 Ising model on the hcp lattice with an antiferromagnetic order. The structures correspond to the antiferromagnetic states of the phase diagram shown in Fig. 2.6 on page 24 according to Ref. [59]. Red circles denote up-spins and blue circles down-spins. Open and filled circles assign different layers.

5.5 Magnetic-field response

The influence of a magnetic field on $Cs_3Fe_2Br_9$ applied along the high-symmetry directions $\|\boldsymbol{c}$ and $\perp\boldsymbol{c}$ is studied by thermal-expansion and magnetostriction measurements in static fields up to 38 T and by pulsed-field magnetization measurements up to 56 T. First, the behavior of $Cs_3Fe_2Br_9$ with $\boldsymbol{H} \perp \boldsymbol{c}$ is presented, $\boldsymbol{H} \| \boldsymbol{c}$ afterwards.

5.5.1 Magnetic field $\perp$ *c*

The in-plane field orientation is perpendicular to the collinear moments. Thus, in this orientation a continuous canting of the moments is expected. The magnetic-field dependence of T_{N1} and T_{N2} up to 30 T is investigated with thermal expansion an magnetostriction measurements, see Fig. 5.16. The thermal expansion in panel (a) qualitatively reproduces both transitions in zero field. Differences in the ordering temperature can be assigned to experimental issues as described in Chapter 3.4. The difference in the relative length change at the transitions might originate from a different detwinning compared to the HelioxVL measurements. In a magnetic field, the transition temperatures show a different field dependence. While T_{N1} reduces to 10.7 K in 30 T, T_{N2} decreases much stronger to 7.2 K. Comparing data with increasing and decreasing temperature does not show any hysteresis effects. The field-dependent length change in panel (b) shows quadratic behavior for

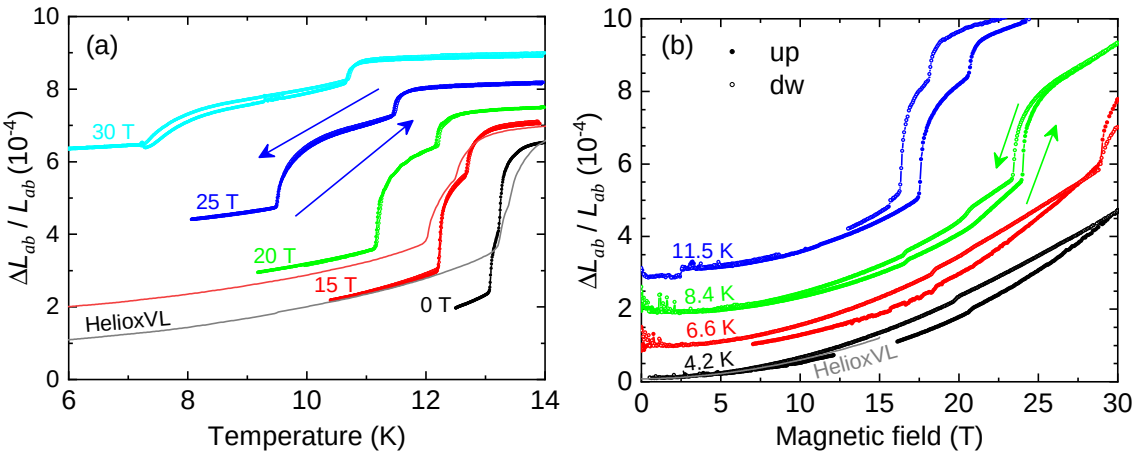

Figure 5.16 Thermal expansion and magnetostriction of $Cs_3Fe_2Br_9$ with $\boldsymbol{H} \perp \boldsymbol{c}$ in fields up to 30 T. (a) shows the relative length change $\Delta L_{ab}/L_{ab}(T)$ and (b) the magnetostriction data. Different fields are shifted according to the magnetostriction. Different temperatures are shifted by $1 \cdot 10^{-4}$. Increasing and decreasing temperature and magnetic field are indicated via • and ∘, respectively. To compare the quality of the measurements, selected HelioxVL data are presented.

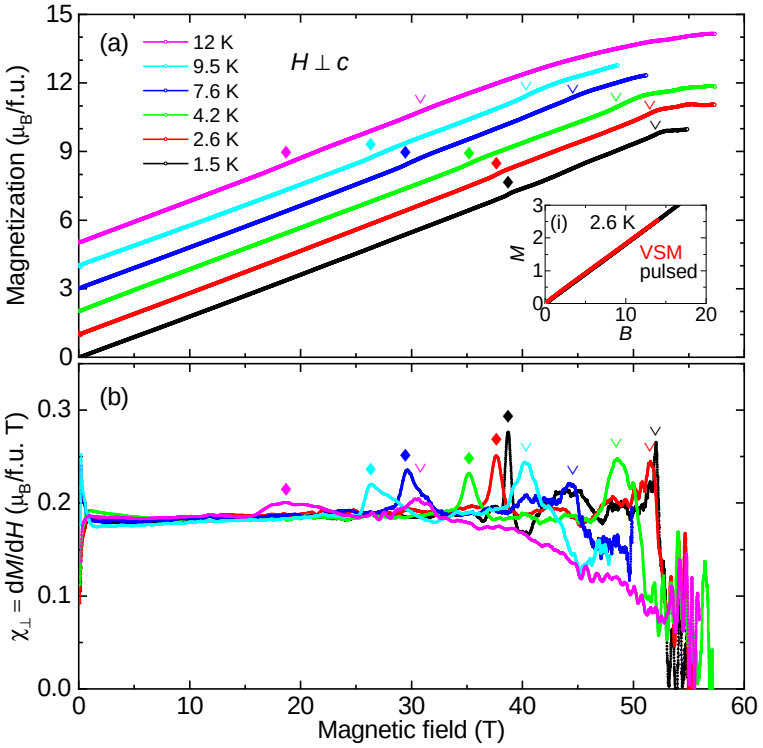

Figure 5.17 Pulsed-field magnetization of $Cs_3Fe_2Br_9$ with $\boldsymbol{H} \perp \boldsymbol{c}$ up to 57 T. (a) shows $M(H)$ for various temperatures measured on increasing magnetic field. Different temperatures are shifted by 1 μ_B/f.u. Absolute values stem from scaling the background-corrected data onto VSM data (i). (b) shows the derivative $\chi_\perp = \mathrm{d}M/\mathrm{d}H$ calculated numerically from the raw signal and smoothed over 50 data points. The transition from P1 to P2 is marked with ◆, the transition to the paramagnetic state with ∨ in both panels.

4.2 K and agrees to the magnetostriction measured in the HelioxVL setup. The quadratic behavior corresponds to a linear magnetization of canting moments. For 6.6 K, a discontinuous phase transition occurs. The critical field reduces with increasing temperature and at 11.5 K, two transitions are observed. The deviations between increasing and decreasing magnetic field, that are not expected from the thermal-expansion data, are not related to the sample, but induced by an instability of the sample temperature. During the measurement, the sample temperature was not controlled actively and the resulting issues are discussed in Chapter 3.4 on page 37.

The magnetization of $Cs_3Fe_2Br_9$ was investigated with a pick-up-coil magnetometer inside a pulsed-field magnet as described in Chapter 3.3. For each measurement, the sample temperature was stabilized to the desired value and then the field pulse starts. Only data on increasing magnetic field are presented. Figure 5.17 shows the magnetization for this field configuration. In order to get an absolute magnetization, the background-corrected data have been scaled onto magnetization data measured in the VSM (PPMS), see inset (i). $M(H)$ is almost linear up to the saturation magnetization of $\sim 10\,\mu_B$/f.u., which is reached for 52 T at 1.5 K. M_{sat} equals the expected value for two Fe^{3+} moments with $S = 5/2$ per formula unit. Two transitions can be identified in the susceptibility $\chi_\perp$ that shows two peaks, both shifting towards smaller magnetic fields with increasing temperature, see Fig. 5.17(b).

The first peak marks the transition to the incommensurate phase and the high-field peak marks the transition to the paramagnetic state. Note, that the given temperatures are only well defined at the beginning of the field pulse. Due to the magnetocaloric effect, a change of magnetic entropy results in a change of the actual sample temperature during the field pulse. An estimation for the upper limit of these changes is shown in the experimental Chapter 3.5. The temperature can be reduced by ~2 K from 0 T to 50 T.

The phase diagram for the in-plane orientation of the magnetic field, see Fig. 5.18, is constructed from anomalies in thermal expansion measured in the HelioxVL dilatometer, the thermal expansion and magnetostriction measured in the 30 T Bitter magnet in Nijmegen and the pulsed-field magnetization data. For this magnetic field orientation, both zero-field transitions T_{N1} and T_{N2} show a negative field dependence. T_{N2} reduces much stronger than T_{N1}.

The anomalies from pulsed-field magnetization measurements (open triangles) at elevated temperatures are systematically off compared to the thermal-expansion anomalies. These data points were corrected according to a magnetocaloric effect. With this correction, the anomalies match the thermal-expansion values. At low temperatures, phase P1 is stable up to ~39 T. Through an almost first-order transition the incommensurate phase P2 is entered. The saturated paramagnetic state is reached at 52 T.

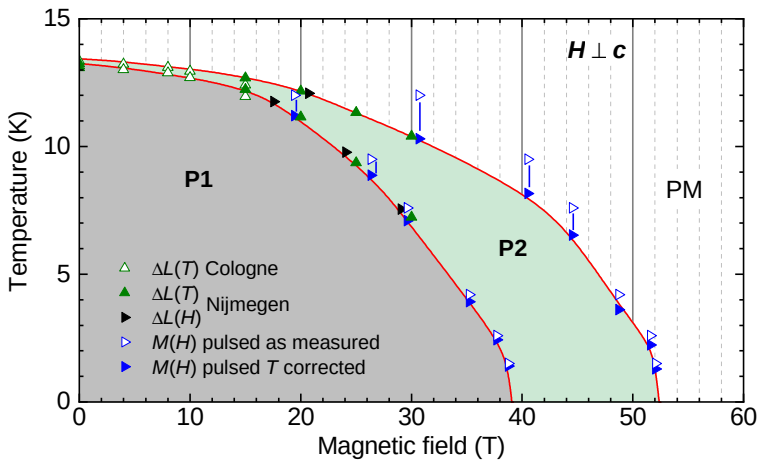

Figure 5.18 Phase diagram of $Cs_3Fe_2Br_9$ with $\boldsymbol{H} \perp \boldsymbol{c}$. Phase boundaries base on anomalies in thermal-expansion, magnetostriction, and magnetization measurements. For the anomalies of the pulsed-field magnetization measurements, the critical temperature T_C was corrected according to the magnetocaloric effect results ▷—▶, see Chapter 3.5.

5.5.2 Magnetic field ∥ *c*

Magnetic fields up to 17 T

Figure 5.19 shows the thermal expansion for the magnetic field parallel to ***c*** measured with the HelioxVL dilatometer inside the Cryogenic magnet dewar in fields up to 17 T. The magnetoelasticity of the antiferromagnetic ordering transition in zero field was already discussed, showing two first-order transitions with sharp contraction in the ordered phases at T_{N1} and T_{N2}. In magnetic fields up to 8 T, both transitions can be identified with different field dependencies. With increasing field, the contraction at T_{N1} systematically reduces and above 7 T, the magnetically ordered phase is elongated. In contrast, the contraction at T_{N2} increases in the same manner. As a consequence, the overall length change from the paramagnetic phase to temperatures below T_{N2} hardly changes up to 8 T. The transition temperatures decrease with increasing fields in this field range. For the intermediate fields of 10 T and 11 T, $\Delta L_c/L_c$ shows multiple phase transitions, but the net length changes are found to be small compared to all other transitions. Above 10 T, T_{N1} splits into two transitions, both showing a small elongation on cooling, see inset (i) in Fig. 5.19. Another phase transition with a small contraction occurs around 7 K. For 12 T, the ***c*** axis elongates tremendously at 3 K. Larger magnetic fields show even more transitions. Up to 16 T, $\Delta L_c/L_c$ shows negative thermal expansion or contraction on heating through four phase transitions. Above this field a shortened phase occurs between 8 K and 10 K. The temperature range grows up to the maximum field, where the phase is stable from 6 K to 11 K. In this phase, the length is reduced compared to the paramagnetic state and almost all other field-induced phases. Figure 5.19(b) shows the corresponding thermal-expansion coefficient $\alpha_c = \frac{1}{L_c}\frac{\partial \Delta L_c}{\partial T}$ for all magnetic fields. Phase transitions of the same character have been connected with lines to illustrate their temperature dependence.

To fully explore the low-field phase diagram, magnetostriction measurements were performed in the same setup, see Fig. 5.20. In the paramagnetic phase at 15 K, the lattice constant changes quadratically as a function of the magnetic field as expected for a paramagnet with a linear magnetization. The relative length change at the lowest temperature of 0.26 K shows multiple field-induced phase transitions, see also the magnetostriction coefficient λ_c in the inset (i). Inside each phase, λ_c is constant. The length change is essentially zero ($\lambda = 0$) up to 6 T, where a kink is found. The length increases linearly ($\lambda_1 > 0$). The transition is of second order. At 11 T, a discontinuous elongation of $2 \cdot 10^{-4}$ indicates a first-order transition to a phase with a linear elongation with λ_2 which is slightly smaller than λ_1. At 14.2 T, another first-order transition is found and above, the length is again constant. The discontinuous length changes are found to be extremely sharp. Such sharp

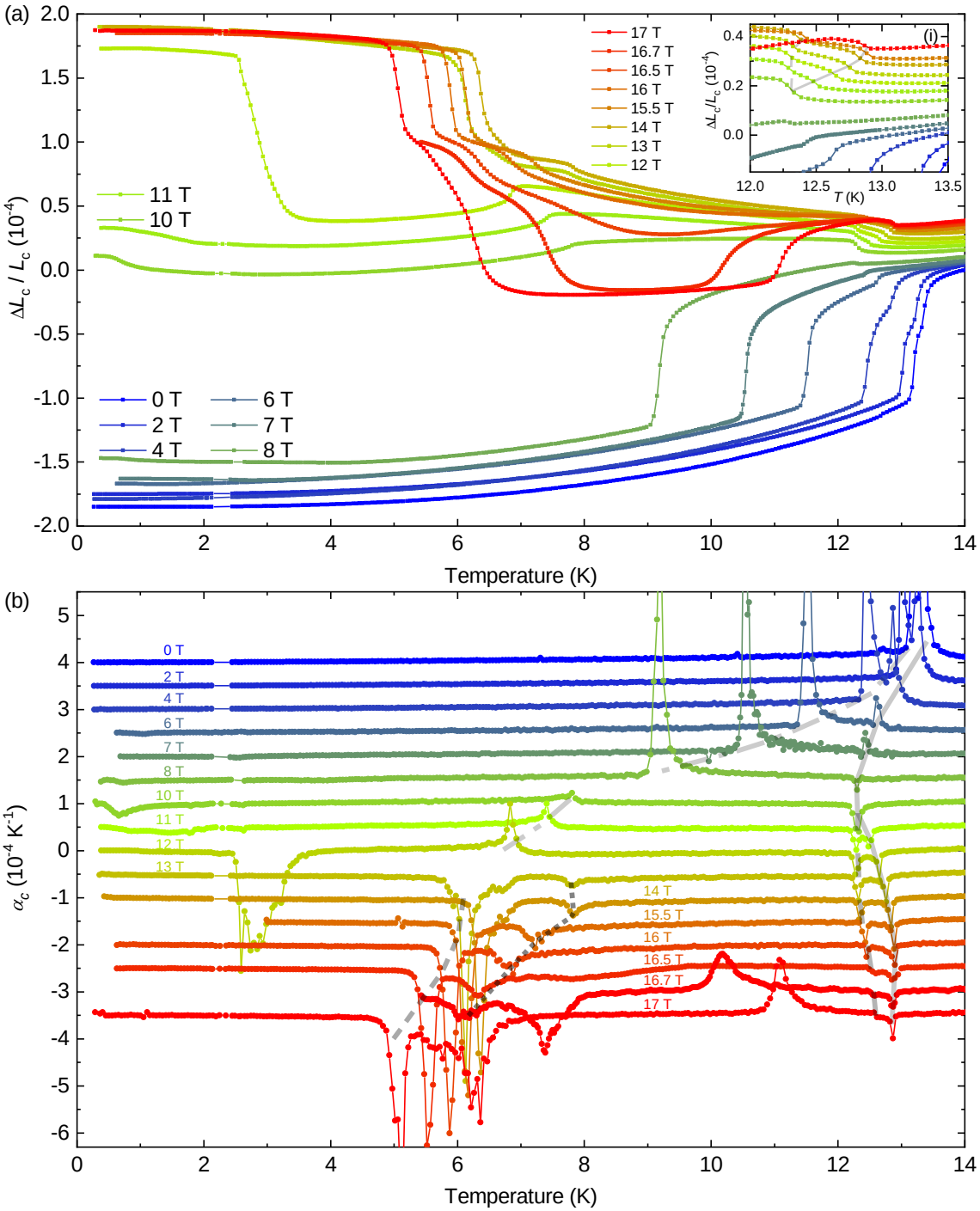

Figure 5.19 Thermal expansion of $Cs_3Fe_2Br_9$ with $\boldsymbol{H} \parallel \boldsymbol{c}$ in fields up to 17 T. (a) shows the relative length change $\Delta L_c/L_c$ measured on heating. The curves are shifted according to their magnetostriction at 14 K. Inset (i) shows an enlarged view on $T \approx T_N$ above 7 T. (b) shows the corresponding thermal-expansion coefficient α_c. Different fields are offset by $0.5{\cdot}10^{-4}\mathrm{K}^{-1}$. Different line styles connect anomalies from different phase transitions.

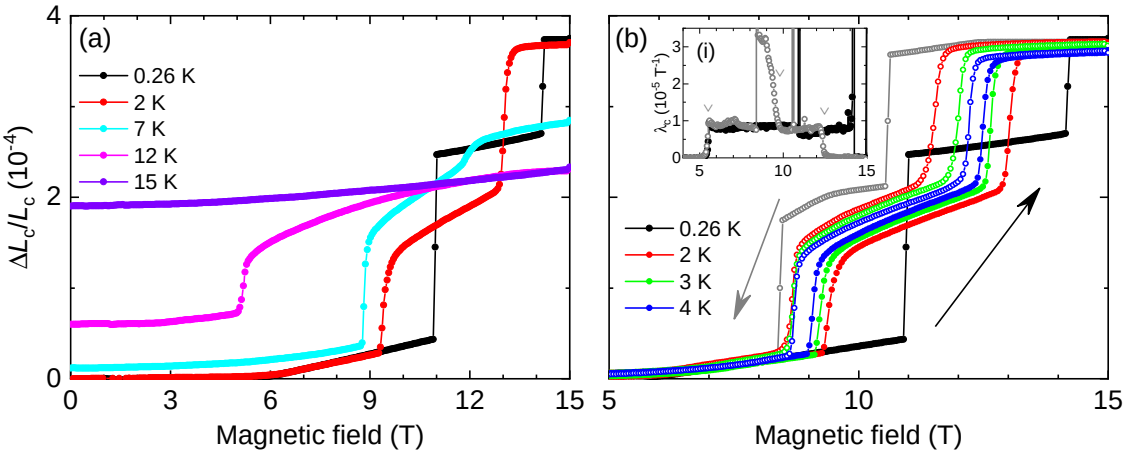

Figure 5.20 Magnetostriction of $Cs_3Fe_2Br_9$ with $\boldsymbol{H} \parallel \boldsymbol{c}$ up to 15 T. (a) shows the relative length change $\Delta L_c/L_c$ measured on increasing magnetic field. The curves are shifted according to their thermal expansion at 0 T. (b) shows measurements on increasing (filled symbols) and decreasing (open symbols) magnetic field for temperatures up to 4 K. Inset (i) shows the magnetostriction coefficient $\lambda_c = \frac{1}{L_c}\frac{\partial \Delta L_c}{\partial B}$ for 0.26 K.

field-induced length changes are untypical for solid-state transitions. The corresponding down-sweep shows a constant length above 12.3 T. There is a kink and below, λ_c becomes finite in between λ_1 and λ_2. A jump is found at 10.6 T followed by a regime with the same slope and a broadened kink at ~9.7 T, where λ_c increases by a factor of 3. At 8.3 T, $\Delta L/L$ shows another jump. From there on, the down sweep is equal to the up sweep and shows a kink at 6 T from where the length is constant down to zero field.

Thus, the first-order transitions show a huge hysteresis. On increasing magnetic field the phase between both first-order transitions is stable between 11 T and 14.2 T. On decreasing magnetic field both critical fields are shifted drastically to 8.3 T and 10.6 T, respectively. Thus, the hysteresis effects of two field-induced transitions overlap and consequently, around 10.6 T and 0.26 K, each of the three different phases can be realized depending on the field-sweep protocol. The additional kinks in the down sweep might stem from a phase mixture, i.e., on decreasing field, the low-field phases begin to nucleate, grow, and at the jump the whole sample changes to the new phase. This happens for both first-order transitions, at 12.3 T and at 9.7 T. An increasing temperature reduces the hysteresis effects. At 2 K, the transitions are still sharp but the length changes are continuous and the hysteresis is reduced to ~1.2 T. Also the nucleation effects vanish.

Figure 5.21 shows the magnetization data obtained with the Faraday magnetometer[7]

[7]These data were obtained with the old technique without the gradient coil magnet by lifting the whole HelioxVL to put the sample in the natural gradient of the main coil.

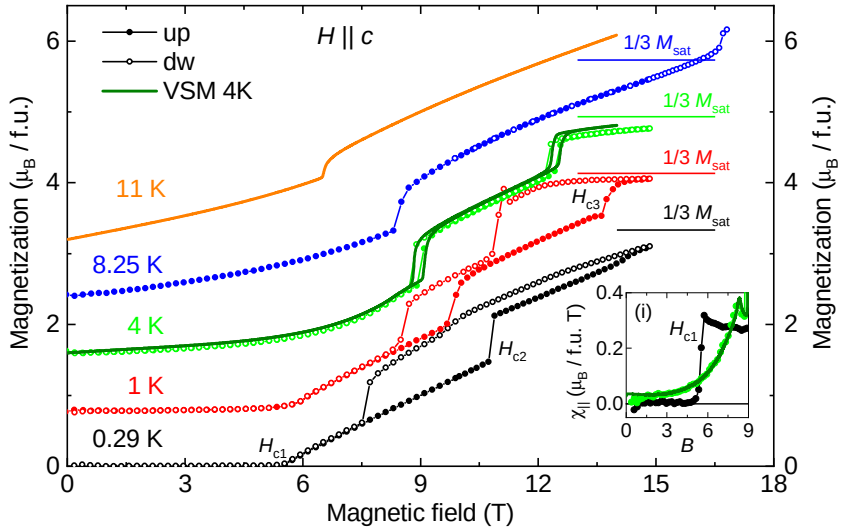

Figure 5.21 Magnetization of $Cs_3Fe_2Br_9$ with $\boldsymbol{H} \parallel \boldsymbol{c}$ up to 17 T. The data sets are shifted by 0.8 μ_B/f.u. Inset (i) shows the magnetic susceptibility $\chi_{\parallel} = dM/dH$ for 0.29 K and 4 K. Circles were measured in the Faraday magnetometer (HelioxVL), lines in the VSM (PPMS).

down to 0.29 K and magnetic fields up to 17 T and the VSM (PPMS). Only selected measurements are presented and further data is shown in the Appendix A.2. The magnetization at low temperatures basically reproduces the behavior of the magnetostriction. $M(H)$ is essentially zero up to H_{c1}. There, the susceptibility $\chi_{\parallel}$ becomes finite (~0.3 μ_B/f.u.T), see Fig. 5.21(i). At $H_{c2} = 10.8$ T, the magnetization increases discontinuously. For increasing magnetic fields, the magnetization again grows linearly. In this regime, $M(H)$ extrapolates towards zero indicating a spin-flop phase. At ~14 T, the slope increases slightly, which is a precursor of the first-order transition that was observed in the magnetostriction. At the maximum field of 15 T, the magnetization is approximately 3 μ_B/f.u. Note, that there are small deviations between the critical fields of the magnetostriction and the magnetization measurements, which is most prominent at the lowest temperatures, where the second discontinuous transition is not yet reached for the magnetization at the maximum field of 14.8 T. On decreasing magnetic field, a slightly enhanced magnetization is found compared to the increasing data. This is related to the precursor effects of the first-order transition. As already discussed for the magnetostriction, the first-order transitions are highly hysteretic. For 1 K, the second discontinuous phase transition is reached and shows another step in magnetization. Above 13.5 T, the magnetization is almost constant slightly below 3.33 μ_B/f.u. = $\frac{1}{3}M_{sat}$. Thus, this phase shows a fractional magnetization state. The data on decreasing field show a kink at 12 T that is related to the precursor nucleation of the

phase below the following first-order transition analogous to the magnetostriction data. With increasing temperature, H_{c1} shifts towards higher magnetic fields and vanishes for 8.25 K and the hysteresis effects decrease. At 8.25 K, the magnetization exceeds the fractional magnetization of $1/3 M_{sat}$ in the first field-induced phase and does not show a plateau, but another discontinuous transition at 16.8 T. The high-field transitions will be discussed further based on high-field measurements in the following.

Magnetic fields from 17 T to 60 T

Using commercial dilatometers [80, 81], thermal expansion and magnetostriction were measured up to 30 T in a large bore Bitter magnet and up to 38 T in a small bore Bitter magnet at the HFML Nijmegen. Experimental limitations of the setups are discussed in Chapter 3.4.

Figure 5.22(a) shows the thermal expansion for magnetic fields from 19.5 T to 30 T. One first-order transition is found, which has a maximum T_C at 21 T of 13.1 K, that reduces with increasing field, while the length change increases. In magnetic fields between 17 T and 19 T, different ordered phases are found with a different behavior of the c lattice constant, see panel (b). The transition temperatures were identified from anomalies of the thermal-expansion coefficient α_c shown in Fig. 5.22(i). An intermediate phase occurs at 19 T, which has a larger c lattice constant than the paramagnetic phase. For smaller mag-

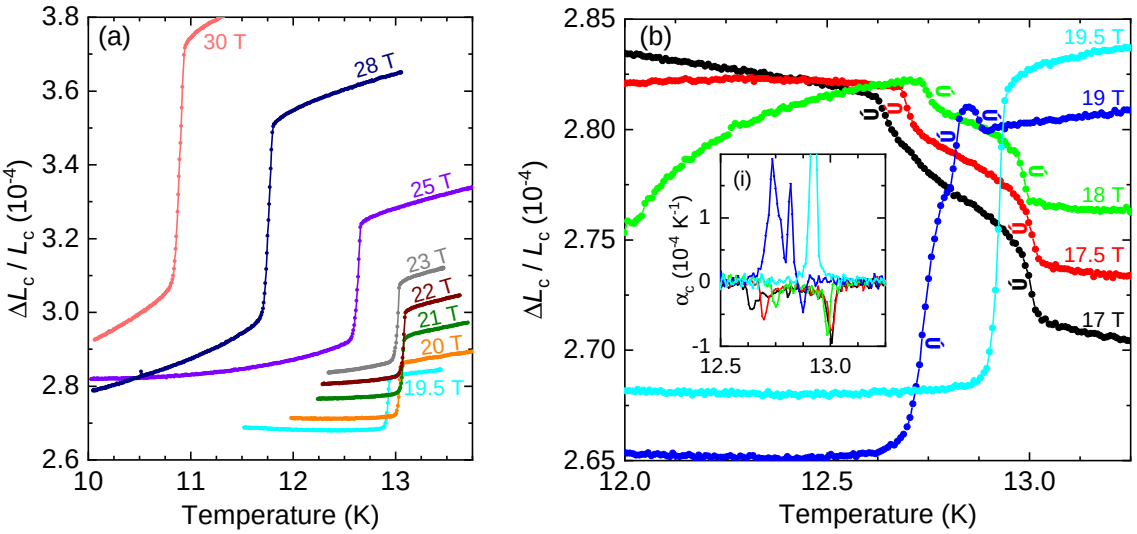

Figure 5.22 Thermal expansion of $Cs_3Fe_2Br_9$ with $\boldsymbol{H} \parallel \boldsymbol{c}$ in fields up to 30 T. (a) shows the relative length change $\Delta L_c/L_c$ for $\mu_0 H \geq 19.5$ T measured on increasing temperature. The curves are shifted according to their magnetostriction at 12 K. (b) presents data between 17 T and 19.5 T and inset (i) shows the thermal-expansion coefficient $\alpha_c = \frac{1}{L_c}\frac{\partial \Delta L_c}{\partial T}$.

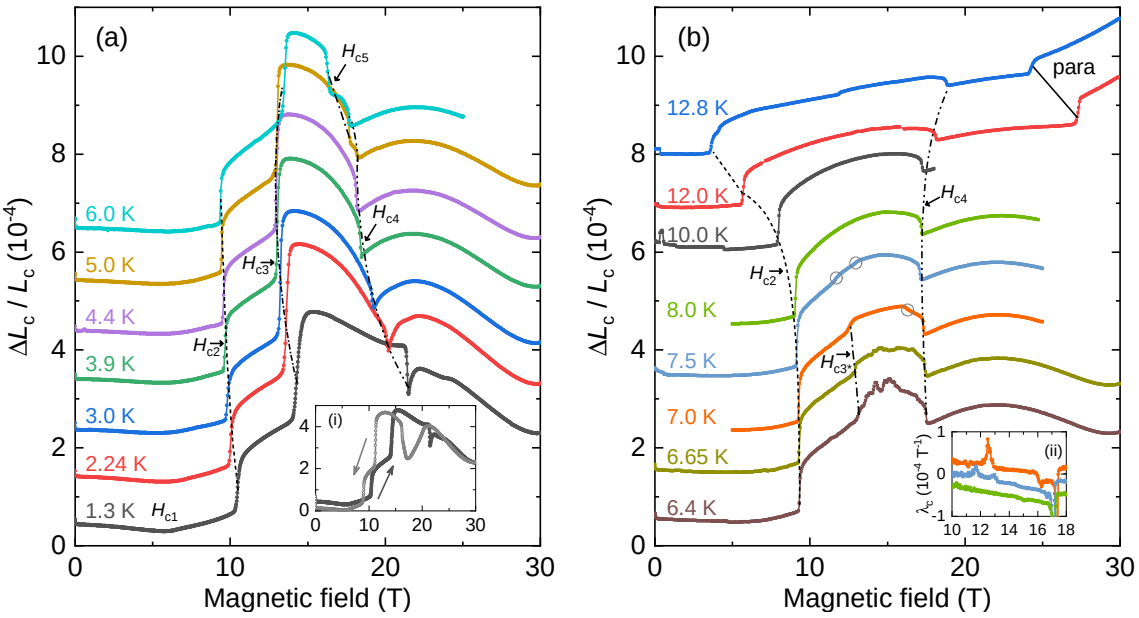

Figure 5.23 Magnetostriction of $Cs_3Fe_2Br_9$ with $\boldsymbol{H} \parallel \boldsymbol{c}$ in fields up to 30 T. (a) shows the relative length change $\Delta L_c/L_c$ measured on increasing magnetic field for temperatures up to 6 K. Inset (i) compares the magnetostriction at 1.3 K for increasing and decreasing magnetic field. Temperatures above 6 K are presented in (b). Different temperatures are shifted by $1{\cdot}10^{-4}$. Critical magnetic fields between the same phases are connected with lines. Tiny transitions are marked with ∘. Inset (ii) shows the magnetostriction coefficient λ_c for 7 K to 8 K offset by $0.3{\cdot}10^{-4}$ T^{-1}.

netic fields, the low-temperature phase is elongated compared to the paramagnetic phase. $Cs_3Fe_2Br_9$ shows two phase transitions where L_c contracts on increasing temperature. The temperature interval of the intermediate phase increases with decreasing magnetic field.

The magnetostriction measurements above 15 T are presented in Fig. 5.23. The field-induced transitions up to 17 T that were presented in Fig. 5.20, are well reproduced in these data. For 1.3 K, $\Delta L_c/L_c$ shows a peculiar anomaly around $H_{c4} = 21.4$ T. The sample shows a discontinuous contraction followed by an elongation, a maximum length at 22.3 T, and finally decreases for larger magnetic fields. Figure 5.23(i) compares the up and down sweep, which shows hysteresis effects. For higher temperatures, the first-order transition and also the maximum shift to smaller magnetic fields. At 5 K, H_{c4} splits into two first-order transitions, which both show a contraction of ΔL_c on increasing field. At 6 K, H_{c3} and H_{c5} shift closer together. For 6.4 K, see Fig. 5.23(b), the elongation at 14 T is much smaller than at the same field for 6 K. This indicates that this is a different transition and thus called H_{c3*}. The transition at H_{c5} is absent. Further small transitions are marked by ∘ in ΔL that are identified via the magnetostriction coefficient λ_c shown in inset (ii).

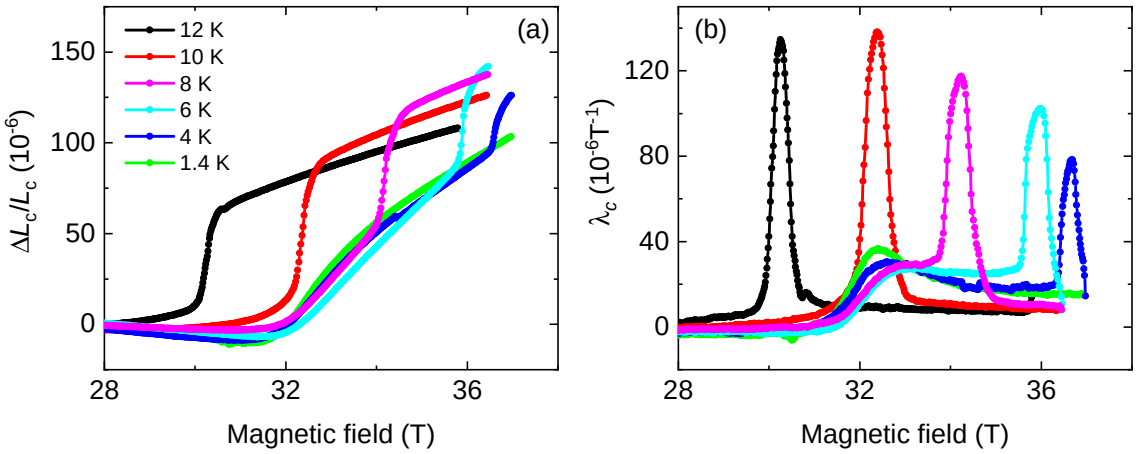

Figure 5.24 Magnetostriction of $Cs_3Fe_2Br_9$ with $\boldsymbol{H} \parallel \boldsymbol{c}$ in fields above 30 T. (a) shows the relative length change $\Delta L_c/L_c$ measured on increasing magnetic field for temperatures up to 12 K. (b) presents the corresponding magnetostriction coefficient λ_c.

Further magnetostriction measurements were performed with the small dilatometer up to 38 T and are presented in Fig. 5.24. For 12 K and 10 K, $\Delta L_c/L_c$ shows a discontinuous elongation to the paramagnetic phase. In the high-field paramagnetic phase, the lattice shows an almost linear magnetostriction. The critical field of the first-order transition increases with decreasing temperature. For lower temperatures, an additional phase transition occurs. While the sample shrinks below 31.5 T, it elongates above that field. The magnetostriction coefficient λ_c presented in Fig. 5.24(b) shows a broadened step at the second-order phase transition and a peak at the first-order transition. For 1.4 K, it is no longer possible to reach the transition to the paramagnetic phase and thus $Cs_3Fe_2Br_9$ is still in the ordered phase at the maximum field.

Figure 5.25(a) shows the magnetization with $\boldsymbol{H} \parallel \boldsymbol{c}$ obtained from pulsed field measurements. The minimal temperature curve at 1.5 K shows the beforehand discussed transitions, namely the second-order kink (H_{c1}) and two first-order discontinuities leading to the $\frac{1}{3}M_{\mathrm{sat}}$ plateau. At $H_{c4} = 20$ T, another jump occurs, followed by another plateau-like magnetization. The magnetization is close to $\frac{1}{2}M_{\mathrm{sat}}$ and crosses this value smoothly on increasing magnetic field. The susceptibility $\chi_{\parallel} = \mathrm{d}M/\mathrm{d}H$, see Fig. 5.25(b), is significantly reduced up to 30 T. From this value to 45 T, $\chi_{\parallel}$ shows a broad maximum with an additional peak at 39 T. Saturation close to the expected value of 10 μ_B/f.u. is not reached through a sharp transition but rather continuously. This prevents an unambiguous assignment of the saturation field. The saturation field is approximated via the crossing point between two linear regimes and yields ~43 T. With increasing temperature, larger magnetic fields are required to reach saturation. The sharp peak as an onset of the broad maximum of $\chi_{\parallel}$

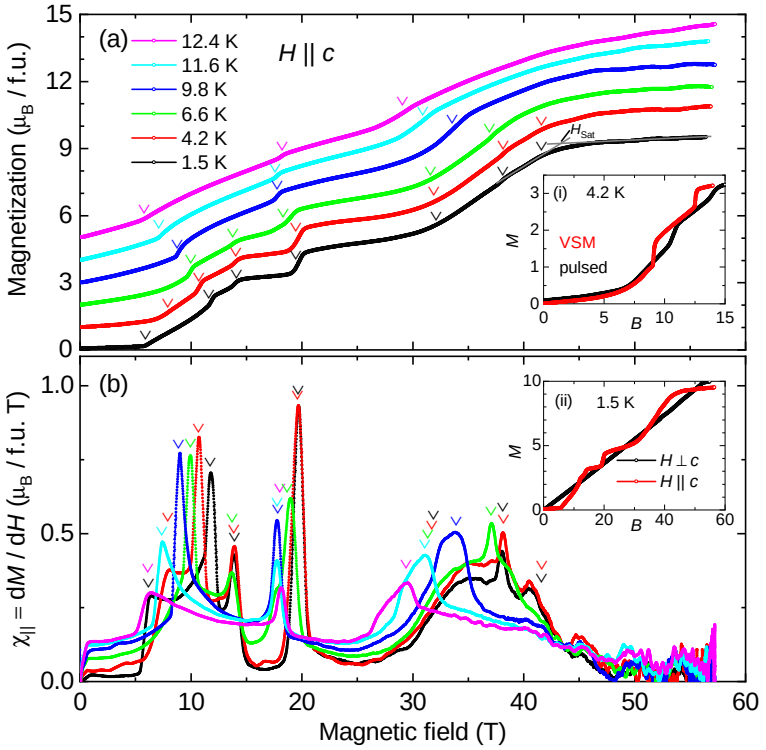

Figure 5.25 Pulsed-field magnetization of $Cs_3Fe_2Br_9$ with $\boldsymbol{H} \parallel \boldsymbol{c}$ up to 57 T. (a) shows $M(H)$ for various temperatures measured on increasing magnetic field. Different temperatures are shifted by 1 μ_B/f.u. Absolute values stem from scaling the background-corrected data onto VSM data (i). (b) shows the derivative $\chi_\parallel = \mathrm{d}M/\mathrm{d}H$ calculated numerically from the raw signal and smoothed over 50 data points. Transitions found via anomalies in the susceptibility are marked with $\vee$ in both panels. (ii) compares the magnetization at 1.5 K for $\boldsymbol{H} \parallel \boldsymbol{c}$ and $\boldsymbol{H} \perp \boldsymbol{c}$.

becomes less prominent and shifts to smaller fields, while the broad feature broadens further. The fractional $\frac{1}{2}M_{sat}$ plateau is present for all temperatures, while the $\frac{1}{3}M_{sat}$ plateau is only visible up to 6.6 K.

Based on the 1.5 K data, an idealized $T = 0$ susceptibility and the corresponding magnetization curve can be guessed, see Fig. 5.26. For the low-field regime, the susceptibility is zero. At the second-order transition, $\chi_\parallel$ becomes finite until the magnetization jumps followed by another interval with a finite, slightly reduced susceptibility. At 15 T, the susceptibility vanishes due to the stability of the $\frac{1}{3}M_{sat}$ niveau. The magnetization jumps to the $\frac{1}{2}M_{sat}$ plateau at 20 T, which is stable up to 32 T. Above this field the susceptibility becomes finite again and is larger than in the low-field regime. At 38 T, $M(H)$ jumps again and afterwards $\chi_\parallel$ is further enhanced. The saturation is reached at 43 T. Future numerical approaches should try to model this behavior using the proposed coupling constants including the lattice distortion presented above.

Figure 5.25(ii) compares both magnetic-field directions at 1.5 K. It is obvious, that the field along $\boldsymbol{c}$ induces multiple anomalies in the magnetization and the curves cross multiple times. As already noted, the saturation fields are $\mu_0 H_{sat}^{\parallel} = 43$ T and $\mu_0 H_{sat}^{\perp} = 52$ T. From

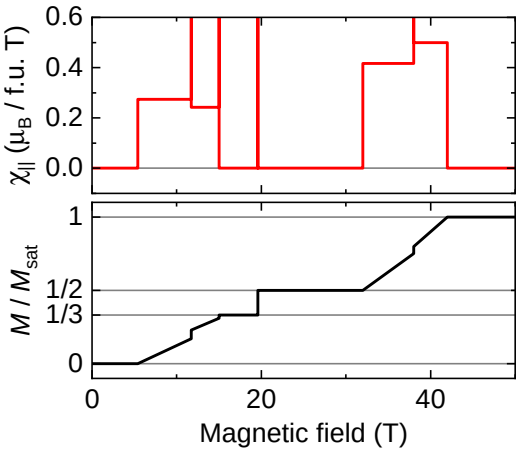

Figure 5.26 Idealized magnetization and susceptibility for $Cs_3Fe_2Br_9$ at $T = 0$ based on the experimental data for the lowest temperature.

these values, the exchange field $\mu_0 H_{ex}$ and the anisotropy field $\mu_0 H_{an}$ are deduced via

$$\mu_0 H_{ex} = \mu_0 \frac{H_{sat}^{\perp} + H_{sat}^{||}}{4} = 24.25\,\mathrm{T} \quad \text{and}$$
$$\mu_0 H_{an} = \mu_0 \frac{H_{sat}^{\perp} - H_{sat}^{||}}{2} = 4.5\,\mathrm{T} \quad .$$

The anisotropy $\delta = H_{an}/H_{ex} = 0.19$ is small compared to strongly anisotropic materials like $BaCo_2V_2O_8$ with $\delta = 9/15.5 = 0.58$ [201], but still large compared to other Fe^{3+} materials like $CuFeO_2$ which has almost the same saturation fields along and perpendicular to the easy axis and thus almost isotropic magnetism [171]. In $Cs_3Fe_2Br_9$, the geometric frustration and probably the bi-octahedron distortion play a crucial role.

Phase diagram

From the measurements presented above, the phase diagram for a magnetic field along the high-symmetry direction $\boldsymbol{H} \parallel \boldsymbol{c}$ is constructed by collecting all anomalies in a H-T diagram. The phase diagram presented in Fig. 5.27 shows in total ten ordered phases. Phase P1 is the antiferromagnetic ground state in zero magnetic field below T_{N2}. At the base temperature, seven magnetic-field induced phase transitions are found. At 5.8 T, a second-order phase transition yields P3. P4 is stable in the field range from 9 T to 13 T. The transition from P3 to P4 is of first order and becomes increasingly hysteretic for lower temperature. The transition from P4 to P5 at 13 T behaves similarly and is again of first order. Another first-order transition is found at 18 T to P6 that shows an even broader hysteresis. At 32 T, P7 is reached through a second-order phase transition. At very low temperatures, magnetization measurements indicate another first-order transition to P8 via a sharp peak

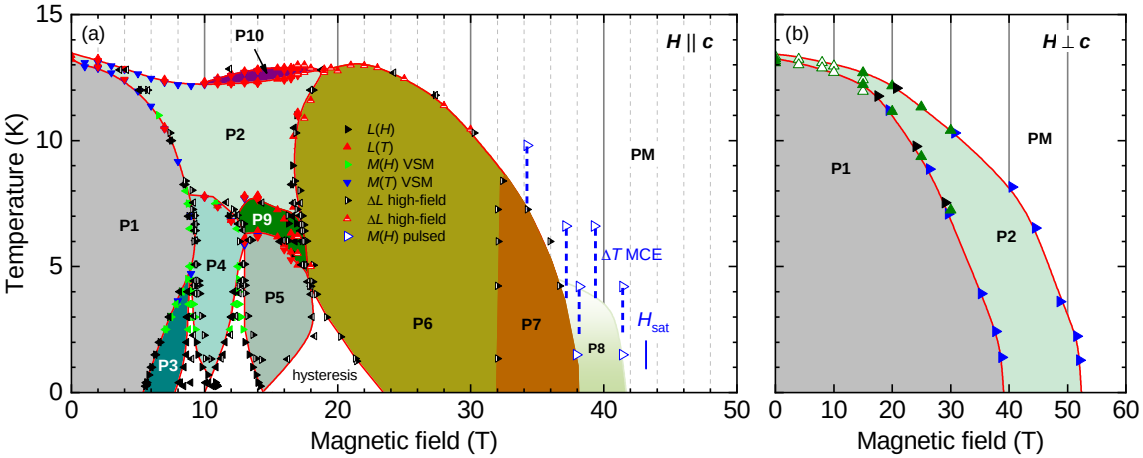

Figure 5.27 Phase diagrams of $Cs_3Fe_2Br_9$. (a) shows the phase diagram for $\boldsymbol{H} \parallel \boldsymbol{c}$. Phase boundaries base on anomalies in thermal-expansion, magnetostriction, and magnetization measurements. For the anomalies of the pulsed-field magnetization measurements, the critical temperature T_C is corrected according to the magnetocaloric effect results as indicated by dashed, blue lines, see Chapter 3.5.

in χ_c. The transition to the paramagnetic state at 40.8 T is a second-order transition and the magnetic saturation is reached at 43 T. At elevated temperatures, the identified anomalies from the pulsed field measurements do not match the phase boundaries found with the other techniques due to the magnetocaloric effect. The temperature is corrected according to the temperature changes of magnetocaloric-effect measurements, see Chapter 3.5, which yields almost perfect agreement.

Besides these field-induced phases, which are found at base temperature, three other phases are stabilized at elevated temperatures in an intermediate field range. P2 is the intermediate phase between T_{N1} and T_{N2} covering a small temperature interval of 0.2 K in zero field. With increasing magnetic field, this interval continuously grows to an interval of 12 K to 7.5 K at 10 T and stays essentially constant in larger magnetic fields. At ~18 T, a transition to P6 occurs. Phase P9 is present in a pocket of the phase diagram in the field range from 12 T to 18 T for temperatures between ~5 K and 8 K. Finally, P10 is the smallest phase, also a pocket. From 10 T to 19 T, this phase obeys the highest critical temperature and is only 1 K wide.

5.6 Dielectric constant and electric polarization

Competing interactions and geometric frustration in magnetic systems can lead to exotic properties such as spin liquid or noncollinear ordering. States with noncollinear magnetic structures can break inversion symmetry and yield polar structures. These can then show ferroelectric polarization that is strongly coupled to the magnetism. Textbook examples with such a multiferroic state are $TbMnO_3$ [202] and $MnWO_4$ [203, 204], where a cycloidal spin arrangement breaks inversion symmetry and induces a ferroelectric polarization via the inverse Dzyaloshinskii-Moriya interaction [205]. Inspired by this finding, multiple other materials were discovered showing multiferroic states based on magnetically ordered states. One example of those is $CuFeO_2$, which hosts a field-induced ferroelectric phase with an incommensurate spin arrangement on a triangular lattice, see Chapter 5.3. Because $Cs_3Fe_2Br_9$ also hosts a large variety of magnetically ordered phases with possibly magnetically induced ferroelectricity, dielectric measurements were performed to look for ferroelectricity.

Figure 5.28 shows the temperature dependence of the dielectric constants ϵ_c and ϵ_{ab}. A thin, plate-shaped sample of $Cs_3Fe_2Br_9$ with surface normals along and perpendicular to $\boldsymbol{c}$ was used as a dielectric material in a capacitor. From the measured capacitance C the dielectric constant is calculated via

$$\epsilon = C\frac{d}{A\epsilon_0} \quad ,$$

where d denotes the sample thickness. The dielectric constant shows anomalies that agree to the previously presented phase diagram. Most prominently, ϵ_{ab} increases when cooling to the ordered phase in small magnetic fields by about $\Delta\epsilon_{ab}/\epsilon_{ab} \approx 1 \cdot 10^{-4}$.

In larger magnetic fields, the anomalies become even smaller. Upon increasing magnetic field, ϵ_{ab} decreases. The absolute value of ~8.95 is reasonable for a dielectric material. The total changes are small ~0.05 %. The dielectric constant measured along $\boldsymbol{c}$ is slightly smaller (~7.885). In this direction, it increases with magnetic field. In the presented magnetic-field range from 9 T to 12.5 T, a sharp peak evolves that grows with magnetic field. $\Delta\epsilon_c$ is about a factor of 2 larger compared to the largest anomalies in the other direction. Compared to multiferroic materials like $LiCuVO_4$ ($\Delta\epsilon/\epsilon \approx 65\,\%$) [206] and $(NH_4)_2[FeCl_5(H_2O)]$ ($\approx 1\,\%$) [207] all these changes are extremely small.

Because ϵ_c shows a sharp peak, pyrocurrent measurements were performed to see whether this corresponds to a ferroelectric phase transition.

Figure 5.29 shows the electric polarization component P_c in the concerning temperature and field range. Panel (a) shows $P_c(E)$ hysteresis measurements at 12.5 T. At multiple

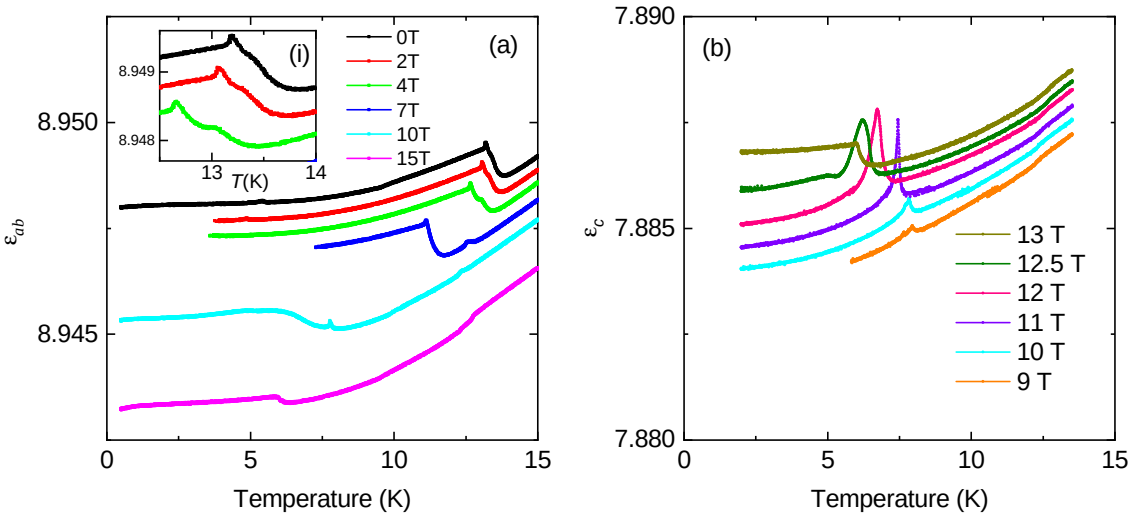

Figure 5.28 Temperature dependence of the dielectric constant of $Cs_3Fe_2Br_9$ for magnetic fields $\boldsymbol{H} \parallel \boldsymbol{c}$ measured on a thin, plate-shaped sample with face normals in the *ab*-plane (a) and along $\boldsymbol{c}$ (b). Inset (i) enlarges ϵ_{ab} close to the Néel temperature.

temperatures, the polarization is measured via the charge on the capacitor plates, while the voltage applied to the capacitor is varied in steps of 100 V. To achieve the presented hysteresis loops, a background signal $P_{\text{ind}} = \epsilon_0 \cdot \chi \cdot E$ with a constant $\chi = 8.194$ and a time-dependent drift was subtracted. The polarization at 6.8 K is essentially zero. At 6.4 K, the hysteresis shows the maximum remanent polarization of 0.45 μC m^{-2}. On decreasing temperature, P_c decreases again and below 5.8 K no hysteresis is detected. The hysteresis itself is not centered with respect to the electric field. The positive (0.5 kV mm^{-1}) and negative coercive field (−0.8 kV mm^{-1}) differ significantly but are constant in the ferroelectric temperature range. Panel (b) shows the temperature-dependent polarization integrated from pyrocurrent measurements of $Cs_3Fe_2Br_9$. The presented data were obtained after cooling the sample in an electric poling field of 0.4 kV mm^{-1} from the paramagnetic phase to 2 K, switching off the electric field, and integrating the pyrocurrent from the subsequent heating curve. In the field range from 9 T to 12.5 T, a polarization along $\boldsymbol{c}$ is found. The polarization increases with increasing magnetic field as expected for the magnetoelectric effect. But, this is not the linear magnetoelectric effect because the polarization does not increase linearly. The polarization can be inverted with the applied electric poling field, which makes it ferroelectric. The used electric poling field was not large enough to yield a fully polarized state since both polarization amplitudes are not the same. A positive voltage yields a larger polarization than the other direction. This finding agrees to the difference of the positive and negative coercive field. This effect can have several origins. Either an ex-

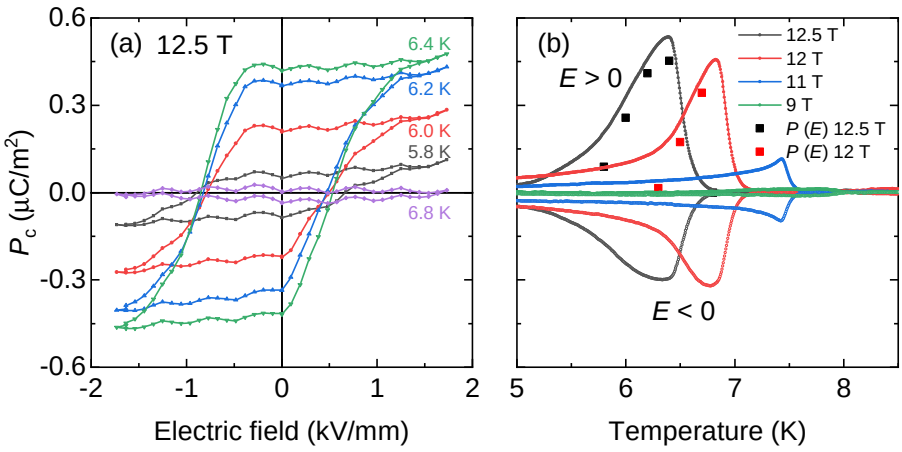

Figure 5.29 Polarization component P_c of $Cs_3Fe_2Br_9$ for $\boldsymbol{H} \parallel \boldsymbol{c}$. (a) shows $P_c(E)$ hysteresis measurement at 12.5 T for various temperatures. (b) presents the temperature-dependent polarization at multiple magnetic fields conducted from pyrocurrent (lines) and hysteresis measurements (points).

ternal bias voltage influenced the sample, or internal effects prefer the polarization to one direction. Interestingly, the polarization does not increase upon decreasing temperature as in usual ferroelectric materials. Approximately 1 K below the critical temperature $T_{\text{P2-P4}}$, and thus inside the phase P4, the polarization vanishes again. The polarization obtained from the $P_c(E)$ hysteresis measurements and the temperature-dependent data are in qualitative agreement. The polarization values differ slightly, but the general behavior of a peak of $P_c(T)$ is reproduced in this magnetic-field range. For higher or lower magnetic fields, no pyrocurrent signals were found.

Compared to other multiferroic materials, e.g., $TbMnO_4$ with 800 μC m^{-2}, $CuFeO_2$ with 300 μC m^{-2}, and $(NH_4)_2[FeCl_5(H_2O)]$ with 4 μC m^{-2}, $Cs_3Fe_2Br_9$ hosts a very small polarization (0.4 μC m^{-2}). Similar to $CuFeO_2$, in this material the first field-induced phase (P4), shows a ferroelectric polarization. Interestingly, this polarization does not increase with decreasing temperature, as an order parameter behaves typically, but vanishes again. Nonetheless, the electric poling works even after the sample was cooled to 2 K, where no polarization is left. Thus, the low-temperature state retains the polar axis. Otherwise a multi-domain state and consequently a reduced polarization should be found upon heating. In the case of $CuFeO_2$, the magnetic structure of the ferroelectric state was characterized as a proper screw that yields a polar point group and induces ferroelectricity via the *d-p* hybridization mechanism [182, 184, 185]. To explain the polarization of P4 in $Cs_3Fe_2Br_9$, more detailed structural knowledge is required.

5.7 Comparison to related models and materials

With the knowledge of the magnetic structure of P1 with parallel aligned moments in each bi-octahedron, the description of the magnetic system was simplified to a hcp lattice with $S = 5$ moments, see Chapter 5.4.3. If the interlayer coupling is small compared to the in-plane couplings, the system further simplifies to the triangular lattice. The size of the Ising anisotropy D has to be quantified, in order to support the applicability of the used models. In the following, the results are compared to related theoretical predictions and related materials

Stacked triangular lattice

First, the phase diagram of $Cs_3Fe_2Br_9$ is compared to the phase diagram of the layered triangular lattice with NN coupling $J_1 = 1$, NNN coupling $J_2 = 0.15$, interlayer coupling $J_\perp = -0.15$, and the anisotropy $D = 0.5$, obtained by Seabra *et al.* using Monte-Carlo simulations [57][8], see Fig. 5.30. Here, the similarities of the model phase diagram to the obtained phase diagram of $Cs_3Fe_2Br_9$ are described.

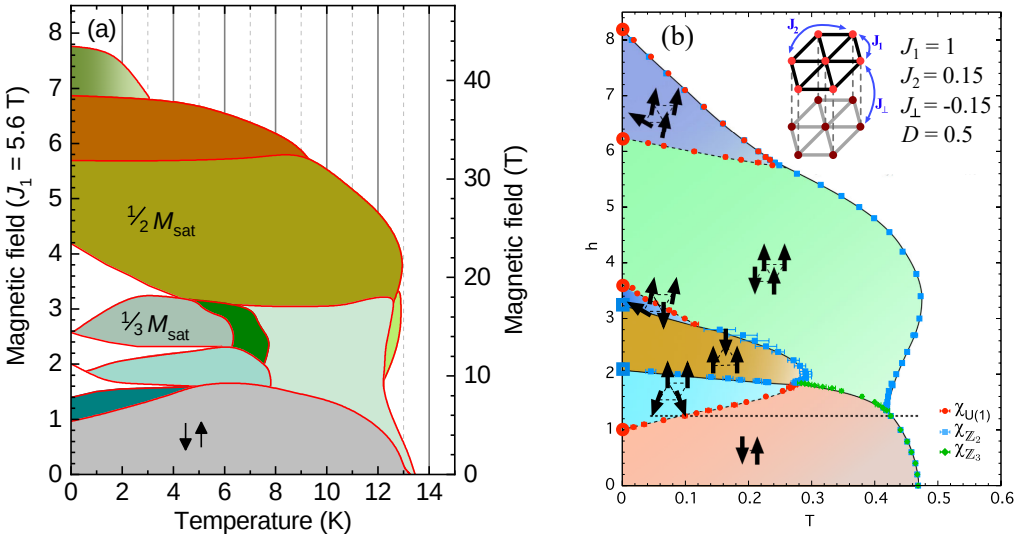

Figure 5.30 Comparison of the phase diagrams of $Cs_3Fe_2Br_9$ and the stacked triangular lattice with a field along the easy axis. In panel (a), the fractional magnetization states are labeled. The y axis is rescaled to the NN coupling constant J_1 as described in the text. (b) shows the phase diagram of the stacked triangular lattice with the given coupling constants taken from Ref. [57].

[8] In the stacked triangular lattice the stacking is so that each layer only has one nearest neighbor in the next layer. Thus, there is no frustration due to $J_\perp$.

The simulations predict that the system orders at $T = 0.47J_1$ into a stripe-like antiferromagnetic phase. At zero temperature, they predict a field-induced second-order phase transition, that is a Bose-Einstein condensation of magnons with finite momentum, into an incommensurate and noncollinear spin structure at a critical magnetic field $H_{c1} = J_1$. The critical field increases linearly with temperature. The model system shows the $1/3 M_{\mathrm{sat}}$ phase above a magnetic field strength of $2J_1$. Another fractional magnetization state follows above $H = 3.6J_1$, which hosts $1/2 M_{\mathrm{sat}}$. The theory predicts an enhanced temperature-stability for the $1/2 M_{\mathrm{sat}}$ phase. Furthermore, a high-field incommensurate phase is found for fields above $H = 6.2J_1$. This phase transition is of second order. Saturation is reached at $H = 8.2J_1$. Table 5.3 compares the critical fields of the model to those of $Cs_3Fe_2Br_9$.

critical field	Seabra *et al.* Ref. [57] (J_1)	$Cs_3Fe_2Br_9$ (T)	scaling factor (T/J_1)
H_{c1}	1	5.7	5.7
H_{c2}	-	9.5	-
H_{c3} ($1/3 M_{\mathrm{sat}}$)	2.01	12	5.97
H_{c4} ($1/2\ M_{\mathrm{sat}}$)	3.6	20	5.55
H_{c5}	6.24	32	5.13
H_{c6}	-	38	-
H_{c7}	8.2	43	5.24

Table 5.3 Critical fields of the stacked triangular lattice [57] and of $Cs_3Fe_2Br_9$.

Obviously, not all critical fields of $Cs_3Fe_2Br_9$ can be found in the model. However, for those transitions that occur in both phase diagrams an almost perfect scaling relation of $J_1 \approx 5.6(3)$ T is found.

A magnetic moment with spin $S = 5$ in this magnetic field gains the Zeeman energy $g\mu_{\mathrm{B}} S B$. Transforming this Zeeman energy into a temperature energy scale via

$$g\mu_{\mathrm{B}} S B = k_{\mathrm{B}} J_1$$

yields $J_1 \approx 38$ K. This corresponds to the ordering temperature via $T_{\mathrm{N}} = 0.47J_1 \approx 18$ K. The actual ordering temperature of $Cs_3Fe_2Br_9$ is 13.3 K. Thus, the prediction from the ordering temperature and the critical fields are astonishingly good even though the model structure is much easier than the real system. Furthermore, Ref. [56] analyzed the same system for multiple anisotropy values. The chosen anisotropy of $D = 0.5J_1$ shows the best agreement which also yields an approximation for the anisotropy of $Cs_3Fe_2Br_9$.[9] The

[9] A smaller D allows a spin-flop phase which does not occur for $D \geq 0.25J_1$.

model Hamiltonian yields saturation fields of $H^{\perp} = 8J_1 + 8J_2 + 2D = 9.2 + 2D$ and $H^{\parallel} = 8J_1 + 8J_2 - 2D = 9.2 - 2D$. These fields correspond to an anisotropy parameter $\delta = 2(H^{\perp} - H^{\parallel})/(H^{\perp} + H^{\parallel}) = 4D/9.2$. Thus, $D = 0.5$ corresponds to $\delta = 0.22$ which is very close to the observed value of 0.19 in $Cs_3Fe_2Br_9$.

Hcp lattice with NN and NNN interaction

The analytical approach of Kudo and Katsura [59] on the hcp lattice with NN and NNN interactions J_1 and J_2, see Chapter 2.2.4, proposed the rich phase diagram and corresponding magnetic structures in a magnetic field that was presented in Fig. 2.6(b) on page 24. The ground state P1 was already found to be IX-1, which refers to an antiferromagnetic coupling J_1 and a ferromagnetic J_2. The model predicts a magnetic-field induced phase transition to phase VIII with a magnetization plateau of $\frac{1}{2}M_{\text{sat}}$ at $H = 2|J_1|$ and saturation at $H = 6J_1$. In $Cs_3Fe_2Br_9$, however, there are three other phases before the $\frac{1}{2}M_{\text{sat}}$ phase is reached at 20 T. Furthermore, the saturation field is only twice as large as the critical field of the $\frac{1}{2}M_{\text{sat}}$ transition.

The proposed J_1-J_2-H phase diagram contains further fractional magnetization phases, namely III and VIII with $\frac{1}{2}M_{\text{sat}}$, and IV and VI with $\frac{1}{3}M_{\text{sat}}$. The corresponding possible magnetic structures are shown in Fig. 5.31. In order to stabilize the $\frac{1}{3}M_{\text{sat}}$ phase, an antiferromagnetic J_2 is required. It cannot be excluded that the coupling changes from ferromagnetic to antiferromagnetic due to the relatively strong lattice distortion. In this case, depending on the ratio of J_1 and J_2 phases IV and VI would show the corresponding fractional magnetization. If the magnetic structure of the $\frac{1}{3}M_{\text{sat}}$ state of $Cs_3Fe_2Br_9$ is known, this should be compared to the proposed structures to see whether the corresponding J_1-J_2

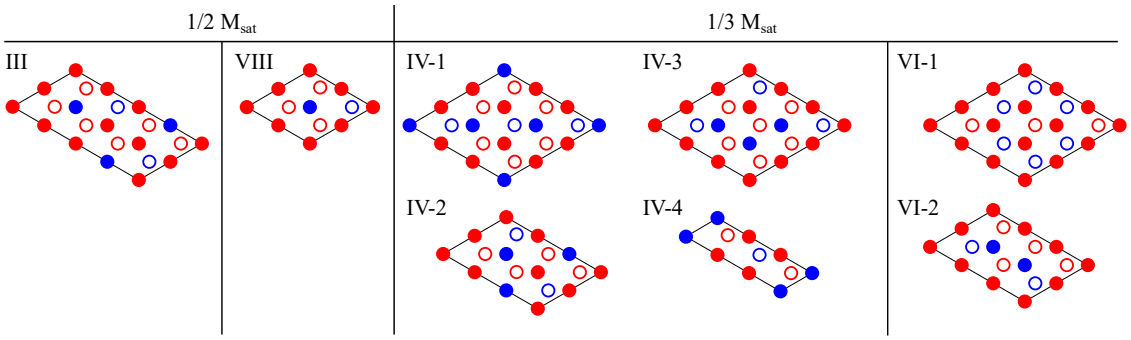

Figure 5.31 Proposed magnetic structures of the J_1-J_2-Ising model on the hcp lattice in a magnetic field with fractional magnetization of $\frac{1}{2}M_{\text{sat}}$ and $\frac{1}{3}M_{\text{sat}}$ according to Ref. [59], see Chapter 2.2.4. Red circles denote up-spins, blue circles down-spins. Open and filled circles depict different layers.

ratio compares to the ground state.

For all antiferromagnetic couplings J_1 and J_2, phase II with a magnetization of $2/3 M_{sat}$ is entered in larger magnetic fields before reaching the fully polarized phase. This fractional magnetization was not found for $Cs_3Fe_2Br_9$ proving that the model cannot fully cover the magnetism in $Cs_3Fe_2Br_9$.

Neutron scattering experiments can be performed up to ~15 T and used to obtain the exchange parameters in that range. Numerical calculations using DFT or Monte-Carlo simulations for the explicit system of $Cs_3Fe_2Br_9$ are desirable in order to get further understanding of the magnetic structures especially in larger magnetic fields, where neutron scattering experiments are not possible.

$Cs_3Cr_2(Cl,Br)_9$

Finally, the results for $Cs_3Fe_2Br_9$ are compared to those of related materials with triangular and hexagonal lattices of transition metal ions. The isostructural compounds $Cs_3Cr_2Cl_9$ and $Cs_3Cr_2Br_9$ were found to show singlet dimers. In a magnetic field, both show Bose-Einstein condensation of magnons, which results in a linear magnetization above H_{c1}. In $Cs_3Fe_2Br_9$, however, the Fe dimers are aligned parallel. Nonetheless, the field-induced Bose-Einstein condensation may explain the linear magnetization in $Cs_3Fe_2Br_9$ above 5.6 T similar to the behavior described in Ref. [57]. For both Cr materials, the intra-dimer coupling J is a factor of 20 or 50 larger than the NN inter-dimer couplings J_c and J_p. $J \gg J_p$ is not fulfilled for $Cs_3Fe_2Br_9$ and thus the inter-dimer couplings enforce the formation of parallel dimers as indicated in Figs. 5.11 and 5.12. The geometrical and energetical considerations for the ground state P1 show, that the in-plane couplings overcompensate the antiferromagnetic intra-dimer coupling and prevent the singlet formation. Especially the coupling J'_p, that connects Fe moments with different z components of neighboring bi-octahedra, is important.

$CuFeO_2$

The delafossite $CuFeO_2$ that consists of weakly coupled triangular layers orders through two transitions into an 2up-2dw antiferromagnetic ground state. A two-step transition is also found in $Cs_3Fe_2Br_9$ but with a different magnetic structure of the ground state. At low temperatures, $CuFeO_2$ shows five field-induced phase transitions. The first field-induced phase shows ferroelectric polarization. Interestingly, $Cs_3Fe_2Br_9$ also hosts a ferroelectric polarization in the temperature range from 8 K to 5 K in the first field-induced phase P4. Detailed studies of the influences of the structural distortions on the coupling constants

made it possible to explain the inelastic neutron scattering results for $CuFeO_2$. The anisotropy of $CuFeO_2$ is important for the description of the low-field magnetism, but in high fields this anisotropy vanishes [171]. Because the presented results for $Cs_3Fe_2Br_9$ show large magnetoelastic coupling and large changes of the lattice parameters at the first-order phase transitions, these changes have to be taken into account for future models for any numerical description.

5.8 Conclusion

$Cs_3Fe_2Br_9$ is a new material that crystallizes in the hexagonal space group $P6_3/mmc$ and consists of face-sharing Fe_2Br_9 bi-octahedra with two $S = 5/2$ moments. Through two temperature-driven transitions the material shows incommensurate (P2) and then commensurate antiferromagnetic order (P1). With the help of neutron scattering, the magnetic structure of the ground state was determined. Interestingly, the moments of the bi-octahedra are not oriented antiparallel yielding a singlet ground state, but are aligned parallel. Even though the geometry of the Fe-Fe intra-dimer exchange should favor antiferromagnetic ordering, this is overcompensated by the in-plane exchange. The ordering transition breaks the 3-fold rotation symmetry and twinning effects arise. The ordered zero-field phases show a large magnetoelastic distortion ascribed to a contraction of antiferromagnetic Fe-Fe bonds and an elongation of ferromagnetic bonds. The similar in-plane length changes for two perpendicular directions e_1 and e_2 show that at least partial detwinning is possible with small pressures. The system is substantially frustrated as indicated by the frustration parameter $f = |\theta|/T_N \approx 4.4$. The description of the magnetic system can be simplified by treating the bi-octahedra as a unit with $S = 5$, resulting in the hcp lattice structure. A magnetic field perpendicular to the easy axis suppresses the magnetic ordering temperature of phases P1 and P2 and no further phases are induced. The saturation is reached at 52 T. The presented detailed study of the thermodynamics and the magnetization reveals an extremely rich phase diagram with ten ordered phases for a magnetic field along the easy $\boldsymbol{c}$ axis. The field-induced first-order transitions from P3 to P4 to P5 to P6 show sharp discontinuous changes in the lattice parameter c of up to 10^{-4} at low temperatures. Via magnetization measurements, two fractional magnetization plateaus with $1/3 M_{sat}$ (P5) and $1/2 M_{sat}$ (P6) were found. Although these states have also been predicted for the hcp lattice of Ising moments, it was shown that the model is not perfectly applicable. A comparison to the stacked triangular lattice [57] shows interesting similarities, i.e., field-induced Bose-Einstein condensation and a sequence of field-induced transitions with critical fields that are consistent with the predictions. The model uses an easy-axis aniso-

tropy of $D = 0.5J_1$. Usually, materials with $S = 5/2$ Fe^{3+} moments show almost isotropic magnetism. In fact, $Cs_3Fe_2Br_9$ has a comparably large anisotropy $\delta = 0.19$ with saturation fields of $\mu_0 H_{\mathrm{sat}}^{\parallel} = 43\,\mathrm{T}$ and $\mu_0 H_{\mathrm{sat}}^{\perp} = 52\,\mathrm{T}$.

Furthermore, $Cs_3Fe_2Br_9$ shows a large magnetocaloric effect which complicates the assignment of a precise temperature to each transition for the pulsed magnetization measurements. Dielectric studies revealed a small ferroelectric polarization P_c in phase P4, which increases with magnetic field. It is unusual for the polarization to reduce again on decreasing temperature, although there is no further phase transition.

$Cs_3Fe_2Br_9$ with its rich temperature vs. magnetic field phase diagram is an interesting system to study the interplay of multiple competing magnetic interactions and the resulting frustration. Due to the large magnetoelastic coupling and the resulting structural changes between the ordered phases, also these effects have to be taken into account for the analysis of neutron scattering experiments and the modeling of the system with DFT and Monte-Carlo methods.

6 Summary

In this thesis, the magnetic materials $SrRuO_3$ and $Cs_3Fe_2Br_9$ were studied by means of thermodynamics and electric transport. Furthermore, the experimental environment for measurements of the magnetization was improved by setting up a gradient magnet. It can be used in combination both with a HelioxVL cryostat, as well as a Kelvinox dilution refrigerator to measure the magnetization down to 260 mK or 30 mK with a Faraday magnetometer. The new setup has an enhanced resolution especially in small fields.

Although the ferromagnetic metal $SrRuO_3$ is known for a long time and has been studied widely in thin films, large floating-zone grown single crystals became available only recently [19]. Previous contradicting studies of the criticality of the ferromagnetic ordering transition were surveyed with these crystals. Specific heat and magnetization measurements have been analyzed according to the expected power laws. It turns out, that the critical behavior in the vicinity of the transition temperature $T_C = 163.6$ K can be described best with critical exponents close to those of the Ising universality class. An Ising-like exchange implies a strong magnetic anisotropy. The easy-axis direction $\boldsymbol{c}$ was confirmed by the combination of magnetization and magnetostriction measurements. In the studied temperature range, $SrRuO_3$ has a distorted orthorhombic perovskite structure, which hosts six twin domains that mimic the cubic high-temperature structure. The presented studies unambiguously show the impact of these domains on multiple quantities. In the ferromagnetic phase, a magnetic field along any cubic $\{1\,1\,0\}_c$ direction changes the domain population and yields a single-domain state, where the easy axis is aligned to the magnetic field. It is astonishing that structural domains that form at 950 K, can be switched at 2 K with magnetic fields as small as 2 T. The reason is that the pinning of the structural domains is weak and thus allows a reorientation of the rotation/tilting scheme of the oxygen octahedra. This state is stable as long the sample remains ferromagnetic. Above T_C, it decays back to a multi-domain state. This effect is called shape-memory effect. Nonetheless, this differs from the typical behavior of shape-memory alloys because the initial shape is recovered at T_C, which is far below the structural phase transition where these materials return to their multi-domain pattern. Furthermore, it is possible to switch between different structural domains which makes $SrRuO_3$ ferroelastic and, therefore, multiferroic. Electric

transport measurements show the nonmonotonic temperature dependence of the anomalous Hall effect in the ferromagnetic phase. Additionally, the subtle influence of domain effects observed in the magnetization is consistently found in the Hall resistivity. The combination with magnetization data allowed an extended description of the anomalous Hall effect above T_C where no spontaneous magnetization is left. In this temperature range a finite magnetic field yields a nonlinear magnetization, and, thus, it allows a distinction of the normal and anomalous Hall effect, which grows with increasing temperature. The temperature dependence cannot be described with the intrinsic effects skew scattering and side jump. Spin-orbit coupling causes spin-split bands that explain the observed behavior. A Weyl point close to the Fermi energy as present in $SrRuO_3$ [17] acts as a magnetic monopole in momentum space and yields an additional term to the electron velocity, which then contributes to the Hall effect. Its impact is not only found in the Hall conductivity but also in the magnon gap and the stiffness. Both quantities also show a nontrivial temperature dependence. The Berry curvature contribution to the Hall conductivity directly softens the gap and the stiffness on decreasing temperature. Agreement between the model and the neutron data is found [145]. This is a strong indication for the validity of the interpretation using the concept of the Berry curvature of the band structure.

The newly synthesized material $Cs_3Fe_2Br_9$ was studied by means of thermodynamics complemented by neutron scattering. The face-sharing Fe_2Br_9 bi-octahedra are arranged in triangular layers stacked to form a hexagonal structure. The material orders antiferromagnetically through two distinct temperature-driven magnetic phase transitions. The intermediate phase for $13.1\,\mathrm{K} < T < 13.3\,\mathrm{K}$ is incommensurate and it becomes commensurate below 13.1 K. Interestingly, the $S = 5/2$ iron moments inside each bi-octahedron are aligned parallel although the intra-dimer Fe-Fe exchange should favor antiferromagnetic singlet dimers. This intra-dimer interaction is overcompensated by the antiferromagnetic in-plane nearest-neighbor interaction. It turns out that the coupling of Fe moments with different z component of neighboring bi-octahedra J'_p is important to stabilize the obtained magnetic structure. The system is substantially frustrated as indicated by the frustration parameter $f \approx 4.4$. The description of the magnetic system can be simplified by treating the bi-octahedra as a unit with $S = 5$, resulting in the hcp lattice structure. The antiferromagnetic stripe ground state represents the theoretical prediction for the hcp lattice with Ising anisotropy for NN and NNN interaction [59]. The zero-field ordered phases show a large discontinuous magnetoelastic distortion. This results from a linear magnetoelastic coupling that contracts antiferromagnetic bonds and elongates ferromagnetic bonds. The T-H phase diagram was studied by magnetostriction and thermal-expansion measurements in fields up to 38 T and pulsed-field magnetization measurements up to

57 T. For an in-plane magnetic field, there are no further phase boundaries. The magnetic field suppresses the ordered states and saturation is reached at 52 T. For $\boldsymbol{H} \parallel \boldsymbol{c}$, there are a total of ten ordered phases. In the first field-induced phase, the magnetization grows linearly from zero indicating a Bose-Einstein condensate of magnons as predicted for other triangular systems [56]. In an increasing magnetic field, several first-order transitions occur. These transitions are highly hysteretic and show discontinuous length changes. The magnetization measurements reveal two fractional magnetization plateaus with $⅓M_{\mathrm{sat}}$ (P5) and $½M_{\mathrm{sat}}$ (P6). Fractional magnetization states have been found in other triangular systems and have also been predicted by simulations of corresponding model Hamiltonians. The stacked triangular lattice with Ising anisotropy [57] shows a similar sequence of field-induced transitions with critical fields that are consistent with those observed in $Cs_3Fe_2Br_9$, even though the structure is different. Nonetheless, for a better agreement similar calculations for this specific system are required. The saturation along the easy axis is reached at 43 T. Thus, $Cs_3Fe_2Br_9$ shows the anisotropy $\delta = 0.19$ which is comparably large for a material with Fe^{3+} moments that are usually isotropic. Beyond that, the material shows a large magnetocaloric effect in pulsed field measurements. Dielectric studies reveal a tiny ferroelectric polarization that grows with magnetic field to $P_c \approx 0.5\,\mu\mathrm{C/m^2}$ at maximum in the first field-induced phase P4. A similar phase was found in $CuFeO_2$, a weakly coupled triangular magnet. Interestingly, the polarization is only present close to the phase boundary and vanishes at low temperatures, although there is no further phase transition. $Cs_3Fe_2Br_9$ is a 3d antiferromagnetic material with a rich phase diagram which allows to study the interplay of competing magnetic interactions on a frustrated lattice. Numerical simulations and further neutron scattering experiments are required to find a proper model Hamiltonian. Also, exchanging iron by 4d or 5d ions with larger spin-orbit coupling could yield interesting phenomena.

A Appendix

A.1 Berry phase

The following introduction to the concept of the Berry phase follows the intuitive explanation of Ref. [23]. For further reading see e.g. [208]. On a closed path in some phase space, it is possible to obtain a nontrivial outcome even though the motion is adiabatic [209]. This is illustrated by an example of a motion on a sphere in the following. From the north pole, an arrow pointing towards the equator is moved south to the equator, then moves along the equator by some angle, and then back up to the north pole. At the end of this closed loop, the position is the same, but the arrow is pointing in a different direction. This rotation is called a geometric phase. This principle can be transferred to a physical state that changes under the influence of a Hamilton operator $\mathcal{H}(\boldsymbol{R})$ if the external parameters $\boldsymbol{R}$ change over time. By this motion through parameter space, the original state can be changed. It gains a geometric phase, the so-called Berry phase. In order to understand this property, we consider a system in the parameter space $\boldsymbol{R}$ that moves along the path Γ. At the initial time t_0, it is in the eigenstate $|\Psi(t_0)\rangle = |m[\boldsymbol{R}(t_0)]\rangle$ with energy $\epsilon_m(t_0)$. Upon changing $\boldsymbol{R}$ adiabatically, the system remains in the eigenstate $|m(t)\rangle$. Without any band crossings the state can only gain a phase

$$|\Psi(t)\rangle = e^{-\frac{i}{\hbar}\int_{t_0}^{t}\epsilon_m(t')\mathrm{d}t'} e^{i\gamma_m(t)} |m[\mathbf{R}(t_0)]\rangle \quad .$$

It can be shown by putting this into the Schrödinger equation, that the phase difference along the path consists of a common dynamical phase

$$\phi_m(t) = -\frac{1}{\hbar}\int_{t_0,\Gamma}^{t} \epsilon_m(t')\mathrm{d}t' \quad ,$$

which relates to the time for the motion along the path and a geometrical phase

$$\gamma_m(t) = i \int_{t_0,\Gamma}^{t} \left\langle m[\boldsymbol{R}(t')] \left| \frac{\mathrm{d}}{\mathrm{d}t} \right| m[\boldsymbol{R}(t')] \right\rangle \mathrm{d}t'$$
$$= i \int_{\boldsymbol{R}(t)_0,\Gamma}^{\boldsymbol{R}(t)} \langle m[\mathbf{R}(t)] \left| \nabla_{\boldsymbol{R}} \right| m[\boldsymbol{R}(t)] \rangle \, \mathrm{d}\boldsymbol{R} = \int_{\boldsymbol{R}(t)_0,\Gamma}^{\boldsymbol{R}(t)} \boldsymbol{A}_m(\boldsymbol{R}) \mathrm{d}\boldsymbol{R} \quad .$$

Here, $\boldsymbol{A}_m(\boldsymbol{R}) = i \langle m[\boldsymbol{R}(t)] \left| \nabla_{\boldsymbol{R}} \right| m[\boldsymbol{R}(t)] \rangle$ is the so-called Mead-Berry potential. It can easily be shown that for a closed loop with $\boldsymbol{R}(t_0 + T) = \boldsymbol{R}(t_0)$ there is no gauge transformation that cancels this geometric phase. We consider the transformation

$$|m[\boldsymbol{R}(t_0)]\rangle \rightarrow |m'[\boldsymbol{R}(t_0)]\rangle = e^{-i\chi[\mathbf{R}(t)]} |m[\boldsymbol{R}(t_0)]\rangle \quad .$$

In the closed loop, $e^{-i\chi(t_0)} = e^{-i\chi(t_0+T)}$ has to be fulfilled, which results in $\chi(t_0) = \chi(t_0 + T) + 2\pi n$. For the geometric phase follows

$$\gamma'_m(\Gamma) = \oint_{\Gamma} \boldsymbol{A}'_m[\boldsymbol{R}(t)] \mathrm{d}\boldsymbol{R} = \gamma_m(\Gamma) + 2\pi n \quad .$$

The Berry potential $\boldsymbol{A}_m$ itself depends on the gauge and consequently cannot be a physical observable. Obviously, there is no transformation that cancels the Berry phase because there remains a multiple of 2π. Furthermore, $e^{i\gamma_m}$ is gauge invariant, and, thus, it can influence physical observables. The closed path integral can be written as a surface integral using Stokes theorem:

$$\gamma_m = \oint_{\Gamma} \boldsymbol{A}'_m[\boldsymbol{R}(t)] \mathrm{d}\boldsymbol{R} = \int_{S} \boldsymbol{\Omega}_m(\boldsymbol{R}) \hat{\mathbf{n}} \mathrm{d}^2 R \quad .$$

Here, $\hat{\mathbf{n}}$ denotes the surface normal and $\boldsymbol{\Omega}_m(\boldsymbol{R}) = \nabla_{\boldsymbol{R}} \times \boldsymbol{A}_m(\boldsymbol{R})$ is the so-called Berry flux or Berry curvature.

The integral over the Berry curvature is related to a topological quantity, called Chern number C_m, if the surface is a closed manifold

$$C_m = \frac{1}{2\pi} \int_{S} \boldsymbol{\Omega}_m(\boldsymbol{R}) \cdot \hat{\mathbf{n}} \mathrm{d}^2 R \quad .$$

This number classifies the total flux through the surface S.
In solid-state physics, we often integrate over the whole Brillouin zone, which is such a closed manifold. Thus, the concept of Berry phases and Chern number has become important in this topic.

A.2 Full data sets $Cs_3Fe_2Br_9$

Ultrasound measurements

In a pulsed magnetic field, it was also tried to characterize the magnetoelastic coupling via ultrasound measurements. Figure A.1(a) shows the basic measurement principle. A voltage signal is applied to a piezo-transducer, which is attached to a sample and creates a corresponding ultrasonic wave excitation inside the sample. The sound wave travels with the velocity $v(\boldsymbol{k}, \boldsymbol{u})$ through the sample, where $\boldsymbol{k}$ denotes the wave vector and $\boldsymbol{u}$ the polarization of the wave. On the opposing surface, another transducer detects the wave and converts it back into a voltage signal. Additionally, a part of the signal is reflected back inside the sample and again travels through it. After another reflection at the incident surface, it reaches the detection-transducer again. This signal is called first echo. Multiple echos can be detected with continuously decreasing intensity. The elastic modulus c_{ij} follows from the sound velocity, e.g., $c_{11} = v_{\mathrm{L}}^2 \cdot \rho$ with the longitudinal sound velocity and the mass density ρ. Further details about the measurement principle and the used setup can be found in Ref. [210].
For the measurements on $Cs_3Fe_2Br_9$, several experimental issues occurred. Fixing the piezo-transducers on the surfaces of a plane-parallel sample turned out to be challenging. The signal and several echos could be detected at room temperature, but the signal was lost upon cooling. Either no signal could be detected at all or defining the beginning and ending of an echo was impossible. Multiple attempts on different samples, glues, and transducers were done with only little output.

Figure A.1(b) shows the few data sets that were collected successfully at the HZDR. For a magnetic-field pulse at 4 K a longitudinal excitation was used with the magnetic field applied perpendicular to $\boldsymbol{c}$. The ultrasound frequency is 37 MHz and yields a longitudinal sound velocity $v_{\mathrm{L}} = 4900\,\mathrm{m\,s^{-1}}$. The analysis was done for two different echos. The black data were obtained at the position of the fifth echo. For this field orientation, two transitions should occur. The sound velocity at the fifth echo shows one anomaly at 50 T. Additionally, the time regime for a higher order, but unknown echo was analyzed. In principle, both echos should show the same $\Delta v/v$, but this is obviously not the case. Here, the sound velocity is essentially constant up to 35 T and then shows a minimum at 38 T and finally a peak at 51 T. If both anomalies stem from the field-induced phase transitions of $Cs_3Fe_2Br_9$, the temperature has to be ~2.8 K. The magnetocaloric effect presented in Chapter 3.5 shows that this temperature reduction is realistic in a pulsed experiment.

For the pulses in Fig. A.1(c) with the magnetic field along $\boldsymbol{c}$, a transversal excitation was used. Two pulses were conducted at 9.3 K, one up to 22 T and the other up to 56 T.

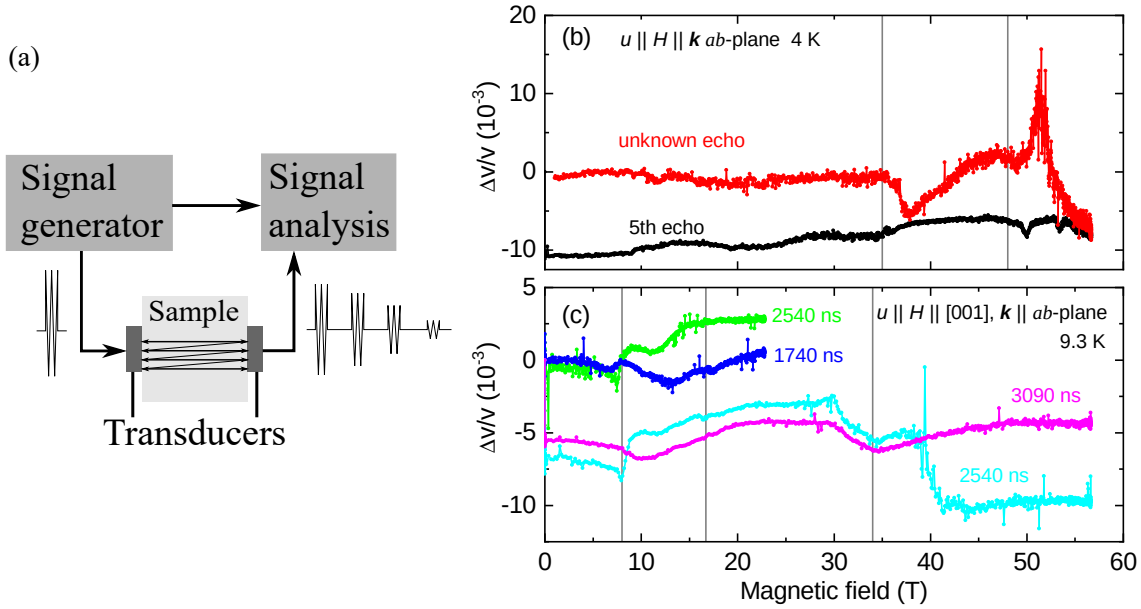

Figure A.1 Sound velocity measurements on $Cs_3Fe_2Br_9$. (a) shows the measurement principle of ultrasound measurements. (b) and (c) present sound-velocity data in pulsed magnetic fields on $Cs_3Fe_2Br_9$ in two different settings. Vertical lines mark the expected critical fields extracted from pulsed magnetization data. The measurements were performed at the HZDR.

The transversal sound velocity is 2250 m s^{-1}. Three transitions are expected at this temperature. Again, qualitative differences are found for different delay times. Basically, the first transition is found in the echo after $\tau = 2540$ ns, which shows a step-like anomaly. The echos with other delay times do not show a clear anomaly at this magnetic field. The second field-induced transition at 17 T does not yield any signal in the sound velocity. The transition at 34 T shows a minimum for both echos. The 2540 ns data show a large step at 40 T that is absent for the later echo. The origin for this step is unknown. Generally, this technique is good to find magnetoelastic phase transitions, but in this case the issues due to bad coupling of the transducers to the sample were not solved within the week of measurement time in Dresden. Mainly, a suitable glue is required that allows to fix the transducers to the sample without degradation of the sample and temperature-stable signal insertion and detection.

SQUID, VSM, HelioxVL

Figure A.2(a) shows the temperature-dependent magnetic susceptibility for magnetic fields up to 14 T measured in the SQUID and VSM. The magnetic field is applied perpendicular to the $\boldsymbol{c}$ axis and thus inside the triangular planes. Figure A.2(b) compares the susceptibility for $\boldsymbol{H} \parallel \boldsymbol{c}$ to the perpendicular direction. The anomalies found in the susceptibilities agree to the anomalies found via thermal-expansion measurements and were equally used to build up the phase diagram.

The magnetic-field dependent magnetization was measured using the VSM for both orientations, see Fig. A.3. Panel (a) shows the data for $\boldsymbol{H} \perp \boldsymbol{c}$ and panel (b) for $\boldsymbol{H} \parallel \boldsymbol{c}$. Because interesting physics and transitions are present close to the limiting maximum field in the PPMS, the lambda stage of the *Cryogenic 17 T* bath cryostat was used to cool the magnet to 2 K and allow maximal magnetic field of 17 T. Additionally, the HelioxVL magnetometer is used in a minimal offset position of 2 cm above the field center to reach the maximum effective field of 16.8 T. Note, that these measurements were performed before the new magnet with the gradient coil was available, and, thus, the previous measurement principle was used.

Temperature-dependent measurements with the HelioxVL Faraday-magnetometer are in general not the strength of this magnetometer, since the thermal expansion of the dilatometer creates a background signal. In this case, a large sample of 61 mg was used to overcome this issue by a sample signal that is much larger than the background. The absolute value is not precise, since this is defined via creating a switchable magnetic moment with the additional coil, and, thus, it is much easier to define the equilibrium capacitance C_0. The temperature-dependent magnetization measurements presented in Fig. A.4 were

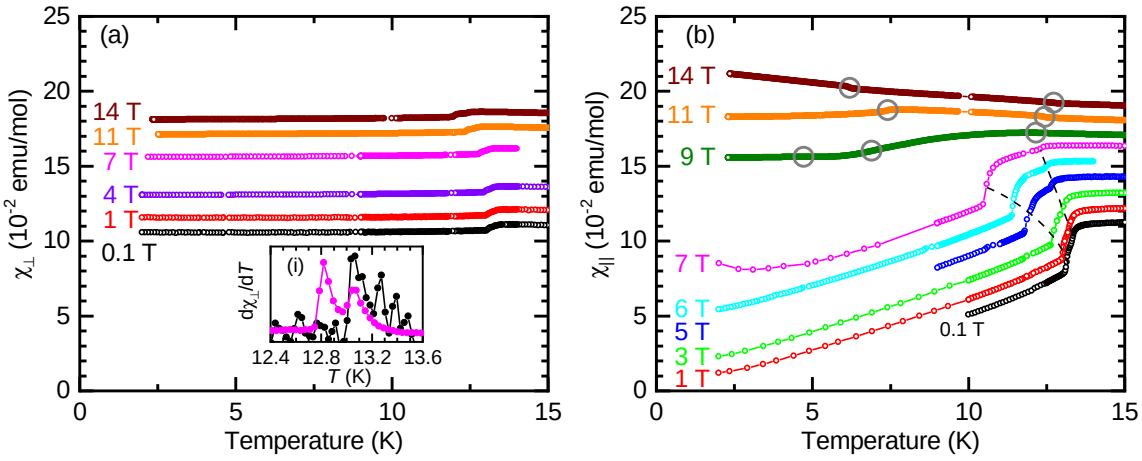

Figure A.2 Temperature dependence of the magnetic susceptibilities $\chi_\perp$ and $\chi_\parallel$ in magnetic fields. (a) shows the in-plane susceptibility $\chi_\perp$ from 0.1 T to 14 T. Curves are shifted by 10^{-2} emu/mol. Inset (i) compares the temperature derivative $d\chi_\perp/dT$ for 0.1 T and 7 T at the transitions T_{N1} and T_{N2}. (b) shows $\chi_\parallel$ for selected magnetic fields from 0.1 T to 14 T. For magnetic fields above 7 T, the anomalies are small and marked by ◯. For smaller magnetic fields, the field dependence of T_{N1} and T_{N2} is marked. All data up to 7 T were measured in the SQUID, for larger magnetic fields the VSM (PPMS) was used.

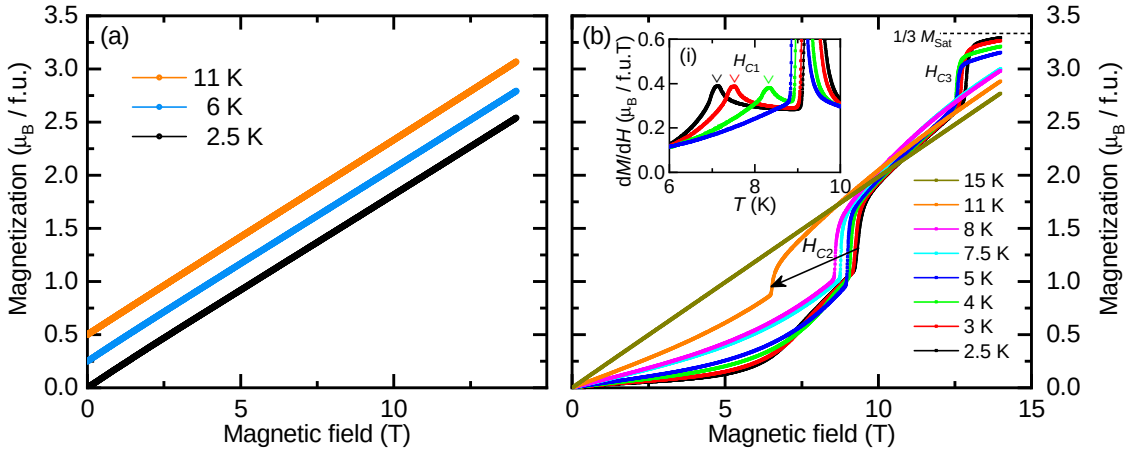

Figure A.3 Magnetization of $Cs_3Fe_2Br_9$ for $\boldsymbol{H} \perp \boldsymbol{c}$ (a) and $\boldsymbol{H} \parallel \boldsymbol{c}$ (b). The data sets in (a) are shifted by 0.25 μ_B/f.u. Inset (i) shows the derivative of the magnetization with respect to the magnetic field dM/dH for the low-temperature data between 6 K and 10 K. The derivative was averaged over 50 points. Identified anomalies are marked by ∨.

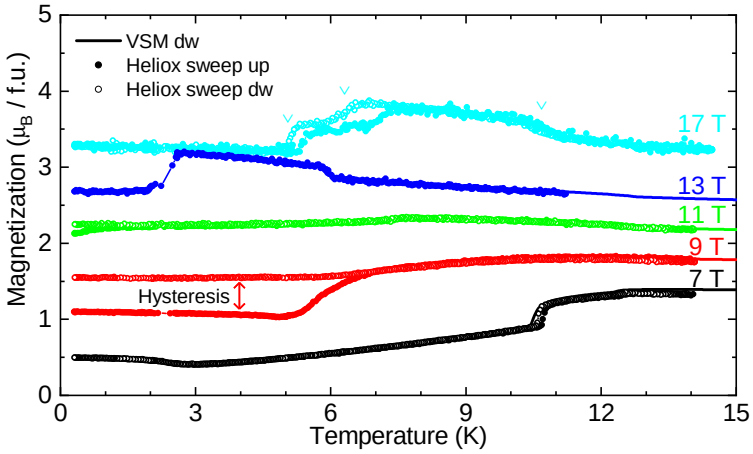

Figure A.4 Temperature-dependent magnetization of $Cs_3Fe_2Br_9$ with $\boldsymbol{H} \parallel \boldsymbol{c}$ up to 17 T measured with the HelioxVL compared to VSM data. The 17 T data show three pronounced steps marked by ∨.

carried out with temperature ramps of 0.1 K min^{-1}. Here, measurements with increasing and decreasing temperature were performed to see hysteresis effects.

In the field range with overlap between the VSM and the Faraday magnetometer, both are in perfect agreement with each other. The 9 T measurement shows a large discrepancy between up and down data. It was performed after zero-field cooling and then applying the field in the subsequent heating and cooling run. Above 7 K no difference is visible but the curves split below. As known from the magnetization measurements, 9 T is right at the first-order transition. The transition is highly hysteretic, and, thus, the heating curve starts in a different phase than where the subsequent cooling curve ends. All measurements cannot resolve the magnetic ordering transition T_{N1} due to the weaker resolution compared to the SQUID magnetometer. For the maximum field, the magnetization shows three transitions. All critical temperatures match with the transitions presented in the phase diagram. In the low-temperature regime, the magnetization increases linearly and extrapolates to $3.33\,\mu_B$/f.u. = $\frac{1}{3}M_{sat}$ for $T = 0$.

A.3 $Dy_{2-x}Ho_xTi_2O_7$

This part shows results for so-called spin-ice compounds after a short introduction to the material class. Further information can be found in, e.g., Ref. [211]. $Dy_2Ti_2O_7$ and $Ho_2Ti_2O_7$ are the main spin-ice compounds. The Dy/Ho ions form a pyrochlore lattice of corner-sharing tetrahedra. The crystal electric field causes a large Ising-like anisotropy forcing the moments to point along their local {111} axis. Thus, each moment has two possible orientations – in or out of the tetrahedron. The magnetic moments ($\mu \approx 10\,\mu_B$) interact via nearest-neighbor exchange and long-range dipole-dipole exchange. For the ground state of a single tetrahedron, two moments point into and two are oriented out of the tetrahedron. This 2in-2out state is the so-called ice rule, named after the analogous behavior of water ice, where for each oxygen atom two neighboring hydrogen atoms are close and two are further apart. A single tetrahedron has a total of $2^4 = 16$ states of which six fulfill the ground-state criterion. Thus, the degeneracy of the ground state, which is the defining theoretical criterion of frustration, does not fulfill the third law of thermodynamics ($S \to 0$ for $T \to 0$). The ground state degeneracy grows exponentially with the number of tetrahedrons N. For water ice, it was shown by Pauling that the number of ground states equals $\Sigma = (3/2)^N$ and a residual entropy of $S = R/2\ln(\Sigma) = 1.69$ J/molK is present [212]. This was also shown by experiment [213]. For spin-ice, first results confirmed this residual entropy, but, as Pomaranski *et al.* showed, there are slow relaxation processes that result in an increasing c_p/T at low temperatures and thus a reduced entropy [214].
The first excited state of a tetrahedron can be achieved by flipping one moment. By this flip, also the neighboring tetrahedron is excited – one into a 3in-1out state and the other into a 1in-3out state. In the single tetrahedron approximation, this excitation gap amounts 2.2 K in $Dy_2Ti_2O_7$ and 3.6 K in $Ho_2Ti_2O_7$. This defines the energy scale on which the interesting spin-ice physics occurs. For the studies of both compounds, especially the field dependence of physical quantities is of interest. The following measurements focus on the [1 1 1] direction. It can be visualized as a stacking of triangular planes and Kagomé planes. Already small magnetic fields polarize the magnetic moments of the triangular planes since their local easy axis is parallel to the field orientation. The moments on the Kagomé planes have to orient so that the 2in-2out rule is still fulfilled. At 1 T for $Dy_2Ti_2O_7$ and at 1.5 T for $Ho_2Ti_2O_7$, the Zeeman energy of those moments is so large that a level crossing occurs and a nondegenerate 3in-1out (1in-3out) configuration becomes favorable. This behavior can be seen, e.g., in magnetization and also in the field dependence of the thermal conductivity κ.

The main interest in studying this system results from so-called fractional excitations.

The smallest excitation of the ground state is a single spin flip, which results in two excited tetrahedrons (3in-1out and 1out-3in). A monopole-antimonopole pair is formed. These excitations are topological defects with properties that are similar to Dirac's magnetic monopoles and have been introduced by Castelnovo *et al.* [215]. Both monopoles carry a magnetic charge of opposite sign and obey the energy of the so-called dumbbell model, which is equal to the exchange Hamiltonian up to small corrections and also yields a residual entropy. A monopole-antimonopole pair can be separated without any further violation of the ice rule on the tetrahedra by flipping further spins. The path along these spin flips is called Dirac string. The only energy cost of the separation results from the long-range Coulomb exchange. Standard electromagnetic theory of Gauss' law does not allow for static magnetic charges as sources of a magnetic field, but only moving charges or magnetic dipoles are sources of the magnetic field. The excitations in spin ice can be regarded as divergences of the magnetic field, which are captured by Gauss' law. These excitation do not posses any dispersion, and, thus, a vanishing group velocity follows. Due to this, the monopoles behave diffusive. The diffusion coefficient $D_{\mathrm{mag}} = \kappa_{\mathrm{mag}}/c_{\mathrm{mag}}$ relates to the thermal heat transport and the specific heat of the excitations.

S. Scharffe and G. Kolland characterized the monopole contribution to the thermal conductivity [216, 217]. Their results unambiguously show that there is a magnetic contribution to the thermal conductivity below 4 K. In zero field, these monopoles are highly mobile. By applying a magnetic field along [1 1 1], κ is suppressed upon entering the Kagomé plateau. Right at the transition to the polarized state, κ shows a peak and decreases rapidly afterwards. On decreasing field, this part reveals hysteresis effects as the thermal conductivity stays approximately constant at the peak value. For magnetic fields above 2 T, a small reduction of κ is observed for $Dy_2Ti_2O_7$, while κ increases for $Ho_2Ti_2O_7$. For higher temperatures, the peak and the hysteresis effects vanish.

S. Scharffe also studied dilution effects on the spin-ice physics. By nonmagnetic Yttrium exchange of the magnetic Dysprosium or Holmium ions, the spin-ice physics can be destroyed [216, 218]. The phononic contribution to κ remains inverted. Mixed crystals of $DyHoTi_2O_7$ were grown and characterized by S. Niesen [201]. The low-temperature magnetization for the [1 1 1] direction shows the usual spin-ice physics with the Kagomé plateau and the polarized niveau. The transition to the polarized state occurs at 1.1 T, which is close to the value of the pure Dy compound and not centered between both parent compounds.

Figure A.5 compares the thermal conductivity of $DyHoTi_2O_7$ to both pure spin-ice compounds $Dy_2Ti_2O_7$ and $Ho_2Ti_2O_7$, obtained by S. Scharffe. At 0.4 K, κ is slightly larger in $DyHoTi_2O_7$ than in the pure Ho based material, but much smaller than in the Dy parent

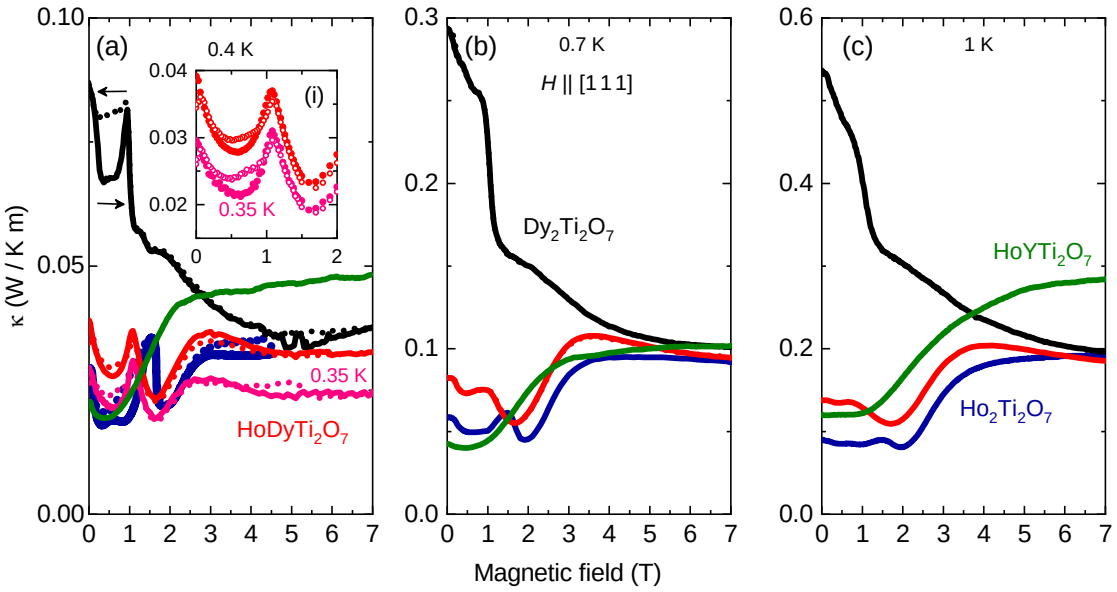

Figure A.5 Magnetic-field dependence of the thermal conductivity of $DyHoTi_2O_7$ for different temperatures. The data is compared to previous results for $Dy_2Ti_2O_7$ and $Ho_2Ti_2O_7$ from Ref. [216].

compound. Upon increasing magnetic field, κ reduces rapidly when entering the Kagomé state. At the transition to the polarized state at 1.1 T, κ peaks to approximately the same value as found in zero field. For larger magnetic fields, the thermal conductivity reduces rapidly and a minimum is found at 1.7 T. For larger magnetic fields, κ increases again up to 2.8 T. From there on, the thermal conductivity reduces slightly and becomes approximately constant around 5 T. On decreasing magnetic field, there is no hysteresis down to 1.1 T. In the Kagomé state, κ is enhanced compared to increasing magnetic field but does not remain at the peak value as it does in $Dy_2Ti_2O_7$. In zero field, the original value is recovered. Thus, the general hysteresis behavior is similar to $Ho_2Ti_2O_7$.

For higher temperatures in Fig. A.5(b) and (c), no hysteresis effects are found. Still, the thermal conductivity of $DyHoTi_2O_7$ is slightly enhanced compared to pure Ho. Also the field dependence is similar. While κ reduces monotonically for the Dy compound in field, for the Ho-containing samples there are small anomalies upon entering the Kagomé state and the polarized state, but the most prominent anomaly is the increase between 2 T and 4 T. Because in $DyHoTi_2O_7$ the thermal conductivity reduces for large magnetic field, the total signal can be described with a convolution of both parent compounds. For small magnetic fields, κ resembles the Ho behavior, while for large fields the Dy contribution dominates. Because the magnetization does not show any anomalies for large magnetic

fields, the anomalies of the thermal conductivity are assigned to the phononic system, which is consequently not field-independent. S. Scharffe proposed the different magnetostriction between the Ho and Dy compound as a potential explanation for the different behavior, but the relative change of κ is comparably large to stem from this effect.

Thermal conductivity measurements do not show any hysteresis in zero field for this field orientation but magnetization measurements show a remanence. This difference raised the guess, that the applied heat current through the sample might reduce or destroy the remanence. To check for this, it was tried to measure both quantities - thermal conductivity and magnetization at the same time in one setup. A sample of $Dy_2Ti_2O_7$ was mounted inside the magnetometer. Additionally, a heater was coupled to the other end of the sample. Multiple attempts were conducted with and without thermometers connected to the sample. In the following, the magnetization was measured at a fixed temperature, while different heat currents were applied to the sample. All magnetization curves show the beforehand known remanence. An enhanced heat current only results in an elevated sample temperature with a reduced remanence, corresponding to the sample temperature. Thus, the hypothesis of a suppressed hysteresis by a heat current could not be proven.

With the capability of the new gradient-coil magnet more detailed magnetization measurements in the low-field regime were possible, since the signal no longer vanishes for vanishing absolute magnetic field as described in the experimental Chapter 3.3.3. With the new setup, it is also possible to measure the magnetization continuously as a function of magnetic field. A fixed magnetic-field gradient is applied, while the absolute magnetic field is varied. The recorded capacity then has to be inverted and its changes $1/C_0 - 1/C(H)$ can be scaled onto absolute values of the magnetization that have been obtained in stable conditions, e.g., for large fields or at least far away from a phase transition. This procedure was applied to $Dy_2Ti_2O_7$ to investigate the low-field magnetization when switching between two Kagomé-ice states. Figure A.6 shows magnetization loops of $Dy_2Ti_2O_7$ between ± 1 T. It compares different magnetic-field sweep rates at 0.3 K. For $|\mu_0 \boldsymbol{H}| > 0.5$ T, the magnetization is approximately independent of the field-sweep direction and is almost constant at 3.33 μ_B/f.u. For smaller magnetic fields, the hysteresis opens. On lowering the magnetic field, a remanence of 1.5 μ_B/f.u. is found. After inverting the magnetic field, sharp jumps of the magnetization are found. For 0.1 T/min, four jumps can be identified. Between two jumps, the slope of $M(H)$ is strongly reduced so that approximately plateaus are established. For slower sweep rates, there are less sharp jumps, but down to -0.135 T, the susceptibility is rather constant. As a consequence, the coercive field is larger for the slow sweep rate. This directly results into the fact, that the hysteresis is larger for a slower rate. This behavior is counter-intuitive as for a usual relaxing system the

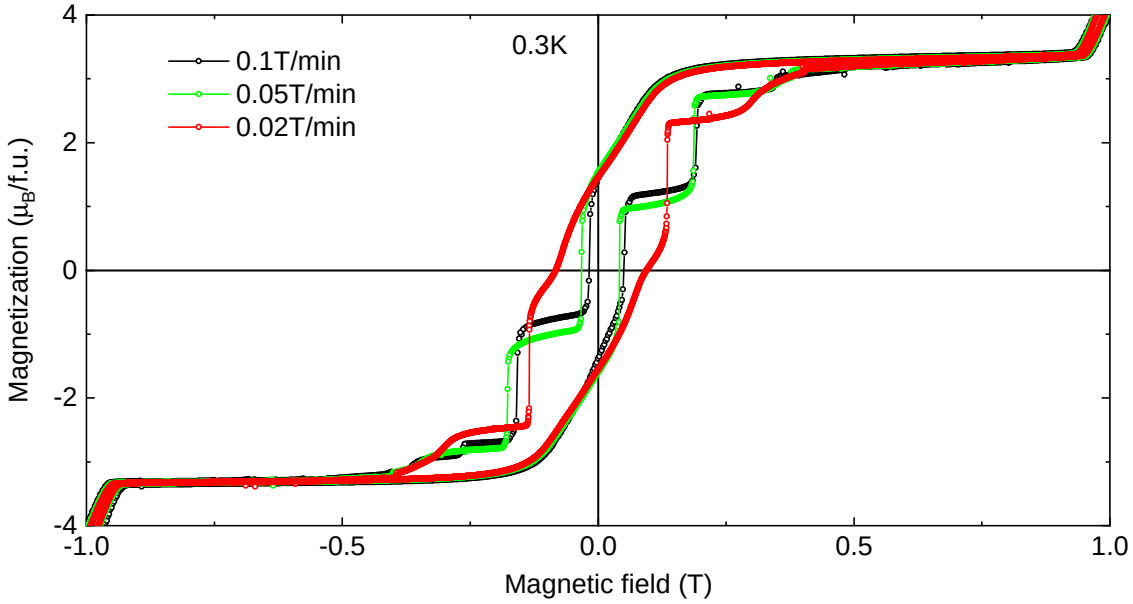

Figure A.6 Magnetization of $Dy_2Ti_2O_7$ obtained for different field sweep rates at 0.3 K in the gradient-coil magnet.

behavior should be inverted. This raises the question of the reason for the magnetization jumps. In literature, multiple publications report on avalanche dynamics [219, 220] for spin-ice materials $Dy_2Ti_2O_7$ and $Ho_2Ti_2O_7$. These publications focus on the magnetization process after zero-field cooling. Both groups report a threshold field-sweep rate of the order of 0.02 T/min above which the avalanches are induced. During an avalanche, the sample temperature increases drastically above 600 mK which defines the equilibrium magnetization after the avalanche. Probably, the sample coupling defines the critical field-sweep rate and thus the critical fields of the avalanches and the intermediate magnetization plateaus. The presented data are in agreement to those findings. Our critical field-sweep rate is below 20 mT/min. In this context, also thermal conductivity measurements have to be interpreted cautiously. The hysteresis effects in zero field have always been unclear. A possible explanation could base on these magnetization dynamics. Depending on the field-sweep rate, the system can either show magnetization avalanches or not. Depending on the history, the sample can either have a large or strongly reduced remanence. Also the assigned temperature is maybe not correct, because every avalanche heats the system for a short time. Future experiments should be performed with a slow field-sweep rate so that the avalanche dynamics can be neglected.

A.4 $LiFe(WO_4)_2$

$LiFe(WO_4)_2$ has recently been characterized as the second multiferroic tungstate compound [221] after $MnWO_4$ [203, 204]. Although the iron moments in $LiFe(WO_4)_2$ are coupled via super-exchange over two oxygen sites compared to only one intermediate site in $MnWO_4$, the magnetic ordering temperature in the Lithium tungstate of 22.6 K is higher than in the manganese compound (13.5 K). Liu *et al.* studied polycrystalline samples and revealed two temperature-driven ordering transitions – one at $T_{N1} = 22.6$ K and another at $T_{N2} = 19.7$ K. They showed ferroelectric polarization below T_{N2} of 10 μC/m^2 [221].

P. Becker grew single-crystalline $LiFe(WO_4)_2$, which is characterized by specific heat and magnetization. Figure A.7(a) shows the specific heat for two different samples. In zero field, sample 1 shows one transition at 22 K. Besides this transition, two more kinks are visible at 19.5 K and 14.4 K. Because in literature only two transitions were reported, another sample was checked. Here, the zero-field data reveals only two transitions. The higher transition T_{N1} shows a sharp peak at 22 K. The second transition at 19 K is broadened. The data was obtained with the new vertical puck, see Chapter 3.5. The magnetic field was applied along $\boldsymbol{b}$ and $\boldsymbol{c}$. For $\boldsymbol{H} \parallel \boldsymbol{b}$, T_{N1} is almost field independent. T_{N2} reduces drastically to 16.3 K at 14 T. If the magnetic field is applied along $\boldsymbol{c}$, T_{N2} is almost field independent, while T_{N1} reduces in the magnetic field by 0.1 K/T. The zero-field data is in agreement with Ref. [221]. The magnetic-field data cannot be compared, as there is an obvious error in the paper, and they used powder samples, while we already showed an anisotropy of c_p.

The magnetization measurements, presented in Fig. A.7(b), for $\boldsymbol{H} \parallel \boldsymbol{b}$ show a Curie-Weiss like susceptibility above 75 K. With a fixed g factor of 2 the fit yields $J = 2.43$ and $\theta = -64.6$ K. The Curie-Weiss analysis indicates strong antiferromagnetic coupling and J is close to the expected spin-only value for Fe^{3+} moments with $L = 0$ and $S = 5/2$. In literature, the second transition at T_{N2} shows another kink in the susceptibility that is absent in our data. Because $LiFe(WO_4)_2$ was characterized as a multiferroic material, it was tried to perform pyrocurrent measurements on oriented samples to find the exact polarization direction. Apparently, the samples are not insulating enough, to apply a poling voltage. The room temperature resistivity of the sample is of the order of 100 Ω and increased to 10 MΩ at 60 K. Although this is an insulating behavior, the resistivity is too small. A voltage of 100 V yields a current of 10 µA, which is far above the expected pyrocurrent signals. Nonetheless, neutron experiments could be performed to prove the proposed incommensurate propagation vector $\boldsymbol{k} = (0.89\,0\,0.332)$ in the ferroelectric phase. For further measurements, the sample quality has to be checked by specific-heat measurements.

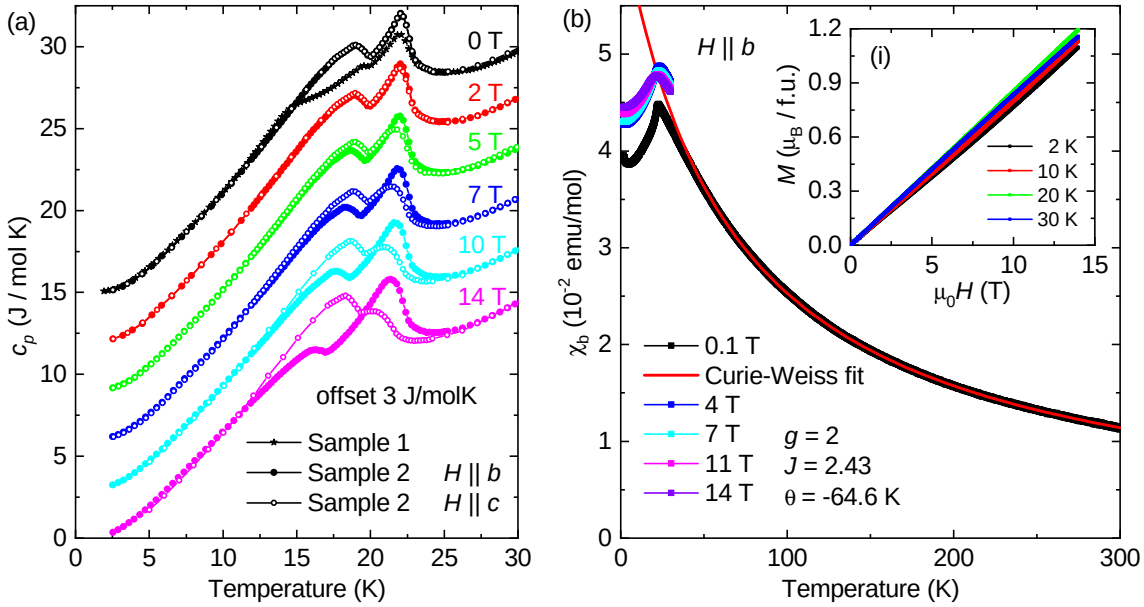

Figure A.7 Specific heat and thermal expansion of $LiFe(WO_4)_2$. (a) compares c_p for two different samples in zero field and for sample 2 in magnetic fields applied along ***b*** and ***c***. (b) presents the magnetic susceptibility χ_b. Inset (i) shows the field-dependent magnetization.

A.5 $Ba_{1-x}Sr_xCo_2V_2O_8$

Low-dimensional spin systems arise a lot of interest because they can be described with rather elementary models. In this context, 1D spin chains of different coupling phenomena, e.g., Heisenberg, XXZ, and Ising anisotropy have been studied. $BaCo_2V_2O_8$ and $SrCo_2V_2O_8$ are two material realizations of spin chains with Ising anisotropy. The crystal field at the Co spins results in an easy-axis anisotropy for the spin-½ moments parallel to [0 0 1], which is also the direction of the spin chains.[1] The 1D Ising chain can be tuned through a quantum phase transition by an external magnetic field perpendicular to the easy axis. In this case, a magnetic field in the *ab* plane drives this phase transition. In Cologne, samples were grown and characterized by S. Niessen [201]. Further studies on these samples investigated the quantum criticality for this transverse field orientation [85] and the dynamics and excitations for the longitudinal ($\boldsymbol{H} \parallel \boldsymbol{c}$) field orientation [222]. In the transverse field orientation, it turned out, that $BaCo_2V_2O_8$ is not isotropic but shows magnetic anisotropy between [1 0 0] and [1 1 0] [223]. In both directions, magnetic fields suppress the 3D order but with different critical fields of ∼10 T and ∼20 T, respectively. For the analogous Sr-based compound, which can be described with the same model but different coupling strengths and corresponding critical fields, an intermediate phase was found for $\boldsymbol{H} \parallel$ [1 0 0] [224]. Furthermore, in the same compound for $\boldsymbol{H} \parallel \boldsymbol{c}$ another intermediate incommensurate phase was reported [225]. In the framework of this work, some measurements on $Ba_{1-x}Sr_xCo_2V_2O_8$ were performed in order to confirm these phase transitions. This was done by ultrasound and thermal-expansion measurements in large magnetic fields. For information about the technique of ultrasound measurements see Appendix A.2.

Figures A.8 and A.9 show results of the ultrasound measurements at the HZDR. In magnetic field pulses with $\boldsymbol{H} \parallel$ [1 1 0], different ultrasound excitations were measured, which trigger different elastic constants. A detailed analysis was not done, since these measurements were mainly performed in order to look for phase transitions. For the longitudinal orientation, meaning $\boldsymbol{H} \parallel \boldsymbol{k} \parallel \boldsymbol{u}$, the sound velocity is essentially constant up to 35 T. For the lowest temperature of 1.5 K, there is a negative peak at 46.3 T. For larger magnetic fields, the sound velocity increases again and even becomes larger than in zero field. At this temperature, there is another low-field anomaly centered around 12 T, that is absent for 6 K and 10.1 K. The occurring transitions match the known critical fields for this field orientation. The main result from this is, that there is no indication of an additional transition in the intermediate field regime between the suppression of the 3D order and

[1] Co^{2+} has a spin $s = 3/2$ and an effective orbital momentum $l = 1$. The ground state is a $j = s - l = 1/2$ doublet.

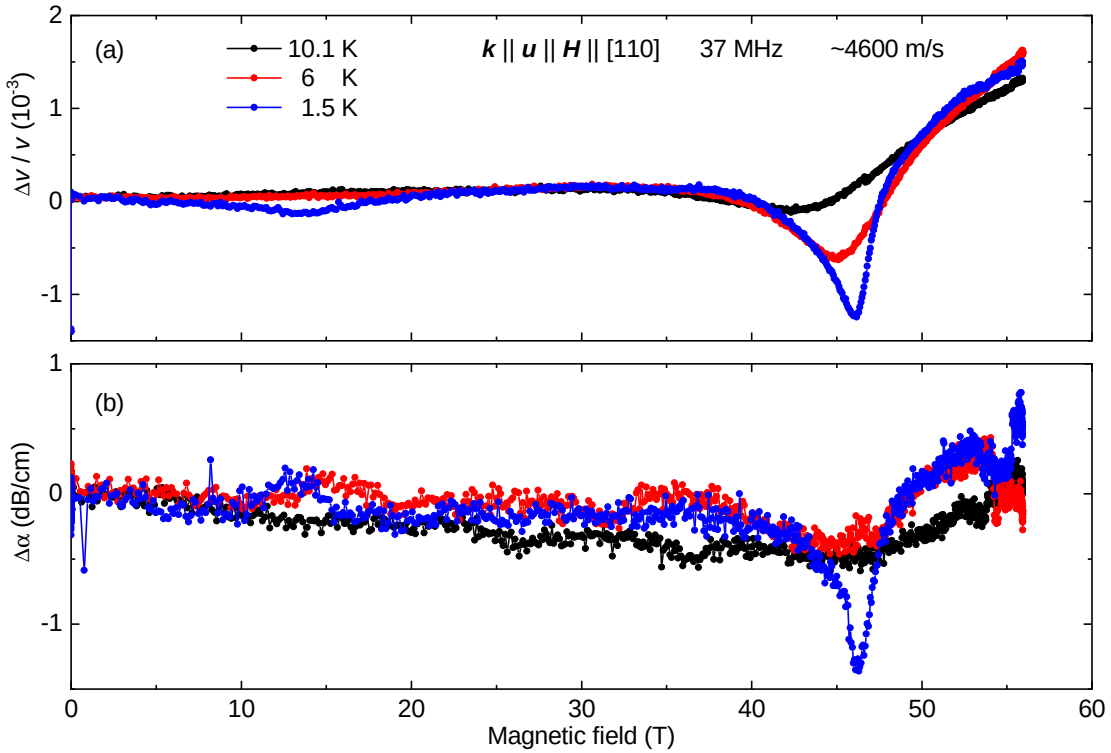

Figure A.8 Ultrasound measurements of $SrCo_2V_2O_8$ with $\boldsymbol{k} \parallel \boldsymbol{u} \parallel \boldsymbol{H} \parallel [1\,1\,0]$. (a) shows the relative changes of the sound velocity and (b) the attenuation for different temperatures. The sound velocity is ~4600 m/s and the transducers excite at a frequency of 37 MHz.

the quantum phase transition. The same anomalies are also found in the attenuation, see Fig. A.8(b), which shows the relative amplitude reduction of the signal inside the sample. However, it shall be noted that the changes of the attenuation are small for this setting.

For the transverse setting, two different ultrasound excitations were studied, namely $\boldsymbol{u} \parallel [0\,0\,1]$ and $[1\,\text{-}1\,0]$. The transverse sound velocity is approximately 2900 m/s, and, thus, it is approximately a factor two smaller than the longitudinal sound velocity. Both data sets were collected at approximately the same temperature (1.6 K and 1.7 K), but show qualitatively different results. For the data with $\boldsymbol{u} \parallel [0\,0\,1]$, we find similar results to the longitudinal setting, one peak at 15 T and another one at 47 T. In this case, both anomalies show a reduced sound velocity v_T, while for the longitudinal case the 3D order anomaly shows an enhanced v_L. The orientation with $\boldsymbol{u} \parallel [1\,\text{-}1\,0]$ shows only one anomaly at 17 T. The sound velocity increases continuously, with a nonphysical jump at 21 T. Also the correspond attenuation shows only one anomaly. Compared to the attenuation in the longitudinal case, here $\Delta\alpha$ is much larger, up to 30 dB/cm.

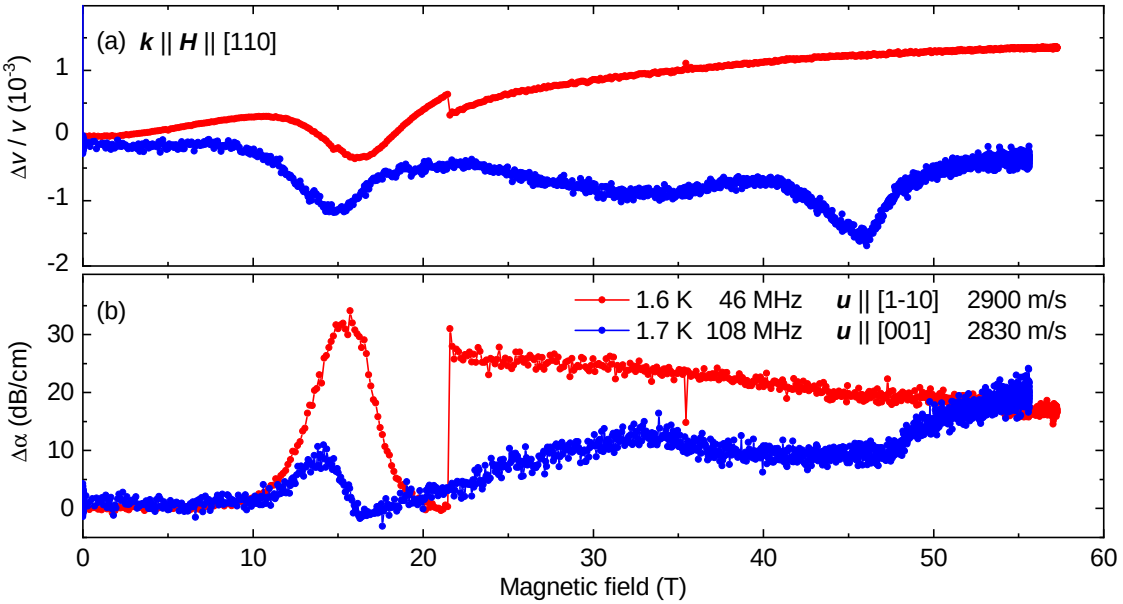

Figure A.9 Transverse ultrasound measurements of $SrCo_2V_2O_8$ with $\boldsymbol{k} \parallel \boldsymbol{H} \parallel [1\,1\,0]$. (a) shows the relative changes of the sound velocity and (b) the attenuation for the polarization directions [1 -1 0] and [0 0 1] at ~1.6 K. The sound velocity amounts to ~2900 m/s and the transducers excite at a frequency of 46 MHz and 108 MHz.

Figure A.10 compares magnetostriction measurements for a magnetic field along [1 1 0] up to 35 T, measured at the HFML Nijmegen. The Barium parent compound shows contraction on increasing magnetic field and thus a negative magnetostriction. With decreasing temperature, a broad anomaly arises that sharpens at 1.4 K to 24.5 T. This peak stems from the quantum phase transition. The half substituted material $Ba_{0.5}Sr_{0.5}Co_2V_2O_8$ shows a drastically reduced magnetostriction. The inset shows a small peak in λ in the low-field regime up to 15 T. Its critical field increases with decreasing temperature. For larger magnetic fields, no further transitions are found. λ decreases up to 20 T and shows a maximum at 29 T. Both extremums are hardly temperature dependent. The pure Sr compound, in contrast to the previously described materials, has a large positive magnetostriction. The whole field range does not contain any transition. The magnetostriction coefficient shows a maximum at 20 T for 1.3 K that shifts to 25 T for 4.2 K. The quantum phase transition is expected to happen at ~46 T, and, thus, it cannot be observed in this data. Because the half-substituted material also shows no high-field anomaly, it can be concluded that the expected quantum phase transition is already shifted above 35 T. Furthermore, with increasing strontium content the magnetostriction is tuned from contraction to elongation. Thus, the magnetoelectric coupling changes drastically.

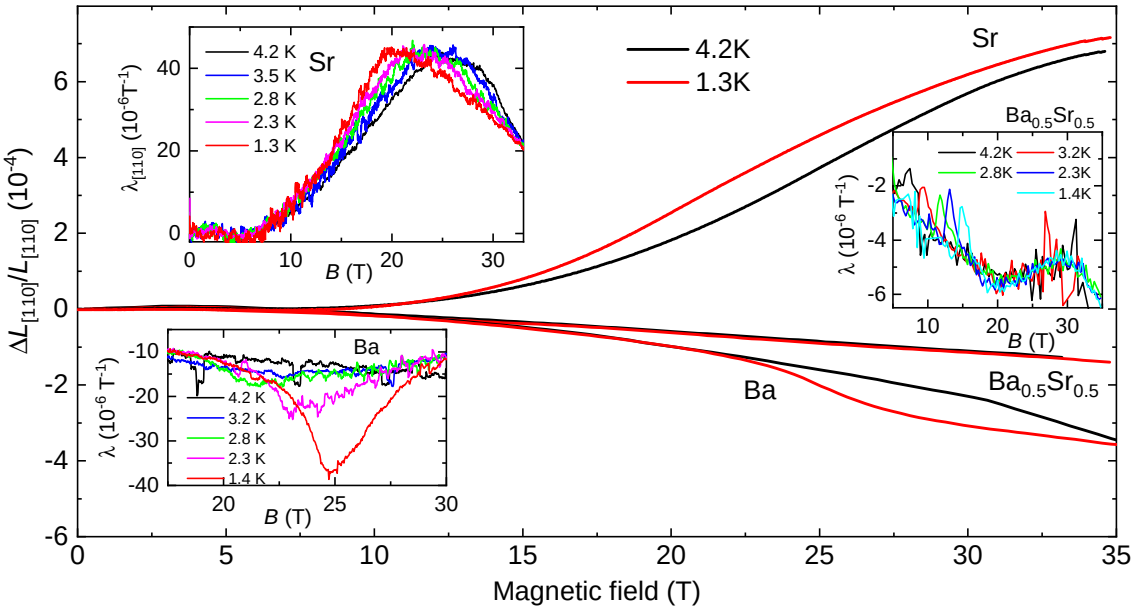

Figure A.10 Comparison of the magnetostriction of $BaCo_2V_2O_8$, $Ba_{0.5}Sr_{0.5}Co_2V_2O_8$, and $SrCo_2V_2O_8$ for $\boldsymbol{H}$ || [1 1 0] up to 35 T. The insets show the magnetostriction coefficient $\lambda_{[110]}$ for multiple temperatures for a single Ba-Sr content.

A.6 Küchler dilatometer cell effect

For thermal-expansion and magnetostriction measurements in the temperature range from 2 K to 300 K, a dilatometer constructed by S. Orbe [62] was used inside a VTI. Additionally, the *tadnull* setup was used for zero-field characterizations. Only recently, Küchler *et al.* [80, 81] constructed dilatometers of different size made from one peace of CuBe. This material has the advantage of a well reduced electric conductivity, while the thermal conductivity does not change too much. The dilatometers can be used for high-field measurements as performed at the HFML Nijmegen, because eddy currents are damped. Such a dilatometer was bought to replace the VTI dilatometer. Figure A.11 shows the measured empty cell effect. The data was fitted with a polynomial function to use this for sample data analysis. In cells made from pure Cu, eddy currents yield a large background signal in magnetostriction measurements that additionally depends on the field-sweep rate. The reduced conductivity of the CuBe dilatometer body results in drastically damped eddy currents, and, thus, the magnetostriction background is essentially zero, see panel (b). The deviations between up and down measurement at 40 K stem from the instability of the temperature. Consequently, the sample data analysis with this dilatometer does not require any cell-effect correction for magnetostriction measurements.

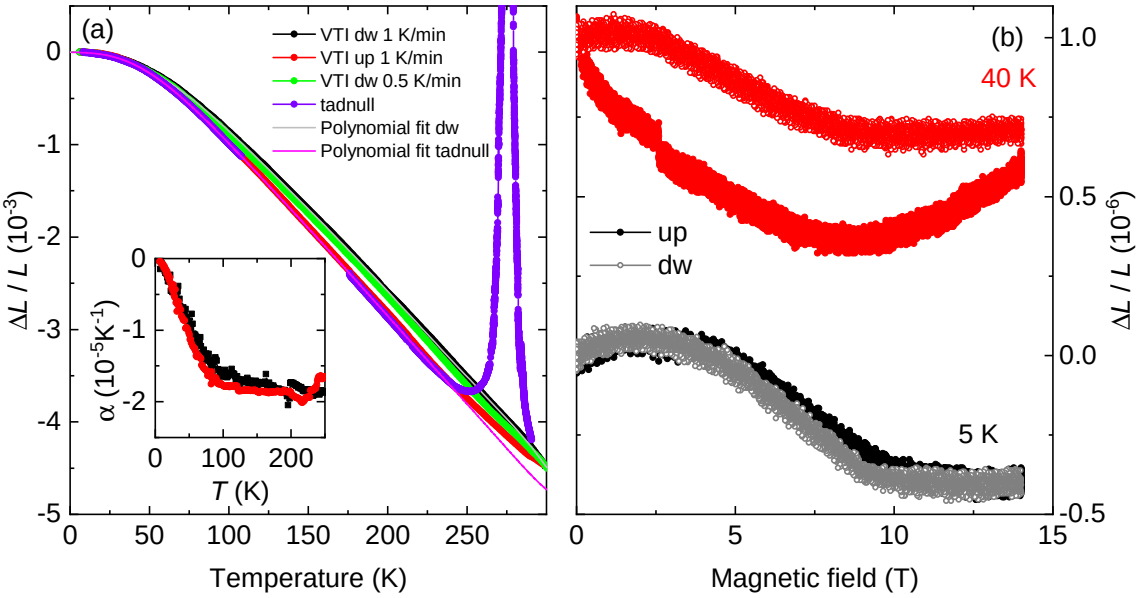

Figure A.11 Cell effect of the Küchler dilatometer [80]. (a) shows the cell effect for thermal-expansion measurements with different temperature ramps measured in the VTI and tadnull. (b) presents the magnetostrictive cell effect at two different temperatures.

A.7 Magnetometer cell effect in the gradient cryostat

Figure A.12 shows the magnetometer cell effect measured in the gradient cryostat. The field-dependent magnetic moment of the cell was obtained with the procedure described in the experimental Chapter 3.3.3. The magnetization as a function of field should be an odd function. It consists of two components, a paramagnetic signal and a diamagnetic signal. It was tried to fit all data with minimal parameters, but this did not work out for the whole temperature range. Thus, a description with Chebyshev polynomials was chosen (solid lines). For the temperature-dependent cell effect, see panel (b), the temperature was changed in small steps between a set of points as described in 3.3.3, but without a stabilization of the temperatures to reduce the measurement time. Nonetheless, smooth background curves were obtained by this technique that is also applicable for sample measurements. Again, the obtained data were described with Chebyshev polynomials (solid lines). All fit results can be loaded to the data analysis software to subtract the cell effect from a measurement with any sample.

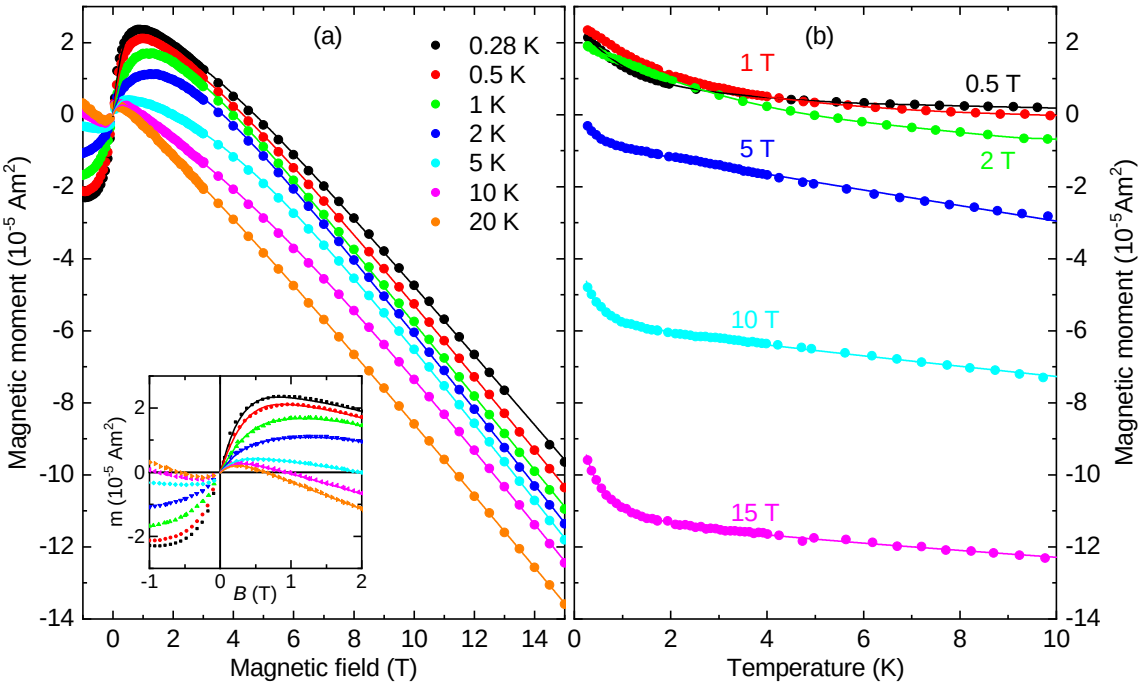

Figure A.12 Cell effect of the magnetometer in the gradient cryostat. (a) shows the magnetization of the empty magnetometer vs. magnetic field. (b) presents the temperature-dependent cell effect. All measurements were performed with the procedure described in Chapter 3.3. This background is fitted with Chebyshev polynomials (solid lines) that can be used in the software to subtract this background.

List of Figures

List of Tables

Bibliography

[1] P. S. Schmidl, J. Arab. Islam. Stud. **1**, 81 (2017).

[2] R. L. Comstock, J. Mater. Sci. Mater. Electron. **13**, 509 (2002).

[3] A. Hirohata, K. Yamada, Y. Nakatani, L. Prejbeanu, B. Diény, P. Pirro, and B. Hillebrands, J. Magn. Magn. Mater. **509**, 166711 (2020).

[4] W. L. Roth, Phys. Rev. **110**, 1333 (1958).

[5] S. Mühlbauer *et al.*, Science **323**, 915 (2009).

[6] A. Kitaev, Ann. Phys. (N. Y). **321**, 2 (2006).

[7] Y. Kasahara *et al.*, Nature **559**, 227 (2018).

[8] J. Chaloupka, G. Jackeli, and G. Khaliullin, Phys. Rev. Lett. **105**, 027204 (2010).

[9] S. K. Choi *et al.*, Phys. Rev. Lett. **108**, 127204 (2012).

[10] T. Dey, A. V. Mahajan, P. Khuntia, M. Baenitz, B. Koteswararao, and F. C. Chou, Phys. Rev. B **86**, 140405 (2012).

[11] A. Revelli *et al.*, Sci. Adv. **5**, eaav4020 (2019).

[12] Y. Maeno, H. Hashimoto, K. Yoshida, S. Nishizaki, T. Fujita, J. G. Bednorz, and F. Lichtenberg, Nature **372**, 532 (1994).

[13] M. K. Wu *et al.*, Phys. Rev. Lett. **58**, 908 (1987).

[14] K. Ishida, H. Mukuda, Y. Kitaoka, K. Asayama, Z. Q. Mao, Y. Mori, and Y. Maeno, Nature **396**, 658 (1998).

[15] A. Pustogow *et al.*, Nature **574**, 72 (2019).

[16] G. Koster *et al.*, Rev. Mod. Phys. **84**, 253 (2012).

[17] Z. Fang *et al.*, Science **302**, 92 (2003).

[18] S. Itoh *et al.*, Nat. Commun. **7**, 11788 (2016).

[19] S. Kunkemöller, F. Sauer, A. A. Nugroho, and M. Braden, Cryst. Res. Technol. **51**, 299 (2016).

[20] S. Hartwig, Ph.D. thesis, Universität Bayreuth (2003).

[21] G. J. Wessel and D. J. W. Ijdo, Acta Crystallogr. **10**, 466 (1957).

[22] T. Ziman, J. P. Boucher, Y. Inagaki, and Y. Ajiro, J. Phys. Soc. Japan **74**, 119 (2005).

[23] R. Gross and A. Marx, *Festkörperphysik*, 3 ed. (De Gruyter, Berlin, 2018).

[24] A. F. Ioffe and A. R. Regel, Prog. Semicond **4**, 237 (1960).

[25] N. F. Mott, *Metal Insulator Transitions* (Taylor and Francis, London, 1974).

[26] N. W. Ashcroft and N. D. Mermin, *Solid State Physics*, 2010 ed. (Brooks/Cole, Cengage Learning, Belmont, CA, 2010).

[27] E. H. Hall, Am. J. Math. **2**, 287 (1879).

[28] E. H. Hall, London, Edinburgh, Dublin Philos. Mag. J. Sci. **12**, 157 (1881).

[29] N. Nagaosa, J. Sinova, S. Onoda, A. H. MacDonald, and N. P. Ong, Rev. Mod. Phys. **82**, 1539 (2010).

[30] L. Berger, J. Appl. Phys. **34**, 1360 (1963).

[31] L. Berger, Phys. Rev. B **2**, 4559 (1970).

[32] R. Karplus and J. M. Luttinger, Phys. Rev. **95**, 1154 (1954).

[33] J. M. Luttinger, Phys. Rev. **112**, 739 (1958).

[34] M. Onoda and N. Nagaosa, J. Phys. Soc. Japan **71**, 19 (2002).

[35] N. Nagaosa, J. Phys. Soc. Japan **75**, 042001 (2006).

[36] M. Gradhand, D. V. Fedorov, F. Pientka, P. Zahn, I. Mertig, and B. L. Györffy, J. Phys. Condens. Matter **24**, 213202 (2012).

[37] M. V. Berry and M. Wilkinson, Proc. R. Soc. London. A. Math. Phys. Sci. **392**, 15 (1984).

[38] Y. Yao *et al.*, Phys. Rev. Lett. **92**, 037204 (2004).

[39] I. V. Solovyev, Phys. Rev. B **67**, 174406 (2003).

[40] P. W. Anderson, Phys. Rev. **115**, 2 (1959).

[41] P. W. Anderson, Solid State Phys. **14**, 99 (1963).

[42] J. B. Goodenough, *Magnetism and the Chemical Bond* (John Wiley and Sons, New York, 1963).

[43] L. D. Landau, Zhurnal Eksp. i Teor. Fiz. **7**, 19 (1937).

[44] R. B. Griffiths, Phys. Rev. Lett. **24**, 1479 (1970).

[45] G. H. Wannier, Phys. Rev. **79**, 357 (1950).

[46] N. D. Mermin and H. Wagner, Phys. Rev. Lett. **17**, 1133 (1966).

[47] J. M. Kosterlitz and D. J. Thouless, J. Phys. C Solid State Phys. **6**, 1181 (1973).

[48] L. Capriotti, A. E. Trumper, and S. Sorella, Phys. Rev. Lett. **82**, 3899 (1999).

[49] T. Takagi and M. Mekata, J. Phys. Soc. Japan **64**, 4609 (1995).

[50] L. Seabra, T. Momoi, P. Sindzingre, and N. Shannon, Phys. Rev. B **84**, 214418 (2011).

[51] M. Yun and G. S. Jeon, J. Phys. Conf. Ser. **592**, 012111 (2015).

[52] A. Sen, F. Wang, K. Damle, and R. Moessner, Phys. Rev. Lett. **102**, 227001 (2009).

[53] B. D. Metcalf, Phys. Lett. A **46**, 325 (1974).

[54] Y. Tanaka and N. Uryû, J. Phys. Soc. Japan **39**, 825 (1975).

[55] E. Wawrzyńska *et al.*, Phys. Rev. B **77**, 094439 (2008).

[56] L. Seabra and N. Shannon, Phys. Rev. B **83**, 134412 (2011).

[57] L. Seabra and N. Shannon, Phys. Rev. Lett. **104**, 237205 (2010).

[58] F. Matsubara and S. Inawashiro, J. Phys. Soc. Japan **55**, 1438 (1986).

[59] T. Kudo and S. Katsura, Prog. Theor. Phys. **56**, 435 (1976).

[60] R. McCormack, M. Asta, D. de Fontaine, G. Garbulsky, and G. Ceder, Phys. Rev. B **48**, 6767 (1993).

[61] U. Brandt and J. Stolze, Zeitschrift für Phys. B Condens. Matter **64**, 481 (1986).

[62] S. Orbe, Diplomarbeit, Universität zu Köln (2011).

[63] M. Hofmann, Ph.D. thesis, Universität zu Köln (2002).

[64] K. Berggold, Diplomarbeit, Universität zu Köln (2003).

[65] S. Kopatz, Masterarbeit, Universität zu Köln (2018).

[66] Oxford Instruments, https://nanoscience.oxinst.com/products/helium3-refrigerators/helioxvl.

[67] J. C. Oersted, Ann. Philos. **16**, 273 (1820).

[68] F. Bitter, Rev. Sci. Instrum. **7**, 479 (1936).

[69] F. Bitter, Rev. Sci. Instrum. **7**, 482 (1936).

[70] HFML Nijmegen, https://www.ru.nl/hfml/research/levitation/diamagnetic-levitation/bitter-solenoid.

[71] S. Zherlitsyn, T. Herrmannsdörfer, Y. Skourski, A. Sytcheva, and J. Wosnitza, J. Low Temp. Phys. **146**, 719 (2007).

[72] Quantum Design, Magnetic Property Measurement System, AC Option User's Manual (1999).

[73] *The SQUID Handbook Vol. I*, edited by J. Clarke and A. I. Braginski (Wiley, Weinheim, 2004).

[74] *The SQUID Handbook Vol. II*, edited by J. Clarke and A. I. Braginski (Wiley, Weinheim, 2006).

[75] Quantum Design, Physical Property Measurement System Vibrating Sample Magnetometer (VSM) Option User's Manual Rev. A-2 (2004).

[76] Quantum Design, Magnetic Property Measurement System, Oven Option User's Manual (1999).

[77] D. Löwen, Diplomarbeit, Universität zu Köln (2011).

[78] O. Heyer, Diplomarbeit, Universität zu Köln (2005).

[79] G. Brändli and R. Griessen, Cryogenics (Guildf). **13**, 299 (1973).

[80] R. Küchler, T. Bauer, M. Brando, and F. Steglich, Rev. Sci. Instrum. **83**, 1 (2012).

[81] R. Küchler, A. Wörl, P. Gegenwart, M. Berben, B. Bryant, and S. Wiedmann, Rev. Sci. Instrum. **88**, 083903 (2017).

[82] O. Breunig, Ph.D. thesis, Universität zu Köln (2015).

[83] D. Brüning, Bachelorarbeit, Universität zu Köln (2014).

[84] A. Scheie, J. Low Temp. Phys. **193**, 60 (2018).

[85] Z. Wang *et al.*, Phys. Rev. Lett. **120**, 207205 (2018).

[86] T. Nomura, Private Communication (2018).

[87] R. L. Byer and C. B. Roundy, Ferroelectrics **3**, 333 (1972).

[88] S. Jodlauk, Ph.D. thesis, Universität zu Köln (2009).

[89] M. Ackermann, Ph.D. thesis, Universität zu Köln (2014).

[90] D. Brüning, Masterarbeit, Universität zu Köln (2016).

[91] A. von Hippel, Rev. Mod. Phys. **22**, 221 (1950).

[92] D. I. Khomskii, *Transition Metal Compounds* (Cambridge University Press, Cambridge, 2014).

[93] J. J. Randall and R. Ward, J. Am. Chem. Soc. **81**, 2629 (1959).

[94] Y. S. Lee, J. S. Lee, T. W. Noh, D. Y. Byun, K. S. Yoo, K. Yamaura, and E. Takayama-Muromachi, Phys. Rev. B **67**, 113101 (2003).

[95] G. Cao, C. Alexander, S. McCall, J. Crow, and R. Guertin, Mater. Sci. Eng. B **63**, 76 (1999).

[96] J. G. Bednorz and K. A. Müller, Zeitschrift für Phys. B Condens. Matter **64**, 189 (1986).

[97] A. P. Mackenzie and Y. Maeno, Rev. Mod. Phys. **75**, 657 (2003).

[98] Y. Maeno, S. Kittaka, T. Nomura, S. Yonezawa, and K. Ishida, J. Phys. Soc. Japan **81**, 011009 (2012).

[99] A. P. Mackenzie, T. Scaffidi, C. W. Hicks, and Y. Maeno, npj Quantum Mater. **2**, 40 (2017).

[100] C. W. Jones, P. D. Battle, P. Lightfoot, and W. T. A. Harrison, Acta Crystallogr. Sect. C Cryst. Struct. Commun. **45**, 365 (1989).

[101] B. J. Kennedy and B. A. Hunter, Phys. Rev. B **58**, 653 (1998).

[102] B. C. Chakoumakos, S. E. Nagler, S. T. Misture, and H. M. Christen, Phys. B **241-243**, 358 (1998).

[103] K. J. Choi, S. H. Baek, H. W. Jang, L. J. Belenky, M. Lyubchenko, and C.-B. Eom, Adv. Mater. **22**, 759 (2010).

[104] R. Bouchard and J. Gillson, Mater. Res. Bull. **7**, 873 (1972).

[105] A. Kanbayasi, J. Phys. Soc. Japan **41**, 1876 (1976).

[106] T. Moriya, in *Metallic magnetism*, edited by H. Capellmann (Springer Verlag, Berlin, 1987).

[107] A. Kanbayasi, J. Phys. Soc. Japan **41**, 1879 (1976).

[108] A. Kanbayasi, J. Phys. Soc. Japan **44**, 108 (1978).

[109] Y. Kats, I. Genish, L. Klein, J. W. Reiner, and M. R. Beasley, Phys. Rev. B **71**, 100403 (2005).

[110] L. Klein *et al.*, J. Phys. Condens. Matter **8**, 10111 (1996).

[111] S. Kolesnik, Y. Z. Yoo, O. Chmaissem, B. Dabrowski, T. Maxwell, C. W. Kimball, and A. P. Genis, J. Appl. Phys. **99**, 08F501 (2006).

[112] Y. Z. Yoo *et al.*, Appl. Phys. Lett. **89**, 124104 (2006).

[113] D. Kim, B. L. Zink, and F. Hellman, Phys. Rev. B **67**, 100406(R) (2003).

[114] G. J. Snyder, arXiv:1904.12193 (2019).

[115] Y. Kats, L. Klein, J. W. Reiner, T. H. Geballe, M. R. Beasley, and A. Kapitulnik, Phys. Rev. B **63**, 054435 (2001).

[116] T. Kiyama, K. Yoshimura, K. Kosuge, Y. Ikeda, and Y. Bando, Phys. Rev. B **54**, R756 (1996).

[117] G. M. Leitus, S. Reich, and F. Frolow, J. Magn. Magn. Mater. **206**, 27 (1999).

[118] A. P. Mackenzie *et al.*, Phys. Rev. B **58**, R13318 (1998).

[119] N. V. Volkenshtein, V. P. Dyakina, and V. E. Startsev, Phys. Status Solidi **57**, 9 (1973).

[120] L. Klein, J. S. Dodge, C. H. Ahn, G. J. Snyder, T. H. Geballe, M. R. Beasley, and A. Kapitulnik, Phys. Rev. Lett. **77**, 2774 (1996).

[121] P. B. Allen *et al.*, Phys. Rev. B **53**, 4393 (1996).

[122] N. Haham, Y. Shperber, M. Schultz, N. Naftalis, E. Shimshoni, J. W. Reiner, and L. Klein, Phys. Rev. B **84**, 174439 (2011).

[123] F. Bern, M. Ziese, A. Setzer, E. Pippel, D. Hesse, and I. Vrejoiu, J. Phys. Condens. Matter **25**, 496003 (2013).

[124] M. Ziese, L. Jin, and I. Lindfors-Vrejoiu, J. Phys. Mater. **2**, 034008 (2019).

[125] G. Santi and T. Jarlborg, J. Phys. Condens. Matter **9**, 9563 (1997).

[126] I. Lindfors-Vrejoiu and M. Ziese, Phys. status solidi **254**, 1600556 (2017).

[127] J. Matsuno *et al.*, Sci. Adv. **2**, e1600304 (2016).

[128] D. Kan, T. Moriyama, K. Kobayashi, and Y. Shimakawa, Phys. Rev. B **98**, 180408 (2018).

[129] L. Thomas, Bachelorarbeit, Universität zu Köln (2019).

[130] N. Kikugawa, R. Baumbach, J. S. Brooks, T. Terashima, S. Uji, and Y. Maeno, Cryst. Growth Des. **15**, 5573 (2015).

[131] G. Cao, S. McCall, M. Shepard, and J. E. Crow, Phys. Rev. B **56**, 321 (1997).

[132] T. Kiyama, K. Yoshimura, K. Kosuge, H. Michor, and A. Gerfried Hilscher, J. Phys. Soc. Japan **67**, 307 (1998).

[133] Y. Maeno *et al.*, J. Phys. Soc. Japan **66**, 1405 (1997).

[134] S.-I. Ikeda, Y. Maeno, S. Nakatsuji, M. Kosaka, and Y. Uwatoko, Phys. Rev. B **62**, R6089 (2000).

[135] M. C. Langner *et al.*, Phys. Rev. Lett. **102**, 177601 (2009).

[136] S. Kunkemöller, D. Brüning, A. Stunault, A. A. Nugroho, T. Lorenz, and M. Braden, Phys. Rev. B **96**, 220406 (2017).

[137] M. Ziese, I. Vrejoiu, and D. Hesse, Phys. Rev. B **81**, 184418 (2010).

[138] A. L. Roitburd, Phys. Status Solidi **37**, 329 (1976).

[139] I. A. Luk'yanchuk, A. Schilling, J. M. Gregg, G. Catalan, and J. F. Scott, Phys. Rev. B **79**, 144111 (2009).

[140] M. Braden, G. Heger, P. Schweiss, Z. Fisk, K. Gamayunov, I. Tanaka, and H. Kojima, Phys. C Supercond. its Appl. **191**, 455 (1992).

[141] Y. Shimakawa, Y. Kubo, and T. Manako, Nature **379**, 53 (1996).

[142] M. Kataoka, Phys. Rev. B **63**, 134435 (2001).

[143] L. Klein, J. Reiner, T. Geballe, M. Beasley, and A. Kapitulnik, Phys. B Condens. Matter **281-282**, 608 (2000).

[144] M. Izumi, K. Nakazawa, Y. Bando, Y. Yoneda, and H. Terauchi, J. Phys. Soc. Japan **66**, 3893 (1997).

[145] K. Jenni *et al.*, Phys. Rev. Lett. **123**, 017202 (2019).

[146] R. Mathieu, C. U. Jung, H. Yamada, A. Asamitsu, M. Kawasaki, and Y. Tokura, Phys. Rev. B **72**, 064436 (2005).

[147] S. V. Streltsov and D. I. Khomskii, Private Communication (2019).

[148] T. Herfurth, S. Streib, and P. Kopietz, Phys. Rev. B **88**, 174404 (2013).

[149] J. Alicea, A. V. Chubukov, and O. A. Starykh, Phys. Rev. Lett. **102**, 137201 (2009).

[150] Y. Tokiwa, T. Radu, R. Coldea, H. Wilhelm, Z. Tylczynski, and F. Steglich, Phys. Rev. B **73**, 134414 (2006).

[151] T. Ono, H. Tanaka, H. Aruga Katori, F. Ishikawa, H. Mitamura, and T. Goto, Phys. Rev. B **67**, 104431 (2003).

[152] S. M. Winter, A. A. Tsirlin, M. Daghofer, J. van den Brink, Y. Singh, P. Gegenwart, and R. Valentí, J. Phys. Condens. Matter **29**, 493002 (2017).

[153] H. Takagi, T. Takayama, G. Jackeli, G. Khaliullin, and S. E. Nagler, Nat. Rev. Phys. **1**, 264 (2019).

[154] O. A. Starykh, Reports Prog. Phys. **78**, 052502 (2015).

[155] H. Schilling, Masterarbeit - Kristallografie, Universität zu Köln (2020).

[156] S. Biesenkamp, Private Communication (2020).

[157] T. Fröhlich, Ph.D. thesis, Universität zu Köln (2020).

[158] I. Cisarova, Private Communication (2018).

[159] F. Wei, F. Brivio, Y. Wu, P. D. Bristowe, and A. K. Cheetham, J. Mater. Chem. C **6**, 3573 (2018).

[160] R. Saillant, R. B. Jackson, W. E. Streib, K. Folting, and R. A. D. Wentworth, Inorg. Chem. **10**, 1453 (1971).

[161] B. Leuenberger, H. U. Güdel, and P. Fischer, J. Solid State Chem. **64**, 90 (1986).

[162] B. Leuenberger, H. U. Güdel, R. Feile, and J. K. Kjems, Phys. Rev. B **28**, 5368 (1983).

[163] B. Leuenberger, A. Stebler, H. U. Güdel, A. Furrer, R. Feile, and J. K. Kjems, Phys. Rev. B **30**, 6300 (1984).

[164] B. Grenier and T. Ziman, Comptes Rendus Phys. **8**, 717 (2007).

[165] B. Leuenberger, H. U. Güdel, D. Petitgrand, and J. K. Kjems, Inorg. Chem. **24**, 1035 (1985).

[166] I. Affleck, Phys. Rev. B **43**, 3215 (1991).

[167] B. Grenier, L.-P. Regnault, Y. Inagaki, Y. Ajiro, T. Ziman, and J. Boucher, Phys. B Condens. Matter **385-386**, 447 (2006).

[168] A. Pabst, Am. Mineral. **23**, 175 (1938).

[169] A. Muir and H. Wiedersich, J. Phys. Chem. Solids **28**, 65 (1967).

[170] J.-P. Doumerc, A. Wichainchai, A. Ammar, M. Pouchard, and P. Hagenmuller, Mater. Res. Bull. **21**, 745 (1986).

[171] T. T. A. Lummen, C. Strohm, H. Rakoto, A. A. Nugroho, and P. H. M. van Loosdrecht, Phys. Rev. B **80**, 012406 (2009).

[172] Y. Ajiro, T. Asano, T. Takagi, M. Mekata, H. Aruga Katori, and T. Goto, Phys. B Phys. Condens. Matter **201**, 71 (1994).

[173] S. Mitsuda, N. Kasahara, T. Uno, and M. Mase, J. Phys. Soc. Japan **67**, 4026 (1998).

[174] M. Mekata, N. Yaguchi, T. Takagi, S. Mitsuda, and H. Yoshizawa, J. Magn. Magn. Mater. **104-107**, 823 (1992).

[175] S. Mitsuda, H. Yoshizawa, N. Yaguchi, and M. Mekata, J. Phys. Soc. Japan **60**, 1885 (1991).

[176] M. Mekata *et al.*, J. Phys. Soc. Japan **62**, 4474 (1993).

[177] N. Terada, S. Mitsuda, H. Ohsumi, and K. Tajima, J. Phys. Soc. Japan **75**, 023602 (2006).

[178] T. Nakajima, N. Terada, S. Mitsuda, and R. Bewley, Phys. Rev. B **88**, 134414 (2013).

[179] T. T. A. Lummen, C. Strohm, H. Rakoto, and P. H. M. van Loosdrecht, Phys. Rev. B **81**, 224420 (2010).

[180] N. Terada *et al.*, Phys. Rev. B **75**, 224411 (2007).

[181] T. Kimura, J. C. Lashley, and A. P. Ramirez, Phys. Rev. B **73**, 220401 (2006).

[182] N. Terada, J. Phys. Condens. Matter **26**, 453202 (2014).

[183] H. Mitamura, S. Mitsuda, S. Kanetsuki, H. Aruga Katori, T. Sakakibara, and K. Kindo, J. Phys. Soc. Japan **76**, 094709 (2007).

[184] T.-h. Arima, J. Phys. Soc. Japan **76**, 073702 (2007).

[185] T. Nakajima *et al.*, Phys. Rev. B **79**, 214423 (2009).

[186] J. T. Haraldsen, M. Swanson, G. Alvarez, and R. S. Fishman, Phys. Rev. Lett. **102**, 237204 (2009).

[187] F. Ye, J. A. Fernandez-Baca, R. S. Fishman, Y. Ren, H. J. Kang, Y. Qiu, and T. Kimura, Phys. Rev. Lett. **99**, 15201 (2007).

[188] N. Terada, S. Mitsuda, Y. Oohara, H. Yoshizawa, and H. Takei, J. Magn. Magn. Mater. **272-276**, E997 (2004).

[189] N. Terada, S. Mitsuda, T. Fujii, and D. Petitgrand, J. Phys. Condens. Matter **19**, 145241 (2007).

[190] S. Kanetsuki, S. Mitsuda, T. Nakajima, D. Anazawa, H. Aruga Katori, and K. Prokes, J. Phys. Condens. Matter **19**, 145244 (2007).

[191] N. Terada, D. D. Khalyavin, P. Manuel, T. Osakabe, P. G. Radaelli, and H. Kitazawa, Phys. Rev. B **89**, 220403 (2014).

[192] H. Tamatsukuri *et al.*, Phys. Rev. B **94**, 174402 (2016).

[193] R. S. Fishman, J. Appl. Phys. **103**, 107 (2008).

[194] T. Nakajima *et al.*, J. Phys. Soc. Japan **80**, 014714 (2011).

[195] T. Nakajima, A. Suno, S. Mitsuda, N. Terada, S. Kimura, K. Kaneko, and H. Yamauchi, Phys. Rev. B **84**, 184401 (2011).

[196] F. Ye, Y. Ren, Q. Huang, J. A. Fernandez-Baca, P. Dai, J. W. Lynn, and T. Kimura, Phys. Rev. B **73**, 220404 (2006).

[197] S. Kimura, N. Nishihagi, H. Yamaguchi, T. Kashiwagi, M. Hagiwara, N. Terada, and K. Kindo, J. Low Temp. Phys. **159**, 80 (2010).

[198] J. Engelmayer, Ph.D. thesis, Universität zu Köln (2020).

[199] R. Nath, K. M. Ranjith, B. Roy, D. C. Johnston, Y. Furukawa, and A. A. Tsirlin, Phys. Rev. B **90**, 024431 (2014).

[200] C. Braschoss, Bachelorarbeit, Universität zu Köln (2019).

[201] S. K. Niesen, Ph.D. thesis, Universität zu Köln (2015).

[202] T. Kimura, T. Goto, H. Shintani, K. Ishizaka, T. Arima, and Y. Tokura, Nature **426**, 55 (2003).

[203] O. Heyer *et al.*, J. Phys. Condens. Matter **18**, L471 (2006).

[204] K. Taniguchi, N. Abe, T. Takenobu, Y. Iwasa, and T. Arima, Phys. Rev. Lett. **97**, 097203 (2006).

[205] D. I. Khomskii, Physics (College. Park. Md). **2**, 20 (2009).

[206] C. P. Grams *et al.*, Sci. Rep. **9**, 4391 (2019).

[207] M. Ackermann, D. Brüning, T. Lorenz, P. Becker, and L. Bohatý, New J. Phys. **15**, 123001 (2013).

[208] R. Resta, J. Phys. Condens. Matter **12**, R107 (2000).

[209] M. V. Berry, Proc. R. Soc. London. A. Math. Phys. Sci. **392**, 45 (1984).

[210] B. Wolf, B. Lüthi, S. Schmidt, H. Schwenk, M. Sieling, S. Zherlitsyn, and I. Kouroudis, Phys. B Condens. Matter **294-295**, 612 (2001).

[211] C. Castelnovo, R. Moessner, and S. Sondhi, Annu. Rev. Condens. Matter Phys. **3**, 35 (2012).

[212] L. Pauling, J. Am. Chem. Soc. **57**, 2680 (1935).

[213] W. F. Giauque and M. F. Ashley, Phys. Rev. **43**, 81 (1933).

[214] D. Pomaranski *et al.*, Nat. Phys. **9**, 353 (2013).

[215] C. Castelnovo, R. Moessner, and S. L. Sondhi, Nature **451**, 42 (2008).

[216] S. Scharffe, Ph.D. thesis, Universität zu Köln (2016).

[217] G. Kolland, Ph.D. thesis, Universtität zu Köln (2013).

[218] S. Scharffe, O. Breunig, V. Cho, P. Laschitzky, M. Valldor, J. F. Welter, and T. Lorenz, Phys. Rev. B **92**, 180405 (2015).

[219] D. Slobinsky, C. Castelnovo, R. Borzi, A. Gibbs, A. Mackenzie, R. Moessner, and S. Grigera, Phys. Rev. Lett. **105**, 267205 (2010).

[220] M. J. Jackson *et al.*, Phys. Rev. B **90**, 064427 (2014).

[221] M. Liu *et al.*, Phys. Rev. B **95**, 195134 (2017).

[222] Z. Wang *et al.*, Phys. Rev. Lett. **123**, 067202 (2019).

[223] A. Herman, Bachelorarbeit, Universität zu Köln (2016).

[224] Y. Cui *et al.*, Phys. Rev. Lett. **123**, 067203 (2019).

[225] L. Shen, O. Zaharko, J. O. Birk, E. Jellyman, Z. He, and E. Blackburn, New J. Phys. **21**, 073014 (2019).

Danksagung

Zum Abschluss dieser Arbeit möchte ich mich bei denjenigen bedanken, die mich während der letzten Jahre begleitet und unterstützt haben. Zuallererst möchte ich meinem Doktorvater Prof. Dr. Thomas Lorenz danken, nicht nur für die Betreuung bei meiner gesamten wissenschaftlichen Arbeit im II. Physikalischen Institut, sondern auch für die Erfahrungen, die er mir über diese Arbeit hinaus ermöglichte, und die stets positive Arbeitsatmosphäre. Außerdem bedanke ich mich bei den weiteren Mitgliedern meiner Prüfungskommission, dass sie sich in schwierigen Zeiten dieser zusätzlichen Aufgabe angenommen haben.

Einen großen Anteil haben auch diejenigen, die mich als Experimentator mit Proben versorgt haben, besonders wenn mal wieder eine Probe der Messung oder meinem Ungeschick zum Opfer gefallen war. Hier ist zuallererst Prof. Dr. Ladislav Bohatý zu nennen, der für die Zucht von $Cs_3Fe_2Br_9$ Kristallen verantwortlich ist und natürlich Dr. Stefan Kunkemöller und Kevin Jenni, die mich immer wieder mit $SrRuO_3$ Kristallen versorgt haben. Alle drei waren in unzähligen Diskussionen am Fortschritt dieser Arbeit und dem Verfassen der Teilpublikationen beteiligt. Außerdem danke ich Dr. Tobias Fröhlich und Sebastian Biesenkamp, die mit der Magnetstrukturbestimmung von $Cs_3Fe_2Br_9$ einen wichtigen Beitrag zum Verständnis der Substanz beigetragen haben. Ein ganz besonderer Dank gilt meinem langjährigen 2er-Büro Kollegen Dr. Oliver Breunig. Als ehemaliges Mitglied der AG-Lorenz und somit alter Hase war er auch trotz neuem Forschungsschwerpunkt immer offen für Fragen zu Software, Geräten und Methoden. Meinem Mitdoktoranden Dr. Johannes Engelmayer danke ich dafür, dass er über die gesamte Zeit stets hilfsbereit Probleme aller Art mit mir angegangen ist. Allen, die diese Arbeit kritisch lektoriert haben, danke ich für ihr schnelles und konstruktives Feedback. Den wissenschaftlichen Kollegen der roten Etage danke ich für über vier Jahre kollegiale, herzliche und nie langweilige Zeit – ob auf DPG Tagungen, CRC Retreats oder außerhalb des wissenschaftlichen Alltags z. B. bei abendlichen LAN Partys. Der gesamten technischen Abteilung des Instituts danke ich für ihre Arbeit, wie der Reparatur von defekten Geräten oder dem Anfertigen von Bauteilen für Messapparaturen. Dabei ganz besonders hervorzuheben sind diejenigen, die mich als Großverbraucher stets mit dem Lebenselixir der Tieftemperaturphysiker - flüssigem Helium - versorgt haben, Dr. Harald Kierspel, Rolf Dommel und Adel Jawadi.

Fern des II. Physikalischen Instituts gibt es auch noch eine Reihe von Menschen, ohne die die Motivation für und besonders die Ablenkung von dieser Arbeit nicht gewesen wäre. Ich danke allen Freunden in Köln, die mit jeder Badmintonstunde, jedem Tischtennistraining, jedem Fußballabend, jeder Karnevalsparty und jeder Grillrunde eine unvergessliche Zeit für mich geschaffen haben. Dazu kommen natürlich noch alle Freunde vom TTG Menden, die mir an den immer selteneren Wochenenden im Sauerland so viel Freude bereiten. Und natürlich die Mendener, die jeder gemeinsamen Unternehmung eine Leichtigkeit verleihen.

Zu allerletzt gilt der größte Dank meiner Familie. Meinen Eltern danke ich für ihre Unterstützung im gesamten Studium. Ihr steht immer an meiner Seite. Auch auf meinen Bruder konnte ich mich immer verlassen und hatte viel Spaß bei der gemeinsamen Freizeit. Aus tiefstem Herzen danke ich meiner Freundin Annkatrin, dass sie immer an meiner Seite stand, mich motivierte, spontane Laborbesuche verständnisvoll begleitete, die Freizeit so abwechslungsreich gestaltete und das Leben mit mir teilt.

Ohne euch alle wäre diese Arbeit nicht möglich gewesen.

Danke

Abstract

In this thesis, the ferromagnetic metal $SrRuO_3$ and the frustrated antiferromagnet $Cs_3Fe_2Br_9$ are investigated. Measurements of the specific heat, thermal expansion, magnetostriction, magnetization, dielectric polarization, and electric conductivity are presented.

The critical phenomena of $SrRuO_3$ at the ferromagnetic phase transition are studied using new high-quality single crystals grown with the floating-zone technique. The 3D Ising universality class is found to describe the magnetization dynamics. The $\boldsymbol{c}$ axis is confirmed as the easy-axis direction. Interestingly, the orthorhombic domain population can be influenced by a magnetic field along any cubic $\{1\,1\,0\}_c$ direction, which is a possible easy axis. A sample becomes single-domain in ~2 T at 2 K. Furthermore, $SrRuO_3$ shows a shape-memory effect and is ferroelastic and thus multiferroic below T_C. Spin-orbit coupling yields spin-split bands and a Weyl point close to the Fermi energy acts as a magnetic monopole in momentum space. This causes an additional term to the electron velocity resulting in an intrinsic contribution to the anomalous Hall effect. This describes the extraordinary temperature dependence. The anomalous Hall effect is traced even above T_C, where the spontaneous magnetization is gone. Furthermore, the anomalous softening of the magnon gap and the stiffness can be described with the Hall conductivity, which makes the explanation via the Berry-curvature contribution conclusive.

The new material $Cs_3Fe_2Br_9$ consists of face-sharing Fe_2Br_9 bi-octahedra that are arranged in triangular layers stacked to form a hexagonal structure. It orders antiferromagnetically through two temperature-driven phase transitions, one at 13.3 K, where the order is incommensurate and it becomes commensurate at 13.1 K. In contrast to other classical spin systems with the same structure that form a singlet ground state, the $S = 5/2$ moments in each bi-octahedron are oriented parallel along $\boldsymbol{c}$. The in-plane nearest-neighbor interaction overcompensates the antiferromagnetic dimer coupling. The antiferromagnetic ground state is substantially frustrated. For magnetic fields inside the triangular layers, there are only the two zero-field phases and saturation is reached in 52 T. For a magnetic field along the easy-axis ($\boldsymbol{c}$), multiple high-field experiments were performed that reveal a rich phase diagram with ten phases. Saturation is reached at 43 T which proves an astonishingly large anisotropy for typically isotropic Fe^{3+} moments. Two phases host a fractional

magnetization and the first field-induced phase hosts a ferroelectric polarization. The results are compared to analytical and numerical predictions for triangular and hexagonal lattices and related materials.

Kurzzusammenfassung

In dieser Arbeit werden das ferromagnetische Metall $SrRuO_3$ und der frustrierte Antiferromagnet $Cs_3Fe_2Br_9$ untersucht. Messungen der spezifischen Wärme, thermischen Ausdehnung, Magnetostriktion, Magnetisierung, dielektrischen Polarisation und elektrischen Leitfähigkeit werden präsentiert.
Das kritische Verhalten von $SrRuO_3$ nahe dem ferromagnetischen Phasenübergang wird an neuen hochreinen Kristallen aus dem Spiegelofen untersucht. Mit der 3D Ising Universalitätsklasse lässt sich dies am besten beschreiben. Als easy-axis wird die $\boldsymbol{c}$ Achse bestätigt. Interessanterweise kann die Besetzung der orthorhombischen Domänen mithilfe eines Magnetfelds entlang einer kubischen $\{1\,1\,0\}_c$ Richtung und somit einer möglichen orthorhombischen $\boldsymbol{c}$ Achse verändert werden. Eine Probe wird bei 2 K in einem Magnetfeld von etwa 2 T monodomänig. Darüberhinaus zeigt $SrRuO_3$ einen shape-memory Effekt und ist unterhalb von T_C ferroelastisch und somit multiferroisch. Aufgrund der Spin-Bahn Wechselwirkung spalten spin-entartete Bänder auf und Weyl Punkte nahe der Fermi Energie wirken wie magnetische Monopole im Impulsraum. Diese führen zu einem zusätzlichen Beitrag zur Geschwindigkeit der Elektronen und verursachen so einen intrinsischen Beitrag zum anomalen Hall-Effekt. Damit lässt sich dessen außergewöhnliche Temperaturabhängigkeit beschreiben. Der anomale Hall-Effekt wird auch oberhalb von T_C gefunden, wo die spontane Magnetisierung verschwunden ist. Dieser Ansatz ermöglicht es außerdem die Temperaturabhängigkeit der Magnonenanregungslücke und ihrer Steifigkeit in Abhängigkeit von der Hall Leitfähigkeit zu beschreiben. Somit ist die Beschreibung mittels der Berry-Krümmung schlüssig.

Das neue Material $Cs_3Fe_2Br_9$ besteht aus flächenverknüpften Fe_2Br_9 Bi-Oktaedern auf einem Dreiecksgitter, die zu einer hexagonalen Struktur gestapelt sind. Es ordnet in zwei Übergängen antiferromagnetisch, wobei zuerst eine inkommensurable Phase bei 13.3 K auftritt, die bei 13.1 K kommensurabel wird. Im Unterschied zu anderen isostrukturellen klassischen Spinsystemen, die einen Singlet Grundzustand zeigen, sind die $S = 5/2$ Momente in den Bi-Oktaedern parallel entlang $\boldsymbol{c}$ geordnet. Die Nächste-Nachbar-Wechselwirkung innerhalb der Dreiecksebenen überkompensiert die antiferromagnetische Intra-Dimer-Kopplung. Der entstehende antiferromagnetische Grundzustand ist erheblich frus-

triert. Wenn das Magnetfeld innerhalb der Dreiecksebene angelegt wird, gibt es neben den Nullfeldphasen keine weiteren Phasen und die Sättigung wird bei 52 T erreicht. Diverse Hochfeldexperimente wurden für ein Magnetfeld entlang der easy-axis ($\boldsymbol{c}$) durchgeführt und zeigen ein reichhaltiges Phasendiagramm mit zehn geordneten Phasen. Bei 43 T erreicht $Cs_3Fe_2Br_9$ die Sättigung. Dies zeigt eine unerwartet große Anisotropie der Fe^{3+} Momente, die sich typischerweise isotrop verhalten. Zwei Phasen zeigen eine fraktionelle Magnetisierung und die erste feldinduzierte Phase zeigt eine geringe ferroelektrische Polarisation. Die Ergebnisse werden mit ähnlichen Materialien und analytischen und numerischen Vorhersagen für verschiedene Dreiecks- und hexagonale Gitter verglichen.

Publikationen

Teilpublikationen

- K. Jenni, S. Kunkemöller, D. Brüning, T. Lorenz, Y. Sidis, A. Schneidewind, A. A. Nugroho, A. Rosch, D. I. Khomskii und M. Braden; *Interplay of Electronic and Spin Degrees in Ferromagnetic $SrRuO_3$: Anomalous Softening of the Magnon Gap and Stiffness*; Phys. Rev. Lett. **132**, 017202 (2019)

- S. Kunkemöller, D. Brüning, A. Stunault, A. A. Nugroho, T. Lorenz und M. Braden; *Magnetic shape-memory effect in $SrRuO_3$*; Phys. Rev. B **96**, 220406(R) (2017)

Weitere Publikationen

- C. P. Grams, D. Brüning, S. Kopatz, T. Lorenz, P. Becker, L. Bohatý und J. Hemberger; *Observation of chiral solitons in the quantum spin liquid phase of $LiCuVO_4$*; arXiv:1912.04705 (submitted to Nature Communications)

- D. Brüning, T. Fröhlich, M. Langenbach, T. Leich, M. Meven, P. Becker, L. Bohatý, M. Grüninger, M. Braden, T. Lorenz; *Magnetoelectric coupling in the mixed erythrosiderite $[(NH_4)_{1-x}K_x]_2[FeCl_5(H_2O)]$*; arXiv:2001.11780 (accepted by Physical Review B)

- L. Rossi, D. Brüning, H. Ueda, Y. Skourski, T. Lorenz und B. Bryant; *Magnetoelectric coupling in a frustrated spinel studied using high-field scanning probe microscopy*; Appl. Phys. Lett. **116**, 26901 (2020)

- C. P. Grams, S. Kopatz, D. Brüning, S. Biesenkamp, P. Becker, L. Bohatý, T. Lorenz und J. Hemberger; *Evidence for polarized nanoregions from the domain dynamics in multiferroic $LiCuVO_4$*; Sci. Rep. **9**, 4391 (2019)

- M. Ackermann, D. Brüning, T. Lorenz, P. Becker und L. Bohatý; *Thermodynamic properties of the new multiferroic material $(NH_4)_2[FeCl_5(H_2O)]$*; New J. Phys. **15**, 123001 (2013)

Erklärung

Ich versichere, dass ich die von mir vorgelegte Dissertation selbständig angefertigt, die benutzten Quellen und Hilfsmittel vollständig angegeben und die Stellen der Arbeit – einschließlich Tabellen, Karten und Abbildungen –, die anderen Werken im Wortlaut oder dem Sinn nach entnommen sind, in jedem Einzelfall als Entlehnung kenntlich gemacht habe; dass diese Dissertation noch keiner anderen Fakultät oder Universität zur Prüfung vorgelegen hat; dass sie – abgesehen von unten angegebenen Teilpublikationen – noch nicht veröffentlicht worden ist sowie, dass ich eine solche Veröffentlichung vor Abschluss des Promotionsverfahrens nicht vornehmen werde. Die Bestimmungen der Promotionsordnung sind mir bekannt. Die von mir vorgelegte Dissertation ist von Prof. Dr. Thomas Lorenz betreut worden.

Teilpublikationen

- K. Jenni, S. Kunkemöller, D. Brüning, T. Lorenz, Y. Sidis, A. Schneidewind, A. A. Nugroho, A. Rosch, D. I. Khomskii und M. Braden; *Interplay of Electronic and Spin Degrees in Ferromagnetic $SrRuO_3$: Anomalous Softening of the Magnon Gap and Stiffness*; Phys. Rev. Lett. **132**, 017202 (2019)
- S. Kunkemöller, D. Brüning, A. Stunault, A. A. Nugroho, T. Lorenz und M. Braden; *Magnetic shape-memory effect in $SrRuO_3$*; Phys. Rev. B **96**, 220406(R) (2017)

Köln, 27. April 2020

Daniel Brüning